LOCKHEED MARTIN ENERGY RESEARCH LIBRARIES
3 4456 0515581 8

CENTRAL RESEARCH LIBRARY
DOCUMENT COLLECTION

1

ORNL-4420
UC-25 – Metals, Ceramics, and Materials

FUELS AND MATERIALS DEVELOPMENT PROGRAM

QUARTERLY PROGRESS REPORT

FOR PERIOD ENDING MARCH 31, 1969

OAK RIDGE NATIONAL LABORATORY
operated by
UNION CARBIDE CORPORATION
for the
U.S. ATOMIC ENERGY COMMISSION

OAK RIDGE NATIONAL LABORATORY
CENTRAL RESEARCH LIBRARY
DOCUMENT COLLECTION
LIBRARY LOAN COPY
DO NOT TRANSFER TO ANOTHER PERSON
If you wish someone else to see this document, send in name with document and the library will arrange a loan.
UCN-7969
(3 3-67)

Printed in the United States of America. Available from Clearinghouse for Federal Scientific and Technical Information, National Bureau of Standards, U.S. Department of Commerce, Springfield, Virginia 22151
Price: Printed Copy $3.00; Microfiche $0.65

LEGAL NOTICE

This report was prepared as an account of Government sponsored work. Neither the United States, nor the Commission, nor any person acting on behalf of the Commission:

A. Makes any warranty or representation, expressed or implied, with respect to the accuracy, completeness, or usefulness of the information contained in this report, or that the use of any information, apparatus, method, or process disclosed in this report may not infringe privately owned rights; or

B. Assumes any liabilities with respect to the use of, or for damages resulting from the use of any information, apparatus, method, or process disclosed in this report.

As used in the above, "person acting on behalf of the Commission" includes any employee or contractor of the Commission, or employee of such contractor, to the extent that such employee or contractor of the Commission, or employee of such contractor prepares, disseminates, or provides access to, any information pursuant to his employment or contract with the Commission, or his employment with such contractor.

ORNL-4420

Contract No. W-7405-eng-26

METALS AND CERAMICS DIVISION

FUELS AND MATERIALS DEVELOPMENT PROGRAM QUARTERLY PROGRESS REPORT FOR PERIOD ENDING MARCH 31, 1969

Compiled by

P. Patriarca

Edited by

D. J. Rucker

AUGUST 1969

OAK RIDGE NATIONAL LABORATORY
Oak Ridge, Tennessee
operated by
UNION CARBIDE CORPORATION
for the
U.S. ATOMIC ENERGY COMMISSION

LOCKHEED MARTIN ENERGY RESEARCH LIBRARIES

3 4456 0515581 8

FOREWORD

This quarterly progress report describes research and development on nuclear fuels and materials performed at the Oak Ridge National Laboratory for the U.S. Atomic Energy Commission. With several exceptions, as noted below in the listing of specific programs, the work is sponsored by the Fuels and Materials Branch of the Division of Reactor Development and Technology. Classified aspects of the Nitride Fuels Development activity and work on fuels and materials for isotopic heat sources are reported separately.

The report is presented in five parts according to AEC Activity titles provided by the Fuels and Materials Branch, RDT.

Program Title	ORNL Division(s)	Person in Charge	Principal Investigator(s)
I. Fuels and Claddings			
Development of Fast-Reactor Oxide Fuels	Metals and Ceramics Chemical Technology Reactor	P. Patriarca	A. L. Lotts J. L. Scott R. E. Brooksbank
Development of High-Performance LMFBR Fuels	Metals and Ceramics Reactor	P. Patriarca	J. L. Scott H. C. McCurdy A. L. Lotts
Fission-Gas Release and Physical Properties of Fuel Materials During Irradiation	Reactor Chemistry	O. Sisman	R. M. Carroll J. G. Morgan
Zirconium Metallurgy	Metals and Ceramics	J. R. Weir, Jr.	P. L. Rittenhouse
II. Coolants			
Alkali-Metal Corrosion Studies	Metals and Ceramics Reactor	W. O. Harms	J. H. DeVan A. P. Litman
III. Radiation Damage to Structural Materials			
Behavior of Refractory Materials Under Irradiation	Reactor Chemistry	G. M. Watson	G. W. Keilholtz

Program Title	ORNL Division(s)	Person in Charge	Principal Investigator(s)
Fast-Neutron Irradiation Effects on Electrical Insulators*	Reactor Chemistry	G. M. Watson	G. W. Keilholtz
Mechanical Properties Research and LMFBR Cladding and Structural Materials Development†	Metals and Ceramics	J. R. Weir, Jr.	H. E. McCoy, Jr.
Radiation Effects in Alloys and Structural Materials	Solid State	D. S. Billington	M. S. Wechsler
IV. Techniques of Fabrication and Testing			
Tungsten Metallurgy	Metals and Ceramics	P. Patriarca	H. Inouye W. R. Martin G. M. Slaughter J. O. Stiegler H. E. McCoy, Jr.
Nondestructive Test Development	Metals and Ceramics	W. O. Harms	R. W. McClung
Joining Research on Nuclear Materials†	Metals and Ceramics	G. M. Adamson, Jr.	G. M. Slaughter
Development of LMFBR Tubing Fabrication‡	Metals and Ceramics	G. M. Adamson, Jr.	W. R. Martin
Development of Fuel Element Fabrication	Metals and Ceramics	G. M. Adamson, Jr.	J. V. Cathcart W. R. Martin R. W. McClung

*Sponsored by Reactor Power Systems Branch, Division of Space Nuclear Systems.

†Partially sponsored by Liquid Metals Branch, Division of Reactor Development and Technology.

‡Sponsored by Liquid Metals Branch, Division of Reactor Development and Technology.

Program Title	ORNL Division(s)	Person in Charge	Principal Investigator(s)
V. Engineering Properties of Reactor Materials			
Physical and Mechanical Metallurgy of Refractory Alloys	Metals and Ceramics	P. Patriarca	H. Inouye R. W. McClung D. L. McElroy G. M. Slaughter H. E. McCoy, Jr.
Cladding Materials for Space Isotopic Heat Sources*	Metals and Ceramics	P. Patriarca	R. G. Donnelly H. Inouye

*Sponsored by Isotopes and Materials Branch, Division of Space Nuclear Systems.

CONTENTS

Page

Summary xiii

Part I. Fuels and Claddings

1. Development of Fast-Reactor Oxide Fuels 3
   - Preparation of $(U,Pu)O_2$ Fuels 4
   - Development of Fabrication Processes 5
     - Sphere-Pac 5
     - Pelletization of Sol-Gel $(U,Pu)O_2$ 6
     - Capsule Fabrication 7
   - Characterization of Sol-Gel $(U,Pu)O_2$ Fuels 13
     - Analytical Chemistry 14
     - Thermal Conductivity of UO_2 at Low Temperatures 14
     - Thermal Conductivity of Lithium Fluoride 16
     - Radial Heat-Flow Apparatus for Measurements at 10 atm and 1000°C 19
     - Deformation of UO_2 19
     - Analytical Characterization 19
     - Thermodynamic Calculations 24
   - Irradiation Testing of $(U,Pu)O_2$ Fuels 24
     - Uninstrumented Thermal-Flux Irradiation Tests 25
     - ORR Instrumented Tests 28
     - Transient Testing of Sol-Gel $(U,Pu)O_2$ 30
     - Fast-Flux Irradiation Tests 33
     - Irradiation Test Calculations 33
2. Development of High-Performance LMFBR Fuels 40
   - Synthesis, Fabrication, and Characterization of Nitride Fuels 41
     - Synthesis and Fabrication of Uranium Mononitride with ^{15}N Isotope 41
     - Synthesis and Fabrication of Mixed Nitrides 43
     - Metal Nitride Synthesis Apparatus 45
     - Characterization of UN and (U,Pu)N 45
   - Synthesis, Fabrication, and Thermodynamic Properties of Carbonitride Fuels 47

Manufacture of UC, UN, and U(C,N) From UO_2 47

Compatibility of Mixed-Nitride and Carbonitride Fuels with LMFBR Cladding Alloys 56

Properties of Vanadium Carbonitride Solutions at High Temperatures 56

The Crystal Structures of UVC_2 and UVN_2 58

Measurements of the Physical Properties of (U,Pu)N Alloys 66

Irradiation Testing of Nitride Fuels for LMFBR Applications 66

Thermal-Flux Irradiation Tests 66

Design Analysis of Irradiation Capsule for ETR 68

3. Fission-Gas Release and Physical Properties of Fuel Materials During Irradiation 71

The Effect of Stored Energy in UO_2 and UN on Measurements of Thermal Diffusivity During Irradiation 71

Effect of Temperature and Burnup on Release of Fission Gas from $(U_{0.75},Pu_{0.25})O_2$ 72

Uranium Nitride Experiment 74

4. Zirconium Metallurgy 77

Fabrication and Texture Control of Zirconium Tubing 77

Texture Effects, Texture Development, and Anisotropy of Properties 79

Texture Development in Zircaloy Tubing 79

Demonstration of Texture Control 82

High-Temperature Deformation of Zirconium Single Crystals 85

Part II. Coolants

5. Alkali-Metal Corrosion Studies 89

Mass Transfer of Interstitial Impurities Between Vanadium Alloys and Sodium 89

Effects of Oxygen on the Compatibility of Vanadium and Sodium 89

Mass Transport of Interstitial Impurities Between Type 300 Series Stainless Steels and Vanadium Alloys 90

Interstitial Contamination of Vanadium and Its Alloys . 92

Compatibility of Stainless Steel and Insulation in LMFBR Systems 92

The Effect of Insulation on the Oxidation of Stainless Steel 93

Effect of Small Sodium Leaks 99

Corrosion of Refractory Alloys in Lithium, Potassium, and Sodium 100

Effect of Oxygen on Compatibility of Refractory Metals and Alkali Metals 100

Corrosion of Refractory Alloys by Lithium 105

T-111 Forced Circulation Loop (FCLLL-1) 106

T-111 Forced Circulation Loop with Tungsten and Tungsten Alloy Test Section (FCLLL-2) 113

Part III. Radiation Damage to Structural Materials

6. Behavior of Refractory Materials Under Irradiation 119

Irradiation Damage to Nonfissionable Refractory Materials . 119

Refractory Metal Carbides 119

Effects of Irradiation on LMFBR Fuels 121

Effects of Helium Gas Produced by Fast Neutrons in Depleted UN 121

Fast-Neutron Effects on Materials for Neutron Absorption in Fast Reactors 121

7. Fast-Neutron Irradiation Effects on Electrical Insulators . . 123

General Survey of Fast-Neutron Effects on Electrical Insulators 123

Irradiation of High-Density Commercial Al_2O_3 Products Considered for Thermionic Insulators 124

Gross Damage 124

Volume Expansion 127

Conclusions 128

8. Mechanical Properties Research and LMFBR Cladding and Structural Materials Development 131

Effects of Irradiation on the Mechanical Properties of Austenitic Stainless Steels 131

Radiation Damage in Incoloy 800 134

Cyclotron Injection of Helium to Simulate Fast-Reactor Irradiation 141

The Effect of Aging on the Creep Properties of Titanium-Modified Type 304L Stainless Steel Containing Cyclotron-Injected Helium 141

Utilization of EBR-II 146

Transmission Electron Microscopy of Stainless Steel and Nickel Irradiated in EBR-II 146

Vanadium Alloy Studies and Effects of Impurities 151

Voids in Vanadium Irradiated in EBR-II 151

Mechanical Properties of Hastelloy N and Related Compositions 158

Aging of Titanium-Modified Hastelloy N 158

Electron Microscopy of Hastelloy N 162

9. Radiation Effects in Alloys and Structural Materials 169

Part IV. Techniques of Fabrication and Testing

10. Tungsten Metallurgy 173

Primary and Secondary Working of Tungsten and Tungsten Alloys 173

Extrusion of Tungsten and Tungsten Alloys 173

Installation of Experimental Tube Reducer 177

Chemical Vapor Deposition of Tungsten Alloys 177

Deposition of Tungsten-Rhenium Alloys 177

Effect of Hydrogen Fluoride on Deposit Morphology . . . 181

Metallurgical Properties of Tungsten Alloys 183

Formation of Gas Bubbles in CVD Materials 183

Long-Time Creep-Rupture Properties of Tungsten Alloys . . . 185

11. Nondestructive Test Development 188

Electromagnetic Inspection Methods 188

Eddy Currents 188

Infrared 192

Ultrasonic Inspection Methods 192

Optical Visualization of Ultrasound 192

Frequency Analysis 193

Penetrating Radiation and Holographic Inspection Methods . . 196

Radiation Attenuation 196

Radiation Scattering 197

12. Joining Research on Nuclear Materials 198

Effect of Minor Variations in Chemical Composition on Weldability 198

Effect of Minor Elements on Hot Ductility of Inconel 600 199

Effect of Minor Elements on Hot Cracking in Inconel 600 199

Weldability of the 18% Cr–8% Ni Class of Stainless Steels 200

Effect of Certain Minor Elements on the Ductility of Incoloy 800 at Intermediate Temperatures 202

Development of Welding Procedures for Commercial and Modified Alloys 207

Joining Development in Support of the Fast Flux Test Facility 207

Effect of Defects on Mechanical Properties of Weldments . . 209

13. Development of LMFBR Tubing Fabrication 211

Fabrication Studies on Type 316 Stainless Steel 211

Drawing of Type 316 Stainless Steel Tubing 211

Effect of Boron on the Hot Ductility of Type 316 Stainless Steels 217

Fabrication Studies on Titanium-Modified Type 304 Stainless Steel 219

Evaluation of Drawn Titanium-Modified Type 304L Stainless Steel Tubing 219

14. Development of Fuel Element Fabrication 222

Fabrication Studies of Dispersion Fuel Plates 222

Effect of Hydrogen in Aluminum — Blisters in Fuel Plates 222

Fabrication of Plates Containing Burned U_3O_8 226

Characterization of Electrolessly Deposited Nickel Coatings 227

Irradiation Testing of Dispersion Fuel Plates 230

Status of Current and Planned Tests in the ETR 230

Preparation and Characterization of Mini-Type Test Plates Containing U_3O_8 231

Preparation and Characterization of Mini-Type Test Plates Containing B_4C 235

Determination of Homogeneity in Fuel Plates 237

Radiographic Densitometry 237

X-Ray Attenuation 238

Part V. Engineering Properties of Reactor Materials

15. Physical and Mechanical Metallurgy of Refractory Alloys . . . 243

Basic Physical Metallurgy Studies 243

Solubility, Diffusivity, and Permeability of Interstitials in Refractory Metals 243

Development of Age-Hardening Refractory Alloys 243

Long-Time High-Temperature Mechanical Properties of Commercial Refractory Alloys 248

Niobium Alloys 248

Molybdenum and Tantalum Alloys 249

Studies of Physical Properties 250

High-Temperature Electrical Resistivity 250

Development of an Electrical Heating Method to Measure Thermal Conductivity 251

Welding and Brazing 251

Development of Brazing Alloys 251

16. Cladding Materials for Space Isotopic Heat Sources 254

Studies of Commercial Superalloys 254

Creep Testing of Haynes Alloy No. 25 254

Interaction of Stress and Vacuum on Properties of Superalloys at Elevated Temperatures 256

Development of Improved Alloys 256

SUMMARY

PART I. FUELS AND CLADDINGS

1. Development of Fast-Reactor Oxide Fuels

We fabricated two fuel pins containing Sphere-Pac fuels for irradiation in the Oak Ridge Research Reactor (ORR) instrumented capsules and fabricated one capsule for irradiation of Sphere-Pac fuels in the Engineering Test Reactor (ETR). Our main emphasis in the fabrication of capsules during the quarter was the fabrication of two capsules for transient testing of sol-gel fuels in the Transient Reactor Test Facility (TREAT). We continued the fabrication of pellets with 85 and 91% of theoretical density for the two TREAT experiments.

We compared the gravimetric and NITROX methods of analyzing the ratio of O to metal. The average of four batches loaded into the Experimental Breeder Reactor-II (EBR-II) fuel rods was 1.987 for gravimetric and 1.985 for the NITROX method. We began trial calculations to determine the important variables in the calculation of burnup. In the continuing studies of the plastic deformation of UO_2, results showed that UO_2 specimens prepared from ammonium diuranate, although of higher density (97 rather than 92%), are more susceptible to deformation than specimens prepared from sol-gel. Further studies were conducted to determine the relationship between lattice parameter, composition, and O activity of $(U,Pu)O_2$ and particularly to determine the effect of thermal gradients on composition. The ratio of O to metal obtained from measurements of lattice parameters of a UO_2 rod that had been placed in a thermal gradient of 1820 to 950°C ranged from 2.002 to 1.998, respectively.

Irradiation of two ETR uninstrumented capsules, which contain Sphere-Pac $(U,Pu)O_2$, continued normally. One of these, operating at a linear heat rate of about 16.5 kw/ft, achieved a burnup level of about 7% fissions per initial metal atom (FIMA). One ETR capsule, which operated at a linear heat rate of 18 kw/ft, achieved its target burnup level of 5% FIMA and was removed from the reactor. The second ORR instrumented capsule containing Sphere-Pac $(U,Pu)O_2$ fuel was placed into operation.

Preliminary analysis of the data from the second capsule, which is now being operated, shows that the conductivity of the Sphere-Pac fuel is essentially the same as that of pellet fuels of comparable smear density; this supports the principal conclusion from the operation of the first instrumented capsule.

Five encapsulated fuel rods, all containing sol-gel-derived $(U_{0.8},Pu_{0.2})O_2$ Sphere-Pac fuel, were incorporated into subassembly X050 of the EBR-II and placed under irradiation on February 27, 1969.

In our continuing development of methods of calculations for irradiation tests, it was shown that predictions of our fuel model are in excellent agreement with experimentally determined burnups for $(U,Pu)O_2$ fuel pins and with measured and calculated temperatures for the first instrumented capsule assembly. We further refined the FMØDEL code for fuel performance to include an analysis for fuel restructuring and temperature distribution, an analysis for eleastic and plastic creep deformation, a calculation for release of fission gas and gas pressure, and an empirical description of intrinsic swelling of the cladding due to the condensation of vacancies formed by irradiation damage.

2. Development of High-Performance LMFBR Fuels

A 500-g batch of $U^{15}N$ pellets was successfully fabricated. These pellets will be used as a standard in a study of the effects of n,p and n,α reactions with ^{14}N on the performance of $U^{14}N$.

The rate-controlling step in the conversion of UC_2 to U(C,N) was identified to be the diffusion of C from the UC_2-U(C,N) interface to the nearest free-C site. The activation energy for the diffusion of C under these conditions is 77.7 ± 3.7 kcal/mole. Thus, the reaction rate is enhanced by a uniform, fine distribution of free C throughout the microstructure.

Studies on the removal of free C from structures consisting of U(C,N) plus C showed that H_2 alone is ineffective. The presence of small amounts water or CO greatly accelerates the removal of C.

The solubility of N_2 in UC_2 was found to be a maximum of 8 at. % at 1700°C at a N_2 pressure of 400 torr.

In studies to assess the compatibility of V with C and nitrides, the complete mutual solubility of VC and UN was observed. The lattice parameters of solid solutions showed negative deviations from Vegard's law.

Two new phases, UVC_2 and UVN_2, were discovered. Their crystal structures were deduced to be isomorphous with $UMoC_2$.

3. Fission-Gas Release and Physical Properties of Fuel Materials During Irradiation

A new experiment using a hollow cylinder of UO_2 has been constructed to measure thermal diffusivity during irradiation.

Spheroids of $(U_{0.75},Pu_{0.25})O_2$ fuel are being irradiated. The gas release shows the same characteristics as cylinders of the same material irradiated previously. We have found that the temperature at which swelling begins is a linear function of burnup.

Metallographic examination of UN specimens irradiated in an Al_2O_3 holder shows the specimens reacted chemically with the holder to form a UO_2 compound by removing O from the Al_2O_3.

4. Zirconium Metallurgy

Experimental fabrication of Zircaloy-4 tubing was completed and described in a topical report. Examination of the texture, texture development, and texture gradients in this tubing is in progress. Our preliminary evaluation of these data indicates that all of the textures can be explained by consideration of the stresses acting in the different fabrication processes.

As a result of our examination of the experimentally fabricated tubing, we have demonstrated the feasibility of texture control through control of the ratio between wall and diameter reductions during fabrication. Also, we have obtained the first direct evidence that the development of texture occurs progressively from the outer surface to the inner surface of the tubing as fabrication proceeds.

The testing of Zr single crystals in a state of pure shear stress is beginning. These experiments will be used to determine the deformation systems acting in Zr at elevated temperatures.

PART II. COOLANTS

5. Alkali-Metal Corrosion Studies

We have evaluated the dependence on time of the interaction of O with V in Na at 600 °C. The tests were conducted in both Mo and stainless steel capsules for 100 to 500 hr. With either type capsule, the O uptake by 1/16-in. V coupons increased with exposure time up to 300 hr and then leveled off.

A thermal convection loop test was started in which unalloyed V serves directly as the heated section. The ratio of the surface areas of V and stainless steel is 0.24. The loop will operate with Na low in O content for 3000 hr at 700 °C maximum temperature.

A vacuum furnace was installed to study the reaction of V alloys with residual gases in vacuum. The interstitial concentrations of specimens of unalloyed V did not change significantly after 810 hr in this diffusion-pumped system at 3×10^{-8} torr.

We have continued studies on the scaling of stainless steels at elevated temperature in moist and dry air as affected by the presence of thermal insulations. Initial experiments were conducted on stainless steel and insulation couples to establish reference data for future studies involving leaks of Na. The oxidation rate of machined surfaces of type 316 stainless steel was significantly lower than that of pickled surfaces. Oxidation rates for pickled type 304L stainless steel approached that for specimens of type 316 stainless steel as machined. The presence of a SiO_2-Al_2O_3 insulating material had little effect on oxidation over the temperature range studied (730 to 815 °C). A small increase in scaling was noted, however, in the case of an asbestos-base material.

The effect of O on the compatibility of Ta with Na was evaluated at 600 °C. Tantalum exposed to Na containing 50 to 2000 ppm O gained weight and exhibited an apparent oxide scale. Additions of O to the Ta before test led to severe penetration of the Ta by Na.

We have evaluated the potential sources of error in the gettering-vacuum-fusion technique used to determine the O content in Na or K.

Transfer of O from the Mo capsule to the Zr specimen contributes a blank of about 10 ppm. Handling steps involved in encapsulating the alkali metals make a negligible contribution.

Bend tests were conducted at room temperature to measure the ductility of specimens of T-222 sheet that had been contained in a T-222 thermal convection loop that circulated Li for 3000 hr at 1350°C. Specimens from an intermediate-temperature zone (1220 to 1280°C) were relatively brittle, while those from either hotter or colder regions were considerably more ductile. Aging temperature appeared to have a more significant effect on ductility than the interstitial changes produced by the Li. We have essentially completed the assembly of a T-111 forced circulation loop (FCLLL-1) designed to circulate Li at 1370°C. A leak check of the loop after it was mounted in the vacuum chamber revealed a crack near an internal weld that anchored a specimen assembly. The crack was successfully repaired by overlaying it with Nb–1% Zr filler metal.

PART III. RADIATION DAMAGE TO STRUCTURAL MATERIALS

6. Behavior of Refractory Materials Under Irradiation

We started the following experiments, which will conclude the investigation of fast-neutron effects on carbides of refractory metals (Ti, Zr, Ta, Nb, and W): (1) short-term, low-temperature irradiations, (2) out-of-reactor postirradiation annealing, and (3) electron microscopy of irradiated carbides. The purpose of these experiments is to obtain additional data for constructing a model for neutron damage. Preliminary results from the annealing experiments indicate that the fractional volume shrinkage during annealing is the same for each of the five types of carbides regardless of the magnitude of the original volume expansion that occurred during irradiation.

Components of a high-temperature (1000°C) assembly for irradiating depleted UN, UC, and U (50 mole % C, N) were fabricated. This experiment is designed for evaluating the effects on nitride fuels of helium gas generated through the $^{14}N(n,\alpha)^{11}B$ fast-neutron reaction.

Planning and engineering design were started on an EBR-II assembly for irradiation of Ta metal, TaC, and possibly other materials with large neutron-absorption cross sections. The objective of this task is to provide information needed for developing materials for control of the reactivity of fast reactors.

7. Fast-Neutron Irradiation Effects on Electrical Insulators

Metallographic examinations of four commercial polycrystalline alumina products irradiated in a short-term ETR assembly were completed. Specimens irradiated at 580 to 1070°C that did not have separation at the grain boundaries expanded in volume linearly with fast fluence. The expansion increased from 1.9 to 3.0% over the fast-fluence range 1.3 to 2.8×10^{21} neutrons/cm^2. Values for specimens with separation at grain boundaries were considerably higher. There was a reduced expansion and no separation at grain boundaries found in specimens irradiated at 1100°C. At very much higher temperatures, however, separation at the grain boundaries became very severe. In general, the severity of this separation increases with increasing volume expansion of the grains and with increasing grain size. No definite correlation could be found between the degree of separation and gross fracturing of specimens, which appears to be related to the presence of impurities or unknown factors in the fabrication.

8. Mechanical Properties Research and LMFBR Cladding and Structural Materials Development

Specimens of standard types 316 and 316L stainless steel and Ti-modified (about 0.2% Ti) types 304, 304L, 316, and 316L stainless steel were irradiated to a fast fluence of 1.4×10^{21} neutrons/cm^2 (> 1 Mev) over a period of 4000 hr at temperatures of 350, 450, and 550°C. The postirradiation yield stresses measured at the respective irradiation temperatures were generally 10 to 30% higher than that of the unirradiated control sample; the Ti-modified type 304L stainless steel was an exception and showed much larger increases. The fracture strains were reduced at all temperatures by irradiation, and the magnitude of the

reduction increased with increasing test temperature. The Ti-modified steels had higher fracture strains than the standard steels.

We have observed that the mechanical properties of Incoloy 800 vary appreciably with thermal treatments as well as irradiation. Electron microscopy has revelaed that the amount and distribution of the precipitates vary with annealing and aging. The precipitates have been identified as $Cr_{23}C_6$ and titanium sulfide.

Samples of Ti-modified type 304 stainless steel were given various heat treatments and then injected with 20 ppm He in a cyclotron. A heat treatment that produced precipitates in both grain boundaries and matrix gave the optimum rupture life; the optimum fracture strains were produced in material that had been recrystallized at 925°C.

Several samples of Ni 270 and type 304 stainless steel were irradiated in the EBR-II to fast fluences of 10^{18} to 10^{20} neutrons/cm^2 over a wide range of temperatures. We used transmission electron microscopy to observe the defects produced and compared the nature of the damage in these two materials. We also observed the defects produced in a type 304L stainless steel shroud tube where the peak fluence was 5×10^{22} neutrons/cm^2 (> 0.1 Mev).

We have examined a piece of V removed from EBR-II after irradiation to a fast fluence of 1.7×10^{22} neutrons/cm^2 (> 0.1 Mev) at 630°C. The measured void density was 5.2×10^{15} voids/cm^3, and the computed swelling was 0.57%. Postirradiation annealing from 600 to 900°C revealed little change in structure at 650°C and complete annealing at 900°C.

An attempt to analyze statistically our aging results on the Ti-modified Hastelloy N revealed that a preaging anneal of 1 hr at 1260°C gave results that contradicted those obtained for other anneals. This may be due to the grain growth that occurs during this anneal or the solution of additional solutes.

The key to a modified Hastelloy N seems to be the correct precipitate structure. The desired structure seems to result when the MC type of carbide is formed, and we have found that Ti, Zr, Hf, and Nb favor the formation of this type.

9. Radiation Effects in Alloys and Structural Materials

This program is being phased out during fiscal year 1969. All progress before termination of the program in fiscal year 1970 will be documented in separate topical reports.

PART IV. TECHNIQUES OF FABRICATION AND TESTING

10. Tungsten Metallurgy

Our studies on the effect of extrusion temperature on the microstructure of duplex-extruded W have shown that at extrusion temperatures of 1450°C and higher, wrought starting structures from the primary extrusion recrystallize during preheat. At extrusion temperatures as low as 1150°C, recrystallization of a wrought starting structure occurs due to the additional heat generated during deformation. The experimental tube reducer has been installed and checked.

In our studies of chemical vapor deposition (CVD), we have found that the optimum pressure for obtaining uniformly thick sheets of W–5% Re is between 50 and 75 torr. Additional experiments with HF additions to the H_2-WF_6 gas mixture have shown that HF does not adversely effect the deposition efficiency or surface texture of W deposits.

Further studies on the formation of gas bubbles in CVD materials have shown a correlation between the fraction of the melting point at which the metal is deposited and the occurrence of gas bubbles after annealing. We believe that the deposition temperature controls the supersaturation of vacancies in the deposited metal, thus controlling the nucleation of gas bubbles.

Additional long-time creep-rupture data have been obtained for arc-cast W alloys and used to determine Larson-Miller master curves for time to 1% creep.

11. Nondestructive Test Development

We are developing new techniques and equipment for the nodestructive testing of materials and components. The major emphasis has been on eddy-current, ultrasonic, penetrating radiation, and holographic methods.

In our analytical work on electromagnetic phenomena, we have continued to use closed-form solutions to integral equations applicable to a variety of eddy-current tests. This work has been directed toward determining optimum coil designs for detecting flaws in tubing.

Transparent plastic models of butt welds containing simulated flaws have been made for use in our schlieren system.

We developed a computer program to calculate x-ray mass-absorption coefficients for Al and U_3O_8 in a fuel plate. Work is in progress for use of radiation scattering for measuring the thickness of cladding.

12. Joining Research on Nuclear Materials

Our work on the effect of minor elements on the hot ductility of Inconel 600 is nearing completion. In addition to the effects of individual elements on zero-ductility temperature (ZDT), we have found that exposure of certain compositions to temperatures 25 to 35°C above ZDT influences their ability to recover ductility on cooling. Preliminary data indicate that ductilities of 8% or less can prevail to temperatures as low as 1200°C.

Studies to determine the effect of selected quantities of minor elements on the propensity of Inconel 600 toward hot cracking have continued under subcontract at Rensselaer Polytechnic Institute. A standard factorial analysis has been conducted on the effects of S, P, Mn, Si, Ti, and Al on cross-sectional area, depth of penetration, and diameter of gas tungsten-arc spot welds in Inconel 600. The various elements exhibited different effects depending upon the criterion involved; for instance, Al drastically decreases penetration while having a much smaller effect on increasing the spot width. However, this type of analysis could not evaluate the effect of varying amounts, and the data are being reevaluated by linear regression analysis.

We are also investigating the relationships between major elements and microstructure that control the contents of delta ferrite in stainless steel weld metal, since delta ferrite is used to control hot cracking. A study of the effect of minor elements on the mechanical properties of Incoloy 800 at intermediate temperatures is well under way. The

mechanical effects have been correlated with microstructure, and electron microscopy studies are also under way.

In our stainless steel program in support of the Fast Flux Test Facility (FFTF), we completed shipment of most test specimens to Battelle Northwest Laboratories.. We purposely made defects in welds in Inconel 600 by electron-beam welding. Studies of surface-connected defects by means of scanning electron microscopy has continued, and it has been documented that hot cracking in the liquid-solid region during welding of TZM leads to more extensive cold cracking upon cooling through the ductile-to-brittle transition temperature.

13. Development of LMFBR Tubing Fabrication

Our fabrication studies have been directed toward type 316 stainless steel since our work on the development of fabrication techniques for Ti-modified type 304 stainless steel has been phased out. Small-diameter tubing, 0.250 in. in outside diameter × 0.016 in. in wall thickness, has been made with six levels of cold work, 5, 10, 20, 30, 40, and 50%. Our investigation of interpass annealing temperatures between 800 and 2050°C indicates that recrystallized material can be obtained and, depending upon the level of cold work, that grain sizes can be as large as ASTM 5 or 6 or as small as ASTM 12.

The effect of B on the hot ductility of type 316 stainless steel was examined and compared with the results obtained for a typical Ni-base alloy, Inconel 600. For B contents between 5 and 200 ppm by weight at 900 to 1200°C, we found no beneficial effect of B on hot ductility. Hot-working temperature appears to be a more important factor than B content.

14. Development of Fuel Element Fabrication

In our studies of blistering, we are trying cyclotron bombardment as a method of adding known quantities of H to Al compacts. Surprisingly, no blisters formed on compacts annealed at temperatures up to 550°C after 0.33 ppm H was added.

Burned U_3O_8 was shown to be compatible with Alcoa 101 Al powder and type 6061 Al cladding, as evidenced by the absence of a reaction, at fabrication temperatures up to 600°C.

Nickel coatings deposited electrolessly on plates of types 6061 and 2219 Al were characterized both before and after heat treatment. In both cases, heating to 500°C caused serious spalling, but heating at 300°C caused no visible changes. The coating on both alloys resisted the thermal shock of being quenched in water from gradually increasing temperatures. No spalling was evident on the type 2219 Al samples after quenching from temperatures up to 475°C or on type 6061 Al after quenching from 350°C. The thickness of the coatings made it difficult to obtain reproducible results for hardness. While the coating became somewhat more hard after the 300°C treatment, it was still surprisingly ductile. As expected, the width of the interface between the materials increased during heat treatment, the increase for type 6061 Al being greater than that for type 2219 Al.

Work has continued on the use of radiography and film densitometry to measure inhomogeneities in dispersion fuel plates. It has been shown that the density of a film may be varied by the length of the film, the orientation of the axis of the x-ray tube, and the kind of safelights used. When fuel plates for the Advanced Test Reactor (ATR) were inspected for fuel inhomogeneity by both densitometry and by x-ray attenuation, the latter method was much quicker and revealed many inhomogeneities missed by radiography.

Testing of miniature fuel plates in the ETR was interrupted by a malfunction of the loop. The samples were not harmed and will be returned to the reactor as soon as possible. The program for future irradiations was agreed upon, and fabrication of samples was started. New samples containing sol-gel and burned U_3O_8 have been prepared as mini-type test plates for insertion later in the year. To determine if the increase in He release during irradiation would cause difficulties in an advanced HFIR core, we prepared and characterized samples for irradiation that contain up to 2.0 wt % B_4C.

PART V. ENGINEERING PROPERTIES OF REACTOR MATERIALS

15. Physical and Mechanical Metallurgy of Refractory Alloys

The diffusivity, solubility, and permeability of N in W between 1000 and 1800°C have been determined.

The aging characteristics and the morphology of the precipitated phases in alloys in the Nb-Hf and Ta-Hf systems depend on the quenching rate and the composition of the alloys. The ductility of alloys exhibiting a uniform dispersion of the second phase is greater than that of alloys showing precipitation at the grain boundaries.

The effect of heat treatment on the creep-rupture properties of SU-16 at 980°C has been determined. The stress-rupture properties of C-129Y at 980, 1095, and 1205°C are reported. Electrical resistivity measurements of Ta to 2600°C were within 5% of the literature values. An electrical heating method to measure thermal conductivity is being developed. The evaluation of alloy 8H (Ti–20% Zr–15% Ge) as an acceptable filler metal for joining graphite has been ascertained. Shear tests of brazements indicate that the braze is equal to or stronger than base metal of a similar geometry.

16. Cladding Materials for Space Isotopic Heat Sources

Creep testing of Haynes alloy No. 25 for short times between 1000 and 1300°C and for long times between 600 and 900°C shows weldments to have the same strength as base metal. Weld failures were quite common at the lower temperatures.

The effects of vacuum on the creep behavior of Haynes alloy No. 25 at 800°C are greatly diminished as the specimen thickness is increased from 0.030 to 0.060 in. At 900°C, the creep rate of a 0.030-in.-thick specimen in vacuum is about 40 times as great and the rupture life is about a twenty-fifth as great as when tested in air. The initial rate of evaporation of Haynes alloy No. 25 is 6 to 10 times the rate of Hastelloy N, but the two are comparable after 1000 hr.

The transformation from disorder to order increases the hardness, tensile strength, and creep strength of alloys and shows no tendency to

overage. The evaporation rate of binary alloys of Co, Ni, or Fe with Pt decreases with the Pt content. The evaporation process increases the Pt content at the alloy surface. Ordered alloys evaporate at a lower rate than disordered alloys.

PART I

FUELS AND CLADDINGS

1. DEVELOPMENT OF FAST-REACTOR OXIDE FUELS

P. Patriarca A. L. Lotts

The objective of this program is to obtain an economically optimized $(U,Pu)O_2$ fuel cycle for a liquid-metal fast breeder reactor (LMFBR) by extending the performance capability and advancing the fabrication technology of oxide fuels. These fuels have the most advanced technology and greatest potential for reliable operation in first-generation LMFBR's. They have been tested in fast-flux environments but as yet have not been exposed under actual prototypic conditions. Currently, the burnup and heat rate are limited to about 50,000 Mwd/metric ton and 16 kw/ft, respectively, based on irradiation experiments with fuels that are not necessarily optimized for thermal, chemical, and mechanical performance.

The capability of oxide fuels can possibly be improved by adjusting structures or void distribution in the fuels. We emphasize irradiating fuels derived from the sol-gel process with thoroughly characterized structures and void distributions different from those of the oxide fuels irradiated heretofore. These include fuels fabricated by Sphere-Pac, vibratory compaction, extrusion, and pelletization. We compare the performance of these with the performance of reference fuels such as pellets derived from mechanically blended powders and coprecipitated material. The development of computer programs to assist in the analysis of test results and the development of a mathematical model to predict the performance of a fuel rod are integrated with the test program.

Preparation of $(U,Pu)O_2$ Fuels

W. T. McDuffee

This quarter we prepared 700 g of dense, $(U_{0.8},Pu_{0.2})O_2$ microspheres; 65% of the product was in the 400- to 600-μm-diam range, and the remainder was in the < 25-μm-diam range. This material, which was shipped to Babcock and Wilcox Company, was prepared from a blend of 20% enriched UO_2 sol and a PuO_2 sol, both of which we prepared.

We pretreated the UO_2 sol to reduce the formate content before we blended it with the PuO_2 sol, and we aged the sol after blending. This treatment led to a superior product with a high yield (Table 1.1).

Table 1.1. Characteristics of Dense, $(U_{0.8},Pu_{0.2})O_2$ Microspheres Shipped to Babcock and Wilcox Company

	Diameter	
	400 to 600 μm	< 25 μm
Ratio of Pu:U+Pu	20.8	19.8
Round and free of cracks, % total	87.0	90[a]
Density, g/cm^3		
Bulk	10.83[b]	6.3
Pressure	10.89	11.42
Surface area, m^2/g	0.0055	0.504
Pore Volume, cm^3/g	0.0005	0.07
Ratio of O to metal, gravimetric	1.994	1.998
Carbon content, ppm	< 20	< 20
Crushing strength, g	1800–2000	

[a]Ninety percent of the fines made were < 25 μm.

[b]Ninety-eight percent of theoretical density.

In addition to these microspheres, we also prepared 300 g (heavy metal) of 9% enriched UO_2 sol that, along with 40 g (heavy metal) of PuO_2 sol, was used in studies of fuel pelletization.

Development of Fabrication Processes

J. D. Sease

Fast reactors that operate at high specific powers will require fuel pins of small diameter with fuel ranging from 80 to 90% of theoretical density and a high fissile loading. Our work is to develop procedures for Sphere-Pac and pelletization and for fabricating irradiation capsules.

Sphere-Pac (W. L. Moore)

Previous development of the Sphere-Pac process has been concerned with laboratory-scale loading.[1,2] We are assessing variables that affect the engineering scale-up and economics of the process. We reviewed the literature and set up additional equipment for development studies.

A vibrator apparatus capable of handling rods up to 1 in. in diameter and 48 in. long was fabricated and installed in a vented hood. Screened funnels, follower rods, hardware, and ThO_2 microspheres were acquired for the initial studies. A study was begun to determine the best method of characterizing the size distribution of both the coarse and fine microspheres. Thoria microspheres with diameters of 530 to 595 μm and < 37 μm were submitted for analysis of the distribution of particles sizes by microscope measurement, Coulter counter, micromerograph, and quantitative television monitor. Initially, studies will center on determining the effects of the diameter of the tube and the height of the coarse bed on the time needed for infiltrating the fine microspheres. Future work will investigate the effect of the distribution of particle sizes of both the coarse and fine fractions on loading time and volume packing.

---

[1]F. G. Kitts, R. B. Fitts, and A. R. Olsen, "Sol-Gel Urania-Plutonia Microsphere Preparation and Fabrication into Fuel Rods," pp. 195–210 in Intern. Symp. Plutonium Fuels Technol., Scottsdale, Ariz., 1967, Nucl. Met. 13, American Institute of Mining, Metallurgical, and Petroleum Engineers, New York, 1968.

[2]R. B. Fitts, A. R. Olsen, and J. Komatsu, "Sphere-Pac Fabrication of Sol-Gel Nuclear Fuels," paper presented at the Fall Meeting of the American Ceramic Society, Nuclear Division, Pittsburgh, Pa., October 6–9, 1968. Abstract only in Am. Ceram. Soc. Bull. 47(9), 844 (1968).

Pelletization of Sol-Gel $(U,Pu)O_2$ (R. A. Bradley)

Urania-plutonia pellets derived by the sol-gel process are required for instrumented irradiation tests in the Oak Ridge Research Reactor (ORR) and for transient tests in the Transient Reactor Test Facility (TREAT). The transient tests in the TREAT require pellets with densities of 84 and 91% of theoretical and a ratio of O to metal of 1.980 ± 0.005. Our task is to develop the necessary fabrication procedures and to produce pellets for these irradiation experiments.

The preparation of the $(U_{0.8},Pu_{0.2})O_2$ powder to be used for the TREAT pellets was described previously.[3,4] The calcination of the powder and the preparation of 84% dense pellets were also described.[5] This quarter our primary effort has been to adjust the ratio of O to metal in pellets and microspheres to be used in loading the TREAT fuel pins. We have also conducted additional calcining experiments and made more low-density pellets.

Adjustment of Ratio of Oxygen to Metal. — In four of the six sintering runs used in making the 84% dense TREAT pellets, we found the ratio of O to metal to be 2.000. According to the thermodynamic data of Rand and Markin,[6] a partial pressure of O_2 corresponding to 40 ppm H_2O in Ar–4% H_2 at 1450°C could yield $(U_{0.8},Pu_{0.2})O_{1.98}$ at equilibrium. In subsequent heat treatments to reduce the ratio of O to metal in the TREAT pellets, a P_2O_5 moisture monitor indicated that the H_2O content of the effluent furnace gas exceeded 100 ppm. We found, even when extreme care was taken to ensure that the furnace system was free of leaks at

---

[3]W. L. Moore and R. A. Bradley, Fuels and Materials Development Program Quart. Progr. Rept. June 30, 1968, ORNL-4330, pp. 7–10.

[4]R. A. Bradley, Fuels and Materials Development Program Quart. Progr. Rept. Sept. 30, 1968, ORNL-4350, pp. 5–7.

[5]R. A. Bradley, Fuels and Materials Development Program Quart. Progr. Rept. Dec. 31, 1968, ORNL-4390, pp. 5–7.

[6]M. H. Rand and T. L. Markin, "Some Thermodynamic Aspects of $(U,Pu)O_2$ Solid Solutions and Their Use as Nuclear Fuels," pp. 637–650 in Thermodynamics of Nuclear Materials, 1967, International Atomic Energy Agency, Vienna, 1968.

room temperature, that it was not always possible to maintain a tight system throughout the heat treatment. When there were no leaks in the furnace, the H_2O content of the effluent gas would decrease to less than 20 ppm after a few hours at 1450°C, and the ratio of O to metal in the pellets would be 1.98 ± 0.01.

The moisture monitor enabled us to determine the temperature at which the urania-plutonia began to be reduced and to observe the rate of reduction. Figure 1.1 shows the temperature of the furnace and the moisture content of the effluent gas during the heat treatment of urania-plutonia microspheres. There was a slight increase in the water content of the effluent gas as the furnace was heated from room temperature to 100°C and another increase at about 500°C, presumably due to the reduction of U. At about 1000°C, there was a large increase due to the reduction of PuO_2. When the temperature reached 1450°C, the moisture level began to decrease until it reached about 15 ppm. The ratio of O to metal in the microspheres was found to be 1.980 ± 0.005.

In attempting to adjust the ratio of O to metal for one batch of 84% dense pellets, we heated them to 1450°C several times and held them at that temperature for a total of 35 hr; the density increased about 4 to 5%. We then heat treated other pellets at 1450°C for various lengths of time to determine their rate of densification. As indicated in Fig. 1.2, the rate of densification is much greater during the first 10 hr than it is after that.

Since all of the 84% dense TREAT pellets had been sintered only 5 hr, it was apparent that their density was not stable. Additional pellets with low density were made for the TREAT fuel pins by sintering 18 hr at 1450°C. We expect that the density of these pellets will be more stable than that of those sintered only 5 hr, since they were sintered longer than the time required for the reduction in densification rate.

Capsule Fabrication (R. B. Pratt, M. K. Preston, R. A. Bradley, W. L. Moore)

EBR-II Capsules. — One of the five capsules fabricated last quarter for testing Sphere-Pac sol-gel fuel in the Experimental Breeder

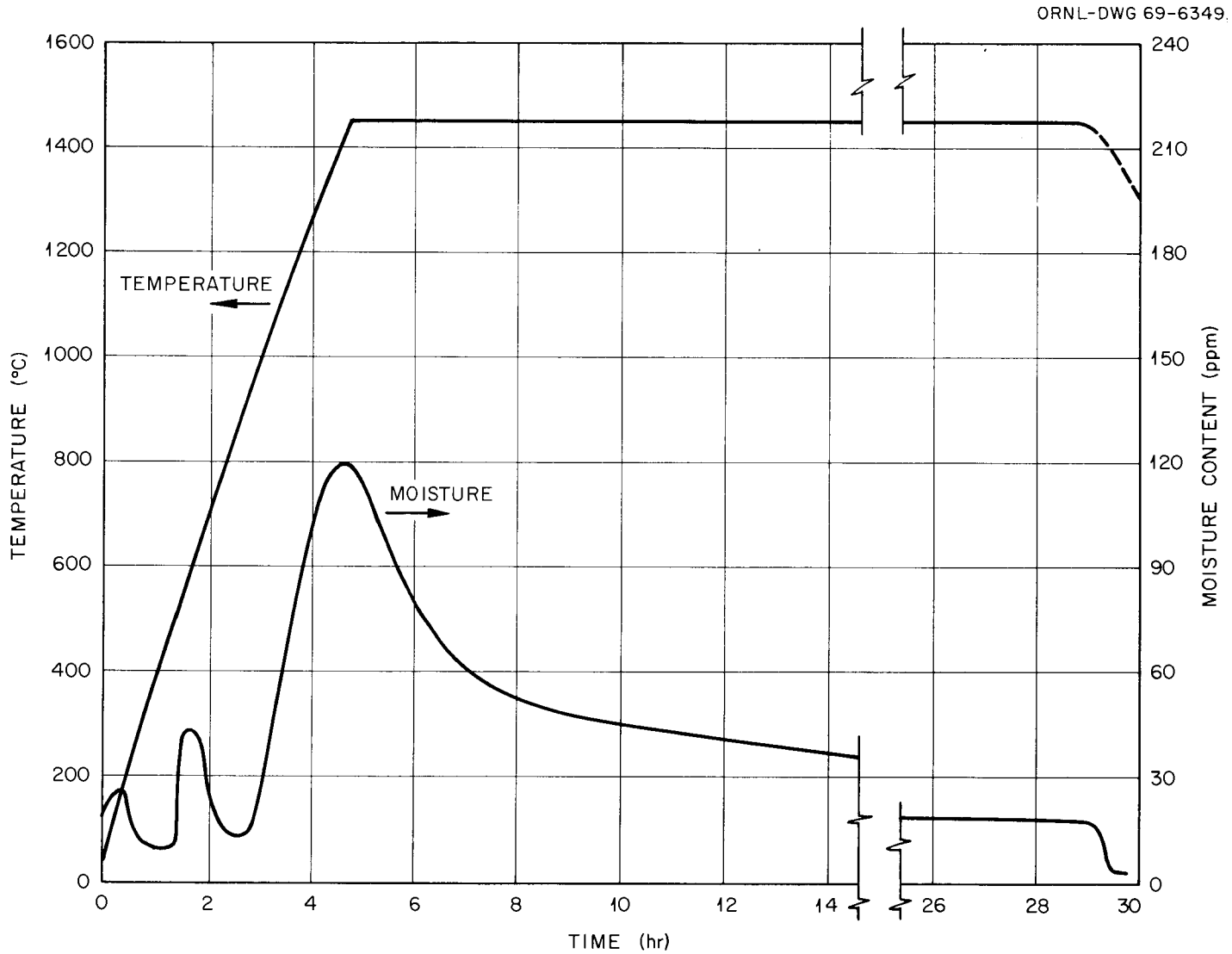

Fig. 1.1. Furnace Temperature and Moisture Content of Effluent Gas Needed During Heat Treatment of $(U_{0.8},Pu_{0.2})O_2$ to Adjust the Ratio of Oxygen to Metal.

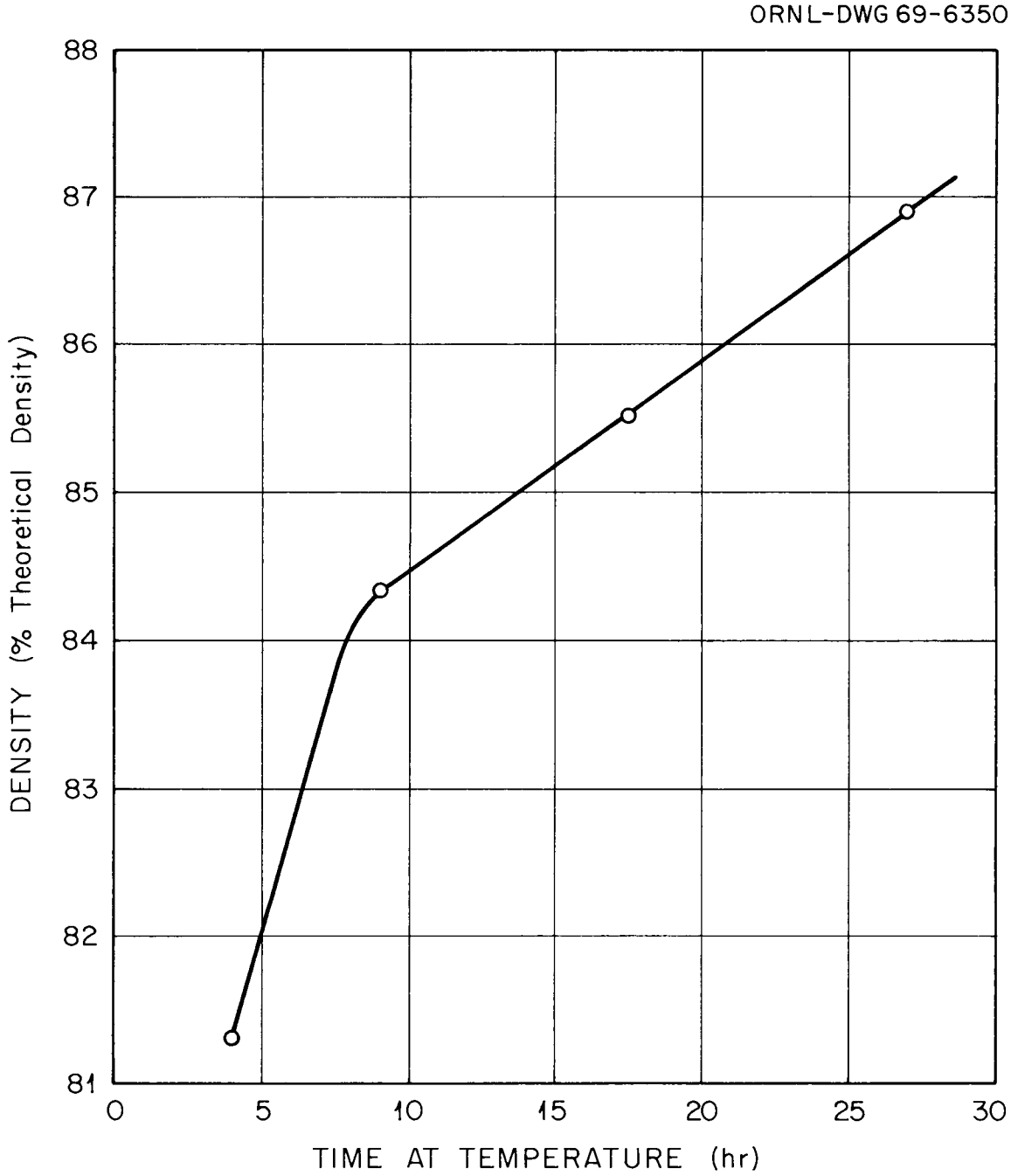

Fig. 1.2. Densification of Urania-Plutonia Pellets During Heat Treatment at 1450°C.

Reactor-II (EBR-II) was returned to ORNL for the repair of a weld, but all five capsules have now been accepted and are being irradiated. A report on the fabrication of the EBR-II series 1 capsules is being prepared.

TREAT Capsules. — During the next several years, we plan to fabricate a number of TREAT capsules. Initially, two capsules (TREAT I and II) are being fabricated for irradiation testing during the summer. We have prepared fabrication procedures, procured tooling, and developed the welding variables. About 98% of the hardware required for fabrication is on hand. We have begun fabricating fuel pins and capsule subassemblies.

A TREAT capsule, depicted in Fig. 1.3, is an instrumented capsule with an overall size of about 3 in. in diameter by 9 ft long and consists of four primary components: fuel rod, inner capsule, heater, and pressure vessel. The fuel rod is composed of a maximum of three 1/4-in.-diam fueled sections for comparative testing. The inner capsule surrounds the fuel rod and contains an Al heat sink instrumented with six thermocouples and bonded to the fuel rod with Na. The tubular heater, consisting of heater wire wound on a 1 1/8-in.-diam stainless steel tube and insulated with fiber insulation, contains six thermocouples and is used to bring the fuel to simulated operating temperature before the irradiation power transient. The pressure vessel, made of AISI-type 4130 steel, consists of a long, cylindrical container with squared flanges and a short nosepiece that contains all necessary leads for power and thermocouples.

In TREAT I and II, each fuel rod will contain three fueled sections. TREAT I will contain two pellet pins that have smear densities of 81 and 88% of theoretical density and a Sphere-Pac pin that has a smear density of 81% of theoretical density; TREAT II will contain two Sphere-Pac pins that have a smear density of 81% of theoretical density and one pellet pin that has a smear density 81% of theoretical density.

For planning and fabrication, we divided the assembly into eleven subassemblies: fuel pins, fuel rods, preassembly of the inner capsule sheath, fuel rod and thermocouple assembly for inner capsule, Na filling

ORNL-DWG 69-5597R

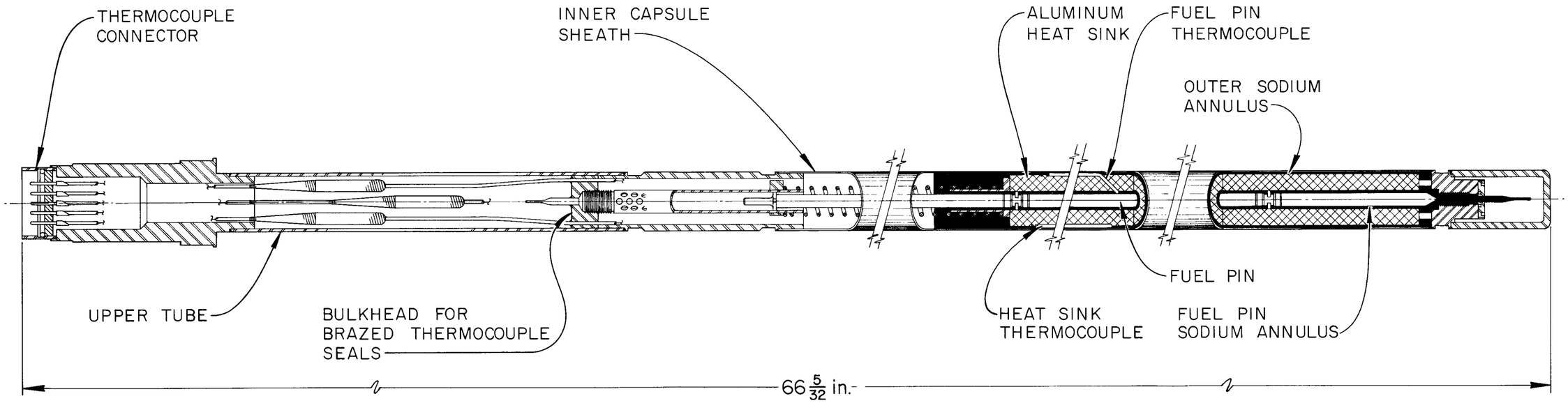

Fig. 1.3. TREAT Experiment Inner Capsule Assembly.

for inner capsule, pressure vessel assembly, extensometer assembly, heater assembly, support assembly for the lower spring, nosepiece assembly, and final assembly. We have prepared fabrication procedures for each subassembly — about 450 individual steps — that have been beneficial in pointing out areas where the design could be improved before fabrication, in determining need for special tooling, and as fabrication and inspection checklists. Scheduling is being done via a modified critical-path method that shows interactions between subassemblies and is updated weekly. All necessary approvals for working with fissile materials have been obtained, and shipping arrangements are being made.

About 20 special tools, including welding fixture, assembly jigs, and He leak-testing chambers, were designed and fabricated and are now being used. Welding and brazing procedures for 17 different joints were developed.

The fabrication of the various subassemblies is proceeding relatively smoothly, and TREAT I and II are about 40% complete. Hardware for three complete TREAT capsules is on hand, but about 50% of the machined components have had to be machined again, either because of failure to meet specifications or because of design changes. The three Sphere-Pac fuel pins for TREAT I and II were fabricated and inspected. Fabrication of the pellet fuel pins is awaiting fabrication of the pellets. Two capsule heaters were fabricated, and we plan to build one more heater as a spare. Our major fabrication problem has been the fabrication of the nosepieces for the pressure vessel. These units, which contain the pressure seals for the thermocouple and power leads to the capsule, are very intricate. After some design change, one unit was successfully fabricated, and two additional units are being fabricated.

ORR Capsules. — The fuel element portions of ORR instrumented capsule SG-2 were fabricated and sent to the Y-12 Plant for insertion into the irradiation capsule. The fuel elements for the ORR capsule consist of two 3-in.-long fueled annuli clad in 3/8-in.-OD Ti-modified type 304 stainless steel with a 1/8-in.-diam central thermocouple well of W. The fuel used in the elements was TREAT microspheres from fuel lot 103, which contained a nominal $(U_{0.8},Pu_{0.2})O_2$ with an adjusted ratio of O to

metal of 1.99. The fuel was loaded by Sphere-Pac to 80.7% of theoretical density in the top element and to 82.5% of theoretical density in the bottom element. The elements were fabricated without great difficulty.

ETR Capsules. — An Engineering Test Reactor (ETR) capsule containing four 7.5-in.-long fuel pins with 3-in.-long fuel columns was fabricated for the Chemical Technology Division. This capsule, which is identical to other doubly encapsulated ETR capsules fabricated by the Fuel Cycle Technology Group, contained $(^{238}U_{0.85},Pu_{0.15})O_{2.00}$ clad in type 304L stainless steel and will be used for studies of fuel reprocessing. The ratio of O to metal in the fuel was near stoichiometric. The rods were loaded by the Sphere-Pac process (Table 1.2). The low density of these pins was due to improper restraint of the coarse bed and to insufficient filtration time for the pins.

Table 1.2. Fuel Loading of ETR Capsule 43-116

Pin Number	Fuel Weight (g)	Fuel Height (cm)	Smear Density (% of theoretical)
46	18.687	8.294	76.2
51	18.266	8.096	76.3
49	18.196	8.016	76.8
50	17.550	7.818	76.0

Characterization of Sol-Gel $(U,Pu)O_2$ Fuels

W. H. Pechin

The development of sol-gel fuel fabrication requires characterization of the material to control the process and to determine which properties are important to irradiation behavior. Characterization requires determining both the chemical composition and the physical

properties. Thermodynamic studies will contribute to the development of the process for the fuel and will aid in predicting fuel performance for both irradiation testing and model studies.

Analytical Chemistry (W. H. Pechin)

The partial results now available from the analysis of three lots of fuel by emission spectroscopy are listed in Table 1.3. The data that now remain to be determined are for Bi and the rare earth elements. The results of chemical analyses for these lots were reported previously.[7]

An analysis of the data from gravimetric determination of O in mixed oxides shows a 95% confidence interval of ±0.005 O-to-metal ratio units. This calculation was taken from triple determinations for a series of sintering runs (three pellets from each run). Since each determination requires a whole pellet, the confidence interval includes the variation in the pellets themselves.

A comparison between the gravimetric and NITROX methods of analysis is now available. Determinations have been made by each method on samples riffled from each lot of microspheres prepared for Sphere-Pac loading. The average of four batches loaded into the EBR-II rods was 1.987 for gravimetric and 1.985 for NITROX.

We have begun trial calculations to determine the important variables in the calculation of burnup. Two types of fuel are involved, the highly enriched U–20% Pu used for the EBR-II irradiations and the natural U–20% Pu used for the thermal irradiations.

The only items investigated so far are the initial isotopic compositions and the ratios of fission to capture in the enriched U–20% Pu fuel. Of these, the calculated burnup is most sensitive to the isotopic composition of the Pu.

Thermal Conductivity of UO_2 at Low Temperatures (D. L. McElroy)

We measured the thermal conductivity of 98% dense polycrystalline UO_2 and of a single crystal of UO_2 between 80 and 400°K. These

[7]W. H. Pechin, Fuels and Materials Development Program Quart. Progr. Rept. Dec. 31, 1968, ORNL-4390, pp. 17–18.

Table 1.3. Impurity Analysis of Microsphere Fuels

Microsphere Lot Number	Composition, wt ppm																					
	Ag	Al	B	Be	Ca	Cr	Cu	Fe	Mg	Mn	Mo	Ni	P	Pb	Si	Sn	V	Zn	Sb	Cd	Ti	Zr
99																						
Coarse	< 1	18	0.1	2	10	5	10	94	20	5	< 2	15	< 100	10	100	5	10	< 10	< 5	< 0.03	< 0.5	< 1
Fine	< 1	22	0.1	2	10	5	10	61	20	5	< 2	5	< 100	10	75	< 5	10	< 10	< 5	< 0.03	< 0.5	< 1
100																						
Coarse	< 1	8	< 0.1	< 1	20	15	20	73	20	15	< 2	10	< 100	5	100	5	5	< 10	< 5	< 0.03	< 0.5	26
Fine	< 1	15	< 0.1	< 1	25	20	25	90	20	10	< 2	15	< 100	10	100	5	5	< 10	< 5	< 0.03	11	11
101																						
Coarse	< 1	15	< 0.1	< 1	10	5	20	50	20	5	< 2	12	< 100	10	75	5	< 5	< 10	< 5	< 0.03	2.8	1.6
Fine	< 1	15	< 0.1	< 1	25	8	15	40	20	5	< 2	10	< 100	5	100	5	< 5	< 10	< 5	< 0.03	0.6	1.8

measurements were made in a guarded, longitudinal heat-flow apparatus that has a most probable accuracy of ±1.2%. These measurements were made to resolve the large disagreement (about a factor of 2) between low-temperature results by other investigators, who used a longitudinal system, and our published results on the thermal conductivity of UO_2 at high temperatures.

Our measurements on both UO_2 samples indicate no significant differences in their thermal conductivities from 80 to 400°K. These new results agree with our previous data[8] in the range of overlap, and they indicate serious errors from 110 to 200°K on the part of the previous investigators. The thermal conductivities of both UO_2 samples show a broad peak at about 200°K.

Thermal Conductivity of Lithium Fluoride (D. L. McElroy)

To assist our understanding of the behavior of nuclear oxides at high temperature and to obtain useful guidelines on the effects of infrared transmission and the formation of vacancies on thermal conductivity, we are studying heat transport in LiF. This optically transparent insulator may allow an evaluation of the magnitude of radiation conduction in other materials where this phenomenon occurs at temperatures where the accuracy of measurement is poor.

Thermal conductivity has been measured[9] on LiF single crystals to 1073°K. We made two tests in the radial heat-flow apparatus, from 343 to 773°K and from 471 to 1073°K. The high coefficient of thermal expansion of LiF (at 800°C, 7.3×10^{-6} deg^{-1}) caused rupture of the potential taps for the cone heater and stopped the first run. The second run was stopped 45 deg below the melting point of LiF, 1115°K, because expansion caused most of the thermocouples to become open circuits.

Figure 1.4 shows the thermal resistivity and temperature relation for the single-crystal disks of LiF for the second run. There is some

---

[8]T. G. Godfrey, W. Fulkerson, T. G. Kollie, J. P. Moore, and D. L. McElroy, J. Am. Ceram. Soc. 48(6), 297–305 (1965).

[9]D. L. McElroy, Fuels and Materials Development Program Quart. Progr. Rept. June 30, 1968, ORNL-4330, pp. 16–17.

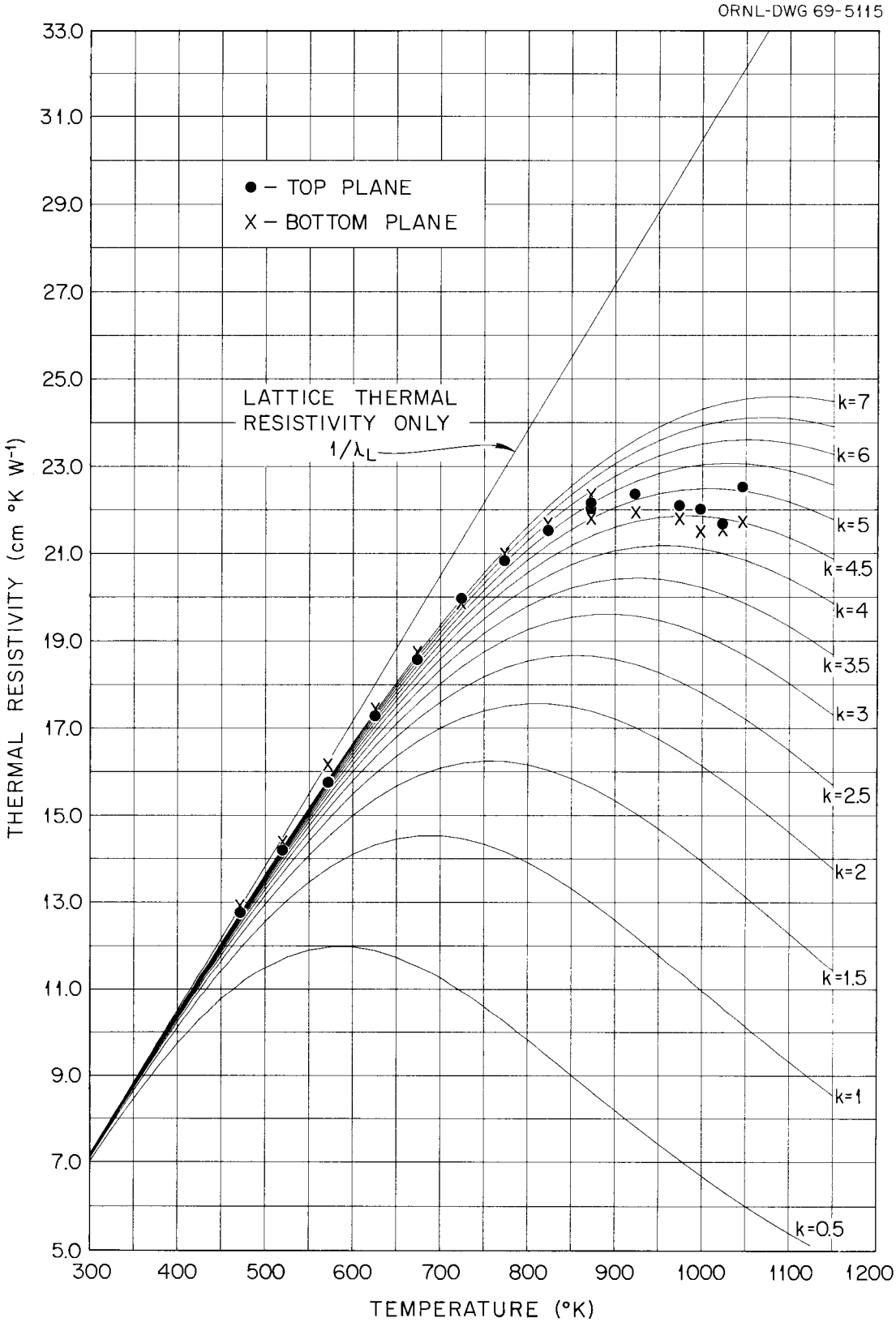

Fig. 1.4. Thermal Resistivity of Lithium Fluoride.

small difference in the two curves since the data are from two different planes. The experimental data are plotted onto a network of curves drawn by computer. The straight line of the computer plot is calculated from the low-temperature linear thermal resistivity reported earlier.[9] We assume that the heat transport at high temperatures is being influenced by radiation transfer, and this accounts for the curved lines. A first estimation for the total thermal resistivity (R) is made as follows:

$$R = \frac{1}{\frac{16\sigma n^2 T^3}{3k} + \lambda_L} ,$$

where

$\sigma = 5.67 \times 10^{-8}$ w m^{-2} deg^{-4}, the Stefan-Boltzmann constant,

n = the index of refraction, taken to be 1.38 for LiF,

T = absolute temperature,

k = the index of absorption, and

λ_L = the lattice conduction part of the thermal conductivity (w cm^{-1} $°K^{-1}$).

This relation is an approximation for "gray absorption," which means that k is assumed to be independent of wavelength and temperature — a suspect assumption at best. Figure 1.4 was generated via the computer for k values from 0.5 to 20 in steps of 0.5. (The lowest case is k = 0.5; k = 20 is the highest.)

The trend of the experimental data plotted on the computer grid shows that up to about 850°K the deviation in R from the linear relation (due to thermal radiation) follows the curve with $k \cong 6$. Above 850°K, the experimental data deviate from the curve. This deviation is possibly due to (1) a change of k with temperature, or (2) an error in measurement of the temperature gradient due to exposure of the inner thermocouple to a larger space angle of energy radiation.

Experimental difficulties at the high temperature prohibited demonstration of the influence of thermally produced vacancies and of thermal diffusion on thermal conductivity. Consequently, a third test is under way on a polycrystalline 100% dense specimen of LiF. The assembly for

this run allows for the thermal expansion of LiF, and we hope this will allow us to obtain data to the melting point. Calculations are in progress to include a wavelength and temperature dependency in the absorption term for a more complete interpretation of the data.

Radial Heat-Flow Apparatus for Measurements at 10 atm and 1000°C (D. L. McElroy)

Design drawings for this system were completed, and bids are being obtained to allow construction and demonstration before July 1, 1969.

Deformation of UO_2 (C. S. Morgan, L. L. Hall, W. H. Pechin, A. R. Olsen)

Additional data on the deformation of UO_2 at high temperatures under constant strain rate are presented in Fig. 1.5. Deformation behavior at different temperatures was measured under compression at a strain rate of 0.00067 min^{-1}. Sol-gel UO_2 specimens were tested, and specimens prepared from ammonium diuranate (ADU) were run for comparison. Tests were made both in Ar–4% H_2 atmosphere and an atmosphere with a ratio of $CO:CO_2$ of 9. The ratio of O:U prevailing in these tests under both atmospheres should have remained at 2.00.

The ADU UO_2 specimens, although of higher density (97 rather than 92%), proved more susceptible to deformation than the sol-gel UO_2 specimens. Although chemical analysis showed that the ADU specimens had an initial ratio of O:U of 2.00, metallography on these specimens is incomplete, and the reasons for this apparent anomaly are not known. It is also not clear why the specimens tested above 825°C in an atmosphere of CO and CO_2 deformed at lower stresses than those tested at the same temperature in Ar–4% H_2.

Sol-gel specimens tended to have a very definite yield point, while the ADU specimens did not.

Analytical Characterization (J. M. Leitnaker, K. E. Spear)

Control of Ratio of Oxygen to Metal. – Uncertainties remain in the determination of ratios of O to metal in fuel materials. Ten determinations of urania with a lattice parameter of 5.4710 ± 0.0001 A by the

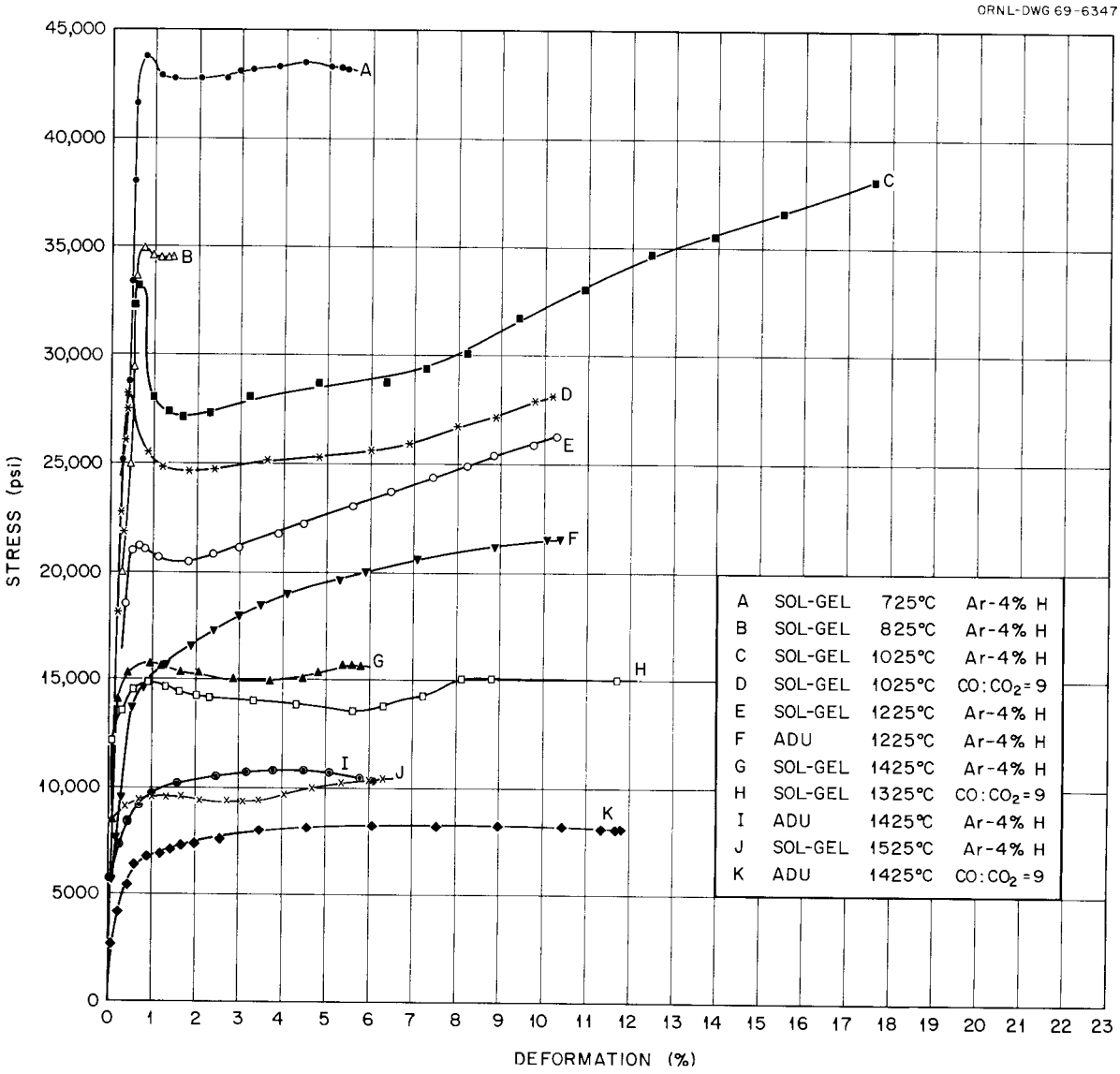

Fig. 1.5. Stress-Strain Curves for UO_2 Specimens Under Constant Compressive Strain Rate of 0.00067 min^{-1}.

NITROX method were reported by Pechin[10] to yield a ratio of O to metal of 1.999 ± 0.006. The material used to standardize the apparatus, however, has a lattice parameter of 5.4680 ± 0.0003 A, indicating that the composition is $UO_{2.026}$ (ref. 11), not $UO_{2.000}$ as assumed. It is difficult to understand why the standard material would have a low lattice parameter if the O content were not high — unless some other unknown contaminant were present.

To further examine the relationship between lattice parameter, composition, and O activity, we modified a furnace to permit quenching UO_2 samples in a water-cooled, stainless steel receiver; the equilibrating gas is the quenching fluid. Quenched samples are examined by x-ray lattice parameter determination, chemical analysis for C, analysis for U by combustion to U_3O_8, metallographic polishing, microscopy, and immersion density measurements. Data obtained to date are shown in Table 1.4. Some conclusions can be drawn from these.

First, the mole ratio of O:U continually decreases on heating at 1200°C for from 1 to 16 hr. The precision of the measurement is about 0.005 in the mole ratio; the values for 6 and 16 hr may not be statistically different.

Secondly, in all but one case the outside of the sample had a smaller lattice parameter than the center. Since the difference was nearly always within two standard deviations, the significance is not clear but may indicate a redistribution of O on cooling. To test this postulate, it is necessary to quench much more rapidly. It is further probable that we will have to be more particular about the temperature of the x-ray specimen, the corrections to the film for shrinkage, and the preparation of the sample.

The third factor to be noted is the high C content of the two samples heated at 1000°C. The decreasing result with time indicates that the 900 ppm C in the starting material is being removed. Spectrographic

---

[10]W. H. Pechin, Fuels and Materials Development Program Quart. Progr. Rept. Dec. 31, 1968, ORNL-4390, p. 16.

[11]W. A. Young, L. Lyndr, J. S. Mohl, and G. G. Ribowitz, An X-Ray and Density Study of Nonstoichiometry in Uranium Oxides, NAA-SR-0765 (1962).

Table 1.4. Results of Heating 1/4-in.-diam Pellets of UO_{2+x} in Atmosphere with $CO:CO_2$ Ratio of 10

Sample Number	Temperature (°C)	Time (hr)	Lattice Constant,[a] A		Analysis, wt %		Mole Ratio[d] O:U
			Center of Pellet	Surface of Pellet	C[b]	U[c]	
5309-90	1200	1	5.47051 ± 16	5.46931 ± 27	0.01	88.053	2.019
5309-92	1200	6	5.47157 ± 19	5.47094 ± 21	0.014; 0.019	88.150	2.000
5309-93	1200	16	5.47094 ± 18	5.47081 ± 28	0.003 0.005	88.172	1.996
5309-96	1000	1	5.46891 ± 25	5.46974 ± 26	0.048	87.769	2.073
5309-97	1000	66	5.47061 ± 20	5.47001 ± 20	0.030		
5309-104	1000	16					

[a]Procedures for determining lattice parameters are detailed in J. M. Leitnaker, "The Ideality of the UC-UN Solid Solution," pp. 317–330 in Thermodynamics of Nuclear Materials, 1967, International Atomic Energy Agency, Vienna, 1968. (Variations refer to the standard deviation and are preceded by a decimal and three zeros.)

[b]By combustion.

[c]By ignition to U_3O_8; average of duplicate samples.

[d]The percentage of O is calculated from 100 − %U = %O.

analysis on the starting $UO_{2\pm x}$ material indicates very low metallic impurities, principally Fe (40 ppm) and Cu (20 ppm).

Study of the Effect of Thermal Gradient on Composition (J. M. Leitnaker, K. E. Spear). — Preliminary tests have been made to determine what sorts of thermal gradients can be obtained in UO_2 and presumably in $(U,Pu)O_2$ by induction heating. A rod of UO_2 was isostatically formed, sintered 40 min at 1550°C in a H_2 atmosphere, and then placed in an eddy-current concentrator, where it was supported by a Cu plate attached directly to the cold wall of the Cu concentrator. A susceptor of Mo was suspended over and around the top of the sample so that the sample could be heated despite the fact that UO_2 cannot be heated inductively at the frequencies available in our furnace (400 kHz). During heating (1 hr), a gas mixture with a ratio of $CO:CO_2$ of 100 flowed through the system. The data obtained are given in Table 1.5.

Table 1.5. Lattice Parameter of Portion of Thermal Gradient Experiment on UO_2 Rod

Sample	Temperature[a] (°C)	Lattice Parameter[b]	Ratio O to Metal[c]
Hot surface	1820	5.47032 ± 0.00016	2.002
Hot center	1800[d]	5.47052 ± 0.00016	2.000
Above crack	1140	5.47091 ± 0.00015	1.998
Cold surface	950	5.47090 ± 0.00018	1.998
Cold center	950[d]	5.47108 ± 0.00017	1.998

[a]Temperatures are measured on surface and may differ from temperatures of x-ray samples by ±100 deg.

[b]The lattice parameter was obtained as described in J. M. Leitnaker, "The Ideality of the UC-UN Solid Solution," pp. 317–330 in Thermodynamics of Nuclear Materials, 1967, International Atomic Energy Agency, Vienna, 1968.

[c]Extrapolation of data given in D. J. Seddon (ed.), Physical Properties of Some Plutonium Ceramic Compounds: A Data Manual, TRG-1601 (1968) p. 11.

[d]Estimated.

These data agree qualitatively with the model proposed by Rand and Markin[12] to account for redistribution of O in fuel materials; that is, the hot portion is richer in O, as determined from the lattice parameter, than the cold portion. If O pressure were the determining factor rather than a constant ratio of $CO:CO_2$, the result would have been reversed.

Thermodynamic Calculations (J. M. Leitnaker, H. L. Davis, K. E. Spear)

In an attempt to understand the entropies of actinide oxides, we constructed a model to account for the low-temperature behavior of UO_2 above 30.4°K. Calculation of the heat capacity and entropy agrees with measurement within experimental error. Although the agreement may be fortuitous, even fortuitous agreement has not been previously obtained. We believe far-infrared spectrophotometric measurements should be attempted to confirm or deny our calculations.

Irradiation Testing of $(U,Pu)O_2$ Fuels

A. R. Olsen

The final evaluation of $(U,Pu)O_2$ fuels will be based upon their irradiation performance. The irradiation testing program is concentrating on comparative tests of three fabrication forms: Sphere-Pac, pellets, and extrusions. The program includes thermal-flux irradiations that permit use of instrumented capsules and achievement of high burnup levels in relatively short times. These tests will provide supplemental information essential to the analysis of the fast-flux irradiation tests, in which the radial fission-rate distribution and cladding damage are more typical of anticipated LMFBR operating conditions. The test program also includes power transient tests to investigate fuel performance under abnormal operating conditions. The development of mathematical

[12]M. H. Rand and T. L. Markin, "Some Thermodynamic Aspects of $(U,Pu)O_2$ Solid Solutions and Their Use as Nuclear Fuels," pp. 637–650 in Thermodynamics of Nuclear Materials, 1967, International Atomic Energy Agency, Vienna, 1968.

models to predict fuel behavior and of computer programs for analyzing fuel performance are integral parts of the irradiation test program.

The objective of the program on mixed oxides is to define the performance limitations for LMFBR applications of various $(U,Pu)O_2$ fuel forms. The first tests in the reactor have concentrated on the evaluation of sol-gel-derived fuel fabricated by the Sphere-Pac technique.[13] Future tests will include pellet and possibly extruded fuels with various macrostructural characteristics for comparison with the Sphere-Pac fuels.

Uninstrumented Thermal-Flux Irradiation Tests (A. R. Olsen, C. M. Cox, R. B. Fitts)

The status of the uninstrumented thermal-flux irradiation tests is given in Table 1.6. Two capsules are being irradiated in the ETR, and three are undergoing postirradiation examination. Each capsule contains four test rods, each with a 3-in.-long fuel column. The simultaneous irradiation permits preliminary comparisons of various fuel forms.

Capsule 43-116, which contains four fuel rods of Sphere-Pac $(U_{0.85},Pu_{0.15})O_2$, will be irradiated for two ETR cycles and returned to ORNL as quickly as possible after irradiation. Other than a postirradiation neutron radiograph, no detailed examination is planned. The fuel rods will be used by the Head-End Process Development Program.[14] Capsules 43-116, 43-117, and 43-118 are to be irradiated for the same program.

Experiment 43-115, which contains three rods of Sphere-Pac $(U_{0.85},Pu_{0.15})O_2$ and one rod of Sphere-Pac UO_2(20% ^{235}U), was removed from the ETR during the midcycle shutdown of cycle 101 on March 30, 1969. The scheduled exposure was designed to provide a peak burnup level of

---

[13]R. B. Fitts, A. R. Olsen, and J. Komatsu, "Sphere-Pac Fabrication of Sol-Gel Nuclear Fuels," paper presented at the Fall Meeting of the American Ceramic Society, Nuclear Division, Pittsburgh, Pa., October 6–9, 1968. Abstract only in Am. Ceram. Soc. Bull. 47(9), 844 (1968).

[14]D. E. Ferguson et al., Chem. Technol. Div. Ann. Progr. Rept. May 31, 1968, ORNL-4272, pp. 41–49.

Table 1.6. Noninstrumented Irradiation Screening Tests of Sol-Gel-Derived Urania-Base Bulk Oxide Fuels

Experiment Number	Fuel		Number of Rods	Peak Burnup (% FIMA)[a]	Peak Linear Heat Rate (w/cm)	Status, May 1969
	Form	Composition				
43-99	Sphere-Pac	$(^{235}U_{0.80},Pu_{0.20})O_2$	2	1.5[b]	1640[b]	Examined
43-100	Sphere-Pac	$(^{235}U_{0.80},Pu_{0.20})O_2$	2	1.4[b]	1470[b]	Examined
43-103	Sphere-Pac Pellet	UO_2(20% ^{235}U) UO_2(20% ^{235}U)	3 1	5	690	Being examined
43-112	Sphere-Pac	$(^{238}U_{0.85},Pu_{0.15})O_2$ UO_2(20% ^{235}U)	3 1	0.7	500	Being examined
43-113	Sphere-Pac	$(^{238}U_{0.85},Pu_{0.15})O_2$ UO_2(20% ^{235}U)	3 1	10[c]	500[c]	In reactor, ≅ 7% FIMA
43-115	Sphere-Pac	$(^{238}U_{0.85},Pu_{0.15})O_2$ UO_2(20% ^{235}U)	3 1	5[c]	600[c]	Being examined
43-116	Sphere-Pac	$(^{238}U_{0.85},Pu_{0.15})O_2$	4	1.5[d]	600[c]	In reactor
43-117 43-118 43-119	Sphere-Pac	$(^{238}U_{0.80},Pu_{0.20})O_2$	4	1.5[d]	600[c]	In preparation

[a]Fissions per initial metal atom.

[b]Rods failed in reactor from overpowering.

[c]These are target design values.

[d]This is an approximate level. This test will be irradiated for two ETR cycles to produce fuel for reprocessing studies.

5% fissions per initial metal atom (FIMA) (50,000 Mwd/metric ton of heavy metal). The capsule will be neutron radiographed at the Materials Testing Reactor (MTR) and then shipped to ORNL. Division of Transportation approval for the shipping cask was requested some time ago. We expect to have such approval before April 15, 1969.

The comparison of predicted burnup from physics calculations with experimental data for experiment 43-112 was completed. This experiment included four 3-in.-long fuel pins clad with stainless steel; three of these contained $(U_{0.85},Pu_{0.15})O_2$, and the fourth contained 20% enriched UO_2. The capsule was irradiated in the ETR for 29.4 effective days of full power. The postirradiation examination of the rods from this capsule was reported.[15]

We calculated power distribution and burnup with the ANISN code[16] with 36 neutron energy groups, using diffusion theory for the six fast groups (> 1.86 ev) and transport theory for the thermal groups. Cross sections were obtained by coupling spectrum-averaged cross sections from the GAM-II (fast) library[17] with the 30-group THERMØS (thermal) library.[18] The unperturbed spectrum was represented by a water spectrum determined by a fine-group ANISN calculation and normalized as a shell source to the capsule based on advertised values for the 2200 m/sec axial flux distribution in the experimental location. The resulting unperturbed spectrum is very similar to that determined by following the procedure suggested by Lewis and Marshall.[19]

---

[15]A. R. Olsen, R. B. Fitts, and J. Komatsu, Fuels and Materials Development Program Quart. Progr. Rept. June 30, 1968. ORNL-4330, pp. 18–20.

[16]W. W. Engle, Jr., A User's Manual for ANISN: A One-Dimensional Discrete Ordinate Transport Code with Anisotropic Scattering, K-1693 (March 1967).

[17]G. D. Joanou and J. S. Dudek, GAM-II – A B_3 Code for the Calculation of Fast-Neutron Spectra and Associated Multigroup Constants, GA-4265 (Sept. 1963).

[18]H. C. Honeck, THERMØS – A Thermalization Transport Theory Code for Reactor Lattice Calculations, BNL-5826 (Sept. 1961).

[19]W. B. Lewis and T. D. Marshall, Distributions of Neutron Density and Neutron Flux, IDO-16614 (July 1960).

After the postirradiation examination, the reactor-physics calculations were renormalized to the ^{60}Co activity in the cladding to give a more accurate analysis of power and burnup. The agreement with radiochemical and isotopic burnup analyses is in general good, as shown in Table 1.7.

We are now checking the DØT code,[20] the two-dimensional equivalent of ANISN, for analysis of effects of flux peaking at the ends of fuel pins.

We are also repeating the calculations for predictions, using the same cross sections and spectrum for other capsules in the uninstrumented test group. Design calculations were begun for a series of irradiations of fuel pins in the ETR to compare pellet and Sphere-Pac performance at low heat rate.

ORR Instrumented Tests (R. B. Fitts, V. A. DeCarlo, K. R. Thoms)

The instrumented irradiation tests in the ORR are designed to monitor the thermal performance of test fuel rods. The temperatures of the cladding and at the fuel center and the rates of heat generation in the fuel rods are continuously measured and recorded. These data are being used to evaluate the thermal characteristics of various fuels in a reactor and the effects of irradiation conditions upon the temperatures and rates of structural change within the operating fuels.

The second capsule in this series, SG-2, is in the reactor. The fuel rods were loaded to 81% smear density with Sphere-Pac $(U_{0.8},Pu_{0.2})O_2$ from the batch of fuel to be used for the first series of TREAT tests.[21,22] The temperature at the fuel center is being used to control operation of the capsule. This temperature has been changed in 100°C steps from 100 to 1100°C.

---

[20] F. R. Mynatt, A User's Manual for DØT, K-1694, in press.

[21] C. M. Cox, "Transient Testing of $(U,Pu)O_2$ Fuel," pp. 30–32, this report.

[22] W. L. Moore, "Sphere-Pac," p. 5, this report.

Table 1.7. Comparison of Calculated and Measured Linear Heat Rates and Burnups for ETR Experiment 43-112

Fuel Pin Section	Fuel Composition	Design Predictions Based on Advertised Unperturbed Flux		Postirradiation Examination					
				Isotopic Analysis	Radiochemical Analysis[b]	^{60}Co Activity[c]	Isotopic Analysis	Radiochemical Analysis[b]	^{60}Co Activity[c]
		(kw/ft)	(% FIMA)[a]	(kw/ft)			(% FIMA)		
43-112-1B	$(U_{0.85},Pu_{0.15})O_2$	8.6	0.47	8.4	9.2	9.2	0.46	0.50	0.50
43-112-2B	UO_2 (20% enriched)	12.0	0.71	10.4	11.6	11.9	0.61	0.68	0.70
43-112-3B	$(U_{0.85},Pu_{0.15})O_2$	12.2	0.65	12.6	12.8	14.3	0.67	0.68	0.76
43-112-4B	$(U_{0.85},Pu_{0.15})O_2$	10.0	0.54	10.5	10.2	10.9	0.57	0.55	0.59

[a]Fissions per initial metal atom.

[b]Average of ^{137}Cs, ^{89}Sr, ^{144}Ce analyses.

[c]Renormalization of reactor-physics calculations, based on neutron activation of the cladding.

There was some drift in the temperature at the fuel center at constant power conditions for central temperatures below 800°C. This same phenomenon was observed in the first capsule in this series and is attributed to the desorption and subsequent migration and reaction of gases on the fuel and cladding surfaces. Further study of this phenomenon is required. At temperatures above 800°C and upon return to lower temperatures, the temperatures are steady.

A preliminary analysis of the data from this capsule yields a slightly higher (about 10%) smeared thermal conductivity for the fuel than that obtained[23] in capsule SG-1. This difference may disappear when the data are examined in more detail. However, the principal conclusion from capsule SG-1 – that the conductivity of the Sphere-Pac fuel is essentially the same as that for pellet fuels of comparable smear density – appears to be verified.

Transient Testing of Sol-Gel $(U,Pu)O_2$ (C. M. Cox, R. E. Adams)

The purpose of the transient tests in the TREAT is to compare the behavior of Sphere-Pac and pelletized $(U,Pu)O_2$ fuels under conditions that simulate power excursions. Unirradiated fuels, capsule loadings, and the intended volume percent of melting of the fuel for the series I tests are given in Table 1.8. The design and hazards analyses are complete, and arrangements have been made to perform the first two experiments at TREAT in June.

We calculated the extent of fuel melting as a function of integrated reactor power, using pulse periods of 155 and 200 msec and two different coefficients of heat transfer for the gap between fuel and cladding. These results are plotted in Fig. 1.6. As can be seen from the initial slopes of the curves, a small change in integrated power or pulse period can make a significant difference in the volume melting of the fuel. Therefore, we have included both Sphere-Pac and pellet fuels in each of the first three capsules to get directly comparable data for fuel performance.

---

[23]R. B. Fitts, Fuels and Materials Development Program Quart. Progr. Rept. Dec. 31, 1968, ORNL-4390, pp. 25–27.

Table 1.8. Transient Tests of Sphere-Pac Fuels Series I
TREAT Tests of Unirradiated Fuel

Capsule Identification	Pin Location	Relative Power,[a] %		Fuel[b]			Planned Percentage Melting of Fuel Volume
		Pin Average	Pin Limits	Fabrication Form[c]	Smear Density[d] (%)	Fuel Length (in.)	
TR-1	Bottom	84	91–74	P	88	8	20
	Center	99	100–98	SP	81	8	25
	Top	83	91–70	P	81	8	20
TR-2	Bottom	84	91–74	SP	81	8	40
	Center	99	100–98	SP	81	8	50
	Top	83	91–70	P	81	8	40
TR-3	Bottom	84	91–74	P	88	8	60
	Center	99	100–98	SP	81	8	75
	Top	83	91–70	P	81	8	60
TR-4		95	100–87	SP	81	21	50

[a]Relative power is based on axial unperturbed flux distribution as measured by Au foil activation.

[b]All fuel will be $(^{238}U_{0.80},Pu_{0.20})O_{1.98}$.

[c]Fabrication form: P – pellets; SP – Sphere-Pac.

[d]Smear density is the percent of theoretical density.

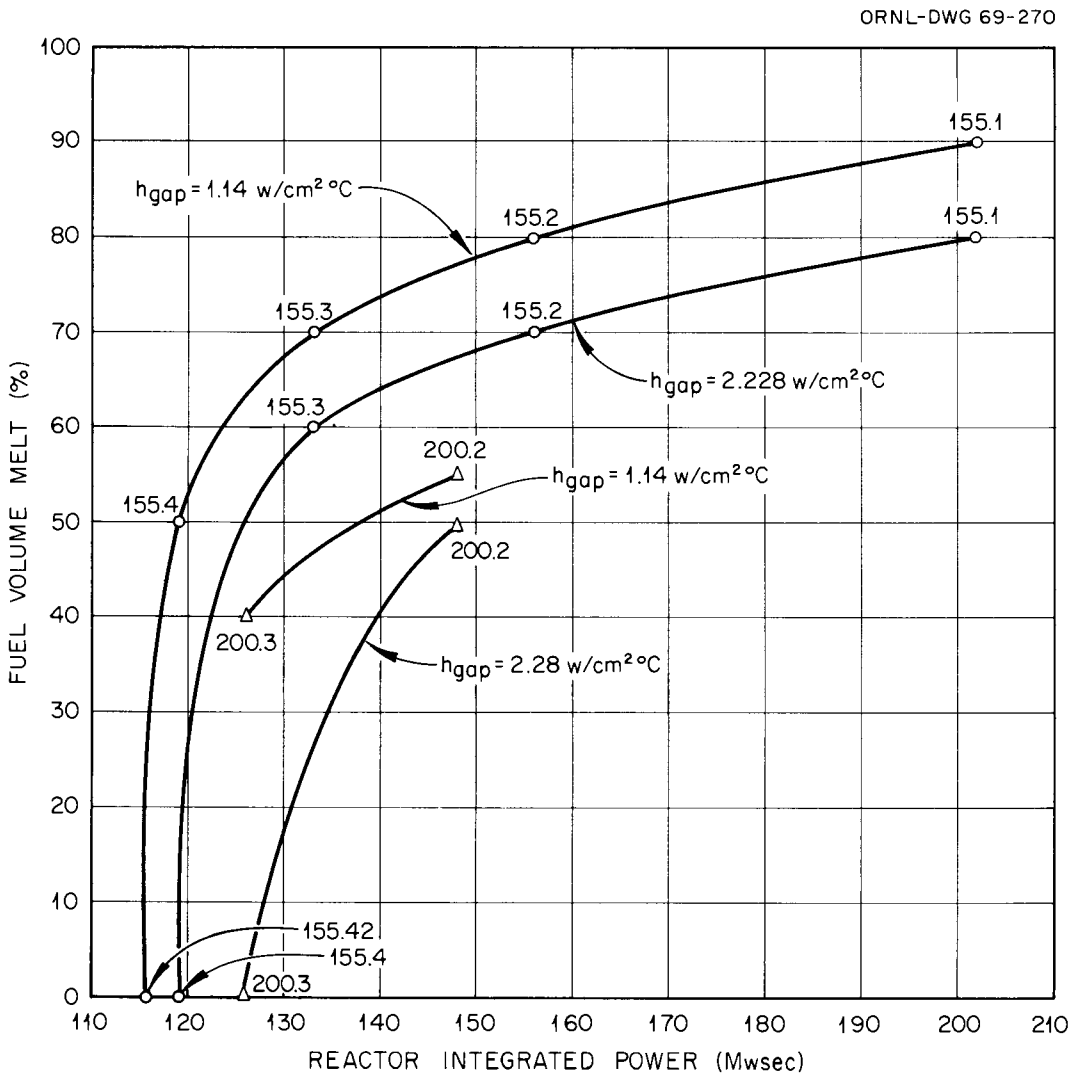

Fig. 1.6. Calculated Melting of Fuel Volume as a Function of Integrated Reactor Power Using Two TREAT Pulse Periods (155 and 200 msec) and Two Coefficients of Heat Transfer (h gap) for the Gap Between Fuel and Cladding.

Two important variables that are expected to influence transient behavior are fuel burnup and cladding fluence. We will investigate the burnup effect by irradiating fuel pins in the ETR at low heat rates to produce a high content of fission gas before transient testing. These pins will then be reencapsulated and pulsed at TREAT.

Fast-Flux Irradiation Tests (A. R. Olsen, C. M. Cox, J. D. Jenkins)

The test capsules for series I were incorporated into subassembly X050 and inserted into the 4C2 position in EBR-II in February. The five encapsulated rods all contain sol-gel-derived $(U_{0.8},Pu_{0.2})O_2$ Sphere-Pac fuel. Details of the individual fuel-rod loadings and their subassembly locations are given in Table 1.9. Irradiation of these fuels began with run 33A of the EBR-II on February 27.

The scheduled irradiation of this subassembly was revised. It is now scheduled for 7500 Mwd of EBR-II operation instead of the 5500 Mwd reported.[24] This revised exposure will provide a peak burnup level in excess of 4% FIMA for the rod with the highest heat rate, S-1-C. As of April 1, 1969, the exposure was 600 Mwd.

We began a detailed reactor-physics analysis of the EBR-II to determine if neutron spectrum shifts in this reactor have a significant effect on the group-averaged neutron energy cross sections. If so, we will prepare multiple cross-section sets that cover the various regions.

Irradiation Test Calculations (C. M. Cox, R. B. Fitts, F. J. Homan)

The predictions of reactor physics and the experimentally determined burnups for $(U,Pu)O_2$ fuel pins were compared in an earlier section of this report.[25] We have similarly compared measured and calculated temperatures for the SG-1 experiment,[26] an instrumented capsule operated in the ORR poolside facility. Instrumentation included a thermocouple in the center of the fuel, three thermocouples in the NaK annulus surrounding the fuel cladding, and a calorimeter formed by four pairs of thermocouples in a Zircaloy-2 sleeve. The $(U_{0.85},Pu_{0.15})O_2$ fuel was fabricated by the Sphere-Pac process to a smear density of 8.8 g/cm^3. The capsule was operated at selected rates of linear heat generation

---

[24]A. R. Olsen and C. M. Cox, Fuels and Materials Development Program Quart. Progr. Rept. Dec. 31, 1968, ORNL-4390, p. 28.

[25]A. R. Olsen, C. M. Cox, and R. B. Fitts, "Uninstrumented Thermal-Flux Irradiation Tests," pp. 25–28, this report.

[26]R. B. Fitts, Fuels and Materials Development Program Quart. Progr. Rept. Dec. 31, 1968, ORNL-4390, pp. 25–27.

Table 1.9. Series I ORNL Oxide Fuel Rods for EBR-II Irradiation

Capsule Identification	Rod Identification	Fuel Column Height (in.)	Fuel Weight (g)	Smear Density		Ratio O to Metal	Subassembly Location[b]
				(g/cm^3)	(% theoretical)[a]		
S-1-A	14-27-E	13.44	76.853	9.096	83.07	1.99	X050-7
S-1-B	14-23-A	13.05	77.183	9.409	85.93	1.99	X050-12
S-1-C	17-1	13.50	73.972	9.041	82.57	1.99	X050-19
S-1-D	17-4-A	13.44	70.755	8.687	79.48	1.98	X050-16
S-1-E	17-4	13.45	73.089	8.966	81.88	1.99	X050-11

[a]The theoretical density for the $(U_{0.80},Pu_{0.20})O_2$ fuel has been adjusted to account for both isotopic analysis and the ratio of O to metal. At a ratio of O to metal of 1.99, theoretical density is 10.95 g/cm^3; and at a ratio of O to metal of 1.98, the theoretical density is 10.93 g/cm^3.

[b]The subassembly X050 is loaded into position 4C2 of the EBR-II grid.

between 5 and 15 kw/ft for about 1200 hr. Figure 1.7 compares calculated and measured temperatures at increasing heat rates. Temperatures from the surface of the capsule to the inside surface of the cladding were calculated with the GENGTC code.[27] The temperature of the fuel surface was calculated from an assumed heat-transfer coefficient of 1.14 w cm^{-2} $°C^{-1}$, appropriate for pellets with a 0.0005-in. gap.[28] We calculated the fuel-center temperatures with the PRØFIL code,[29] using a radial power distribution from an ANISN calculation with a water-spectrum shell source. The thermal conductivity function for a $(U,Pu)O_2$ pellet, described by Baily, Aitken, Asamoto, and Craig,[28] was applied to the Sphere-Pac fuels of comparable stoichiometry by substituting the smear density of the bed for the pellet density. The low-density fuel was assumed to densify to 0.96 of theoretical for temperatures above 1400°C and to 0.98 of theoretical for temperatures above 1900°C. The calculated and measured central fuel temperatures shown in Fig. 1.7 are close enough to verify the usefulness of this model. The temperature changes measured at the fuel center, indicated by the arrows in Fig. 1.7, are due to fuel densification at temperatures above 1300°C and to changes in operating power at the lower temperatures.

Work has continued on the development of the FMØDEL code for fuel performance, which is designed to predict the temperature distributions, fuel restructuring, and deformations for a fast-reactor fuel pin. The code now includes an analysis for fuel restructuring and temperature distribution similar to that used in PRØFIL, a modification of Puthoff's[30]

---

[27]H. C. Roland, GENGTC — A One-Dimensional CEIR Computer Program for Capsule Temperature Calculations in Cylindrical Geometry, ORNL-TM-1942 (December 1967).

[28]W. E. Baily, E. A. Aitken, R. R. Asamoto, and C. N. Craig, "Thermal Conductivity of Uranium-Plutonium Oxide Fuels," pp. 293–308 in Intern. Symp. Plutonium Fuels Technol., Scottsdale, Ariz., 1967, Nucl. Met. 13, American Institute of Mining, Metallurgical, and Petroleum Engineers, New York, 1968.

[29]C. M. Cox and F. J. Homan, PRØFIL — A One-Dimensional FØRTRAN IV Program for Computing Steady-State Temperature Distributions in Cylindrical Ceramic Fuels, ORNL-TM-2443 (March 1969).

[30]R. L. Puthoff, A Digital Computer Program for Determining the Elastic-Plastic Deformation and Creep Strains in Cylindrical Rods, Tubes, and Vessels, NASA-TM-X-1723 (January 1969).

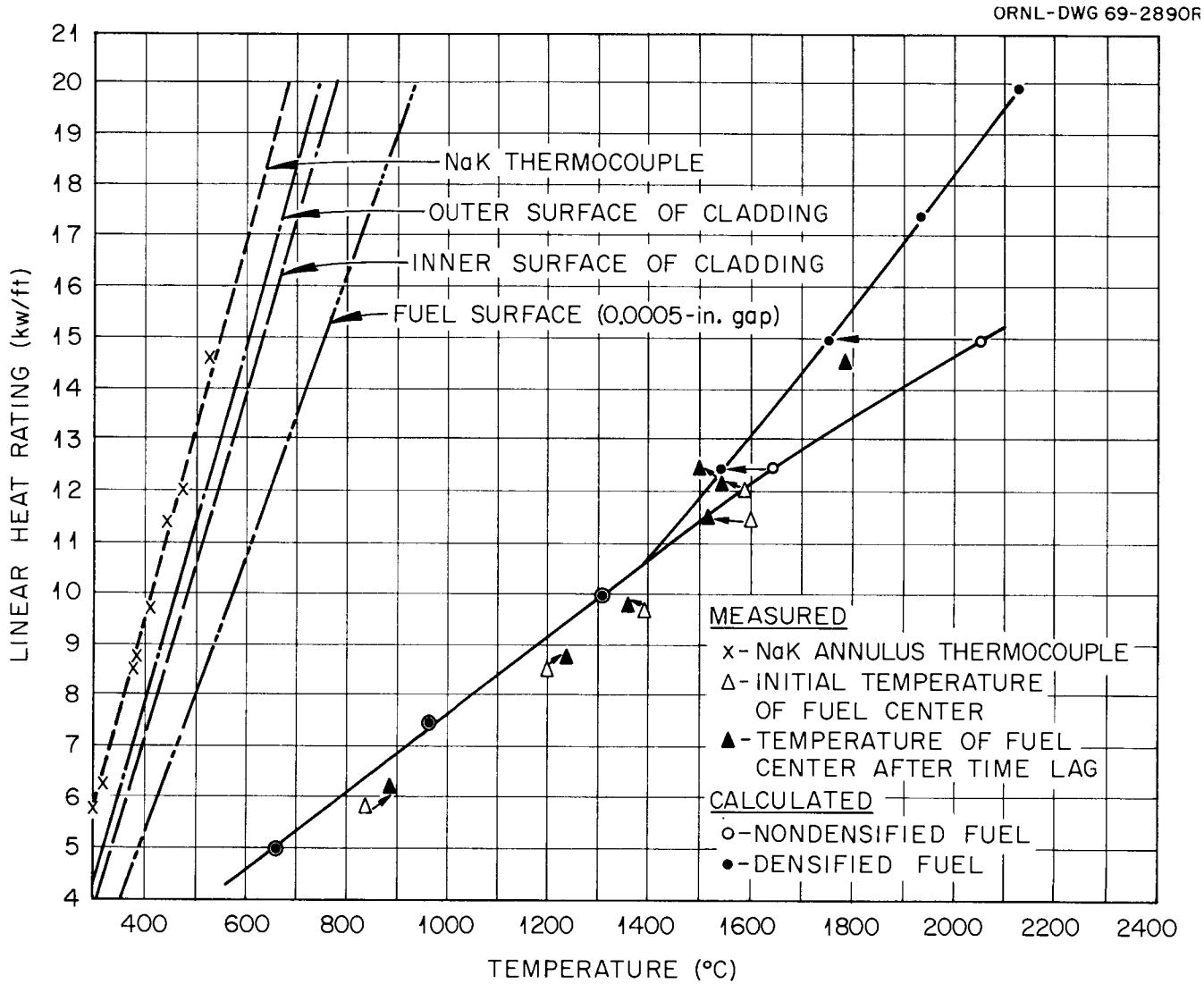

Fig. 1.7. Operating Conditions and Predicted Conditions for Capsule SG-1 Based on GE Pellet Conductivity.

analysis for elastic and plastic creep deformation, a calculation for release of fission gas and gas pressure, a fuel swelling model based on Greenwood and Speight,[31] and an empirical description of intrinsic swelling of the cladding due to condensation of vacancies formed by radiation damage.

We have begun correlating release of fission gas from $(U,Pu)O_2$ as a function of temperature and burnup in fast-flux irradiation experiments. Data taken from a review by Cox[32] are shown in Fig. 1.8. The FMØDEL code was used to calculate the average temperature of the fuel volume in all cases where enough information was available. The dependence of release of fission gas on temperature in the burnup range of 5 to 6% FIMA was examined, as shown in Fig. 1.9. It is clear that data from many more pins must be examined in order to establish a meaningful correlation; however, the data plotted in Fig. 1.9 suggest that Vi-Pac fuels release more gas than pellets and that release of fission gas can be consistently evaluated on the basis of average fuel temperature, burnup, and fabrication form.

---

[31] G. W. Greenwood and M. V. Speight, J. Nucl. Mater. 10(2), 140–144 (1963).

[32] C. M. Cox, "Irradiation Performance of Uranium-Plutonium Mixed Oxide Fuel Pins." To be published.

ORNL-DWG 69-2815

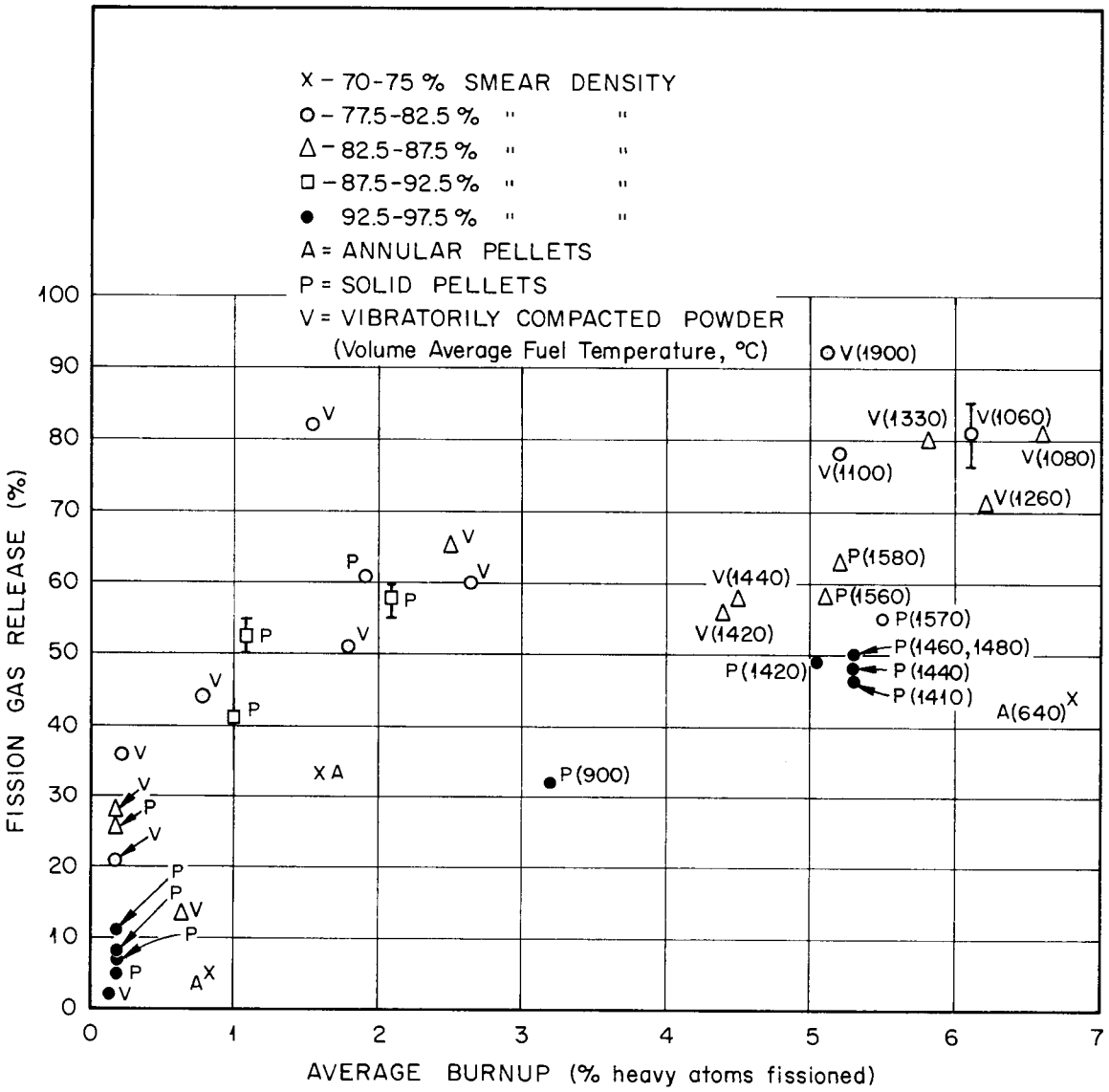

Fig. 1.8. Release of Fission Gas From Mixed-Oxide Fast-Flux Experiments.

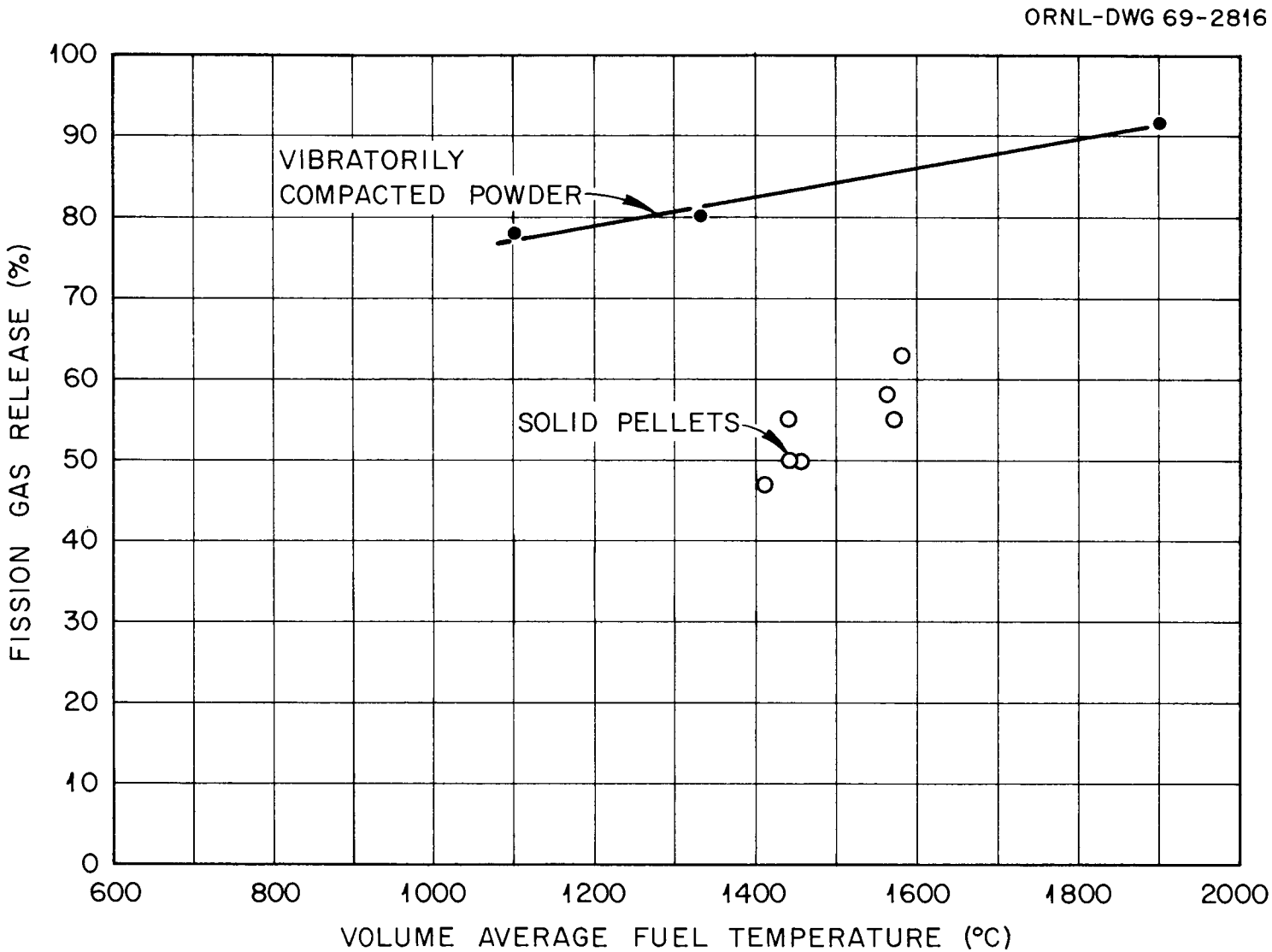

Fig. 1.9. The Effect of Fuel Temperature on Release of Fission Gas From Mixed-Oxide Fast-Flux Experiments at 5 to 6% Average Burnup.

2. DEVELOPMENT OF HIGH-PERFORMANCE LMFBR FUELS

P. Patriarca J. L. Scott

The goals of this program are to investigate the properties and behavior of those U- and Pu-based ceramic fuels that we term conductors — such as the mononitrides, carbonitrides, and monocarbides — and to compare their potential as liquid-metal fast breeder reactor (LMFBR) fuel with that of $(U,Pu)O_2$, which by comparison is an insulator. Since the thermal conductivity of the ceramic conductors is about ten times that of $(U,Pu)O_2$, it is theoretically possible to operate a conductor at ten times the power density with the same temperature at the center of the fuel. In practice, heat-transfer limitations, thermal stresses in the cladding, and high rates of swelling at high temperatures limit the power density that can be achieved with thermal conducting fuels to about two or three times that of $(U,Pu)O_2$ — still a challenging improvement. Additionally, the margins for transient overpower in the ceramic conductors are much higher than those for $(U,Pu)O_2$.

We seek to provide the information necessary for evaluating the true potential of nitrides, carbonitrides, and carbides in comparison to each other and to mixed oxides. We need to define the structures, composition, and quality control required to achieve 150,000 Mwd/metric ton at peak linear heat ratings of 30 to 50 kw/ft. We must also demonstrate the possibility of a low-cost fuel cycle for manufacturing fuel with the needed properties. And since austenitic stainless steel is a poor conductor of heat, we seek to establish the physical and thermodynamic criteria for the new cladding material that will probably be required to exploit the conducting fuels.

Our work is now oriented toward fabricating and characterizing (U,Pu)N with controlled low or high porosity distributed in different ways. The requisite void volume in a fuel pin may be provided in several ways if dense fuel is used, such as by a large Na-filled gap between fuel and cladding or by dished or annular pellets. It may also be provided by the internal porosity of low-density fuel pellets. We use both hot pressing and cold pressing and sintering. In our

characterization work, emphasis is being placed on reliable chemical analyses of U, Pu, C, O, and N. We have glove boxes with less than 20 ppm O and 10 ppm moisture that allow us close control of O content, and we have facilities in operation for x-ray, metallographic, thermogravimetric (TGA), and differential thermal (DTA) analyses. We are also assessing the effects of temperature gradient and burnup on the activities of N, C, and O. Finally, we are developing the information needed to design the decisive experiments that will demonstrate the best type of pin for meeting LMFBR requirements.

Synthesis, Fabrication, and Characterization of Nitride Fuels

Synthesis and Fabrication of Uranium Mononitride with ^{15}N Isotope (R. A. Potter, T. G. Godfrey)

A 500-g batch of $U^{15}N$ was successfully snythesized and fabricated into pellets. As described previously,[1] this material is to be used to assess the effect of the ^{14}N (n,α) ^{11}B reaction in UN, since the n,α process will not occur in the $U^{15}N$ material.

Depleted U metal was converted to powder by the usual hydride-dehydride-nitride procedure in our synthesis equipment. A specially constructed gas system admitted the $^{15}N_2$ to the synthesis retort through a heated getter furnace from the two 1-liter high-pressure cylinders. High-pressure valves and fittings were used throughout the system for gas supply. After the nitriding was completed, the unreacted $^{15}N_2$ was removed from the retort and associated piping by molecular-sieve sorption pumps through high-vacuum piping with Cu gaskets so that we could conserve our limited supply of $^{15}N_2$. When the sorption pumps were subsequently baked, the gas desorbed, producing a positive pressure that allowed us to transfer most of the gas back into the high-pressure cylinder at the temperature of liquid N_2.

The results of analysis by mass spectrometer of this reclaimed gas and of the newly arrived second cylinder are shown below with the earlier analysis[1] of the first cylinder:

---

[1]R. A. Potter and T. G. Godfrey, Fuels and Materials Development Program Quart. Progr. Rept. Dec. 31, 1968, ORNL-4390, pp. 36–38.

Component	First Cylinder Initial (wt %)	First Cylinder Reclaimed (wt %)	Second Cylinder (wt %)
H_2	0.03	1.53	0.01
H_2O	0.01	0.97	0.09
$^{14}N_2$ + CO	0.15	0.52	0.15
O_2	0.003	0.04	0.02
Ar	0.003	3.26	0.01
CO_2	0.003	0.01	0.01
$^{15}N_2$	99.79	93.67	99.74
$^{14}N:^{15}N$	0.11:99.89	0.36:99.64	0.34:99.66

The analysis of the reclaimed gas indicates that a significant quantity of H_2 was present in the retort or in the U powder when the nitriding began. This H_2 is not considered, however, to be deleterious. The Ar was intentionally added at the beginning of the nitriding step to serve as a buffer to the exothermic nitriding reaction. As will be noted later, the moderately high content of water and O_2 in the reclaimed gas was reflected in the sintered pellets. The gas in the second cylinder was very clean and almost isotopically pure, as that in the first cylinder initially was.

When the synthesis retort was unloaded, the first portion of the powder was stripped away, since it was the most likely to be contaminated with O_2. The remaining powder (500 g) was dry pressed in steel dies at 45 tsi into 60 pellets, each 0.4 in. in diameter by 0.5 in. long.

The system for gas supply was moved from the synthesis station to the sintering furnace, and a twofold test was performed. A pellet of the $U^{15}N$ material and a pellet from a lot of UN powder that was used previously were sintered with an atmosphere of normal N_2 in the furnace. Both pellets sintered well to high density and were free of oxide phase, which indicated that the $U^{15}N$ powder was sinterable and free of gross contamination with O_2 and that the additional piping had not adversely affected the furnace.

The $U^{15}N$ pellets were loaded into the furnace on a two-tier setter (normally only a single tier is used, but because of the limited supply of $^{15}N_2$, only one furnace run could be made). The furnace was heated

to 1500°C under a vacuum of 10^{-5} torr to decompose any UN_{1+x} present, and then both cylinders of $^{15}N_2$ were exhausted into the furnace. This yielded a pressure of about 500 torr, and Ar was added to a total pressure of 780 torr. The pellets were sintered at 2100°C rather than at the usual 2250°C because of the reduced N_2 overpressure and the resultant possibility that free metal would form at the higher temperatures.

When the furnace was cooled to 1500°C, the mixture of N_2 and Ar was removed by the sorption pumps for eventual return to the pressure cylinders. The pressure in the furnace was then further reduced to 10^{-6} torr by diffusion pump.

A pellet from each tier was examined metallographically. The pellet from the upper tier contained a small amount of uniformly distributed oxide phase, while the pellet from the lower tier contained a lesser amount. We cannot say with certainty when the O_2 entered, but we believe that it most likely was concurrent with the admission of the $^{15}N_2$. Chemical analysis is not complete at this time, and we can only estimate the contents for the upper and lower tiers at 2500 and 1500 ppm O, respectively. While this contamination is more severe than we expected, the material is acceptable for the intended irradiation experiments.

Synthesis and Fabrication of Mixed Nitrides (E. S. Bomar)

Following introduction of Pu metal into our glove-box line, we prepared several batches of PuN. We found, as others have also reported, that Pu metal reacts quite rapidly with H_2 at room temperature as opposed to U, which must be heated to about 250°C to obtain a fairly rapid rate of hydriding. Pieces of Pu 1/2 in. in diameter and 3/4 in. long are converted to the hydride in a few hours at room temperature. A portion of some pieces failed to react with the H_2 atmosphere even on heating. We found, however, that after these pieces were separated from the hydride powder, crushed (they were easily broken), and again exposed to H_2, they readily reacted even at room temperature. The plutonium hydride was decomposed by heating to 500°C under vacuum and then converted to PuN by introducing N_2 at a reduced pressure and slowly raising the temperature to 800°C. Since Pu does not form a higher nitride, it is not necessary to heat to about 1050°C as with U to decompose U_2N_3.

We plan to examine the effectiveness of both mechanical mixing of separately prepared PuN and UN and prealloying of the metallic Pu and U on the homogeneity of the (U,Pu)N product. In the absence of capability for arc melting Pu-bearing materials, we melted a U–20% Pu charge in a graphite boat coated with a yttrium oxide wash. The molten metal penetrated the oxide layer, however, resulting in extensive reaction with the graphite. So far, subsequent attempts to sinter a yttrium oxide coating onto an aluminum oxide boat in order to get a mechanically stronger coating have not been successful.

Incidental to the melting experiment, we found that beta and gamma activity on the gloves in the boxes rose by a factor of five or six to 35 mr after we handled the graphite boats and alloyed U and Pu. Routine melting operations would, therefore, require a far more frequent changing of gloves than would otherwise be necessary.

The two tube furnaces that are to serve the dual functions of nitride synthesis and sintering were found to heat to only 1590°C, somewhat short of their rating of 1750°C. A supply voltage of 195 v, rather than the 208 v specified, accounted in part for the low, limiting temperature. While this condition was being corrected, we pressed and sintered the initial three pellets of UN, PuN, and (U,Pu)N; the results are shown in Table 2.1. Increasing the voltage to 208 v raised the

Table 2.1. Data for Pellets[a] Pressed at 30 tsi in Steel Die Lubricated with Stearic Acid and Sintered 1 hr at 1590°C

Sample	As Pressed		Sintered		
	Density		Weight	Density	
	(g/cm^3)	(% theoretical)	(g)	(g/cm^3)	(% theoretical)
UN	9.65	67.4	1.998	10.44	72.9
$(U_{0.8},Pu_{0.2})N$	9.56	66.9	2.010	9.18	64.2
PuN	9.72	68.2	1.998	10.65	74.9

[a]Each pellet weighed 2.000 g.

limiting temperature of the furnace to 1659°C. The manufacturer admits to a failure to properly estimate the rate of heat loss for this particular design and has supplied two booster transformers, which we shall soon install.

Glove boxes for our furnace with W resistors and for the apparatus for measuring vapor pressure were received. Several minor modifications are being made before we install the boxes.

Metal Nitride Synthesis Apparatus (K. E. Spear, V. J. Tennery, J. M. Leitnaker)

An improved apparatus for preparing high-purity metal nitrides in research quantities of 5 to 50 g has been constructed and is in use. This apparatus will be used in nitriding metals and alloys by hydride-nitride cycles. Thus far, U metal and three alloy compositions of U and V have been nitrided.

The apparatus consists of a metal vacuum system capable of producing about 1×10^{-6} torr, two independent reaction chambers of quartz, and a gas ballast tank. The reaction chambers are heated with clam-shell furnaces capable of producing 1000 to 1100°C. The progress of hydriding or nitriding can, therefore, be followed visually by opening the furnace and looking through the glass reaction tube at the sample. The gases used are purified by UN placed in a boat immediately in front of the sample. Samples will be analyzed for O impurity to determine whether this purification scheme needs to be modified. The reaction tube is constructed so that all of the loading and unloading of samples can be done in an Ar-filled glove box. At no time is it necessary for the samples to be exposed to air.

Characterization of UN and (U,Pu)N (V. J. Tennery, E. S. Bomar)

X-Ray Diffraction Facility of Interim Plutonium Facility. — The x-ray table required for the Debye-Scherrer camera for work with samples containing Pu was installed and made operational. The x-ray cameras have been received and are being tested on the unit. The diffractometer part of this system is now fully operational. The techniques required

for the control of the spread of alpha activity within the glove-box suite of this system are ready for testing with alpha-active materials other than Pu. As soon as these tests are completed and the appropriate safety approvals have been obtained, the samples containing Pu will be introduced into the facility.

Chemical Analysis of UN. — The results of chemical analyses on several batches of UN prepared with the equipment in the Interim Plutonium Facility are given in Table 2.2. The results show that some U_2N_3 is present in the UN (5.55% N theoretical) that was held at 1050°C under a vacuum of 10^{-5} torr for about 1/2 hr. Multiple samples taken from one batch of UN and submitted for analysis at three intervals gave a large scatter for O content, as is also shown in Table 2.2. Our attempts to correlate the results from analytical chemistry with x-ray diffraction and metallographic examinations have raised further questions on the accuracy of the analyses for N and O. We are, therefore, systematically evaluating the suitability of both the sample-handling and the analytical techniques currently used for analysis of UN and mixtures of UN and U_2N_3.

Table 2.2. Results of Chemical Analysis of UN Powders Prepared in Interim Plutonium Facility

Batch Number	Composition, wt %				Balance (%)
	U	N	C	O[a]	
UN-2	94.10	5.69	0.020	0.152	99.96
UN-3	94.21	5.76	0.022	0.163	100.15
UN-4	94.30	5.67	0.016	0.170	100.16
UN-5	94.09	5.99	0.014	0.130	100.18
UN-6	94.20	5.77	0.022	0.064	100.06
UN-8-1[b]				0.113	
UN-8-2				0.119	
UN-8-3				0.119	
UN-8-4				0.027	
UN-8-5				0.028	
UN-8-6				0.029	
UN-8-11				0.443	
UN-8-12				0.441	
UN-8-13				0.444	

[a] The U metal used to prepare the UN powder contained 0.0095 wt % O.

[b] Average particle size for lot UN-8, based on measurement of surface area, is 5 μm as synthesized.

Synthesis, Fabrication, and Thermodynamic Properties of Carbonitride Fuels

Manufacture of UC, UN, and U(C,N) From UO_2 (T. B. Lindemer, J. M. Leitnaker)

The kinetics of the conversion of sol-gel UO_2 to uranium carbides, nitrides, and carbonitrides is being studied to determine the mechanisms that control the rate of the conversion processes. This information, which is fundamental to the design of reactor fuel cycles, is a prelude to the conversion of mixed $(U,Pu)O_2$ to the carbonitride.

Kinetics of the UC_2-N_2 Reaction. — We analyzed all the results obtained during this study to determine the mechanism that controls the rate of the reaction of UC_2 microspheres with N_2. Previous reports[2–4] contain our experimental results and the theoretical models used for the analysis of reactions in spheres.

One factor that complicated the analysis was the presence of free C in the initial UC_2 microspheres.[5] Additional C precipitated on these sites during the reaction, thus giving a two-phase mixture of U(C,N) or UC_2 and free C. This internal C may have served as a diffusion path for N_2 and also increased the amount of interface between C and the carbide available for interface reactions. Fortunately, we were able to make a quantitative measurement of the internal surface area of the interface between free C and the carbides. We used this information in modified models for reactions in spheres to include the effects of the internally precipitated C, as will be developed below.

The effect of each mechanism in the conversion process must be examined to determine if it is the one controlling the reaction. These mechanisms can be divided into two classes: interface reactions and diffusion. The interface reactions shown in Fig. 2.1 occur at phase

---

[2]T. B. Lindemer, Fuels and Materials Development Program Quart. Progr. Rept. June 30, 1968, ORNL-4330, pp. 32–39.

[3]T. B. Lindemer and J. M. Leitnaker, Fuels and Materials Development Program Quart. Progr. Rept. Sept. 30, 1968, ORNL-4350, pp. 39–47.

[4]T. B. Lindemer and J. M. Leitnaker, Fuels and Materials Development Program Quart. Progr. Rept. Dec. 31, 1968, ORNL-4390, pp. 42–44.

[5]As used here, UC_2 represents the nominal dicarbide; the ratio of C:U is always less than two.

ORNL-DWG 69-6352

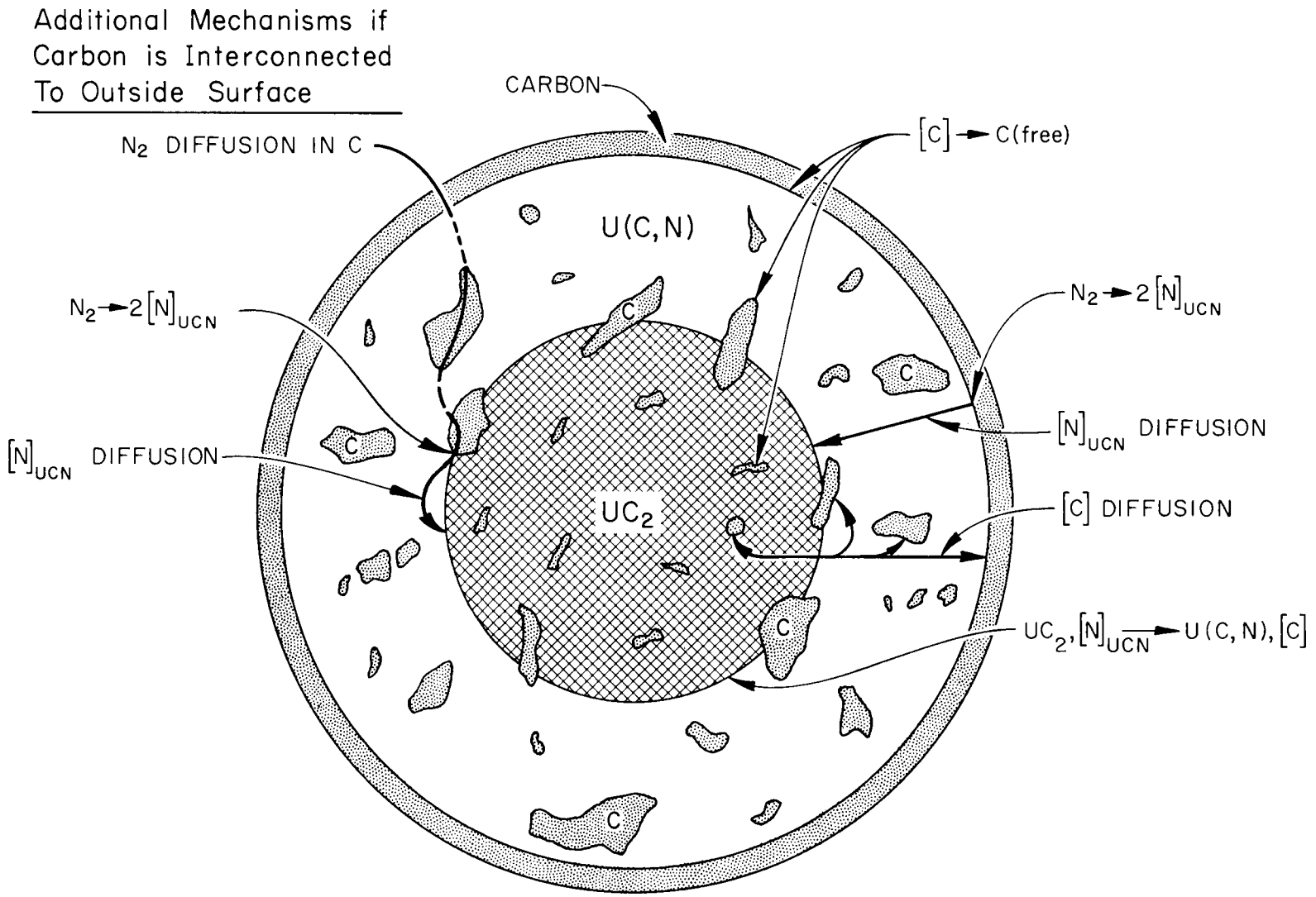

Fig. 2.1. Mechanisms Postulated to Occur in the Reaction of UC_2 with Nitrogen to Produce U(C,N) and Free Carbon.

interfaces and are postulated to be the following:[6]

1. $N_2 \rightarrow 2\ [N]_{U(C,N)}$ at the interface between the sphere and N_2.

2. $N_2 \rightarrow 2\ [N]_{U(C,N)}$ at the surface of the sphere and at internal interfaces between C and both U(C,N) and UC_2.

3. $[C] \rightarrow C_{(free)}$ at the sphere surface and at internal free-C sites.

4. $[N]_{U(C,N)}$, $UC_2 \rightarrow U(C,N)$, [C] at the interface between U(C,N) and UC_2.

The diffusion mechanisms are postulated to be these:

5. [C] diffusing from the interface between UC_2 and U(C,N) through the U(C,N) or UC_2 to the free-C sites.

6. $[N]_{U(C,N)}$ diffusing from the sphere surface through the U(C,N) to the interface between UC_2 and U(C,N).

7. $[N]_{U(C,N)}$ diffusing from all interfaces of C and U(C,N) to the interface between UC_2 and U(C,N).

8. N_2 diffusing through the free C.

The second, seventh, and eighth mechanisms would be rate controlling if the free C served as an interconnected path for N to diffuse from the surface to the interior of the sphere. We have not been able to demonstrate whether a C interconnection exists at all stages of the reaction, even though we know from C-stripping experiments that the C is interconnected with the sphere surface at 100% reaction.[3]

The kinetic models used for the analysis of our results for conversion versus time permit us to eliminate many of these possible mechanisms as the ones controlling the conversion process. The first mechanism can be eliminated because a plot of the data for such a reaction at the sphere surface is not linear with time (see Fig. 2.3 of ref. 3). The second and third mechanisms can be analyzed after the development of a new kinetic model for surface control that includes the effect of the time-dependent generation of new carbon-carbide surface. If we define Q as the volume of UC_2 reacted, then

---

[6]Brackets indicate a species in solid solution.

$$\frac{dQ}{dt} = k_c\left[4\pi r_o^2 + \frac{4\pi r_o^3}{3} S(t)\right] , \tag{2.1}$$

in which k_c is the proportionality constant for a reaction controlled at an interface between C and carbide, t is time, $4\pi r_o^2$ is the surface area of the sphere, and S(t) is the time-dependent area of internal interfaces between C and carbide per unit volume of the solid system. As will be shown below, we can measure S(t) by standard methods of quantitative metallography. Also,

$$\frac{dQ}{dt} = \frac{d}{dt}(V_o - V_t) = -4\pi r^2 \frac{dr}{dt} , \tag{2.2}$$

in which V_o is the original volume of the sphere and V_t is the volume and r is the radius of the UC_2 core at time t. From these equations one can obtain

$$k_c\left[\int_o^t dt + \frac{r_o}{3}\int_o^t S(t)dt\right] = \frac{1}{r_o^2}\int_r^{r_o} r^2 dr , \tag{2.3}$$

which leads to

$$\frac{r_o\left(1 - \frac{r^3}{r_o^3}\right)}{3t + r_o\int_o^t S(t)\, dt} = k_c . \tag{2.4}$$

Evaluation of the left side of Eq. (2.4) at different times gives values of $k_c(t)$. If this quantity were constant at all times, it would indicate that the reaction is controlled by the second or third mechanisms; conversely, if it varied with time, it would indicate that the reaction is not controlled by these mechanisms. The values used were obtained from experiment A5164-12 (see Fig. 2.4 in ref. 7) and are listed in Table 2.3. The integral of S(t) was evaluated from these data

[7]T. B. Lindemer and J. M. Leitnaker, Fuels and Materials Development Program Quart. Progr. Rept. Sept. 30, 1968, ORNL-4350, pp. 39–47.

Table 2.3. Data from Specimen A5164-12 (Tested at 1700°C Under 380 torr Nitrogen Pressure) Used for Evaluation of Eq. (2.4)

t (min)	$r_o\left(1 - \frac{r^3}{r_o^3}\right)$ [a] (cm)	$S(t)$ [b] (cm^2/cm^3)	$\sigma_{\bar{S}}$ [c] (cm^2/cm^3)	$r_o \int S(t)\, dt$ [d] (min)	k_c (cm/min)
					$\times 10^6$
0	0	70 [e]	0	0	0
180	0.004788	274	32	768	3.66
363	0.009227	350	44	2184	2.82
542	0.012873	316	56	3662	2.43
720	0.017744	348	39	5128	2.43
900	0.021017	486	63	6989	2.17
1080	0.021477	372	33	8904	1.77
1245	0.023423	455	61	10600	1.64
1440	0.024002	355	52	12560	1.42

[a] Average of 25 spheres at each time.

[b] Average obtained from 5 or 6 sphere microstructures, with about 10 test lines placed on each microstructure. $S(t) = 2N_L$, where N_L is the number of intersections made by that unit length of test line with the internal interface between C and carbide.

[c] Standard deviation of the average of $S(t)$, $\sigma_{\bar{S}} = \sigma_S/\sqrt{n}$.

[d] $r_o = 0.0248$ cm, the average of 200 determinations of r_o.

[e] Estimated.

by use of the trapezoidal rule. These results illustrate that k_c decreases with time; therefore, the second and third mechanisms do not control.

The sixth and eighth mechanisms can also be eliminated. If the free C were not interconnected, the sixth mechanism would be possible, and the eighth would be possible if the C were interconnected. If either of these were controlling, the conversion should have followed a model for diffusion control. We have seen that it does not (Fig. 2.3 of ref. 7).

We are left with only the fourth, fifth, and seventh mechanisms and must now deduce the one controlling mechanism. We have observed

the fourth mechanism both in microspheres that did and those that did not contain free C (Figs. 2.6 and 2.7 of ref. 8). The conversion rate was about twice as fast in the microspheres that contained C and, therefore, could not have been controlling in the microspheres without C. We would assume from the small difference in rates that this mechanism did not control in the microspheres that contained C either. The seventh mechanism is like the second, for both require interconnection of free C with the surface of the sphere and, therefore, with an unlimited supply of N_2. It seems very unlikely that this interconnection exists in the initial stages of the reaction, when the amount of free C is small (Figs. 2.3 and 2.4 of ref. 8), although it is probable in the last 20% of the reaction. In addition, we found[8] that the reaction was independent of the pressure of N_2 in the range 180 to 580 torr. These observations indicate that the mechanism is not controlled by any process involving N. Therefore we conclude that the fifth mechanism, the diffusion of [C] from the interface between UC_2 and U(C,N) to the nearest free-C site, is controlling during the greater portion of the reaction in microspheres both with and without C. The activation energy for the diffusion of C under these conditions is 77.7 ± 3.7 kcal/mole (ref. 7).

We must resolve one final point. The kinetic models used for these analyses demonstrated that the reaction was controlled very near the interface between UC_2 and U(C,N) (Fig. 2.3 of ref. 7). This implies at first that the chemical reaction, the fourth mechanism, is controlling. However, the uniform internal distribution of free C in the microsphere would maintain an approximately constant C:C separation during the entire conversion process. This would permit an approximately constant flux of C from the interface between UC_2 and U(C,N) to the nearest C particle (according to Fick's first law). The flux, in grams of C per square centimeter of interface between U(C,N) and UC_2 per unit time, limits the rate of conversion of UC_2 near the interface between UC_2 and U(C,N). The reaction would, therefore, follow the model for interface control even though the diffusion of C was actually controlling the reaction.

---

[8]T. B. Lindemer, Fuels and Materials Development Program Quart. Progr. Rept. June 30, 1968, ORNL-4330, pp. 32–39.

Kinetics, Thermodynamics, and Gas-Solid Reactions. — We are often concerned with the minimum time necessary to complete a reaction that involves a gaseous product. Typical reactions would be those of UO_2-C sols to produce UC, UC_2, and CO, or C stripping with H_2 to produce CH_4 and C_2H_2. These reactions are often performed in fluidized beds in which gas at a given flow rate is used to fluidize the reactants. We also know that the fluidization gas cannot accommodate more than the equilibrium pressure of product gas. Therefore, if one knows the flow rate, the equilibrium pressure of the product gas, and the total amount of product gas to be removed, one can calculate the minimum time necessary for completion of the reaction. A simple case would be one in which there were no reactant gases and the one product gas had a small (< 0.05 atm) equilibrium pressure in a system at one atmosphere of total gas pressure. If such a reaction were considered per mole of the single-product gas, the equilibrium pressure would be equal to K_{eq}, the equilibrium constant, if the activity of the solids in the system were unity. The minimum time for the conversion would then be

$$\text{time} = \frac{\text{total volume of product gas}}{(K_{eq})(\text{flow rate, volume/time})} .$$

Relations of this type can be derived readily for more complicated systems and may be useful in processes used for sol-gel conversion.

C-H_2 Reactions in U-C-N Systems. — We applied the developments of the preceding section to determine whether H_2 could be used to strip free C from particles. This was of especial interest in removing free C from the products of the reaction of UC_2 and N_2 and from the U(C,N) produced by reacting sol-gel mixtures of UO_2 and C in N_2. The equilibrium pressures of the hydrocarbon products were so low that it was not possible to remove significant amounts of C with H_2 at practical times and temperatures.

We also realized that we had erroneously reported (Fig. 2.6 of ref. 8) that H_2 was used to strip C from a U(C,N)-C microsphere produced by the reaction of UC_2 and N_2. A review of the experimental procedures indicated that it was impossible to remove the C with H_2 in the times indicated; instead, we found that a small amount of O_2 had been

introduced during the changing of a gas tank during the run. This O_2 stripped the C and produced CO, which has a high equilibrium pressure at the experimental conditions. Repeating the experiment so that no O_2 was admitted showed that the H_2 stripping was, indeed, extremely slow.

Solution of N_2 in UC_2. – We reported[9] a definite effect of exposure to N_2 at 1600°C on the lattice parameters a_o and c_o of UC_2. We now believe that this has occurred via substantial solution of N in UC_2. Several arguments substantiate this conclusion.

One argument is based on the change in the lattice parameter a_o and the observation by Eyre and Sole[10] that $\{001\}_{UC}$ are parallel to $\{001\}_{UC_2}$ and that $\langle 100\rangle_{UC}$ are parallel to $\langle 110\rangle_{UC_2}$. From this it is evident that $\sqrt{2}\ (a_o)_{UC_2} \cong (a_o)_{UC}$. In Fig. 2.2 we plot the values of the lattice parameters measured for the quenched specimens (reported earlier in Table 2.3 of ref. 9) versus the time of exposure to N_2 at 1600°C and a N_2 pressure of 380 torr. No change in parameter was noted for longer exposure times. Although our initial value for the lattice parameter of UC_2, 3.5172 A, is less than the 3.519 A given by Storms[11] for well-annealed UC_2, our value is consistent with the trend of our data and with Storms's[11] observation that the lattice parameter is smaller for quenched specimens. Therefore, we have a change in lattice parameter from 3.5172 to 3.5132 A, or a change of 0.0040 A.

This can be converted to a value for the ratio of N:N+C by means of the data that Leitnaker et al.[12] developed for the U(C,N) solid solutions. The change of 0.0040 A in the lattice parameter of UC_2 is equivalent to a change of $\sqrt{2} \cdot 0.0040$ A in the lattice parameter of UC as it takes N_2 into solution. Using 4.9602 A as the lattice parameter of UC (ref. 12) and subtracting our equivalent change, we get 4.9546 A as the value of the lattice parameter of U(C,N). This is used in the expression[12]

---

[9]T. B. Lindemer and J. M. Leitnaker, Fuels and Materials Development Program Quart. Progr. Rept. Sept. 30, 1968, ORNL-4350, pp. 39–47.

[10]B. L. Eyre and M. J. Sole, Phil. Mag. 9, 545 (1964).

[11]E. K. Storms, The Refractory Carbides, p. 187, Academic Press, New York, 1967.

[12]J. M. Leitnaker, R. A. Potter, K. E. Spear, and W. R. Laing, "The Lattice Parameter of U(C,N) as a Function of Composition," Journal of High Temperature Science. Accepted for publication.

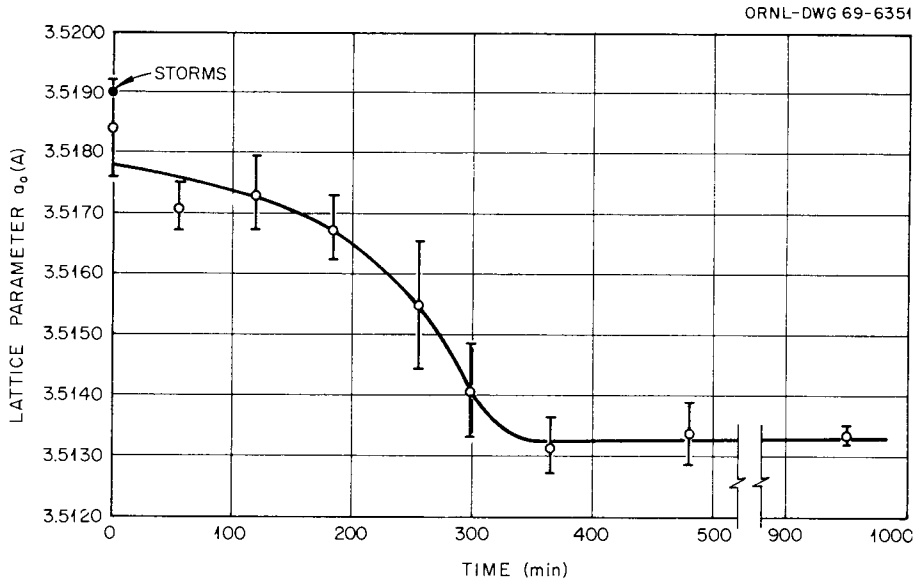

Fig. 2.2. The a_o Lattice Parameter of $U(C,N)_2$ Versus Time of Exposure to Nitrogen at a Pressure of 380 torr and 1600°C. The standard deviation of each point is also shown. (Ref. E. K. Storms, The Refractory Carbides, p. 187, Academic Press, New York, 1967.)

$$N{:}N{+}C = 1.00 - 13.2488\,\Delta + 42.5072\,\Delta^2 + 213.035\,\Delta^3 - 13767.7\,\Delta^4 ,$$

where $\Delta = (a_o)_{UC_2} - (a_o)_{UN}$ (the lattice parameter of UN is 4.8892 A). From this we get N:N+C = 0.123 in the U(C,N) system; we assume that this ratio is also representative of the $U(C,N)_2$ system. This assumption leads to the maximum calculated solubility of N_2 in UC_2.

The uranium dicarbonitride composition can be estimated from this ratio and the amount of free C observed metallographically in the compound after the reaction with N_2 but before significant amounts of U(C,N) have formed. Table 2.2 of ref. 9 shows that there was 4.1 vol % free C; the other 95.9 vol % was $U(C,N)_2$. Using 5.33 and 22.4 cm^3/mole as the molar volumes of C and the dicarbonitride respectively, the volume percentages are equivalent to 0.180 mole of free C per mole of dicarbonitride. The reaction can then be written

$$UC_{1.86} + 0.118\ N_2 \rightarrow U(C_{0.877},N_{0.123})_{1.92} + 0.180\ C\ .$$

It can be seen that the dicarbide reacts to take on substantial N and that the ratio of C+N:U increases over that for C:U in the dicarbide. The substantial solution of N in UC_2 has not been observed previously.[11]

Compatibility of Mixed-Nitride and Carbonitride Fuels with LMFBR Cladding Alloys

Properties of Vanadium Carbonitride Solutions at High Temperatures

(K. E. Spear, J. M. Leitnaker)

We have previously reported on the properties of vanadium carbonitride solutions at high temperatures.[13,14] This report summarizes the results and conclusions reached after further work on this system. These studies are a prerequisite to the evaluation of the compatibility of V alloys with the carbonitrides of U and Pu.

The lattice parameters of V(C,N) solutions in equilibrium with C and N_2 were reported[14] for N_2 pressures of 50, 100, 300, and 600 torr at 1200 to 1600°C. These results indicated a dependence of the lattice parameter on starting material. We attributed this dependence to the formation of a thermodynamically active form of C as a product of the VC reaction with N_2 to form V(C,N) solutions.

The curve for lattice constant versus composition given previously[14] is still valid within the range of our data (N:V = 0.0 to 0.3 molar ratio). However, the unusual minimum in the curve for a ratio of N:V of about 0.8, which resulted from the data of Brauer and Schnell,[15] is now more doubtful as a result of data published by Roubin and Paris.[16] Brauer and Schnell's data in that composition region are probably for samples that do not have a maximum N+C:V ratio (samples not in equilibrium with C and N_2). Figure 2.3 shows a revised plot of lattice parameter versus the N:V ratio for nonmetal-rich V(C,N). The curve is a visual fit of the data.

---

[13] K. E. Spear and J. M. Leitnaker, Fuels and Materials Development Program Quart. Progr. Rept. June 30, 1968, ORNL-4330, pp. 43–49.

[14] K. E. Spear and J. M. Leitnaker, Fuels and Materials Development Program Quart. Progr. Rept. Dec. 31, 1968, ORNL-4390, pp. 50–54.

[15] G. Brauer and W. D. Schnell, J. Less-Common Metals 7, 23–30 (1964).

[16] M. Roubin and J. M. Paris, J. Less-Common Metals 15, 227–233 (1968).

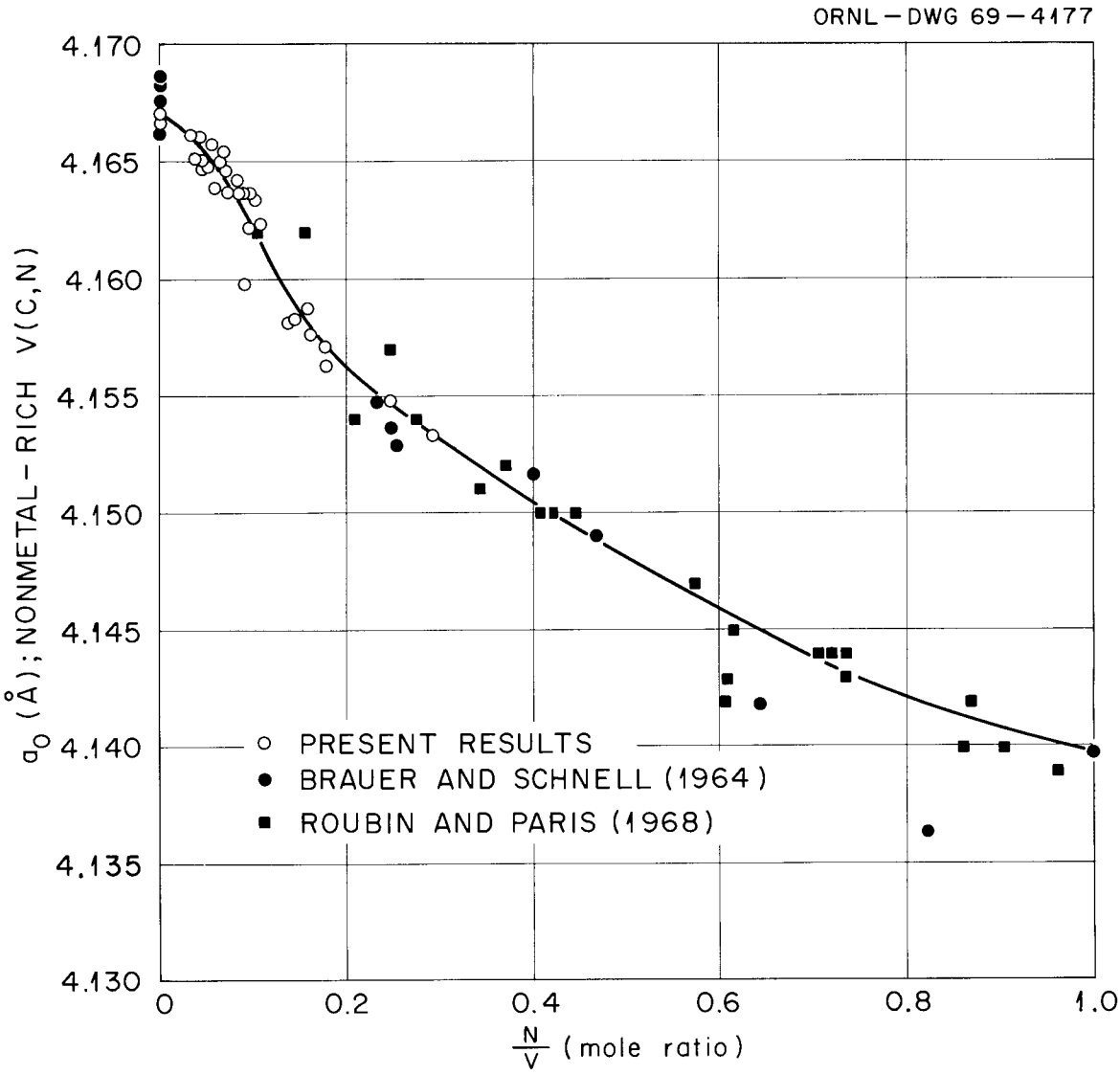

Fig. 2.3. Relationship Between Lattice Parameter and Composition for Nonmetal-Rich V(C,N) Solutions. [Refs. G. Brauer and W. D. Schnell, J. Less-Common Metals 7, 23–30 (1964); M. Roubin and J. M. Paris, J. Less-Common Metals 15, 227–233 (1968).]

Plots of N+C:V versus N:N+C are given in Fig. 2.4; Fig. 2.4(a) shows the data of Roubin and Paris[16] and Fig. 2.4(b) gives our results along with those of Brauer and Schnell.[15] The two curves shown are identical and are a visual fit of the data in Fig. 2.4(b).

Superstructure lines caused by vacancy ordering, similar to that observed in C-rich VC, have been observed in x-ray diffraction patterns of carbonitrides. The intensities of the lines decrease with increasing N content and disappear at a N:N+C ratio greater than about 0.1. In this same composition region, the N+C:V molar ratio is constant at 0.89 ± 0.02. As the N content increases the ratio of nonmetal to metal increases to unity at pure VN.

Apparently, as N atoms are added to the solution, the vacancy lattice becomes disordered. Then, the vacancies start being filled when the ratio of N+C:V starts increasing from 0.89 ± 0.02 toward unity.

The Crystal Structures of UVC_2 and UVN_2 (K. E. Spear, J. M. Leitnaker)

Two new phases, UVC_2 and UVN_2, have been discovered and their crystal structures deduced to be isomorphous with that of $UMoC_2$ (ref. 17). Several ternary carbides of this type have been previously reported, but UVN_2 is the first known nitride of this type. Others such as $UCrN_2$ and $UMoN_2$ probably exist, but have not been looked for. It would be surprising and very interesting if these and other such nitride compounds were not found, particularly since similar ternary carbide compounds with Cr, Mo, W, Mn, Tc, and Re are known.[18] Perhaps $UTiN_2$ exists, since the total number of electrons in this compound is the same as that in $UCrC_2$ and since Ti and Cr are about the same size.

In this report, only the data and results relating directly to the crystal structure analyses of UVC_2 and UVN_2 are given. Investigations of the phase behavior in the U-V-C and U-V-N ternary systems will be reported at a later date.

---

[17] D. T. Cromer, A. C. Larson, and R. B. Roof, Jr., Acta Cryst. 17, 272–276 (1964).

[18] H. J. Goldschmidt, Interstitial Alloys, pp. 156–159, Plenum Press, New York, 1967.

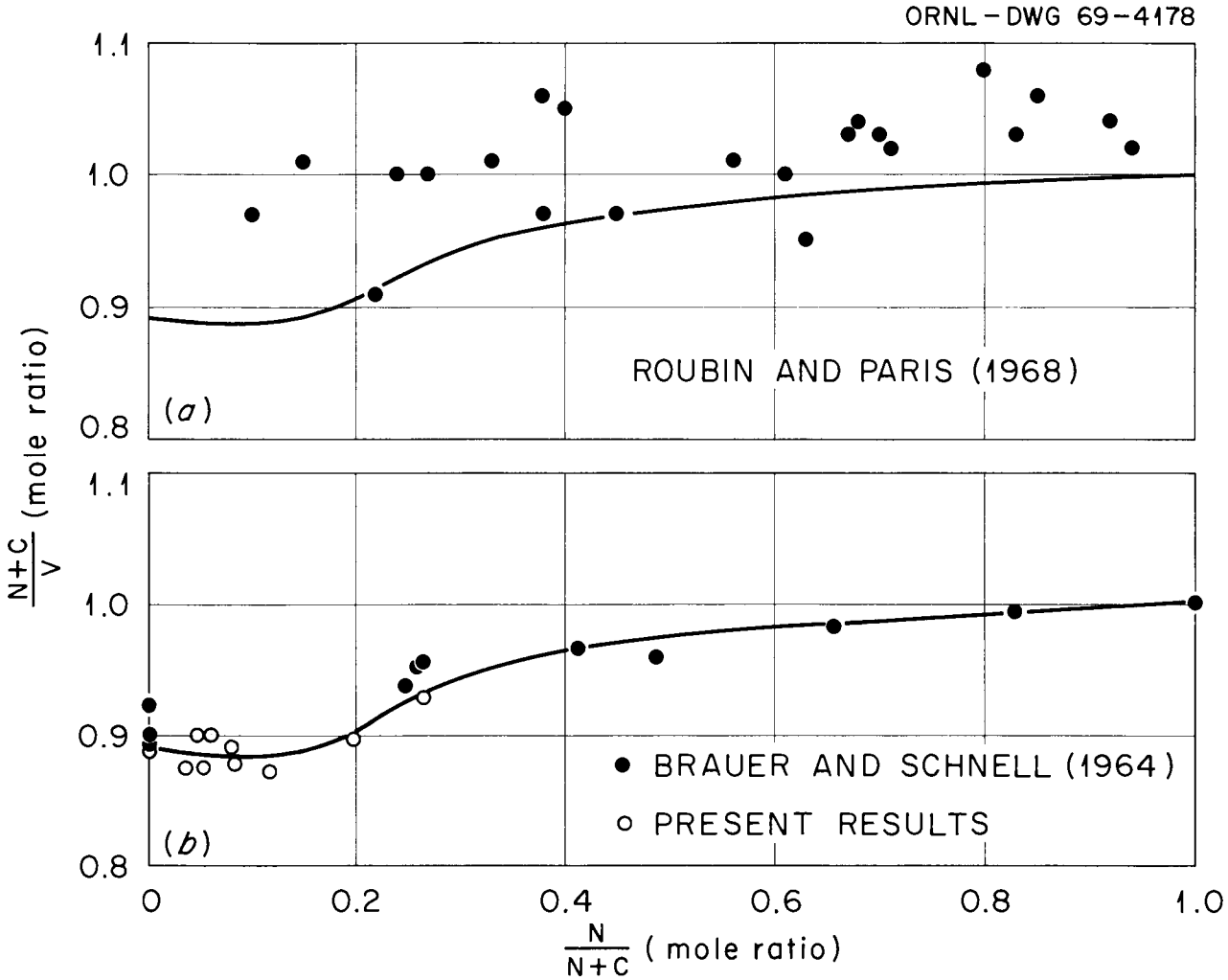

Fig. 2.4. Relationship of N+C:V and N:N+C for Nonmetal-Rich V(C,N) Solutions. [Refs. G. Brauer and W. D. Schnell, J. Less-Common Metals 7, 23–30 (1964); M. Roubin and J. M. Paris, J. Less-Common Metals 15, 227–233 (1968).]

Crystallographic data were obtained from Debye-Scherrer x-ray powder diffraction patterns. The samples were −325 mesh (−44 μm) powder loaded into 0.3-mm Lindemann glass capillaries. A camera of the Straumanis type with a 114.6-mm radius was used with CrK_{α} radiation. Respective values for α_1, α_2, and $\alpha_{1,2}$ of 2.28962, 2.29351, and 2.29092 A were used. Lattice constants were calculated on a digital computer by the procedure detailed by Vogel and Kempter[19] using a Nelson-Riley extrapolation.[20]

The diffraction lines on the x-ray powder films were measured visually on a film reader, the calculated diffraction angles were corrected for film shrinkage, and the intensities of the lines were estimated.

Relative intensities for all possible diffraction lines were calculated with the use of the equation given by Cullity,[21]

$$I = |F|^2 \, p\left(\frac{1 + \cos^2 2\theta}{\sin^2 \cos\theta^2}\right), \qquad (2.5)$$

where I = relative integrated intensity (arbitrary units), F = structure factor, p = multiplicity factor, and θ = Bragg angle. This equation is restricted to the Debye-Scherrer method and is most accurate in comparing lines of approximately the same diffraction angle. The relative integrated intensity is the relative area under the curve of intensity versus 2θ. Structure factor calculations were based on the orthorhombic $UMoC_2$ space group (Pnma) and atom positions given by Cromer, Larson, and Roof.[17]

Tables 2.4 and 2.5 list the x-ray data for UVC_2 and UVN_2, respectively. The observed and calculated $\sin^2\theta$ and relative intensity are

---

[19]R. E. Vogel and C. P. Kempter, Acta Cryst. 14, 1130–1134 (1961).

[20]H. P. Klug and L. E. Alexander, X-Ray Diffraction Procedures, pp. 440–490, John Wiley and Sons, Inc., New York, 1954.

[21]B. D. Cullity, X-Ray Diffraction, p. 132, Addison-Wesley Publishing Company, Inc., Reading, Mass., 1956.

Table 2.4. X-Ray Data for Orthorhombic UVC_2

Miller Indices			$\sin^2\theta$ [a]		Relative Intensity	
h	k	l	Observed	Calculated	Observed	Calculated
			$\times 10^{-4}$	$\times 10^{-4}$		
1	0	1	558	544	medium weak (mw)	4.3
1	0	2	903	887	weak (w)	2.2
0	1	1	1373	1357	medium (m)	3.2
1	0	3	1477	1459	medium strong (ms)	4.2
2	0	0	1741	1720	very weak (vw)	1.0
1	1	1	1808	1787	vw	1.5
0	0	4	1852	1829	strong (s)	2.9
2	0	1		1835		3.2
1	1	2	2148	2130	very strong (vs)	10.0
1	0	4	2287	2259	w	0.3
0	1	3		2271		0.4
1	1	3	2722	2701	m	1.8
2	0	3	2774	2749	mw	1.1
2	1	0	2983	2963	ms	1.4
2	1	1	3091	3077	w	0.6
2	1	2	3570	3420	w	0.3
1	1	4		3501		0.3
2	0	4		3549		0.8
0	1	5	4119	4100	s	1.7
0	0	6		4115		0.2
3	0	2	4351	4328	ms	0.9
1	1	5	4600	4530	ms	0.2
1	0	6		4545		0.2
2	0	5		4578		1.1
2	1	4	4815	4791	s	1.0
0	2	0	4983	4969	m	1.1
3	1	1	5247	5227	vs	1.7
1	2	1	5520	5513	w	0.4
3	0	4	5805	5700	ms [b]	0.3
1	1	6		5787		1.5
2	1	5		5820		0.6
1	2	2		5856		0.3
1	0	7	6050	6031	m	1.0
3	1	3	6163	6142	s	2.0
1	2	3	6438	6428	m	1.2
2	2	0			vw [c]	0.4

Table 2.4. (continued)

Miller Indices			$\sin^2\theta$ [a]		Relative Intensity	
h	k	l	Observed	Calculated	Observed	Calculated
			$\times 10^{-4}$	$\times 10^{-4}$		
0	2	4	6811	6798	s	1.1
2	2	1		6803		1.2
4	0	0		6881		0.2
4	0	1	7008	6996	mw	0.8
2	1	6	7087	7077	mw	0.9
1	2	4		7228	mw [b,c]	0.2
1	1	7		7273		0.4
0	0	8		7315		0.4
2	2	3	7723	7718	mw	0.8
1	0	8		7745		0.3
4	0	3		7910	vw [c]	0.4
3	1	5	7988	7971	m	0.4
3	0	6		7986		0.6
4	1	0	8129	8123	mw	0.6
4	1	1	8243	8238	vw	0.2
2	2	4	8522	8518	w	1.1
4	1	2		8581		0.1
4	0	4	8714	8710	vw	0.4
1	1	8	8977	8978	w	0.9
2	0	8		9025	vw [b,c]	0.2
0	2	6		9073		0.4
4	1	3		9142		0.1
3	2	2	9289	9286	s	2.8
1	2	6	9537	9503	s	0.6
2	2	5		9536		4.1
1	0	9	9729	9678	m	0.3
4	0	5		9728		2.6
4	1	4		9941	s [c]	8.2

[a] The $\sin^2\theta$ values less than 0.89 are for $CrK_{\alpha_{1,2}}$ radiation (2.29092 A). The larger values are for CrK_{α_1} (2.28962 A). The calculated values are for lattice parameters a_o = 5.5234 A, b_o = 3.2500 A, and c_o = 10.714 A.

[b] The line was very diffuse.

[c] A line was observed, but its $\sin^2\theta$ value was not measured.

Table 2.5. X-Ray Data for Orthorhombic UVN_2

Miller Indices			$\sin^2\theta$[a]		Relative Intensity	
h	k	l	Observed	Calculated	Observed	Calculated
			$\times 10^{-4}$	$\times 10^{-4}$		
1	0	1	571	557	weak (w)	4.4
1	0	2	921	903	w	2.2
0	1	1	1428	1409	medium weak (mw)	3.0
1	0	3	1499	1479	medium (m)	4.3
2	0	0	1779	1766	w	1.0
0	0	4	1866	1845	medium strong (ms)	2.9
1	1	1		1850		1.4
2	0	1	1899	1882	m	3.1
1	1	2	2215	2196	very strong (vs)	10.0
1	0	4		2287	very weak (vw)[b]	0.3
0	1	3		2331		0.4
1	1	3	2783	2773	mw	1.8
2	0	3		2804		1.2
2	1	0	3072	3060	m	1.5
2	1	1	3182	3175	w	0.6
2	1	2	3616	3521	w	0.4
1	1	4		3580		0.3
2	0	4		3611		0.9
0	0	6	4187	4151	ms	0.2
0	1	5		4176		1.7
3	0	2	4439	4435	mw	1.0
1	0	6	4674	4593	mw	0.2
1	1	5		4618		0.2
2	0	5		4649		1.2
2	1	4	4925	4905	mw	1.0
0	2	0	5189	5174	mw	1.1
3	1	1	5405	5383	ms	1.8
1	2	1	5761	5731	vw	0.4
3	0	4	5844	5819	vw	0.3
1	1	6	5905	5886	m[c]	1.6
2	1	5		5943		0.6
1	2	2	6113	6077	mw	0.4
1	0	7		6092		1.0
3	1	3	6322	6305	vs	2.0
1	2	3	6668	6653	ms	1.2
2	2	0		6940	vw[b]	0.4
0	1	7		6944		0.1

Table 2.5. (continued)

Miller Indices			$\sin^2\theta$ [a]		Relative Intensity	
h	k	l	Observed	Calculated	Observed	Calculated
			$\times 10^{-4}$	$\times 10^{-4}$		
0	2	4		7019		1.2
2	2	1	7039	7055	strong (s) [c]	1.3
4	0	0		7065		0.2
4	0	1	7211	7181	m [c]	0.8
2	1	6	7391	7211	mw	0.9
0	0	8		7380		0.4
1	1	7		7385	vw [b]	0.4
1	2	4		7460		0.2
1	0	8		7822	vw [b]	0.3
2	2	3	7980	7978	w	0.9
4	0	3		8103		0.4
3	0	6	8132	8125	mw	0.6
3	1	5		8150		0.4
4	1	0	8347	8359	m	0.7
4	1	1		8474	vw [b]	0.2
2	2	4	8779	8785	s	1.3
4	1	2		8820		0.2
4	0	4		8910	vw [b]	0.5
1	1	8	9117	9115	ms	1.1
2	0	8		9146		0.2
0	2	6	9323	9325	vw	0.5
4	1	3		9397		0.1
3	2	2	9601	9598	vs	3.9
1	2	6		9755		1.0
1	0	9	9815	9771	s	0.4
2	2	5		9812		7.2
4	0	5		9937	m	6.0

[a] The $\sin^2\theta$ values less than 0.95 are for $CrK_{\alpha_{1,2}}$ radiation (2.29092 A). The larger values are for CrK_{α_1} (2.28962 A). The calculated values are for lattice parameters a_o = 5.451 A, b_o = 3.185 A, and c_o = 10.667 A.

[b] A line was observed, but its $\sin^2\theta$ value was not measured.

[c] The line was very diffuse.

given for each (h, k, l) with a calculated intensity greater than 0.5% of that of the most intense line. The differences in the observed and calculated $\sin^2\theta$ values for the smaller angles are caused by the systematic errors inherent in the Debye-Scherrer method. The Nelson-Riley extrapolation that was used in the calculations of lattice parameter is a technique for correcting systematic errors. Therefore, the calculated $\sin^2\theta$ values are the more nearly correct ones; the observed ones are systematically in error.

The agreement between the observed and calculated intensities is very good. Any apparent differences may be explained by the methods for obtaining the values. The calculated values are integrated intensities (defined above as the area under an I vs 2θ curve), and the visual estimates tend to be comparisons of the "darkness" of the lines. A broad line and a sharp one may have the same integrated intensity, but visually, the sharp line appears darker.

The lattice values calculated for UVC_2 and UVN_2 are given in Table 2.6. As with the UC-UN (ref. 22) and VC-VN (ref. 23) pairs, the carbide has larger lattice dimensions than the nitride.

---

[22] J. M. Leitnaker, R. A. Potter, K. E. Spear, and W. R. Laing, "The Lattice Parameter of U(C,N) as a Function of Composition," Journal of High Temperature Science. Accepted for publication.

[23] K. E. Spear and J. M. Leitnaker, "Equilibrium Investigations of Carbon-Rich V(C,N) Solutions." To be submitted for publication to the Journal of High Temperature Science.

Table 2.6. Lattice Parameters of UVC_2 and UVN_2

Phase	Parameter, A[a]		
	a_o	b_o	c_o
UVC_2	5.5234 ± 5	3.2500 ± 4	10.714 ± 2
UVN_2	5.451 ± 2	3.185 ± 1	10.667 ± 3

[a] The uncertainty given is for the last figure to the right of the decimal and is the computed standard deviation.

Measurements of the Physical Properties of (U,Pu)N Alloys

S. C. Weaver D. L. McElroy

Capital equipment funds were recently approved for purchase of the equipment outlined in the last report.[24] Design of the glove boxes has been completed, and design of the equipment components is about half finished. We have begun fabricating some of the components that have been designed, and we expect to order the boxes and some of the instrumentation soon. An investigation into techniques for fabricating samples suggests that the preparation of samples will be an area of primary concern.

Irradiation Testing of Nitride Fuels for LMFBR Applications

T. N. Washburn

The objective of this program is to establish the irradiation performance of the nitrides and carbonitrides of U and Pu. The nitrides and carbonitrides have a thermal conductivity about five times higher, a theoretical density 30% higher, and a metal content in the compound 7% higher than the oxide. These properties make the nitride and carbonitride strong contenders as advanced fuel for an LMFBR.

Thermal Flux Irradiation Tests (T. N. Washburn)

The initial series of irradiation tests will be uninstrumented tests in the Engineering Test Reactor (ETR). These tests are of the "screening" type to evaluate the performance of carbonitrides relative to carbides or nitrides synthesized from metal. Linear heat ratings will be 25 and 35 kw/ft to burnups of 30,000 and 60,000 Mwd/metric ton. Neutron

---

[24] S. C. Weaver and D. L. McElroy, Fuels and Materials Development Program Quart. Progr. Rept. Dec. 31, 1968, ORNL-4390, pp. 54–55.

radiography will be used to monitor fuel swelling, and scheduled burn-ups may be shortened or extended in accordance with the indications of this nondestructive test.

We have investigated the basic requirements of capsule design and find that the capsule being used by ORNL for uninstrumented irradiation testing of oxide fuels in a thermal flux will probably be adequate for testing of nitride fuels to 35 kw/ft.

We are investigating the feasibility of using NaK instead of Na as a thermal bond between fuel and cladding in our thermal flux tests. The melting point of Na (98°C) is much higher than the coolant temperature in the ETR or Oak Ridge Research Reactor (ORR). During initial insertion or any successive reactor shutdown, the Na surrounding the fuel would be solid. The shrinkage of Na during solidification leads to the formation of voids in the Na adjacent to the fuel during reactor shutdown. When the reactor is started again, the expansion of Na as it becomes molten is blocked, and severe damage or rupturing of the fuel specimens can occur.[25] This problem can be eliminated by using NaK as the bond between fuel and cladding, since eutectic NaK (Na–78% K) is liquid at room temperature. The use of Na–19% K looks especially attractive. Argonne National Laboratory has used this composition and reports that at room temperature it has a consistency similar to that of toothpaste;[26] thus, it remains in the bond gap when specimens are placed in a horizontal position but offers no significant resistance to fuel movement or NaK expansion when the reactor is started. We are continuing to investigate possible use of this composition.

Synthesis of (U,Pu)N from metal is under way in the Interim Plutonium Facility. We expect the mixed nitride pellets to be available for fuel pin fabrication beginning on July 1, 1969. Our tentative schedule is to insert the first capsule into the ETR during the cycle starting in late September.

---

[25]W. N. Beck and F. J. Fousek, Instrumented Temperature-Controlled Capsules for Irradiation in the CP-5 Reactor, ANL-6554 (1962).

[26]J. H. Kittel, personal communication, Feb. 27, 1969.

Design Analysis of Irradiation Capsule for ETR (C. M. Cox)

Reactor-physics and heat-transfer calculations have been completed for the first two capsules with mixed nitride for irradiation in the ETR. Preliminary design data are summarized in Table 2.7. The radial power distribution and the required unperturbed neutron flux in an X-basket facility in the Al reflector were determined by use of the ANISN code.[27] Temperatures at the fuel surface were calculated with the GENGTC code,[28] and the radial temperature distribution for the fuel was calculated with the PRØFIL code.[29]

We are evaluating the desired operating conditions, since it is possible to increase the temperature of the cladding surface to any reasonable value ($\leq 650°C$) by adjusting the outer diameter of the capsule. This would, of course, correspondingly increase the fuel temperatures.

The thermal conductivity of the mixed nitride was taken as

$$\lambda = (1 - P)(0.1125 - 1.888 \times 10^{-4}\ T + 4.603 \times 10^{-7}\ T^2 - 2.877 \times 10^{-10}\ T^3 + 5.627 \times 10^{-14}\ T^4)\ \mathrm{w\ cm^{-1}\ {}^\circ K^{-1}}\ , \quad (2.6)$$

where P is the fractional porosity and T is the temperature in °K. This function was taken from a curve fit to the data of Van Craeynest, Weilbacher, and Salbreux.[30]

---

[27]W. W. Engle, Jr., A Users Manual for ANISN, A One-Dimensional Discrete Ordinate Transport Code with Anisotropic Scattering, K-1693 (March 30, 1967).

[28]H. C. Roland, GENGTC, A One-Dimensional CEIR Computer Program for Capsule Temperature Calculations in Cylindrical Geometry, ORNL-TM-1942 (December 1967).

[29]C. M. Cox and F. J. Homan, PRØFIL, A One-Dimensional FØRTRAN IV Program for Computing Steady-State Temperature Distributions in Cylindrical Ceramic Fuels, ORNL-TM-2443 (March 1969).

[30]J. C. Van Craeynest, J. C. Weilbacher, and J. C. Salbreux, "Thermal Conductivity of Mixed Uranium and Plutonium Carbides, Nitrides, and Carbonitrides," paper presented at Eighth Conference on Thermal Conductivity at Purdue University, Lafayette, Indiana, October 7–10, 1968. To be published in the proceedings.

Table 2.7. Preliminary Design Data for Mixed Nitride ETR Capsules N-1 and N-2

	Capsule	
	N-1	N-2
	Fuel Pin Data	
Fuel composition	$(U_{0.85},Pu_{0.15})N$	Same
U isotopic	0.68% ^{235}U, 99.32% ^{238}U	Same
Pu isotopic	88.6% ^{239}Pu, 9.9% ^{240}Pu, 1.4% ^{241}Pu, 0.1% ^{242}Pu	Same
Solid pellet diameter, in.	0.200	0.250
Pellet density, g/cm^3	13.6	Same
Surface-to-center radial power depression	2.5	3.3
Fuel length, in.	3	Same
Cladding material	type 316 stainless steel	Same
Cladding dimensions, in.	0.250 OD × 0.015 wall thickness	0.300 OD × 0.015 wall thickness
Fuel-to-cladding bond	Na–19% K	Same
Peak linear heat rate, kw/ft	25	35
Maximum temperature at cladding surface, °C	480	519
Maximum temperature at fuel surface, °C	583	636
Maximum temperature at fuel center, °C	941	1065
Temperature at fuel center for flat power source, °C	1032	1214
	Capsule Data	
Cladding-to-capsule bond	Na–44% K	Same
Capsule material	type 304L stainless steel	Same
Capsule dimensions, in.	0.501 OD × 0.039 wall thickness	Same
Pins per capsule	4	Same

Table 2.7. (continued)

	Capsule	
	N-1	N-2
	Capsule Data (continued)	
Peak-to-average axial power	1.08	Same
Temperature of capsule surface, °C	103	121
Peak unperturbed 2200 m/sec neutron flux	1.7×10^{14}	1.9×10^{14}

3. FISSION-GAS RELEASE AND PHYSICAL PROPERTIES OF FUEL MATERIALS DURING IRRADIATION

O. Sisman

The purpose of this work is to measure the variables that control the release of fission gas from highly characterized nuclear fuels. These parameters are evaluated in terms of a generalized model to predict release from operating fuel materials. Thermal diffusivity is measured in-reactor in analogous experiments.

The Effect of Stored Energy in UO_2 and UN on Measurements of Thermal Diffusivity During Irradiation

R. M. Carroll R. B. Perez

We have been using a perturbation method to measure the thermal diffusivity of fuels during irradiation. The data have been unsatisfactory because of too much scatter and unexplainably low values. We found that stored energy was being released during the step changes in irradiation conditions and that this unsuspected energy source was causing the thermal diffusivity to appear low.[1]

By using a pair of step changes to produce alternate heating and cooling curves, we believe we can measure both the thermal diffusivity and the stored energy. Since our accumulated data do not include such measurements, a new experiment is necessary. We have constructed an apparatus that contains a hollow cylinder of UO_2, with natural enrichment and large grains, for measuring thermal diffusivity. The UO_2 is 98.8% of theoretical density and is 0.0601 cm in outside diameter and 2.94 cm long. The central hole is 0.325 cm in inside diameter.

An unusual feature of the construction is that the specimen is supported by a tight-fitting spiral of small-diameter W wire to prevent

[1]R. M. Carroll and R. B. Perez, Fuels and Materials Development Program Quart. Progr. Rept. Dec. 31, 1968, ORNL-4390, pp. 58–64.

the specimen from falling apart if it should crack. The W wrappings weigh only 0.0877 g and give the lowest thermal inertia of any specimen holder used to date. Irradiation of this specimen will begin in May.

Effect of Temperature and Burnup on Release of Fission Gas from $(U_{0.75},Pu_{0.25})O_2$

R. M. Carroll

We have described the release of fission gas from two pellets of high-density mixed oxide.[1] The most important observations were that the pellets had small, interconnected passages that allowed the fission gas to trickle out with the appearance of diffusion. The small passages were closed by irradiation sintering, reducing the gas release to about 17% of its original rate. In an effort to sinter the specimen at a faster rate, we increased the temperature of the pellets from 1100 to 1450°C (they had been sintered at 1650°C during their manufacture). The instantaneous release of a large amount of fission gas overloaded all our instruments and indicated catastrophic failure of the fuel. We estimate that the release approached 100%. We assumed that the gas release was caused by extensive fracturing and that the pellets must have collapsed into powder. When the capsule was opened, however, the fuel appeared to be a homogeneous mass but so swollen that it could not be removed from its W holder. As best we could see down into the holder, the pellet appeared to have a porous surface. This can be verified when we perform a metallographic examination of a section through the W holder.

This observation implies that this mixed-oxide fuel is so plastic at 1450°C that the internal pressure of fission gas generated by 0.28% burnup (6×10^{19} fissions/cm^3) was able to boil out of the fuel and cause swelling. Further, this means that we can detect the onset of the swelling by the beginning of this breakaway release of fission gas.

In the succeeding experiment, the specimen consisted of 21 spheroids with diameters of 0.0903 cm (cut from the same type of fuel but from a different batch). These spheres showed the same sort of results as had

the pellets except that the release of fission gas was lower by about half. This can be explained by the method by which the spheroids were manufactured. Since any weak or porous sections of the pellets would break rather than grind, the spheroids represented a better selection of high-density fuel than the pellets from which they were ground.

The spheroids were irradiated below 1100°C to avoid swelling. After about 1% burnup, however, we observed that the rate of gas release began to increase exponentially even though the irradiation conditions were constant. The rate of air cooling was adjusted to lower the temperature, and the release rate remained constant for several days and then again began to show breakaway release of gas. By manipulating the temperature of the specimen just above and below the onset of the exponential gas release, we obtained the data shown in Fig. 3.1.

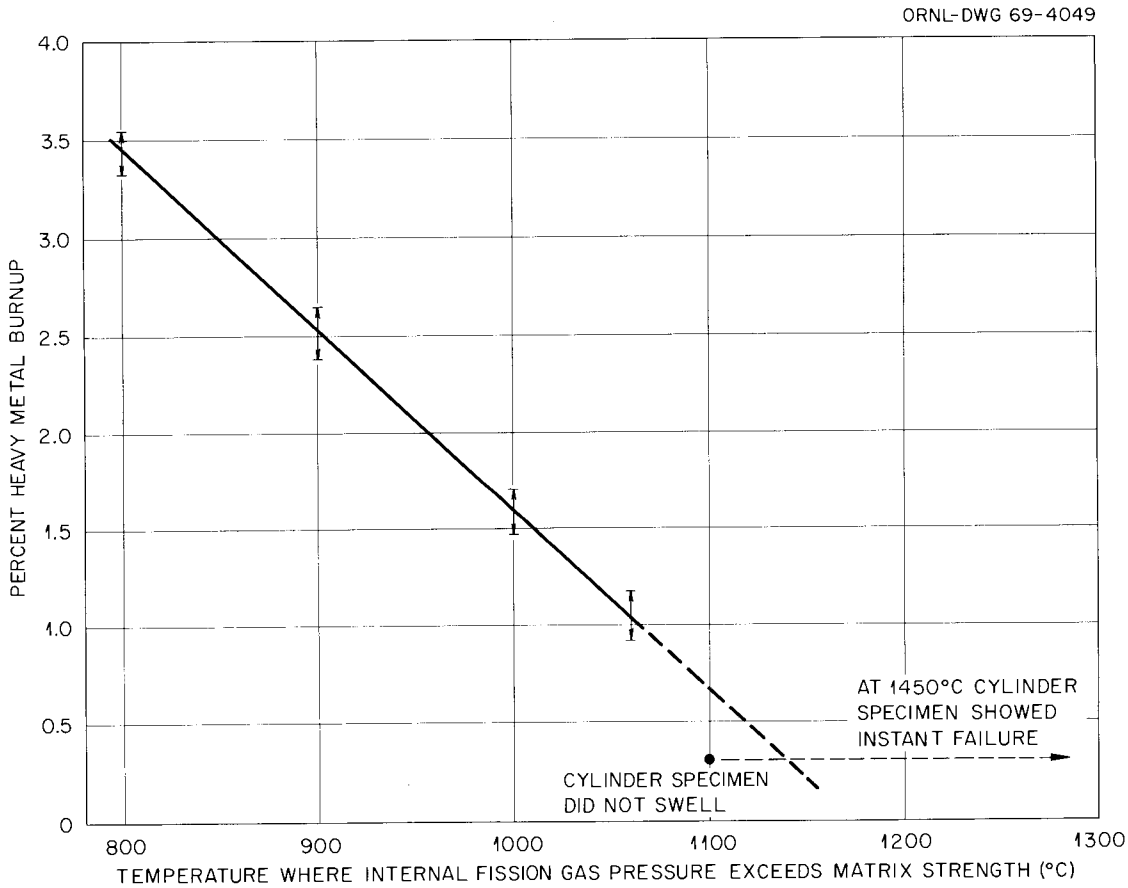

Fig. 3.1. Temperature Versus Burnup for Breakaway Gas Release from Unrestrained $(U_{0.75},Pu_{0.25})O_2$ Fuel.

The cylindrical specimen shown for comparison in Fig. 3.1 did not show breakaway gas release at 1100°C. If the extrapolation of data is valid, the breakaway gas release would have started at 1140°C. The 1450°C temperature was so much higher than this point that the gas was released almost explosively.

The irradiation of the spheroids is still in progress. After the irradiation has been completed, it may be possible to calculate the strength of the fuel matrix during irradiation by the proper boundary assumptions. We believe that the matrix strength is not changing greatly with burnup; rather, the data of Fig. 3.1 reflect the increasing gas pressure as burnup progresses.

Uranium Nitride Experiment

R. M. Carroll E. L. Long, Jr.
W. Fulkerson

We have irradiated a specimen consisting of three UN bushings stacked inside an Al_2O_3 holder. The release of fission gas from the UN indicated that the specimens were cracking at low temperatures, low fission densities, and low burnups.[2] Postirradiation examination showed that some sort of chemical reaction had caused the cracking during irradiation.[3]

The metallography of the specimens showed that most of the reaction had occurred where the UN specimen had touched the Al_2O_3 holder. Figure 3.2 shows a transverse slice through the bottom pellet. There was some reaction at the outside surface [Fig. 3.2(a)] that resulted in small cracks where the specimen was in loose contact with the Al_2O_3 sleeve. The greatest reaction, however, was on the inside surface [Fig. 3.2(b)] where the pellet was mounted on an Al_2O_3 peg. The reacted

---

[2]R. M. Carroll et al., Fuels and Materials Development Program Quart. Progr. Rept. June 30, 1968, ORNL-4330, pp. 57–58.

[3]R. M. Carroll and J. G. Morgan, Fuels and Materials Development Program Quart. Progr. Rept. Sept. 30, 1968, ORNL-4350, pp. 72–74.

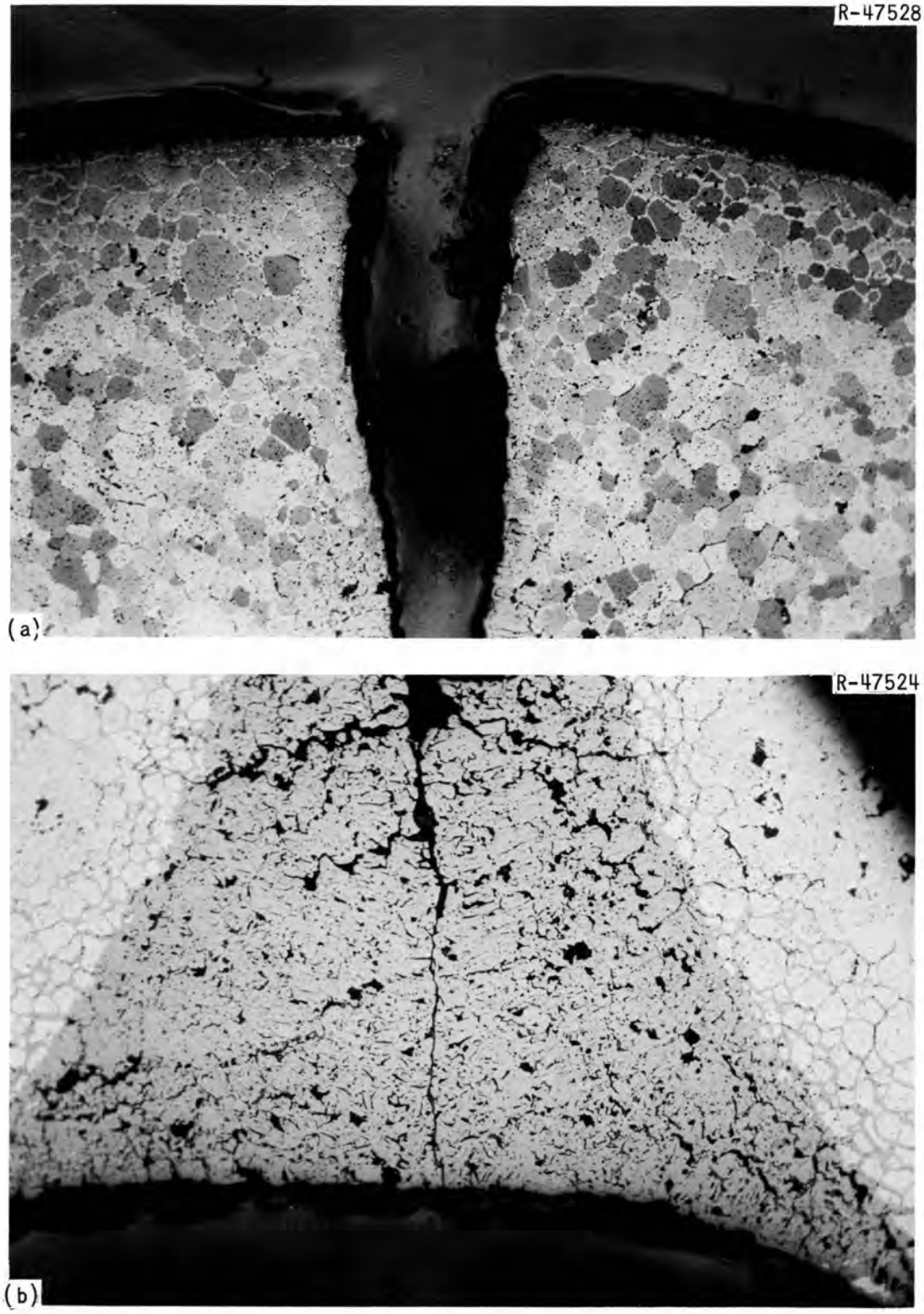

Fig. 3.2. Reaction Between UN and Al_2O_3. (a) Outside surface of bottom pellet of UN, specimen C1-23. Etched, 100×. (b) Inside surface of bottom pellet of UN, specimen C1-23. Etched, 100×. 12% reduction.

material appeared to be UO_2, which implied that there was a reaction between UN and Al_2O_3 where the UN removed O from the alumina.

The possibility of such a reaction had been discussed during the planning of the capsule design, and, on theoretical grounds, we believed that UN and Al_2O_3 were compatible. After the irradiation test, a bench test was run to find if such a reaction could occur. We found that Al_2O_3 did indeed react with UN. Apparently, we had not considered the proper reaction in the thermodynamic evaluation, and we still do not know what reaction occurred. Any future experiments will include safeguards to prevent such a reaction.

4. ZIRCONIUM METALLURGY

J. R. Weir, Jr. P. L. Rittenhouse

The object of this program is to optimize the properties of Zr alloy tubing used in nuclear reactors by study of fabrication procedures and their interaction with crystallographic deformation modes. Rather than following the usual practice of designing fuel element cladding on the basis of minimum strength values, we are attempting to control the crystallographic texture in the tubing to permit the strongest direction in the tubing to be matched against the highest service stress. This technique can also be used to control the orientation of potentially embrittling hydride platelets that form from absorption of H_2 that is released by corrosion. Success in this program can reduce the cost of producing nuclear power by making possible longer core life, higher operating temperatures, and the use of tubing with thinner walls.

Fabrication and Texture Control of Zirconium Tubing

T. M. Nilsson

Our investigation[1] of the Zircaloy-4 tubes that cracked during planetary and ordinary swaging has continued. These tubes were susceptible to cracking at about 40% cold reduction under sinking conditions, but not under ironing operations. A probable explanation for the better workability in the latter case is that solid mandrel support is provided during ironing. Also, the bulging of the tube between the neighboring hammers of the swager is greater during sinking, and this leads to metal fatigue.[2]

---

[1]T. M. Nilsson, Fuels and Materials Development Program Quart. Progr. Rept. Dec. 31, 1968, ORNL-4390, pp. 72–76.

[2]P. Murray, Westinghouse Electric Corporation, private communication.

During planetary swaging, the degree of deformation in the outer surface layer is higher than that in the remainder of the tube (see Fig. 4.1). This causes a finer grain size to be developed in the surface layer during annealing. The working of the tube during ordinary hammer swaging is more homogeneous, and the grain size after annealing is, therefore, more uniform across the thickness of the wall (see Fig. 4.2). This difference in deformation behavior as a result of working technique may explain why, in addition to cracks on the inner surface, cracks are found on the outer surface of the tubes that are planetary swaged.

A description of the experimental fabrication schedules and the results of the fabrication has been written and will be published.[3]

---

[3]T. M. Nilsson and P. L. Rittenhouse, Experimental Fabrication of Zircaloy-4 Tubes, to be published.

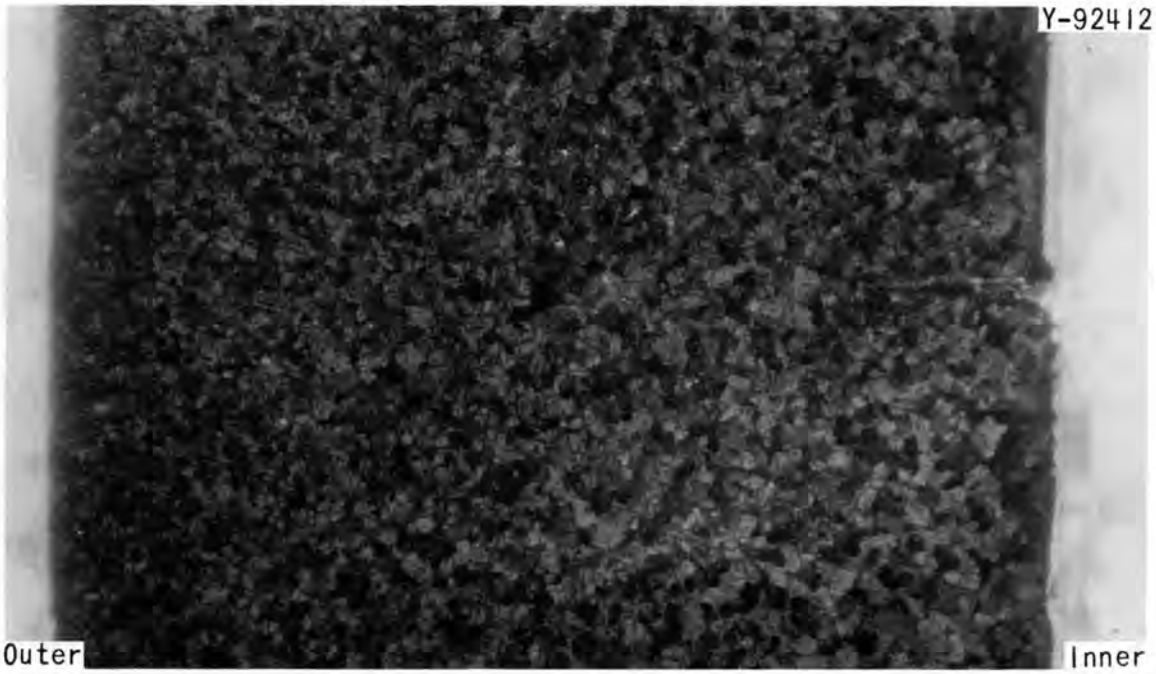

Fig. 4.1. Wall Section of Zircaloy-4 Tube Cold Worked 31% by Planetary Swaging. Notice the heavier deformation of the outer surface layers. 150×. (Ref. Schedule XI in T. M. Nilsson, Fuels and Materials Development Program Quart. Progr. Rept. Dec. 31, 1968, ORNL-4390, pp. 72–76.)

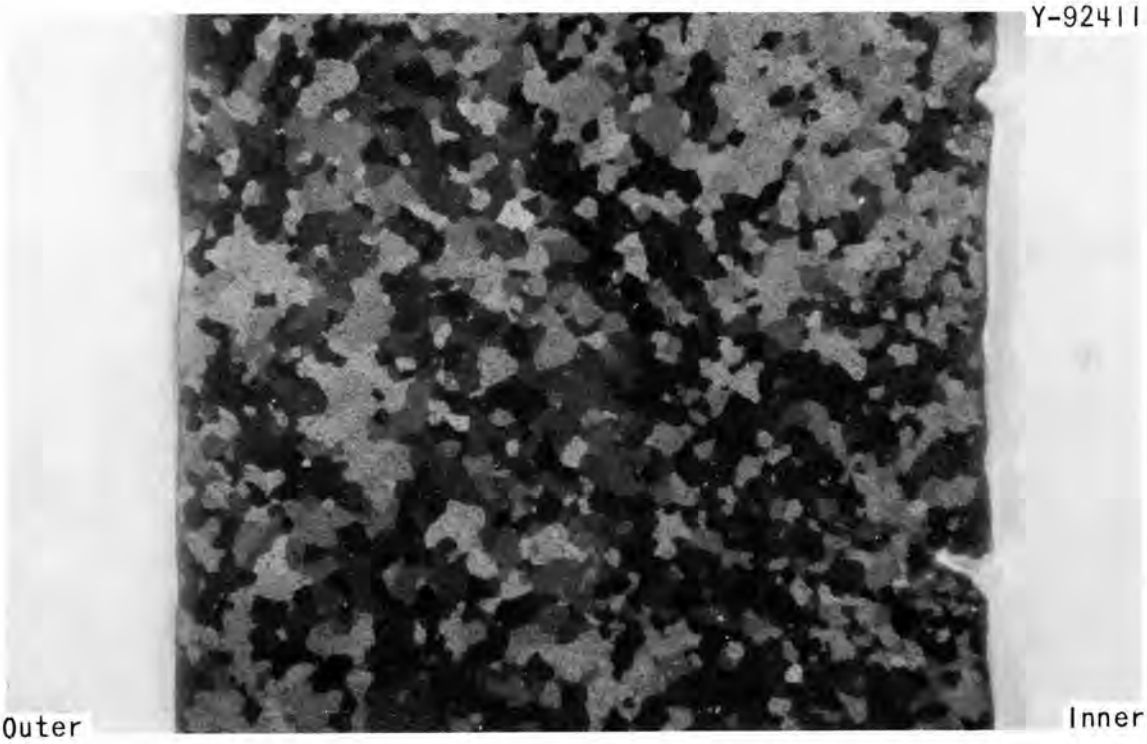

Fig. 4.2. Wall Section of Zircaloy-4 Tube Cold Worked 54% by Hammer Swaging and Annealed. Notice that the grain size is rather uniform across the thickness of the wall. 150×. (Ref. Schedule XII in T. M. Nilsson, Fuels and Materials Development Program Quart. Progr. Rept. Dec. 31, 1968, ORNL-4390, pp. 72–76.)

Texture Effects, Texture Development, and Anisotropy of Properties

Texture Development in Zircaloy Tubing (E. Tenckhoff, D. O. Hobson)

We have reported earlier on the development of texture in Zircaloy tubing.[4,5] This tubing was extruded and then tube reduced or ball swaged with different and unusually extreme ratios between wall and diameter reductions. We concluded that different processing conditions cause markedly different final textures. Texture development and the

---

[4]E. Tenckhoff and P. L. Rittenhouse, "Texture Gradients in Thin-Walled Zircaloy Tubing," paper presented at ASTM Symposium on Applications Related Phenomena in Zirconium and Hafnium and Their Alloys, Philadelphia, Pennsylvania, November 5–7, 1968. To be published in the proceedings.

[5]E. Tenckhoff, Fuels and Materials Development Program Quart. Progr. Rept. Sept. 30, 1968, ORNL-4350, pp. 82–83.

texture variation through the wall thickness were explained by consideration of the stresses acting and strains produced during the particular fabrication processes.

During this quarter we investigated tubing fabricated with less extreme ratios between wall and diameter reductions. Textures were determined after each fabrication step, from the extrusion shell to the final tubing. Here, tubing produced by tube reduction, drawing, planetary swaging, and hammer swaging was examined. The influence of the following variables is being evaluated:

1. different sequences of reduction ratios
2. different extrusion shells, and
3. change in deformation direction on successive passes.

Texture measurements from the outer, middle, and inner layers of the tube walls are now completed. All of the more than 100 pole figures have not yet been thoroughly evaluated, but the following general conclusions are evident.

1. Although the texture development in these tubes is not as dramatic, corresponding to the milder reduction ratios, these results confirm those given previously.[4,5]

2. All of the textures can be explained, as before, by considering the stresses acting in the different fabrication processes.

3. Similarly fabricated lots of tubing from different extrusion shells have essentially identical textures. Also, change in deformation direction has no effect on texture.

More specifically, our recent evaluations of these materials have led to the first direct evidence that the development of texture occurs progressively from the outer surface of the tubing into the inner surface as fabrication proceeds. Figure 4.3 shows the shift in the positions of the peaks of maximum intensity in the textures of a series of drawn tubes. Reduction in area is plotted on the abscissa and the peak position on the ordinate. A basal-poles-radial texture has a maximum intensity peak at a value of $\Phi = 0°$, the radial direction. A basal-poles-tangential texture has maxima at ±90° from the radial position. Textures were determined at three positions in the wall of each tube — on the outer

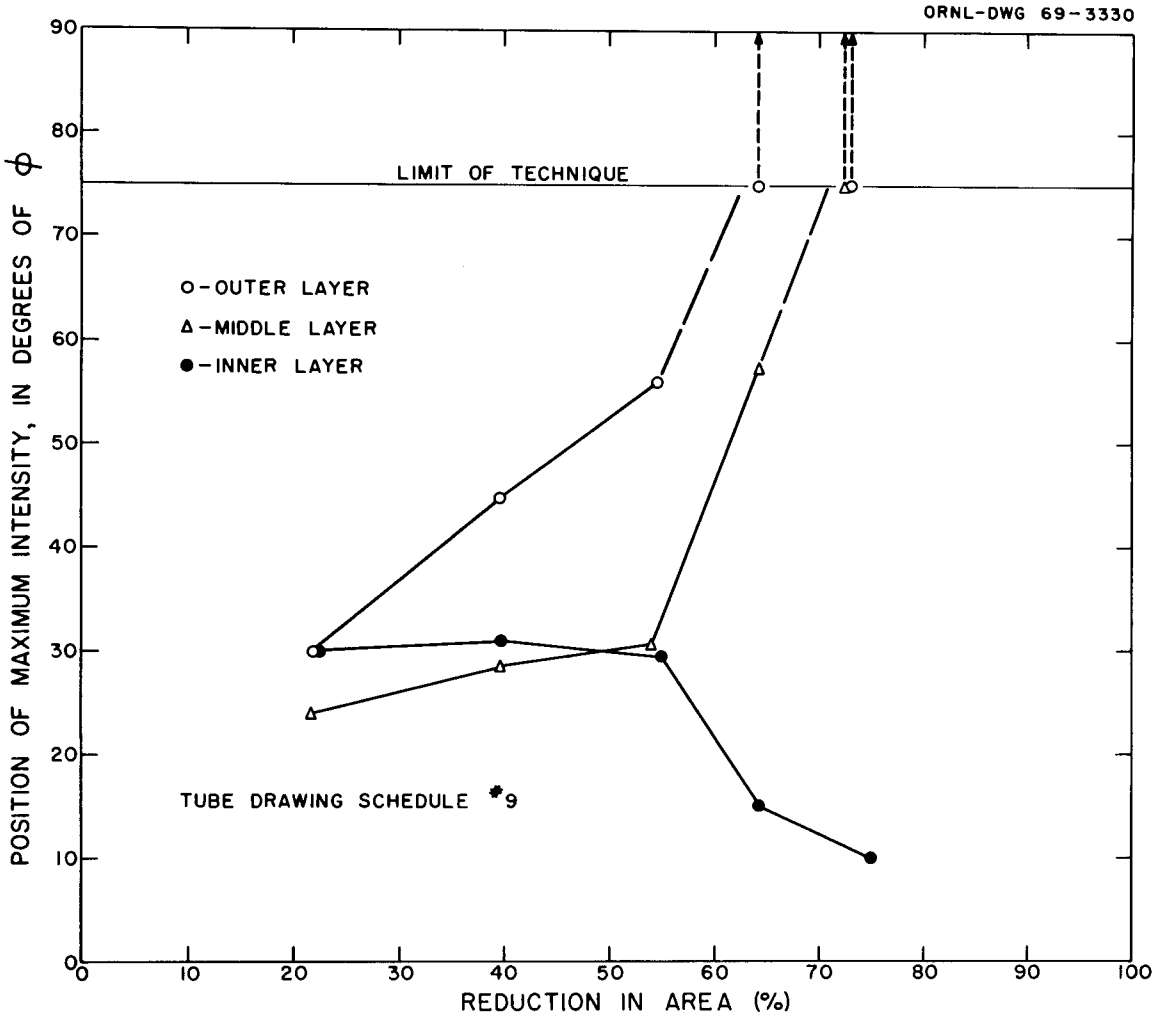

Fig. 4.3. Maximum Intensity Positions for (0002) Reflections as a Function of Reduction in Area. This figure demonstrates the relationship between reduction in area during fabrication and the angular position of the (0002) maximum intensity for textures taken from the outer, middle, and inner layers of a tube wall.

layer, inner layer, and the layer at the midwall position. After the first pass of about 22% reduction in area, the basal poles of the textures in all three layers were positioned between 24 and 30° on each side of the radial direction. The next pass, giving a total of about 40% reduction, caused the basal poles of the texture in the outer layer to start to spread while those of the other two layers remained undisturbed. Subsequent passes caused the basal poles of the textures in the outer and middle layers to continue to spread. However, instead of

spreading, the basal poles of the texture of the inner layer tended to rotate toward the radial direction. It is apparent, from this result and other similar examinations, that when a fabrication procedure causes a texture change, the change begins at the outside of the tube and then spreads progressively through the wall to the inner surface.

Demonstration of Texture Control (D. O. Hobson)

We predicted some time ago[6] that appropriate ratios of wall-to-diameter reduction would permit control of the textures formed in tubing. We are now able to do this in a practical sense. Consider Fig. 4.4, where reduction in area is plotted versus Q ratio (reduction in wall thickness divided by reduction in inside diameter) on a semilog scale to produce lines of constant reduction in wall thickness and reduction in outside diameter. This particular plot is for a tube with an initial ratio of inside diameter to outside diameter of 0.8, and, theoretically, a separate plot is required for each ratio. However, the plot changes only slightly with change in diameter ratio for Q numbers below about 10 and thus can be used for a wide range of diameter ratios. The fabrication data are plotted on this chart as cumulative reduction in area versus cumulative Q ratio. The fabrication schedule appears as a path, and the slope and position of the path determine the type of texture that will be formed. The drawing schedules for three lots of tubing are illustrated in Fig. 4.5. Schedule 9 had a cumulatively decreasing Q ratio, schedule 10 had a nearly constant Q ratio, and schedule 5 had a predominantly increasing Q ratio. Textures determined for these three schedules of tubing showed that schedule 9 produced basal poles tangential, schedule 10 produced basal poles about 40° toward the tangential direction, and schedule 5 produced basal poles radial. Work is continuing to prove that this method of plotting fabrication data is truly consistent with experimental results. If so, it will be extremely useful in tailoring textures to specific needs. We believe this analysis to be valid regardless of the method of fabrication.

---

[6]M. L. Picklesimer, A Preliminary Examination of the Formation and Utilization of Texture and Anisotropy in Zircaloy-2, ORNL-TM-460 (Feb. 28, 1963).

ORNL-DWG 69-3331

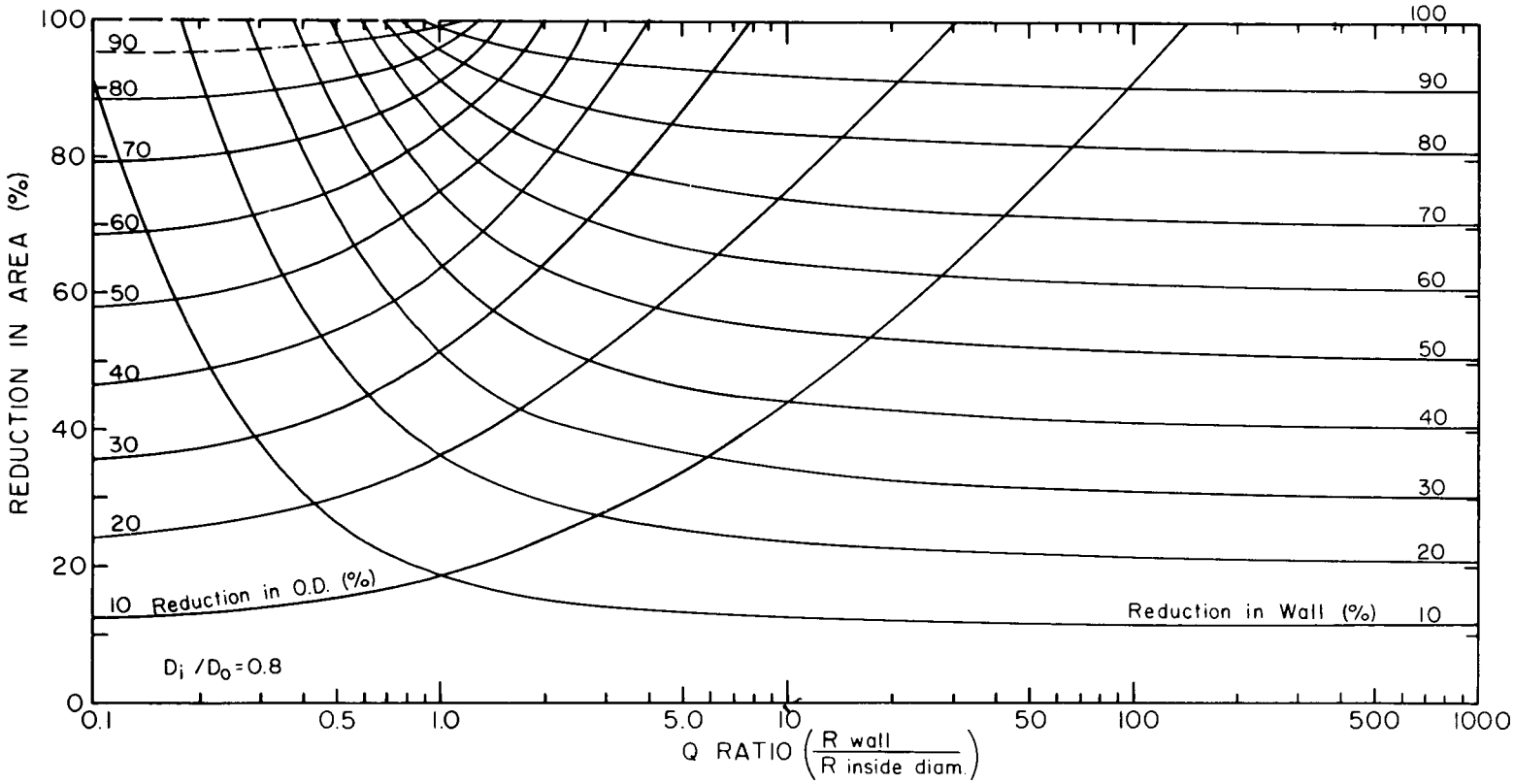

Fig. 4.4. Plot of Fabrication Variables. Reduction in area is plotted versus Q ratio (i.e., reduction in wall thickness divided by reduction in inner diameter) to obtain lines of constant diameter reduction. This particular chart is for a tube with initial ratio of inside diameter to outside diameter of 0.8. Any series of tubing fabrications can be represented on such a chart.

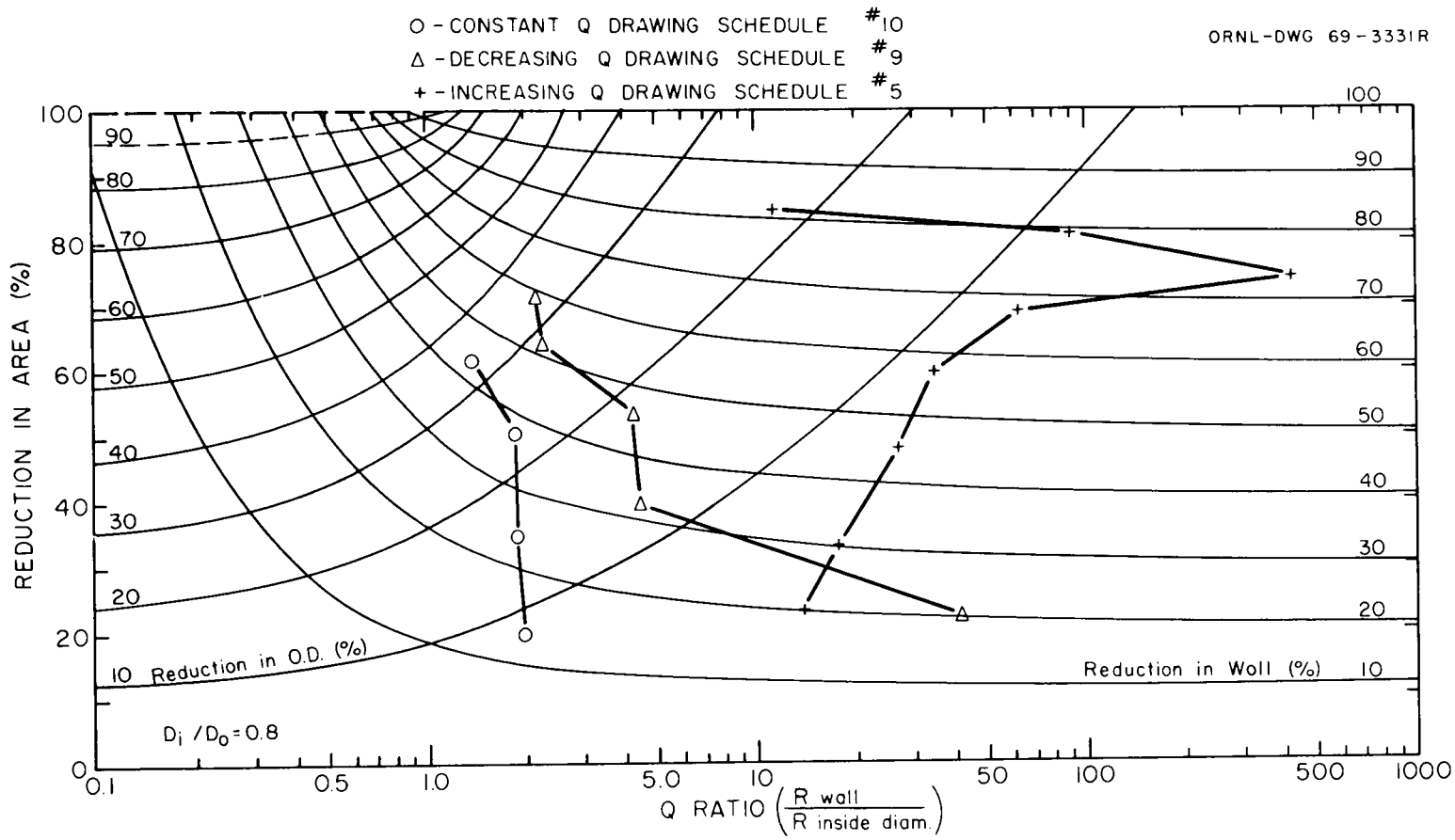

Fig. 4.5. Fabrication Variables for Three Drawing Schedules. The fabrication sequences for three drawing schedules are shown on a plot of fabrication variables. Schedules 9, 10, and 5 had decreasing, constant, and increasing ratios of reduction in wall thickness to reduction in inner diameter, respectively.

High-Temperature Deformation of Zirconium Single Crystals (E. Tenckhoff)

Our study[7] of the high-temperature deformation of Zr single crystals has been delayed by the press of other work but is now being resumed. In this study, Zr single crystals will be stressed in pure shear along well-defined crystallographic planes and directions. The experiments will be used to determine stress-strain behavior and the deformation systems operating at elevated temperatures.

Some of the single crystals have been completed, and others are in various stages of preparation. Extreme care must be exercised to ensure that deformation is avoided during the machining of the cubic specimen and its cylindrical gage section. Further, each of the cube faces must be oriented exactly with respect to the shearing plane and direction.

The shearing experiments will be performed on an Instron tensile machine. The deformation apparatus — a dovetail-led shearing jig, a furnace, and a vacuum system — are ready for the experiments, and the first test will soon be run. After the test, the sheared portion of the cube (0.5-mm-thick disk of 3-mm diameter) will be carefully removed from the remainder of the specimen and thinned electrochemically so that it may be studied by electron microscopy.

---

[7]E. Tenckhoff, Fuels and Materials Development Program Quart. Progr. Rept. June 30, 1968, ORNL-4330, pp. 62–63.

PART II

COOLANTS

5. ALKALI-METAL CORROSION STUDIES

W. O. Harms J. H. DeVan A. P. Litman

The purpose of this program is to investigate the chemical and metallurgical effects produced in structural materials during exposure to alkali metals. The program is designed to guide the selection of container materials for Na-cooled fast breeder reactor systems and Li-cooled space power reactor systems in which K serves as the Rankine-cycle working fluid. Forced circulation loops of engineering scale are included in the latter program.

Mass Transfer of Interstitial Impurities Between Vanadium Alloys and Sodium

Although V alloys are highly resistant to dissolution by Na, they are quite reactive with nonmetallic impurities in Na, particularly with C, N, and O. Accordingly, we are investigating the mechanisms by which V alloys are attacked in Na at impurity levels typical of service conditions in a reactor. Our program is concerned with four basic aspects of the oxidation process for V alloys in Na: (1) the partitioning of O between V alloys and Na; (2) the effects of alloying additions of Cr and Zr on the diffusion coefficient of O in V; (3) the effects of Cr and Zr in V on the oxide formed and on the dissolution of the alloys in Na; and (4) the solubility of V in Na as affected by the presence of O in either metal. We are also examining the kinetics of the transfer of C and N between V alloys and types 304 and 321 stainless steel in an Na circuit.

Effects of Oxygen on the Compatibility of Vanadium and Sodium (R. L. Klueh)

We are continuing our study of the processes involved in the interaction of O contained in Na with unalloyed V. Last quarter[1] we compared

[1]R. L. Klueh, Fuels and Materials Development Program Quart. Progr. Rept. Dec. 31, 1968, ORNL-4390, pp. 85–86.

the effects of O on V exposed in both Mo and stainless steel capsules to Na contaminated with O. The results reported were for tests of 500 hr at 600°C. The initial O content of the Na was adjusted to about 2000 ppm by adding Na_2O to the Na before filling. Additional tests of the same type have now been conducted for 100, 200, 300, and 400 hr at 600°C.

Table 5.1 compares the results of the tests for 500 hr with those for the shorter time periods. With either capsule material, the weight of the V coupons increased as a function of exposure time up to 300 hr and remained relatively constant thereafter. This behavior is consistent with the rate at which O diffuses in V at 600°C and with the thickness of the V specimen (about 1/16 in.). However, the weight gain appeared to level off at a value slightly less than the weight of O initially present in the capsule (Table 5.1). The specimens are being analyzed to determine the concentration and distribution of interstitial impurities as a function of exposure time.

Mass Transport of Interstitial Impurities Between Type 300 Series Stainless Steels and Vanadium Alloys (J. H. DeVan, D. H. Jansen)

We are conducting a series of tests in thermal convection loops to investigate the partitioning of C and N between V alloys and stainless steels in an Na circuit. Heated portions of the loops are constructed of V or its alloys, and the isothermal and cooled portions are of either type 304 or type 321 stainless steel. Details of the design and fabrication procedures were reported earlier.[2]

The first test in this series is operating at the conditions shown in Table 5.2. The vertical hot leg of the loop is composed of unalloyed V tubing with the following interstitial content: 1300 ppm O; 500 ppm N; 170 ppm C. Tensile specimens of V, with the interstitial composition 130 ppm O, 8 ppm N, and 110 ppm C, are located within the hot leg. Loop tubing and insert specimens in the isothermal and cooled

[2]J. H. DeVan and D. H. Jansen, Fuels and Materials Development Program Quart. Progr. Rept. Sept. 30, 1968, ORNL-4350, pp. 91–93.

Table 5.1. Time Dependence of Weight Gain by Vanadium Specimens Exposed at 600°C to Sodium Containing Oxygen

Container Material	Time (hr)	Oxygen Added[a] (mg)	Weight Gained by Specimen[b] (mg)
Molybdenum	100	15.5	9.4
	200	15.6	9.4
	300	15.5	14.6
	400	15.5	13.3
	500	15.5	14.6
Type 304 stainless steel	100	14.2	7.2
	200	14.2	7.8
	300	14.2	12.0
	400	14.2	10.0
	500	14.2	11.2

[a]Oxygen added as Na_2O. Original concentration was approximately 50 ppm O (approx 0.4 mg).

[b]Specimen size: 1 × 0.5 × 0.062 in.

Table 5.2. Operating Conditions of Loop for Testing Compatibility of Type 304 Stainless Steel, Vanadium, and Sodium

Temperature, °C	
Heater outlet	712
Heater inlet	540
Rate of Na flow	
fpm	11.6
g/min	557
Chamber pressure, torr	3×10^{-8}
Surface area of V tubing, in.^{2}	27
Surface area of stainless steel tubing, in.^{2}	140
Specimen surface area, in.^{2}	
Vanadium	9
Stainless steel	9
Scheduled operation, hr	3000

regions are of type 304 stainless steel. The concentration of O in the Na was reduced to < 10 ppm by Zr gettering before the loop was filled to provide a reference test in which O is eliminated as a test variable.

A second test loop is being constructed to operate under similar conditions but with stainless steel components of type 321 rather than type 304.

We are interested in comparing the rates of interstitial transport in these systems with those in a static, isothermal system and have constructed a series of stainless steel vessels that can accommodate sheet specimens of both V and stainless steel for tensile tests. The relative surface areas of stainless steel and V will be adjusted to correspond to the ratios set for our thermal convection loops.

Interstitial Contamination of Vanadium and Its Alloys (R. L. Wagner)

We installed a furnace with a temperature gradient of 400 to 900°C along its length for studies of the interstitial contamination of V and its alloys. The temperature of a specimen is determined by its position in the furnace. The base pressure of the diffusion-pumped, cold-trapped system at temperature is 3×10^{-8} torr. After 810 hr at this pressure, the interstitial chemistry of the 0.006-in.-thick specimens of unalloyed V, which were positioned at 100 deg temperature intervals, was not changed more than ±100 ppm. The starting compositions were 390 ppm C, 420 ppm N, 330 ppm O, and 3 ppm H. We will use this system to determine the effect of low-pressure O_2 on the contamination of V with O.

Compatibility of Stainless Steel and Insulation in LMFBR Systems

C. D. Bopp A. P. Litman

We are studying the compatibility of stainless steel and thermal insulation, with and without the presence of Na, to guide the selection of containment piping and insulation for the Fast Flux Test Facility (FFTF) and for future liquid-metal fast breeder reactor (LMFBR) systems.

We continued studies on the scaling of couples between stainless steels and insulation in moist and dry air at elevated temperatures.

These studies are intended to provide reference data against which we can compare future experiments with Na. We completed design of the test apparatus for studying the corrosion and erosion effects of small Na leaks in these systems.

The Effect of Insulation on the Oxidation of Stainless Steel

There is little systematic information about the scaling of stainless steels, although recent reports suggest that exfoliation is serious at 815°C (refs. 3–6). This more recent information contradicts earlier conclusions that many stainless steels can be used to 870°C without excessive scaling even when thermally cycled.[7,8] Part of the disagreement is due to wide variations in the test conditions, especially to effects from unintended thermal perturbations. We have paid particular attention to this in our studies, and our work to date has been under closely controlled conditions typical of an LMFBR system.

Tubular specimens of types 316 and 304L stainless steel, 3/4 in. in outside diameter and either 0.065 or 0.035 in. in wall thickness, were exposed to moist air (saturated at 20°C) at 730 to 815°C in the apparatus previously described.[9] Table 5.3 shows the chemical composition of these steels.

---

[3]L. A. Morris, Metals Eng. Quart. 8(2), 30 (May 1968).

[4]G. E. Lien (ed.), Behavior of Superheater Alloys in High Temperature, High Pressure Steam, pp. 67–113, The American Society of Mechanical Engineers, New York, 1968.

[5]H. L. Eiselstein and E. N. Skinner, "The Effect of Composition on the Scaling of Iron-Chromium-Nickel Alloys Subjected to Cyclic Temperature Conditions," pp. 162–172 in Symposium on Effect of Cyclic Heating and Stressing on Metals at Elevated Temperatures, Am. Soc. Testing Mater. Spec. Tech. Publ. 165, American Society for Testing and Materials, Philadelphia, Penn., 1954.

[6]C. T. Fujii and R. A. Meussner, J. Electrochem. Soc. 111, 1215 (1964); 110, 1195 (1963).

[7]Taylor Lyman (ed.), Metals Handbook, 8th Ed., Vol 1, American Society for Metals, Metals Park, Ohio, 1961, pp. 482, 498, 613; 1948 Ed., p. 554.

[8]Seamless Steel Tubing, Tubular Products Division, Babcock & Wilcox Company, Beaver Falls, Penn., 1959, p. 17.

[9]C. D. Bopp, Fuels and Materials Development Program Quart. Progr. Rept. Dec. 31, 1968, ORNL-4390, pp. 91–92.

Table 5.3. Chemical Composition of Stainless Steel Alloys Tested for Scaling in Moist Air at 730 and 815°C

Type Stainless Steel	Composition, wt %										
	Cr	Ni	Mo	C	Mn	P	S	Si	Cu	Co	Fe
316	17.04	13.14	2.75	0.057	1.37	0.027	0.015	0.376			Bal
304L	19.13	10.29	0.24	0.021	1.50	0.023	0.018	0.24	0.26	0.14	Bal

In these tests the external surfaces of the specimens were in contact with Al_2O_3-SiO_2 fibrous insulation. Since surface preparation of the materials is known to have an important bearing on the protectiveness of the oxide scales,[10–12] we exposed both specimens that were lathe machined and that were acid pickled (1 hr in 2% Hf–20% HNO_3 at 70°C). Figure 5.1 plots the metal consumed as oxide (based on the amount of O_2 consumed) against time.

It is clear that at 760°C, the upper limit of the range for FFTF and LMFBR applications, the work hardening induced by machining type 316 stainless steel (curve 1) appears to provide more resistance to oxidation than does pickling (curve 4). The beneficial effect of work hardening is thought to result from increased Cr diffusion and, therefore, formation of a more protective scale that is rich in Cr_2O_3 (refs. 8–10). At 815°C the scale formed on machined material (curve 5) was still thinner and more protective than that formed at 760°C on pickled material (curve 4). Upon thermal cycling, however, the former scale was more susceptible to spalling, and the curves cross after about 440 hr exposure. Jansson[10] found that, at higher temperatures and long exposure times, material that had been work hardened by

[10]S. Jansson *et al.*, Brit. Corrosion J. 4, 21 (1969).

[11]S. Jansson and B. Lehtinen, Metallurgie (Mons, Belg.) 7(2), 61 (1967).

[12]M. Warzee, C. Sonnen, J. Cremer, and Ph. Berge, Corrosion of Stainless Steel and High Nickel Content Alloys in High Temperature Superheated Steam, EURAEC 1895 (July 1967).

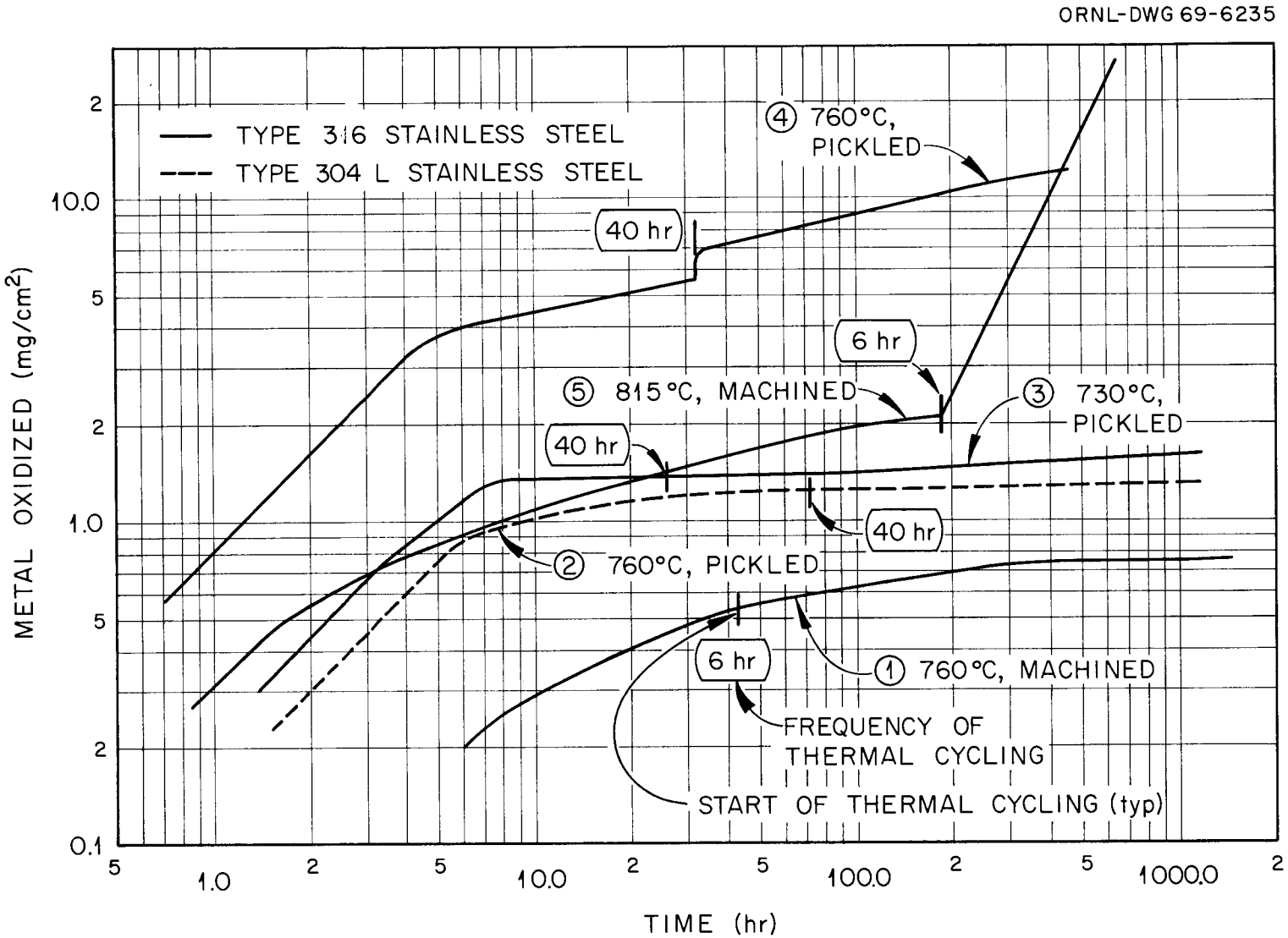

Fig. 5.1. Oxidation of Couples Between Stainless Steel and Insulation in Moist Air.

grinding did not resist oxidation as well as did pickled material; Warzee et al.,[12] however, showed that work hardening by lathe machining limited oxidation more effectively than grinding.

At 760°C the resistance to oxidation of pickled type 304L stainless steel (curve 2) is nearly as great as that obtained by work hardening type 316 stainless steel (curve 5). In material sensitized by prior thermal treatment, Warzee et al.[12] noted that type 316 stainless steel had less resistance to oxidation than did type 304L stainless steel; they attributed this to depletion of Cr from the matrix by precipitation of the sigma phase. Our study was conducted in the temperature range in which type 316 stainless steel becomes sensitized, and, since thermal cycling was used, repeated sensitization could have occurred. Therefore, it seems reasonable to ascribe the lower resistance to oxidation that we found in type 316 stainless steel to its greater susceptibility to the formation of the sigma phase.

We used temperature cycling to simulate expected LMFBR service conditions for these experiments. The data obtained to date indicate that, although cycling considerably lowers the temperature at which the scale becomes unprotective, the frequency of cycling is not very important. Under conditions in which spalling is produced by cycling, most oxidation probably occurs immediately after the brief cooling period permitted by the thermal cycles; however, the curves in Fig. 5.1 have been smoothed so that this effect is not evident.

A photograph of the specimen (No. 5) exposed at 815°C is shown in Fig. 5.2(a). Figure 5.2(b) is a photomicrograph of the outside surface of the specimen that contacted the Al_2O_3-SiO_2 fibrous insulation, Kaowool.[13] The duplex corrosion products formed are typical of the morphology of the scale for stainless steel oxidized in air.[14,15] The average

---

[13]Trade name of Babcock & Wilcox Company for refractory fibrous insulation of the composition 51.9% SiO_2, 45.1% Al_2O_3, balance other oxides.

[14]L. A. Morris, Metals Eng. Quart. 8(2), 30 (May 1968).

[15]G. E. Lien (ed.), Behavior of Superheater Alloys in High Temperature, High Pressure Steam, pp. 67–113, The American Society of Mechanical Engineers, New York, 1968.

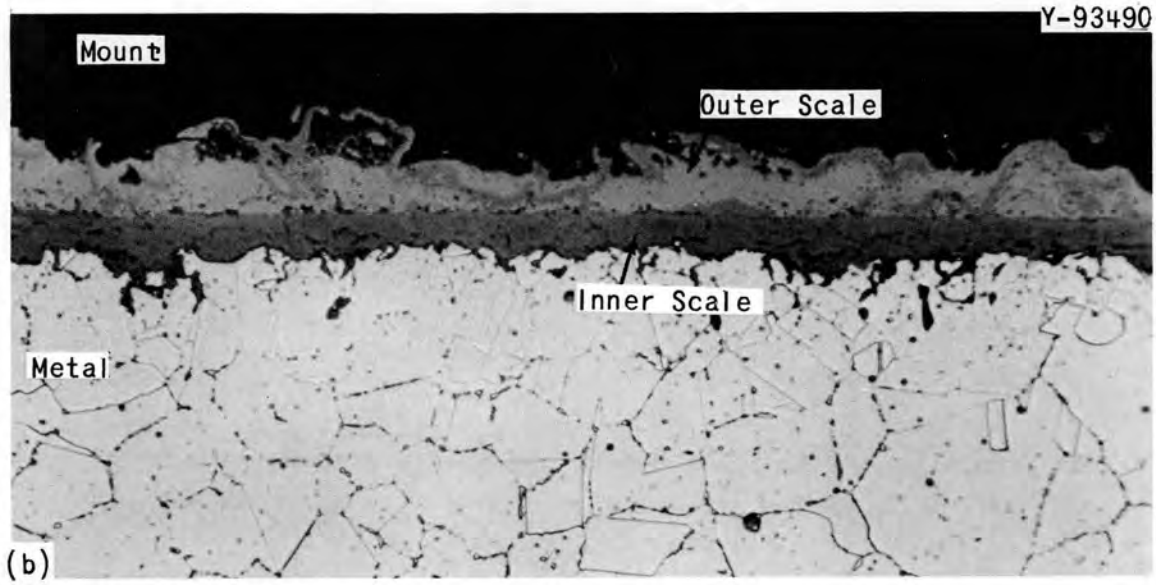

Fig. 5.2. Oxidation of Type 316 Stainless Steel in Moist Air. Cycled 40 times between 150 and 815°C during 550 hr exposure. (a) Specimen after test, showing similarity between outside surface, in contact with Al_2O_3-SiO_2 fibrous insulation, and bare inside surface. 3×. Reduced 44.5%. (b) Photomicrograph of duplex scale typical of that formed on both surfaces. 500×.

thickness of the scale adhering to this surface of the specimen was 21 μm, while 60% of the total scale that formed, or 31 μm, spalled during test. Little difference was observed between the surface shown and the surface that did not contact thermal insulation (the inside surface of the tube).

The results of an analysis of the spalled scale from this specimen (No. 5) are shown below:

Scale Composition, wt %

Al	Si	Cr	Mo	Ni	Cu	Fe
< 0.3	0.1	5	< 0.1	2	< 0.03	Balance

There was not a significant amount of Al or Si. This indicates that little, if any, sintering reaction occurred between the insulation and the scale.

For a few experiments, we used a semirigid insulation of amosite asbestos.[16] The specimen was clamped between semicylinders of the asbestos-base insulation and the silica alumina blanket insulation so that one-half of the outer surface of the specimen was in contact with the blanket insulation and one-half was in contact with the asbestos insulation. Examination after exposure showed more scaling on the half that contacted the asbestos-base insulation. This could have resulted from (1) O starvation that stabilizes the less protective wustite-type scale[17,18] (since the asbestos-base insulation is less permeable), (2) contamination of the scale by S (detected by the odor of H_2S in the exhaust gas), or (3) contamination by sodium silicate from the insulation. If there was a sufficient degree of contamination by sodium silicate, catastrophic corrosion might result.[19] That this was not

---

[16] "Unibestos," Pittsburgh Corning Corporation trade name for amosite asbestos plus sodium silicate binder and (diatomaceous) silica filler.

[17] C. T. Fujii and R. A. Meussner, J. Electrochem. Soc. 111, 1215 (1964); 110, 1195 (1963).

[18] M. Warzee, C. Sonnen, J. Cremer, and Ph. Berge, Corrosion of Stainless Steel and High Nickel Content Alloys in High Temperature Superheated Steam, EURAEC 1895 (July 1967).

[19] L. A. Morris, Metals Eng. Quart. 8(2), 30 (May 1968).

observed suggests that most sodium silicate did not leave the insulation.

Effect of Small Sodium Leaks

We completed a design for the apparatus for evaluating the effect of small quantities of Na on the compatibility of stainless steel and insulation. Figure 5.3 shows the internal configuration – the remainder of the apparatus is similar to our present rigs.[20] As envisaged, the stainless steel tube would be loaded with stick Na in a vacuum chamber.

[20]C. D. Bopp, Fuels and Materials Development Program Quart. Progr. Rept. Dec. 31, 1968, ORNL-4390, pp. 91–92.

ORNL-DWG 69-6236

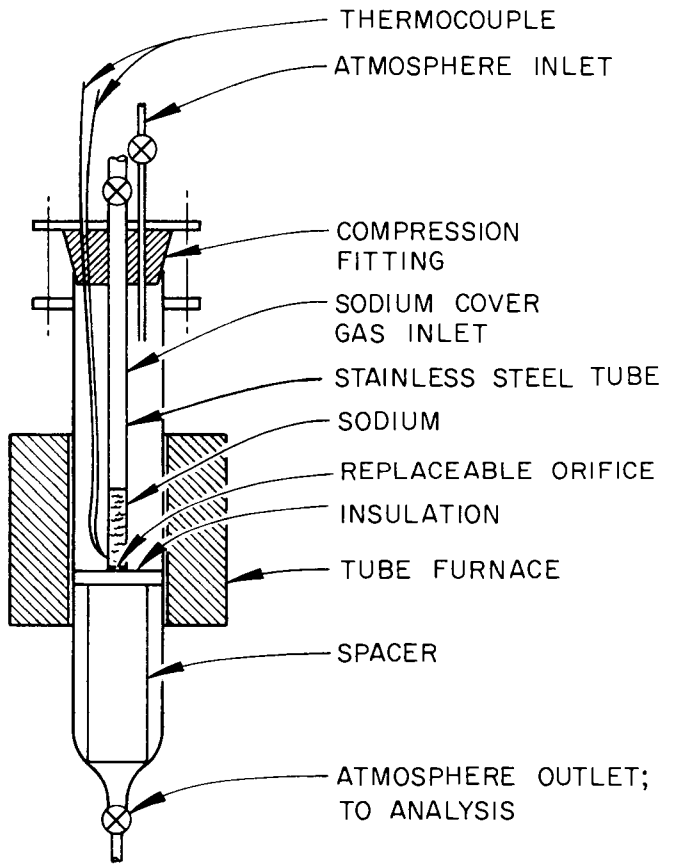

Fig. 5.3. Experimental Arrangement for Evaluating the Effect of Small Sodium Leaks.

External inert gas pressure would force the alkali metal through the orifice so that it would interact with the insulation and stainless steel orifice. Characterization of conditions for self-sealing of a leak in the containment for Na, the effects of inert versus active gases, orifice size, and temperature will be some of the variables evaluated in this phase of the program.

Corrosion of Refractory Alloys in Lithium, Potassium, and Sodium

J. H. DeVan A. P. Litman W. R. Huntley

Requirements for auxiliary electricity or ion propulsion for space vehicles necessitate power plants of high efficiency that will operate at high temperatures. For these applications, nuclear power systems have been proposed in which alkali metals are used to transfer heat, drive a turbogenerator, and lubricate rotating components. Accordingly, we are investigating the corrosion properties of candidate alkali metals, primarily Li and K, under conditions of interest for space applications. Because of the relatively high temperatures (> 1000°C), the investigation is concerned largely with refractory-metal container materials.

Effect of Oxygen on Compatibility of Refractory Metals and Alkali Metals (R. L. Klueh)

Oxygen Effects in the Tantalum-Sodium System (R. L. Klueh). — We have recently examined the behavior of O in the Ta-Na system at 600°C. Five Ta capsules containing Ta specimens with 40 ppm O were exposed to Na of different O concentrations; two other capsules containing Ta specimens with 800 and 1400 ppm O, respectively, were exposed to Na with about 50 ppm O. Results are shown in Table 5.4.

These tests show some important differences between Ta and Nb systems at equivalent conditions. As discussed earlier,[21] Nb specimens

[21] R. L. Klueh, Fuels and Materials Development Program Quart. Progr. Rept. Sept. 30, 1968, ORNL-4350, pp. 125–126.

Table 5.4. Effect of Oxygen on Compatibility of Tantalum and Sodium at 600°C

Initial Oxygen Content of Sodium[a] (ppm)	Oxygen in Tantalum (ppm)		Weight Change[c] (mg)	Tantalum in Sodium (ppm)
	Before[b]	After[b]		After
50	40	50	+0.1	40
300	40	110	+0.8	20
700	40	120	+0.7	80
1100	40	220	+1.3	200
2000	40	360	+1.1	230
50	800	750	+3.2	20
50	1400	1200	+6.5	10

[a]Oxygen initially present plus that added as Na_2O.

[b]Oxygen concentration determined by vacuum fusion.

[c]Specimen size: 1 × 0.5 × 0.04 in.

exposed to Na with up to 1000 ppm O did not exhibit a surface scale, nor were corrosion products identified by x-ray diffraction. In contrast, the Ta specimens appeared to form a scale at all O concentrations, and, on the specimen exposed to 2000 ppm O, x-ray diffraction analysis identified $NaTaO_3$. Also, as the O content of the Na was increased, the Nb lost weight at an increasing rate while the Ta consistently gained weight (Table 5.4).

Metallographic examination of the specimens exposed to the Na containing 2000 ppm O showed what appeared to be the beginning of penetration by the Na (Fig. 5.4). The penetration is similar to the type of attack observed when O is added to the Ta before exposure to Na.

In the case of Ta specimens that were oxidized before test, metallographic examination indicated heavy penetration (Figs. 5.5 and 5.6) much more severe than that for Nb with similar O content.[21] The O content of all Ta specimens increased during test, although we have not yet determined what part of the increase is due to the corrosion scale and what part to O dissolving in the Ta.

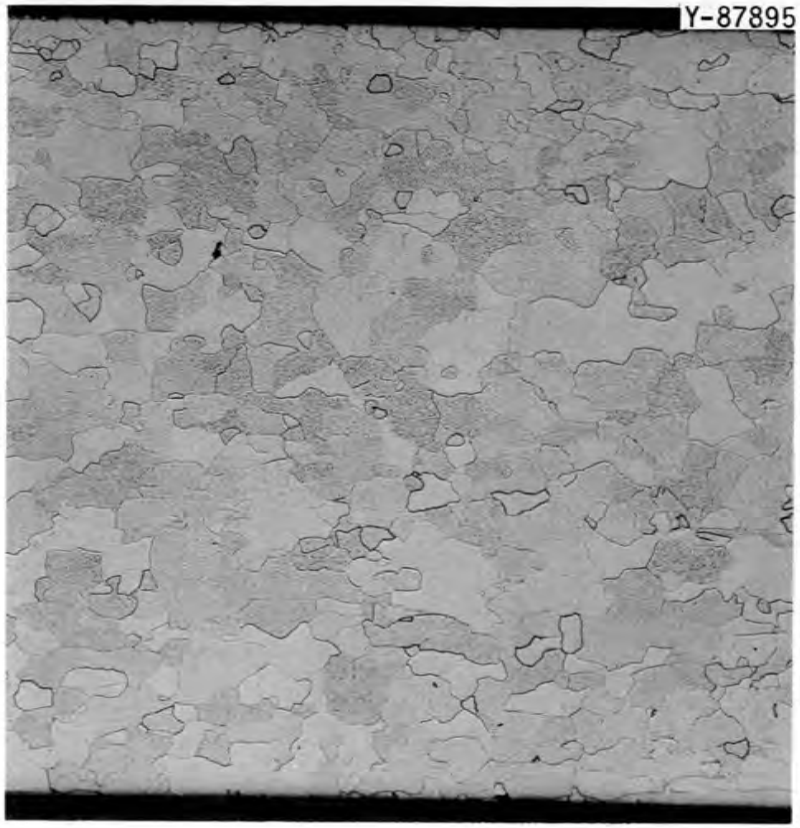

Fig. 5.4. Tantalum Specimen Exposed to Sodium Containing 2000 ppm O for 500 hr at 600°C. Note what appears to be incipient attack at the grain boundary near the edge of the specimen. Etched in a solution of H_2O, HNO_3, and NH_4HF. 100×.

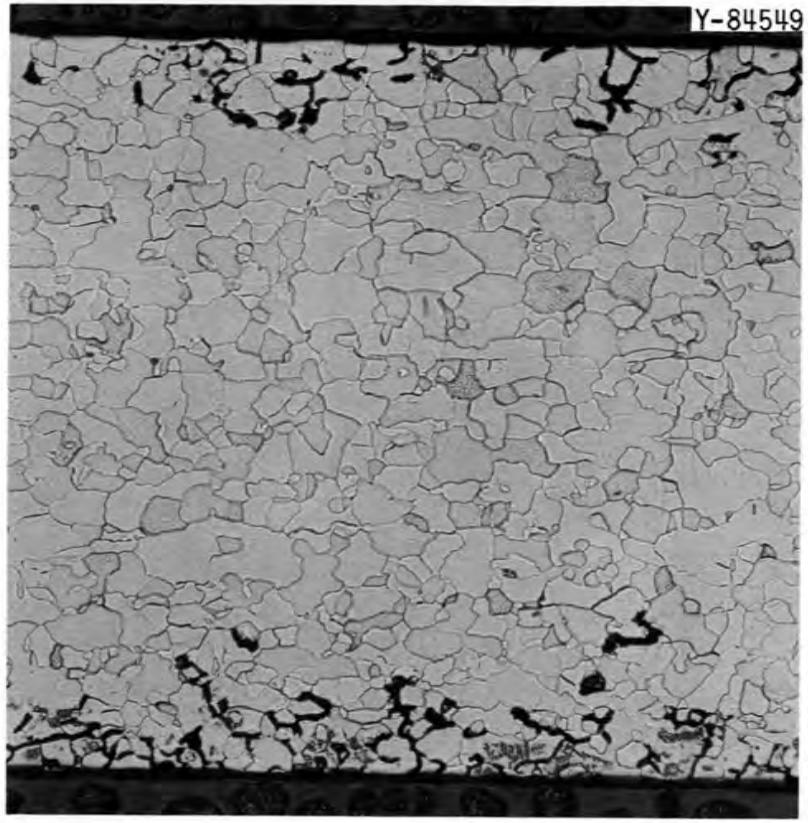

Fig. 5.5. Tantalum that Initially Contained 800 ppm O After Exposure to Sodium for 500 hr at 600°C. Etched in a solution of H_2O, HNO_3, and NH_4HF. 100×.

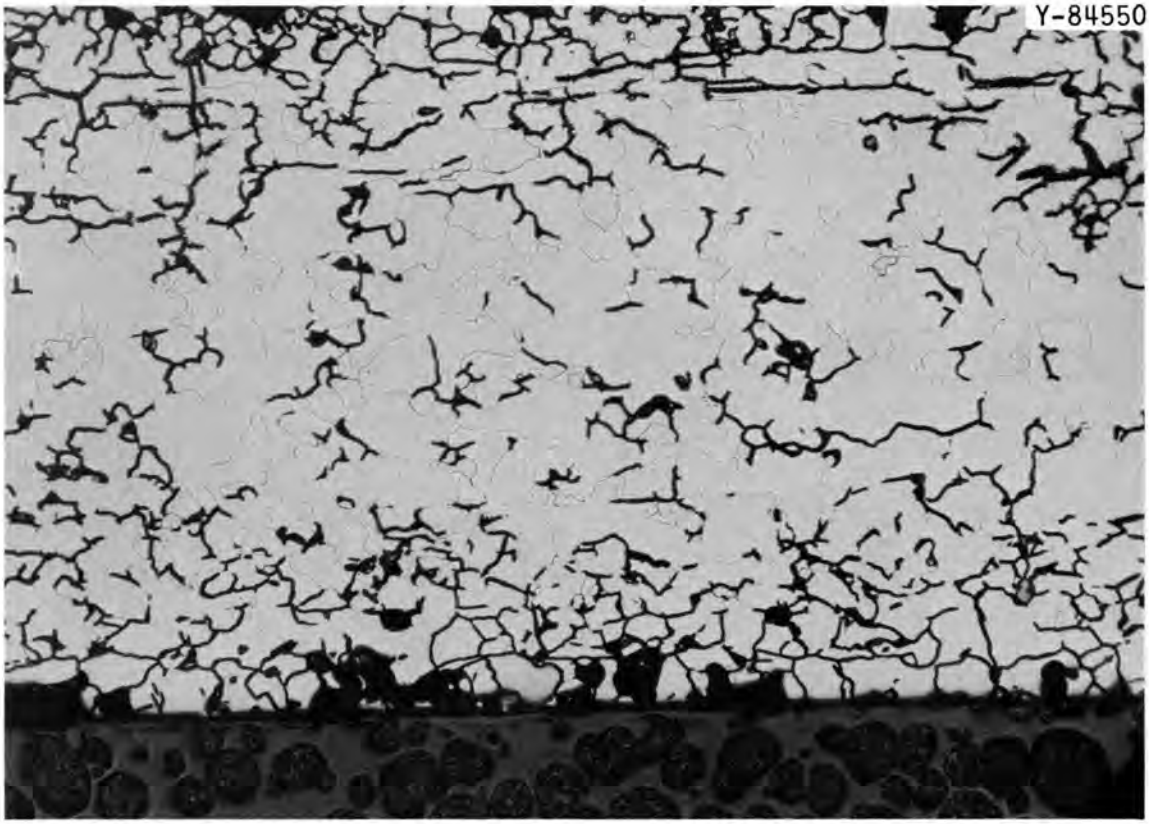

Fig. 5.6. Tantalum that Initially Contained 1400 ppm O After Exposure to Sodium for 500 hr at 600°C. Etched in a solution of H_2O, HNO_3, and NH_4HF. 100×.

Partitioning of Oxygen Between Potassium and Zirconium and Between Sodium and Zirconium (R. L. Klueh). — We have applied the ability of Zr to getter O from liquid alkali metals to the quantitative detection of O in Na and K [i.e., the gettering-vacuum-fusion (GVF) method for O analysis]. The primary sources of error in the method are those introduced by the accuracy of the vacuum-fusion analysis for O in Zr and by the O introduced from the Mo containers and the inert-gas atmosphere during loading of the GVF capsule.

The accuracy of the GVF technique is ±10% (ref. 22). To determine the amount of O contributed by the container and the inert-gas atmosphere,

---

[22]W. R. Laing and H. G. Davis, ORNL Master Analytical, TID-7015, Suppl. 1 (November 1959).

two capsules containing K low in O were held for 100 hr at 815°C, after which the capsules were opened and the Zr tabs removed. Another Zr specimen was then added to the first capsule while the K from the second capsule was poured into a new Mo container and another Zr specimen was inserted. Both capsules were again heated for 100 hr at 815°C. This same procedure was repeated two more times. The results are shown in Table 5.5.

Table 5.5. Effect of Molybdenum Container and Atmosphere Chamber on Accuracy of Gettering-Vacuum-Fusion Analysis

Specimen Number	Specimen Weight		Potassium (g)	Oxygen in Zirconium (ppm)		Oxygen Gettered from Potassium (ppm)
	Initial (g)	Gain (mg)		Before	After	
First capsule[a]						
1	1.7462	0.6	10.05	29	240	36
2	1.8271	0.1		29	36	1
3	1.9221	0.1		29	39	2
4[b]	1.9651	0.1		21	21	0
Second capsule[c]						
1	1.9034	0.6	9.98	29	240	40
2	1.9785	0.4		29	90	12
3	2.0035	0.3		29	95	14
4	1.8715	0.2		21	84	12

[a]Capsule remained unchanged throughout; only the Zr specimen was changed.

[b]Potassium was melted and exposed to the inert-gas atmosphere for the same amount of time as required to melt and pour the K into the second capsule.

[c]Capsule and Zr specimen were changed after each exposure. Same K was used throughout.

The largest source of extraneous O was the Mo container. The O concentration of the Mo container decreased from about 35 to 20 ppm after one exposure and from about 35 to 10 ppm after four exposures. Before the last test on the first capsule, the capsule was heated to melt the

K and expose it to the inert-gas atmosphere for the same amount of time as would have been required to melt and pour it into another container. The O picked up by the K in this case was still negligible, which shows handling of the K per se to be a minor source of error.

We considered the possibility of using a container material other than Mo. We eliminated Nb and Ta because the effect of O on the solubility of these materials in alkali metals is greater than it is for Mo. Furthermore, these materials in tube form generally contain up to three times as much O as Mo. Similar problems prohibit the use of stainless steel containers. Nickel is subject to dissimilar-metal mass-transfer interactions with refractory metals, and so, presumably, is Zr. Thus, Mo remains the best choice, although under our test conditions it contributes a blank of about 10 to 15 ppm O to the 10-g sample of K.

Corrosion of Refractory Alloys by Lithium

Thermal Convection Loop Tests (J. H. DeVan). — We are continuing our analysis of thermal convection loop TCL-6R, which circulated Li for 3000 hr at a maximum temperature of 1350°C. The loop was constructed of the Ta alloy T-222 and contained T-222 insert specimens.

During disassembly of this loop and subsequent removal of chemical and metallurgical specimens, we noted that tubing sections parted in a relatively brittle manner as they were being cut. Certain areas of the tubing had become contaminated externally as a consequence of heater outgassing, and a loss of ductility was expected in these sections.[23] But since the relatively brittle behavior extended to tubing sections where no changes in interstitial content had been shown by chemical analyses, we conducted a series of bend tests at room temperature on sheet specimens that had been contained within the loop. Each specimen was 0.030 in. thick and was bent over a 5T mandrel at 22°C. The maximum strain produced in the outer fiber was about 16%.

The object of these bend tests was to evaluate the changes in ductility produced by a combination of thermal aging at the test

[23] J. H. DeVan, Fuels and Materials Development Program Quart. Progr. Rept. Dec. 31, 1968, ORNL-4390, pp. 100-104.

temperature and interstitial changes caused by the Li; insert specimens were used to circumvent the effects of any external contamination. Figure 5.7 shows the temperatures of the specimens during exposure to Li and the interstitial levels at each loop position after test. Note that the C and O levels remained relatively constant among the specimens; the N concentration, however, increased from the hot zone to the cold zone.

As shown in Fig. 5.7, three kinds of bending behavior were displayed by the specimens. Those from the coldest part of the loop, which had bulk N levels from 250 to 450 ppm, showed cracks after 16% strain but did not completely fracture. The cracks were about 1/16 in. long and on opposite sides of the specimen, parallel to the bending axis. Specimens from an intermediate temperature zone (1220 to 1280°C) fractured completely at a relatively small bend angle. These specimens contained from 90 to 250 ppm N. The third group of specimens, from the hottest zone (1280 to 1370°C), survived the full 16% strain without cracking. This latter group of specimens contained between 27 and 60 ppm N.

Obviously the aging temperature had a more significant effect on the bend ductility than did the N content of the specimens. The ductility minimum for specimens exposed at 1220 to 1280°C is consistent with the 3000 hr aging behavior observed for T-111 with a C content comparable to that in these experiments (about 150 ppm) (ref. 24).

We are now examining the distribution of interstitials in these specimens in terms of their concentration gradients and the microstructural locations of interstitial compounds. The specimens will also be examined metallographically to determine the morphology of the cracks.

T-111 Forced Circulation Loop (FCLLL-1) (D. L. Clark, C. W. Cunningham, B. Fleischer)

Procurement of Material and Assembly of Loop. — We are constructing a forced circulation loop (FCLLL-1) to gain corrosion information on structural and fuel cladding materials for power systems cooled by Li.

---

[24] D. T. Bourgette, personal communication.

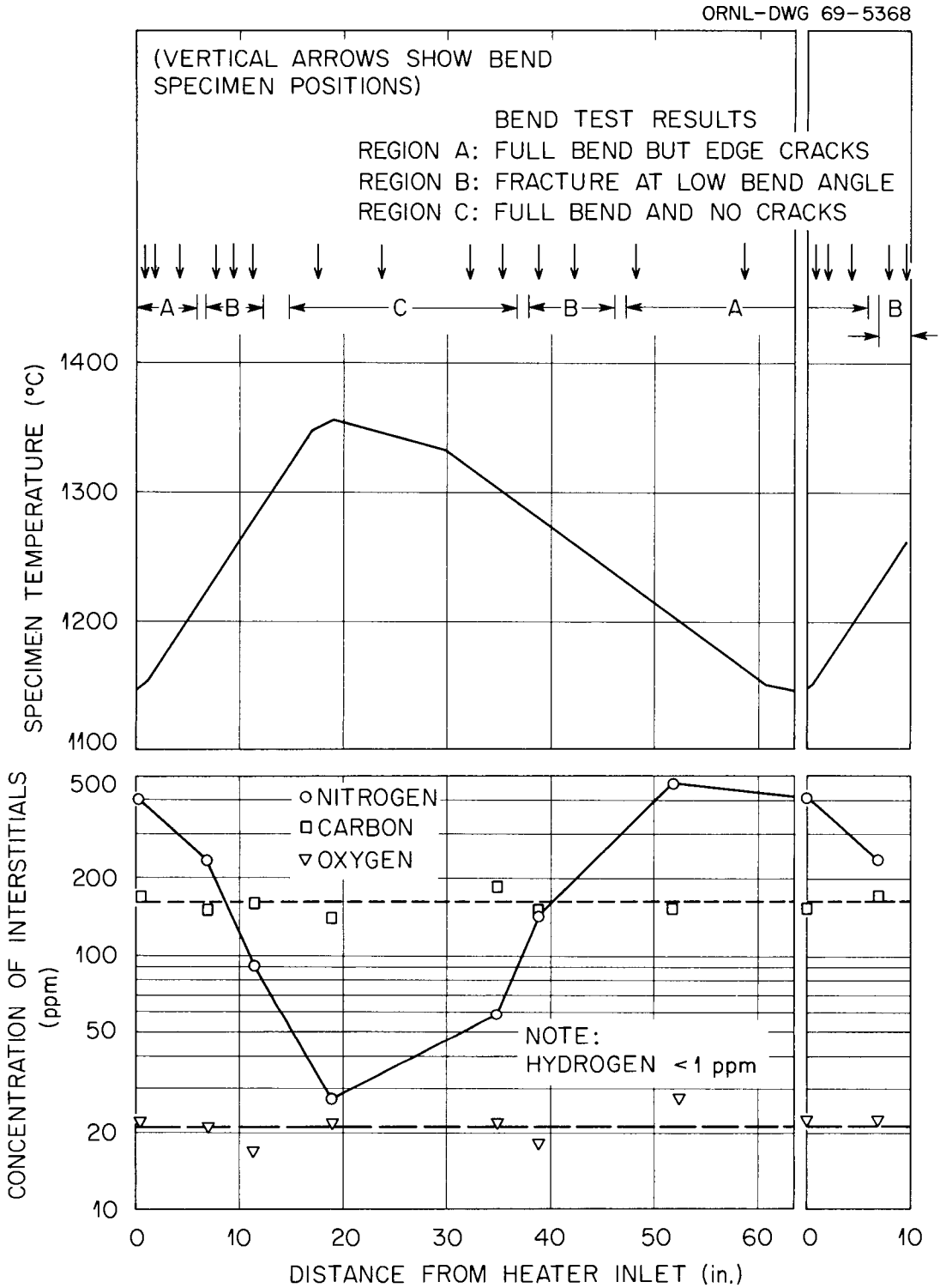

Fig. 5.7. Results of Bend Tests for T-222 Insert Specimens From Loop TCL-6R. Specimen temperatures and interstitial impurity compositions are indicated as functions of their loop position. Specimens were exposed for 3000 hr.

Assembly of the loop is essentially complete; only minor work remains to be done before the installation of the bell housing of the vacuum chamber. Tantalum shimstock remains to be installed over the eight bare-wire thermocouples on the loop.

The thermocouples are composed of 0.005-in.-diam wires, one of W–25% Re and the other of W–3% Re. The hot junctions of the thermocouples were made by spot welding the two wires individually to the loop wall as shown in Fig. 5.8. The wires were strung through BeO insulators, which were then strapped to the Ta reflective insulation. Alumina insulators were used once the wires left the vicinity of the loop. A loop was provided near the junction of each thermal element to allow for differential expansion. An Ar purge was maintained over the entire vicinity of the junction area during spot welding. We used a "Unitek" Weldamatic Model No. 1-048-03 with an electrode tipped with Mo. The controls were set for 14 wsec of power, which was determined during practice welding to be the optimum setting.

We had some difficulty handling the W-Re bare-wire thermal elements because of breakage where the long alumina insulator sleeves butted. Very short sleeves, or beads, will be used to minimize this problem.

The penetrations through the walls of the vacuum chamber for the bare-wire thermocouples were made with tube-type octal feedthroughs and type RTSN (60% Ag–30% Cu–10% Sn) solder. Each thermal element was strung through a 0.090-in.-OD × 0.070-in.-ID stainless steel tube and was centered in the tube with alumina sleeves. The alumina sleeves were recessed about 1/8 in. into the tube, and this volume was filled with RTSN solder. Since the solder was applied on the vacuum chamber side of the tubes, the braze surface could easily be cleaned of flux and other contaminants.

Final cleaning of the loop and structural components and installation of the reflector shutter assembly are the only other work remaining to be done inside the vacuum chamber. When these are completed, the bell housing will be placed over the vacuum chamber.

We completed the upgrading of the vacuum equipment associated with chamber rough pumping and loop evacuation. A schematic of the improved

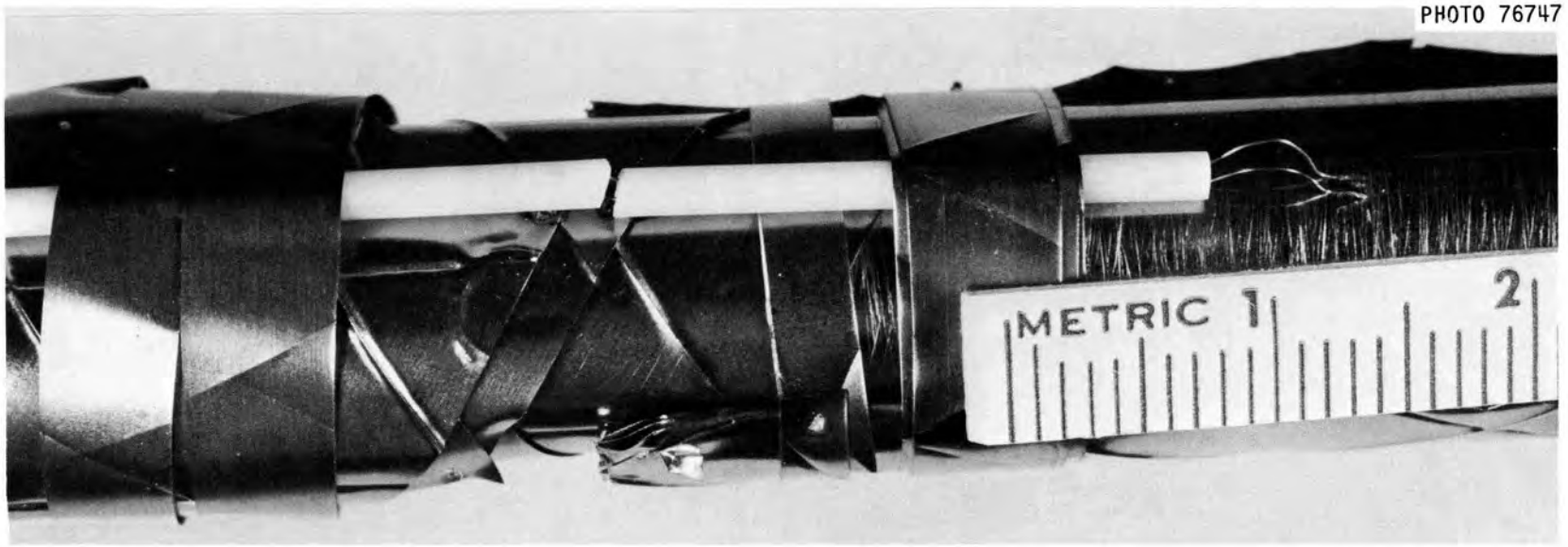

Fig. 5.8. Typical Installation of Bare-Wire, Tungsten-Rhenium Thermocouple.

system is shown in Fig. 5.9. This auxiliary equipment has been used to evacuate the FCLLL-1 loop to less than 1×10^{-6} torr.

The fill tank containing Li was connected to the line sampler and fill valve. We found leaks in the welded cap plug of the drum when we evacuated the system. Since the drum probably had these leaks since the initial filling, it is being replaced with a new drum of Li, the container for which was supplied by ORNL.

Field Repair of Cracked Tubing. — After assembly of the loop piping in the vacuum chamber, a leak check revealed a leak near the outlet lug of the resistance-heated hot-leg section. Penetrant inspection showed a crack about 3/16 in. long in the 7/8-in.-OD tubing adjacent to the weld that joins the tubing to the adapter fitting for the outlet lug. The crack could not be seen by field x-ray examination nor in x rays taken before installation in the test stand. The x rays did, however, show a specimen stringer tack welded to the inside surface of the tubing at the approximate position of the penetrant indication. This weld area had been leak checked and inspected by penetrant on two previous occasions, once after completion of the weld and again after completion of the annealing treatment. No indications were found during these inspections, and the parts were not intentionally or accidently stressed thereafter.

Previously, we experienced cracking problems[25] with the piping for the flow meter and with the baffles that were welded to the head of one pump cell. Each of these was symptomatic of a ductility loss near the welding temperature. Once during welding, a part dropped from the fixture, hit the floor of the dry box, and cracked in the weld. Subsequent analysis of the weld metal showed no evidence of interstitial contamination. If we assume that this problem is related to ductility near the fusion temperature, cracking would be promoted by residual stresses from previous welding cycles and also any movement or stressing during welding or cooling. It is still unexplained, however, why the crack

[25]D. L. Clark and B. Fleischer, Fuels and Materials Development Program Quart. Progr. Rept. Dec. 31, 1968, ORNL-4390, pp. 105–106.

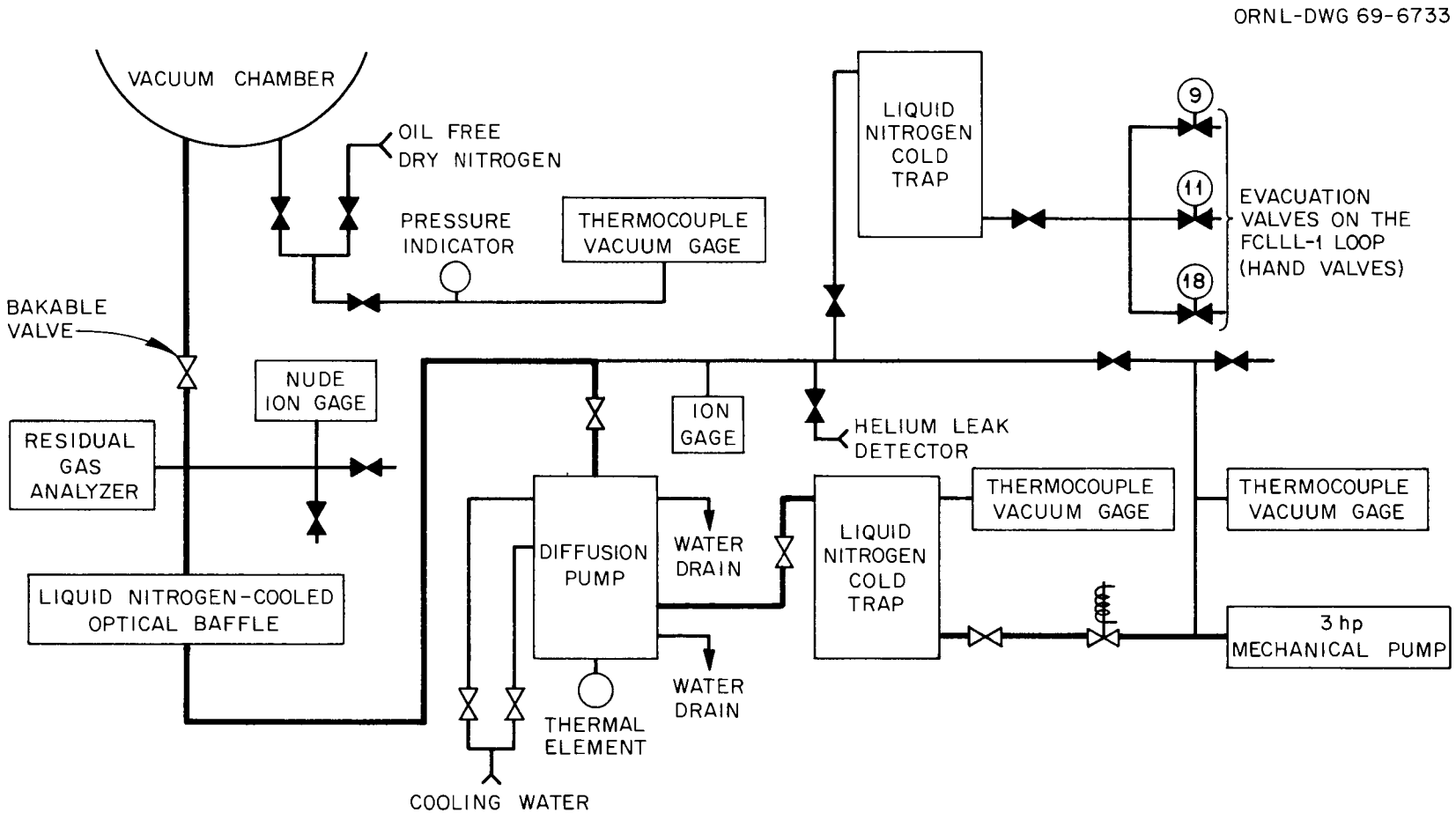

Fig. 5.9. Auxiliary Vacuum Equipment Block Diagram.

near the lug of the electrical heater was not revealed by previous inspections. It may be that the crack progressed with time. The same behavior was noticed for the piping of the flow meter, since it was quite some time after welding before we discovered the cracks there. In this case, however, the welds had only been inspected visually before annealing, and the cracks were detected by leak check and visual inspection after annealing.

Repair of the crack near the outlet lug required either (1) cutting out two field welds and removing the economizer hot-leg section for repair in the dry box or (2) making a field repair. Since the first approach would have required removing insulation and many thermocouples, remaking the field welds, and reinstalling the thermocouples and insulation, it would have caused a considerable loss of time. Consequently, we chose the second approach, using a procedure based on braze welding. The apparent low ductility of T-111 at the normal welding temperature suggested that the best chance of repairing the crack without producing more cracks would be achieved by using a filler metal with a melting point well below that of T-111; we selected Nb–1% Zr. Calculations of stresses accompanying loop operation indicated that this alloy would be acceptable if a section thickness of 1/16 in. of metal could be provided. The filler metal was applied over the cracked region in six passes. The passes over the crack were started in sound metal and then brought toward the midpoint of the crack until complete coverage was obtained.

To achieve a protective atmosphere during the repair, we fabricated a square glove box from plexiglass and mounted it on the portion of the pipe to be repaired. One side of the box was closed with a large plastic bag that served as a bladder for displacement of gas from the inside of the box. The bag could be pushed into the box to displace about 90% of the volume and then be inflated with inert gas to at least twice the volume of the box. A heavier plastic bag protected the bladder bag during expansion. Joints and openings were sealed with plastic tape and Apiezon vacuum-sealing compound. A bubbler was placed on the flush line to assure positive pressure in the box during both expulsion of gas and

inflation of the bag. The glove box was purged and backfilled five times before welding and, during welding, the gas flow on the welding torch served as an additional purge. A picture of the assembly as it appeared during welding is shown in Fig. 5.10.

Welding periods were limited to about 10 sec to minimize outgassing of the materials comprising the containment vessel. To assure cleanliness, we made a practice pass on a sample of T-111 tube before each pass on the part to be repaired. Both the sample and the repaired tubing remained bright throughout the welding session. There was no hardening of the Nb–1% Zr weld metal or adjacent surfaces as determined by light abrasion with a file. Neither dye penetrant inspection nor He leak checking showed any indication of cracks in the repaired area.

The sample weld was exposed to Li at 816°C in a stainless steel capsule for 100 hr to determine if adequate cleanliness had been achieved. Metallographic examination after test revealed some intergranular corrosion at the surfaces of the Nb–1% Zr and near the edges of the weld; it did not appear, however, that the attack would seriously affect the integrity of the weld even if it were not heat treated. To check the integrity of other welds in the heater section, the loop will be thermally cycled to 1370°C and leak checked before it is filled with Li.

T-111 Forced Circulation Loop with Tungsten and Tungsten Alloy Test Section (FCLLL-2) (B. Fleischer)

Our objective is to investigate interactions between T-111 and W-base materials that are candidates for fuel cladding. The materials selected for this test are presented in Table 5.6. Chemically vapor deposited (CVD) W was included because it offers a potential economic advantage over arc-cast material, particularly if it can be used as deposited. The CVD materials will be tested only as cylindrical insert specimens. The other materials will be tested as flat, tab specimens in midstream.

The T-111 is included as a reference material, since it is in FCLLL-1 and is also the primary containment material. Astar 811C is included to determine whether or not alloys strengthened by interstitials will retain their strengthening elements under engineering conditions.

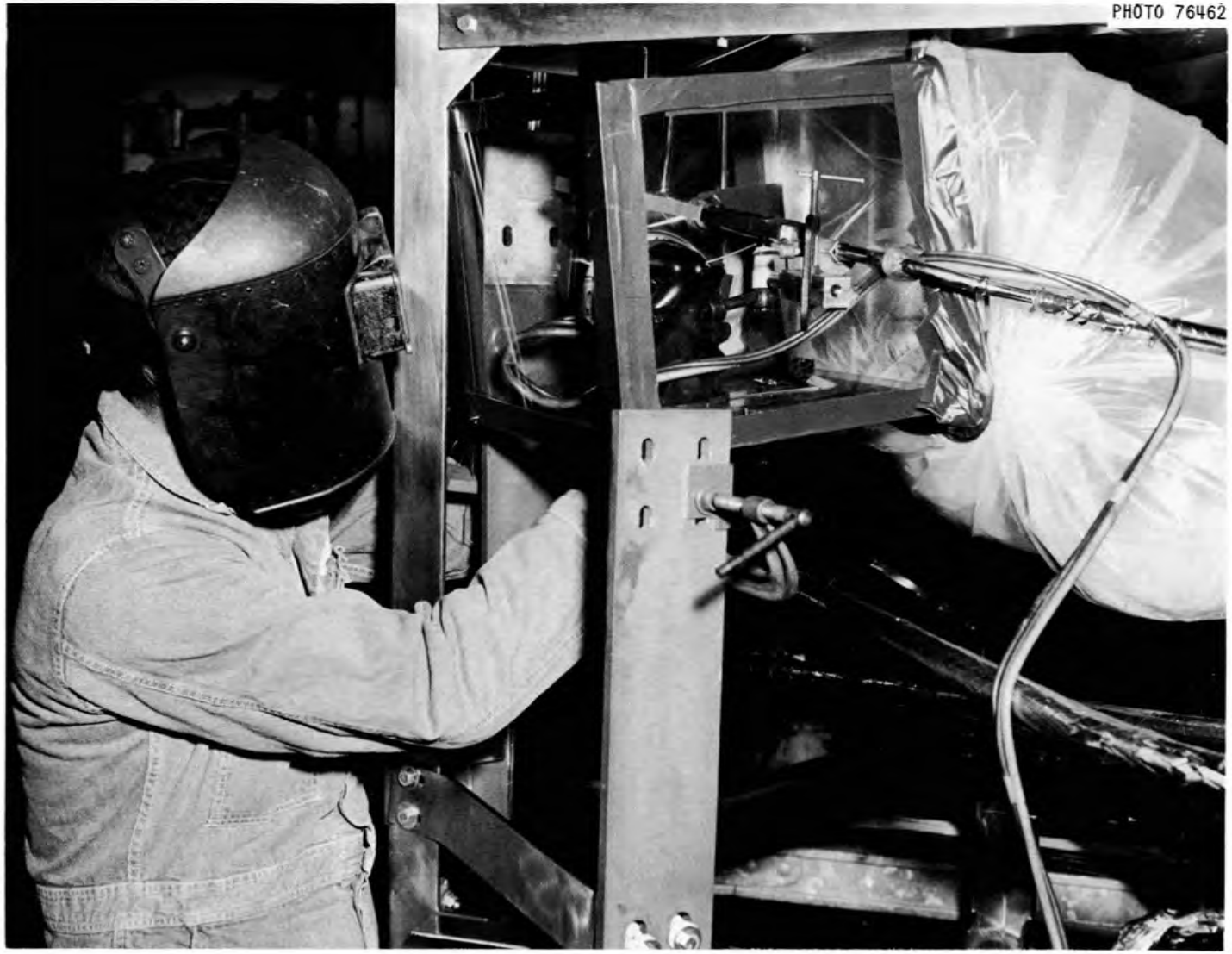

Fig. 5.10. Apparatus for Repair of Cracked Weld in T-111 Tubing.

Table 5.6. Test Materials for Forced Circulation Liquid Lithium Loop-2

Material	Condition		
	Arc Cast, Wrought	Chemically Vapor Deposited	
		As Deposited	Wrought
W	X	X	X
W—25% Re	X		
T-111	X		
Astar 811C	X		

The W—25% Re alloy will yield information regarding the disposition of Re and its effect on dissimilar-metal interactions.

Requisitions have been issued for all the materials. Astar 811C has been ordered from Westinghouse Astronuclear Laboratory and is expected to be delivered by May 1, 1969. The W materials and specimens are being procured and/or made by the Materials and Processing Group.

PART III

RADIATION DAMAGE TO STRUCTURAL MATERIALS

6. BEHAVIOR OF REFRACTORY MATERIALS UNDER IRRADIATION

G. W. Keilholtz R. E. Moore
D. A. Dyslin[1] H. E. Robertson

The purpose of this program is to evaluate the effects of high fast-neutron fluences at 150 to 1100°C on the properties of refractory nuclear materials for both space and civilian power reactors. Investigations of the carbides, nitrides, and silicides of refractory metals are nearing completion. The emphasis in the program is now turning toward nitrides and carbides of depleted U and toward materials for use as neutron absorbers in control rods of fast-flux reactors.

Irradiation Damage to Nonfissionable Refractory Materials

Refractory Metal Carbides

Results of irradiations of carbides of refractory metals (Ti, Zr, Ta, Nb, and W) at both low temperatures (300 to 700°C) and high temperatures (1000 to 1100°C) have been reported previously.[2–4] Work still in progress on carbides includes (1) short-term irradiations in the Engineering Test Reactor (ETR) at 150°C to establish property changes in the absence of thermal annealing, (2) out-of-reactor annealing experiments to determine the rate of shrinkage of the dimensions of carbide specimens, which had swelled during low temperature irradiations, and

---

[1]General Engineering Division.

[2]G. W. Keilholtz, R. E. Moore, and D. A. Dyslin, Fuels and Materials Development Program Quart. Progr. Rept. Dec. 31, 1968, ORNL-4390, pp. 113–114.

[3]G. W. Keilholtz, R. E. Moore, and M. F. Osborne, Nucl. Appl. 4, 330 (1968).

[4]G. W. Keilholtz and R. E. Moore, "Fast Neutron Stability of Refractory Metal Carbides at High Temperatures," paper to be presented at the 15th Annual Meeting of the American Nuclear Society, Seattle, Washington, June 15–16, 1969. To be published in the transactions.

(3) replication electron microscope studies of irradiated carbides, both as polished and as etched, to determine whether high-energy regions are produced within the crystal lattices by collisions of fast neutrons with atomic nuclei. This work was started during the past quarter. The objective is to acquire additional data needed for constructing a model for damage that will include both thermal annealing and neutron annealing.

Preliminary results from experiments on annealing out of the reactor after irradiation indicate a similarity between irradiated refractory-metal carbides and SiC. Results for SiC were reported by Thorne, Howard, and Hope.[5] Specimens of refractory-metal carbides that had swelled during irradiation at temperatures between 300 and 700°C shrank to steady values during annealing at 700°C in a period of 24 hr or less. The fractional volume shrinkage for each of the five carbides was the same regardless of the magnitude of the original volume expansion of the individual specimens of each carbide. The steady values of this fractional shrinkage at 700°C are as follows: TiC, 0.40; ZrC, 0.17; TaC, 0.20; NbC, 0.32; WC, 0.30.

A possible explanation of the observed equality of fractional shrinkage is that it represents the fraction of displaced atoms produced during irradiation that can be thermally restored to regular lattice sites at any chosen annealing temperature. If this is true, the steady values of $\Delta V/V$ obtained during annealing of specimens that have maximum values for $\Delta V/V$ after irradiation will be greater than the maximum values for $\Delta V/V$ that would have been achieved during irradiation at the annealing temperature. The reason for this is that neutron annealing during irradiation at the annealing temperature would further reduce the values of $\Delta V/V$. This interpretation is consistent with the data of Thorne *et al.*[5] on SiC. The annealing program is expected to yield data useful for constructing a model for neutron damage to carbides.

---

[5]R. P. Thorne, V. C. Howard, and B. Hope, J. Brit. Ceramic Soc. 7, 449 (1967).

Effects of Irradiation on LMFBR Fuels

Effects of Helium Gas Produced by Fast Neutrons in Depleted UN

Fuels containing N, such as UN or UCN solid solutions, are being considered for use in fast-breeder reactors. An understanding of the effects of gas generated within nitride fuels would aid in their development. In addition to Xe and Kr produced as fission products, nitride fuels would also generate He through the $^{14}N(n,\alpha)^{11}B$ fast-neutron reaction. The effect of the generation of He by itself (i.e., in the absence of the generation of fission gas) will be evaluated in irradiations of depleted fuel.

During the past quarter, specimens for the irradiations were prepared by the ORNL Metals and Ceramics Division, and the components of the first irradiation assembly were fabricated. This assembly will contain four types of specimens in the form of solid cylinders (0.400 in. long × 0.25 in. in diameter) alternately stacked over the flux profile of the ETR: depleted UN, depleted UN with ^{15}N enrichment, depleted UC, and depleted U (50 mole % C,N). The specimens will be irradiated at 1000°C to fast-neutron fluences ranging from 0.5 to 2.0×10^{21} neutrons/cm^2 (> 1 Mev). Irradiation will begin near the end of FY 1969. A low-temperature (150°C) irradiation is also planned to begin early in FY 1970.

Postirradiation examinations will include dimensional measurements, metallography, and electron microscopy. Comparisons of the results for depleted UN and depleted UN with ^{15}N enrichment will directly measure the effect of the (n,α) reaction, for this reaction does not occur in $U^{15}N$. The results for UN, U(C,N), and UC will provide data for calculating the effects of the dilution of UN with UC on the property changes caused by He generated internally.

Fast-Neutron Effects on Materials for Neutron Absorption in Fast Reactors

Materials with large neutron-absorption cross sections are required for fabricating safety rods and shim rods for control of the

reactivity of fast reactors. The materials for control of reactivity must be able to withstand irradiation in an intense fast flux. This part of the program is aimed at investigating the effects of fast neutrons on several materials that are candidates for use in controlling reactivity, such as TaC and Ta metal. In order to eliminate effects produced by absorptions of thermal neutrons, the irradiations will be carried out in an EBR-II facility that has almost no thermal component of the neutron spectrum.

Planning and engineering design of the irradiation assembly were begun. Specimens of Ta metal, TaC, and possibly other neutron absorbers in the form of 3/8 × 3/8-in. solid cylinders will be irradiated for six months in row 8 of the EBR-II beginning in July 1969. Each type of specimen will be irradiated at three temperatures, 370, 700, and 1000°C, at different positions in the neutron-flux profile. Flux monitors will be included to establish the flux profile and the spectrum of neutron energy. Temperature monitors of SiC and melt wires will be included to establish maximum temperatures.

Postirradiation examinations will include dimensional measurements, metallography, x-ray diffraction studies, electron microscopy, electron probe examinations to determine transmutation of Ta, and radial gamma scans to determine self-shielding effects.

7. FAST-NEUTRON IRRADIATION EFFECTS ON ELECTRICAL INSULATORS

G. W. Keilholtz R. E. Moore
D. A. Dyslin[1] H. E. Robertson

The purpose of this program is to establish the effects of fast neutrons on the mechanical, physical, and electrical properties of materials suitable for use as electrical insulators in thermionic converters and to evaluate the mechanisms of neutron damage in these materials from 150 to 1100°C.

General Survey of Fast-Neutron Effects on Electrical Insulators

This task is aimed at preliminary investigation of a variety of high-temperature electrical insulators for determining the most promising materials for later, more exhaustive investigations. Because previous work[2] on polycrystalline alumina has shown that separation at grain boundaries is most severe at temperatures of greatest interest in thermionic applications, the immediate emphasis in this task has turned toward materials in which such separation is least likely. A low-temperature (150°C) experiment is planned for the Experimental Test Reactor (ETR) in which specimens fabricated from single-crystal Al_2O_3 (synthetic sapphire), single-crystal MgO, and zirconia-doped Y_2O_3 will be irradiated. Separation at grain boundaries cannot occur in single-crystal materials. Since zirconia-doped Y_2O_3 is cubic, separation caused by anisotropic expansion will not occur. This material has a much better microstructure than the yttria that we previously investigated in which severe gross fracturing occurred. We hope that the improved yttria will be superior to ordinary yttria with respect to gross fracture.

---

[1]General Engineering Division.

[2]G. W. Keilholtz, R. E. Moore, D. A. Dyslin, and H. E. Robertson, Fuels and Materials Development Program Quart. Progr. Rept. Dec. 31, 1968, ORNL-4390, pp. 117–120.

Irradiation of High-Density Commercial Al_2O_3 Products Considered for Thermionic Insulators

Four commercial polycrystalline alumina products are being evaluated at temperatures from 400 to 1230°C. Specimens were irradiated in two identical assemblies in the ETR J-12 core position for different times. An assembly containing specimens of three of the four commercial products will be irradiated in a facility in the EBR-II to provide information on the effect of neutron energy on radiation damage. Types and numbers of specimens in each experiment are given in Table 7.1.

Observations of gross fracturing and gross volume expansion of the specimens irradiated in the short-term ETR assembly were reported previously.[2] Metallographic examinations have now been completed. The results make it possible to define more clearly the factors that cause changes in properties during irradiation. A few typical photomicrographs of irradiated specimens are shown in Figs. 7.1 through 7.3 to illustrate various degrees of separation at grain boundaries found in many of the specimens. The causes of separation and its effect on gross damage and volume expansion are discussed below.

Gross Damage

Gross fracturing of specimens irradiated in the short-term ETR assembly correlates much better with the purity of the specimen types than with any other known variable. Of course, since each of the four specimen types were fabricated differently, it is possible that some other unknown variable in fabrication is responsible. The grain size of Type II (Wesgo) is much larger than we previously believed, but the striking difference in gross fracture between it and Type IV (ref. 2), which has about the same grain size, seems to eliminate grain size as an important variable as far as gross fracture is concerned.

In general, the metallographic results do not show a definite correlation between the degree of separation at grain boundaries and gross fracture. There is no question, however, that propagation of macrofractures can occur readily in specimens with severe separation at grain boundaries. A possible example of this can be seen in Fig. 7.2.

Table 7.1. Types and Numbers of Commercial Alumina Specimens in Irradiation Experiments

Type	Trade Name	Grain Size (μm)	Number of Specimens					
			ETR Short-Term Experiment		ETR Long-Term Experiment		EBR-II Experiment	
			Solid Cylinders[a]	Cylindrical Shells[b]	Solid Cylinders[a]	Cylindrical Shells[b]	Solid Cylinders[c]	Cylindrical Shells[d]
I	Coors AD-995	13	9	7	9	7	10	10
II	Wesgo AL-995	23	11	7	11	7	10	10
III	GE Opaque Lucalox	6	11	7	11	7	10	10
IV	GE Translucent Lucalox	25	6	0	6	0	0	0

[a]Diameter: 0.493 in.

[b]Diameter: 0.493 in.; wall thickness: 0.020 in.

[c]Diameter: 0.400 in.

[d]Diameter: 0.400 in.; wall thickness: 0.020 in.

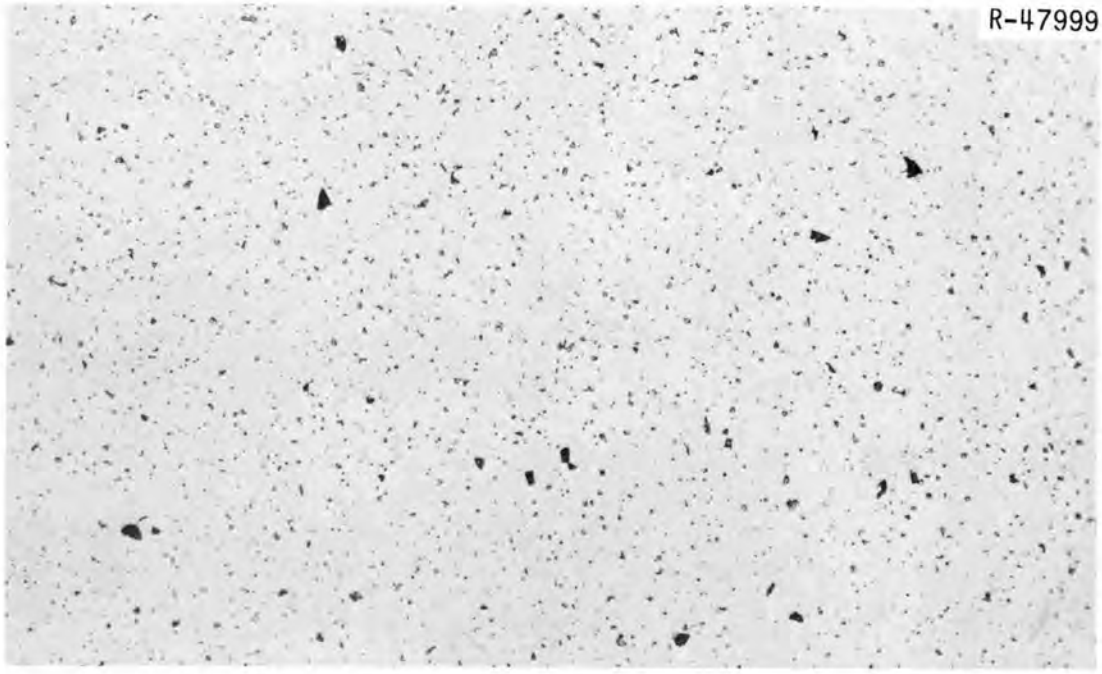

Fig. 7.1. Wesgo Alumina Irradiated at About 750°C to a Fast-Neutron Fluence of 2.0×10^{21} neutrons/cm^2 (> 1 Mev) Showing a Small Amount of Separation at Grain Boundaries. As polished, 100×.

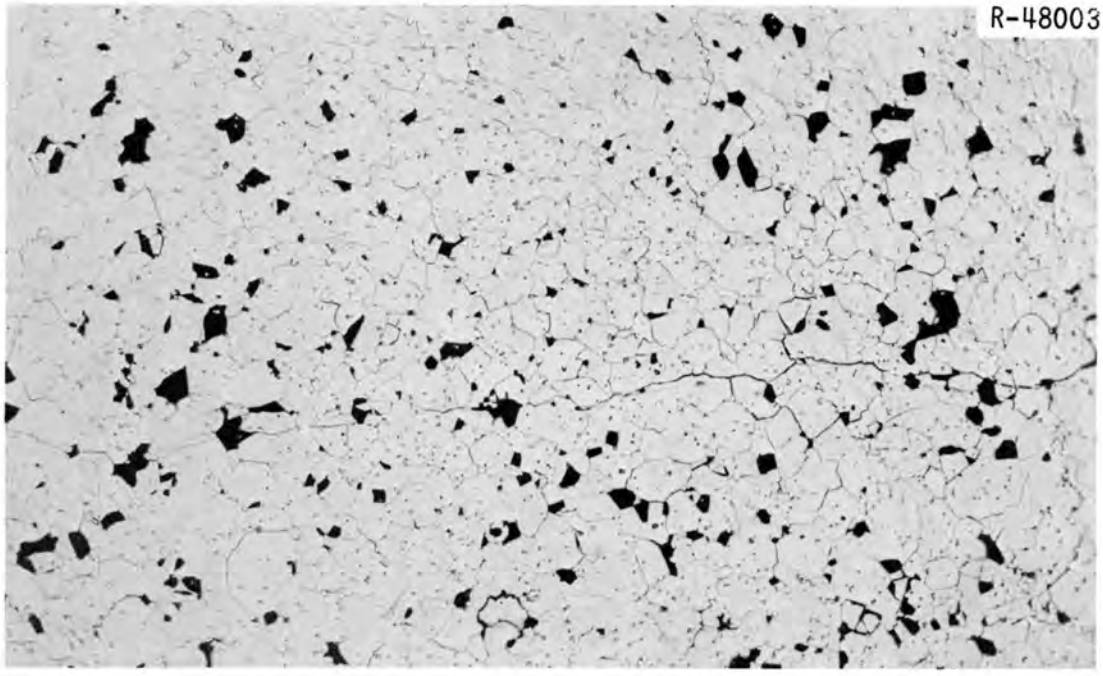

Fig. 7.2. Wesgo Alumina Irradiated at About 930°C to a Fast-Neutron Fluence of 3.0×10^{21} neutrons/cm^2 (> 1 Mev) Showing Severe Separation at Grain Boundaries with Grain Pullouts that Occurred During Polishing. A very thin crack is present. As polished, 100×.

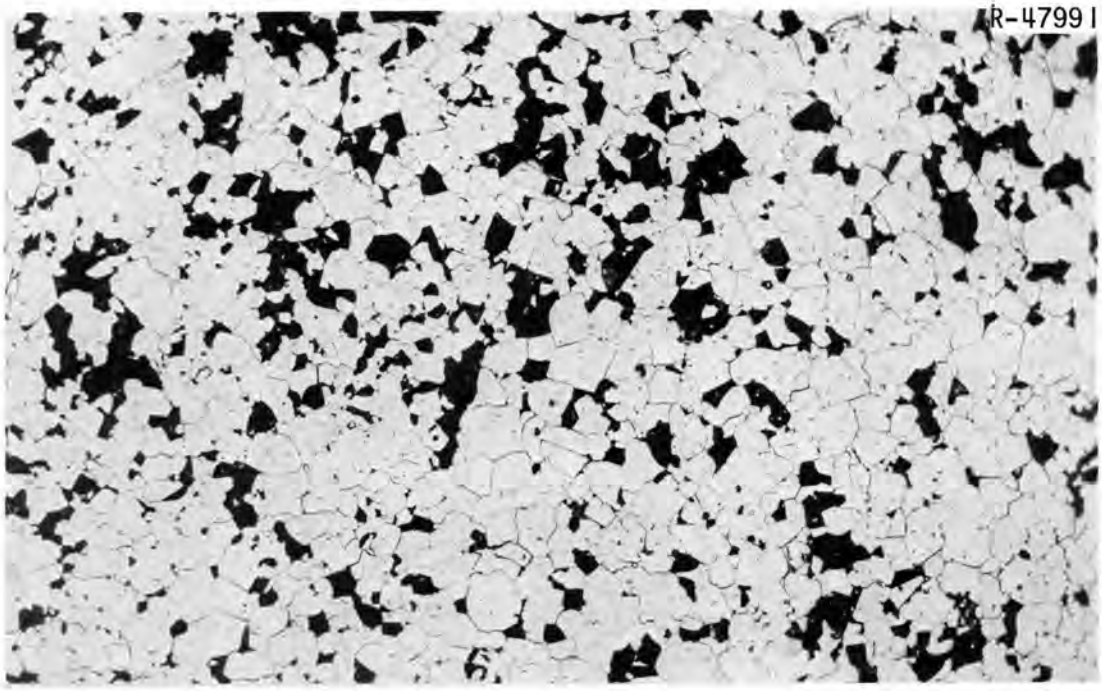

Fig. 7.3. Wesgo Alumina Irradiated at About 1230°C to a Fast-Neutron Fluence of 2.4×10^{21} neutrons/cm^2 (> 1 Mev) Showing Very Severe Separation at Grain Boundaries and Many Grain Pullouts. As polished, 100×.

Also, it is certainly true that alumina with severe separation at the grain boundaries will be fragile. Mechanical or thermal stress on such an alumina component in a thermionic device would, therefore, probably result in gross fracture or even crumbling to powder.

The least amount of separation at grain boundaries was found in specimens of Type III alumina, which was also one of the two best types of alumina with respect to gross fracture. Type III is the purest type, but it also has the smallest grain size, which is probably the main reason for its resistance to separation at grain boundaries.

Volume Expansion

The expansion in volume resulting from neutron irradiation of polycrystalline alumina may be expressed as

$$\Delta V/V = (\Delta V/V)c + (\Delta V/V)g \ ,$$

where $(\Delta V/V)c$ is the fractional volume expansion resulting from expansion of the crystals themselves and $(\Delta V/V)g$ is the additional expansion contributed by separation at the grain boundaries if any is present. Figure 7.4 is a plot of volume expansion against fast-neutron fluence for specimens irradiated in the short-term ETR assembly. The only data included are for specimens that were examined metallographically and found to have little or no separation at grain boundaries. A curve[3] for Type IV alumina irradiated at lower temperatures (300 to 600°C) is included for comparison. Two calculated points, at 150 and 650°C, are also plotted from data of Wilks et al.[4] on single crystals.

The upper, solid line represents the crystal expansion at high temperatures (580 to 1070°C); specimens with appreciable separation at grain boundaries expanded to values considerably above this line. The dashed line represents crystal expansion at lower temperatures (300 to 600°C). Apparently, the upper temperature limit of 600°C was not actually achieved. The data of Wilks et al. for single crystals are consistent with our polycrystalline results.

Our results indicate that, at a fixed fluence, the greatest increase of volume expansion with increasing irradiation temperature occurs at temperatures below 600°C. There is little change from 600 to about 1100°C, where in-reactor annealing greatly reduces the volume expansion. Irradiation at much higher temperatures (1230°C), however, results in very severe separation at grain boundaries (Fig. 7.3) and increased volume expansion.

Conclusions

Conclusions based on the results of the short-term ETR experiment are as follows:

1. Gross fracturing of alumina during irradiation is primarily caused by effects of impurities and/or unknown fabrication factors

---

[3]G. W. Keilholtz and R. E. Moore, Nucl. Appl. 3(11), 686–691 (1967).

[4]R. S. Wilks, J. A. Desport, and J.A.G. Smith, The Irradiation-Induced Macroscopic Growth of α-Al_2O_3 Single Crystals, AERE-R-5460 (May 1967).

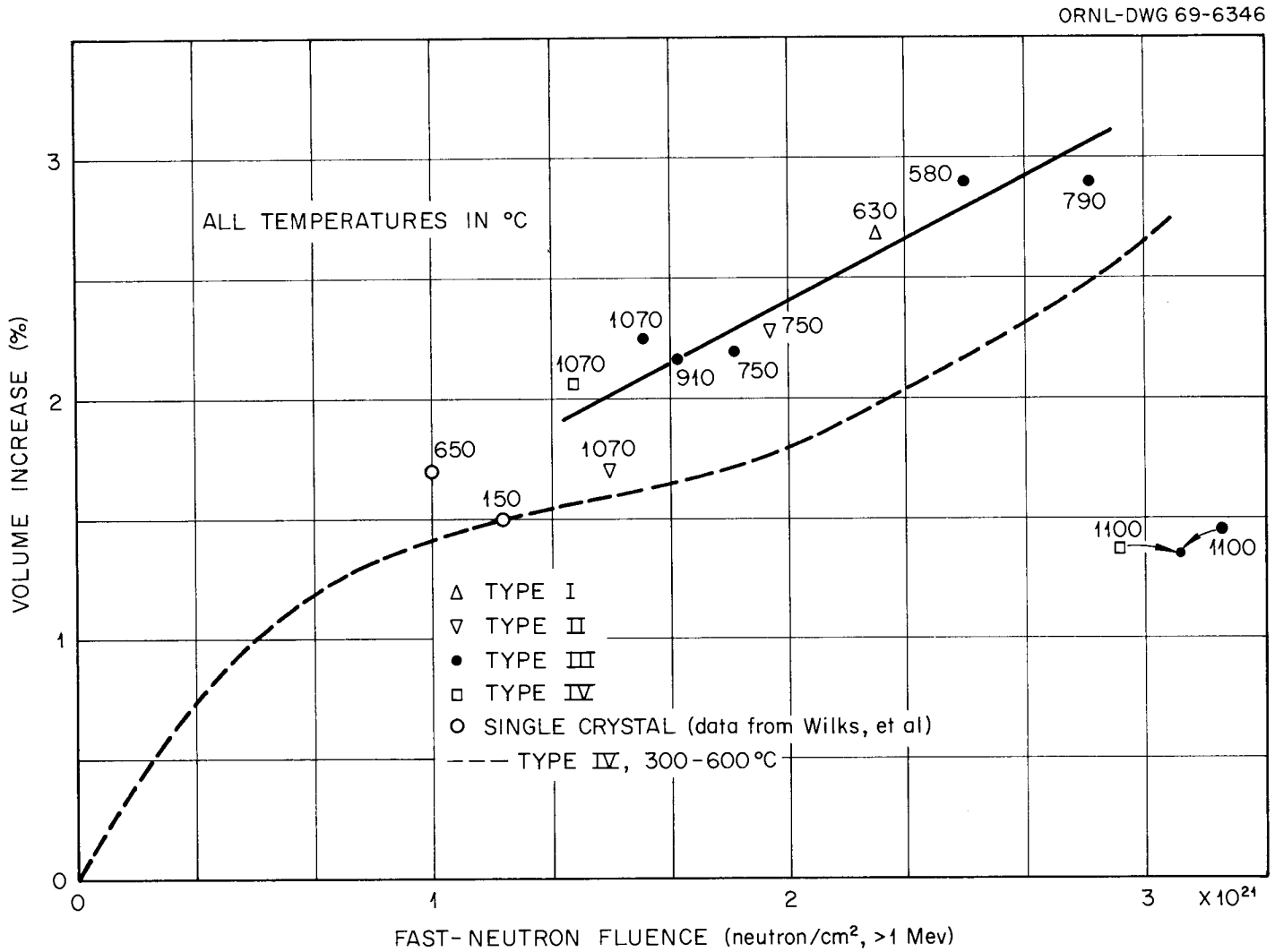

Fig. 7.4. Volume Increase of Specimens of Commercial Polycrystalline Alumina. Separation at the grain boundaries is absent or negligible. [Ref. R. S. Wilks, J. A. Desport, and J.A.G. Smith, The Irradiation Induced Macroscopic Growth of α-Al_2O_3 Single Crystals, AERE-R-5460 (May 1967).]

except for specimens in which severe separation at grain boundaries occurs as a result of stresses on the grain boundaries caused by anisotropic expansion of the grains.

2. In such cases of severe separation at grain boundaries, the specimens are fragile, and fracturing can easily occur along grain boundaries regardless of the purity of the specimens or other factors.

3. Volume expansion of grains during irradiation not only increases with increasing neutron fluence, but as the irradiation temperature is increased from 150 to about 600°C, the expansion increases and also becomes more anisotropic.

4. At temperatures between about 600°C and about 1050°C, there is little change of volume increase of grains at comparable fluences, but at 1100°C in-reactor annealing reduces the volume increase of irradiated specimens.

5. Irradiation at temperatures much higher than 1100°C produces severe separation at grain boundaries, probably through a mechanism of grain growth.

6. Separation at grain boundaries, which causes an expansion in volume of polycrystalline alumina in excess of that contributed by expansion of the grains, becomes more severe with (1) increasing volume expansion of grains, (2) increasing anisotropy of the volume expansion of grains, and (3) increasing original grain size.

8. MECHANICAL PROPERTIES RESEARCH AND LMFBR CLADDING AND STRUCTURAL MATERIALS DEVELOPMENT

J. R. Weir, Jr. H. E. McCoy, Jr.

Work in this program includes studies of the high-temperature irradiation embrittlement and other technologically important aspects of radiation damage to fuel cladding materials at high neutron fluence. The work centers around types 304 and 316 stainless steel, Incoloy 800, and Hastelloy N and the effects of Ti concentration in these alloys on radiation damage.

Effects of Irradiation on the Mechanical Properties of Austenitic Stainless Steels

E. E. Bloom

Specimens of standard types 316 and 316L stainless steel and Ti-modified types 316, 316L, 304, and 304L stainless steel were irradiated in a core position of the Oak Ridge Research Reactor (ORR) for about 4500 hr at 350, 450, 550, and 650°C to neutron fluences of about 1.8×10^{21} neutrons/cm^2 (thermal) and 1.4×10^{21} neutrons/cm^2 (> 1 Mev). The compositions of the alloys and the preirradiation annealing treatments are listed in Table 8.1. After the irradiation, specimens of each alloy were tensile tested at their respective irradiation temperatures at a strain rate of 0.002 min^{-1}. Specimens of each alloy were also annealed and then aged at 350, 450, and 550°C for 4000 hr to separate changes in mechanical properties that resulted from thermal aging from those that resulted from irradiation.

Strength properties are shown as a function of temperature in Fig. 8.1. For each alloy, the ultimate tensile strengths of thermal control and irradiated specimens were similar and did not appear to vary consistently as a function of test temperature.

Table 8.1. Composition and Preirradiation Heat Treatment of Austenitic Stainless Steels Irradiated in EBR-II

Type Stainless Steel	Preirradiation Heat Treatment for 1 hr at Temperature (°C)	Composition, wt %										N	
		C	Cr	Ni	Mo	Ti	Mn	Si	P	S	B	Total	Soluble
316	1050	0.044	17.5	12.6	2.8	0.02	2.1	0.8	0.012	0.014			
316L	1050	0.018	16.9	12.7	2.7	0.02	2.3	0.6	0.013	0.015	0.0002	0.057	0.014
Ti-modified 316	1050	0.064	17.0	12.0	2.4	0.23	0.5	0.4			0.0007		
Ti-modified 316L	1050	0.012	17.0	12.0	2.6	0.21	1.8	0.4			0.0007		
Ti-modified 304	925	0.05	19.0	10.0		0.21	0.7	0.8	0.013	0.002	0.0027	0.009	0.003
Ti-modified 304L	925	0.012	19.5	11.2		0.19	1.0	0.05	0.006	0.013	0.0003	0.006	

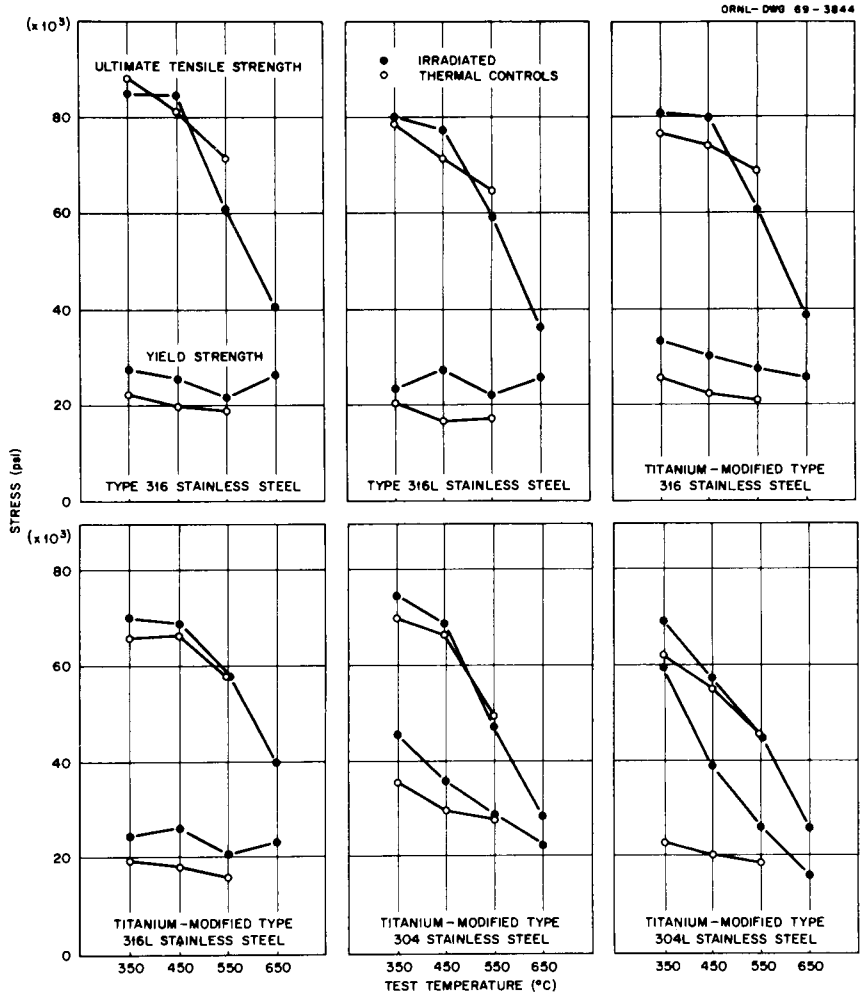

Fig. 8.1. Effect of Irradiation on the Yield and Ultimate Tensile Strength of Several Austenitic Stainless Steels. Specimens were irradiated at the test temperature to 1.8×10^{21} neutrons/cm^2 (thermal) and 1.4×10^{21} neutrons/cm^2 (> 1 Mev). Strain rate 0.002 min^{-1}.

Irradiated specimens of standard and Ti-modified types 316 and 316L stainless steel each exhibited consistently higher yield strengths than did the thermal control specimens at 350, 450, and 550°C. The aged, Ti-modified type 304 stainless steel had higher yield strengths than did the other alloys. Yield strengths for the alloy after annealing for 1 hr at 925°C were 28,900, 26,400, and 23,700 psi at 500, 600, and 650°C, respectively, thus indicating that aging at these temperatures does not affect the yield strength. Irradiation of Ti-modified type 304 stainless steel at 350°C resulted in an increase in yield strength of

about 10,000 psi over that of the thermal control specimen. As the irradiation temperature increased, the yield strength of the irradiated and control specimens converged until they were nearly equal at 550°C. The Ti-modified type 304L stainless steel increased greatly in yield strength after irradiation at 350°C and, similarly to the behavior of the Ti-modified type 304L stainless steel, increase in yield strength induced by irradiation became less as the irradiation temperature increased.

Ductility values are shown as a function of temperature in Fig. 8.2. With the exception of Ti-modified type 304L stainless steel, irradiation at 350 and 450°C produced a small but consistent reduction in tensile ductility; for the Ti-modified type 304L stainless steel there was a rather large reduction in elongation that resulted from the increased yield strength and lower uniform elongation. At 550°C, all of the alloys began to show marked reductions in ductility. At 650°C, the results agree reasonably with those of an earlier experiment[1] that showed that these heats of Ti-modified types 316 and 316L stainless steel have higher tensile ductilities than do standard types 316 and 316L stainless steel after irradiation at 650°C to 9×10^{20} neutrons/cm^2 (thermal) and 7×10^{20} neutrons/cm^2 (> 1 Mev).

Radiation Damage in Incoloy 800

D. G. Harman R. E. Gehlbach

We are evaluating Incoloy 800 at 650°C after irradiation at 500 and 700°C to thermal and fast fluences of about 0.8×10^{21} neutrons/cm^2 (ref. 2). We reported lower creep and tensile ductility for specimens (0.12% C, 0.10% Ti) annealed at 1150°C and irradiated or aged (control) at 500°C

[1]E. E. Bloom, Fuels and Materials Development Program Quart. Progr. Rept. Sept. 30, 1968, ORNL-4350, pp. 149–152.

[2]D. G. Harman, Fuels and Materials Development Program Quart. Progr. Rept. Dec 31, 1968, ORNL-4390, pp. 127–129.

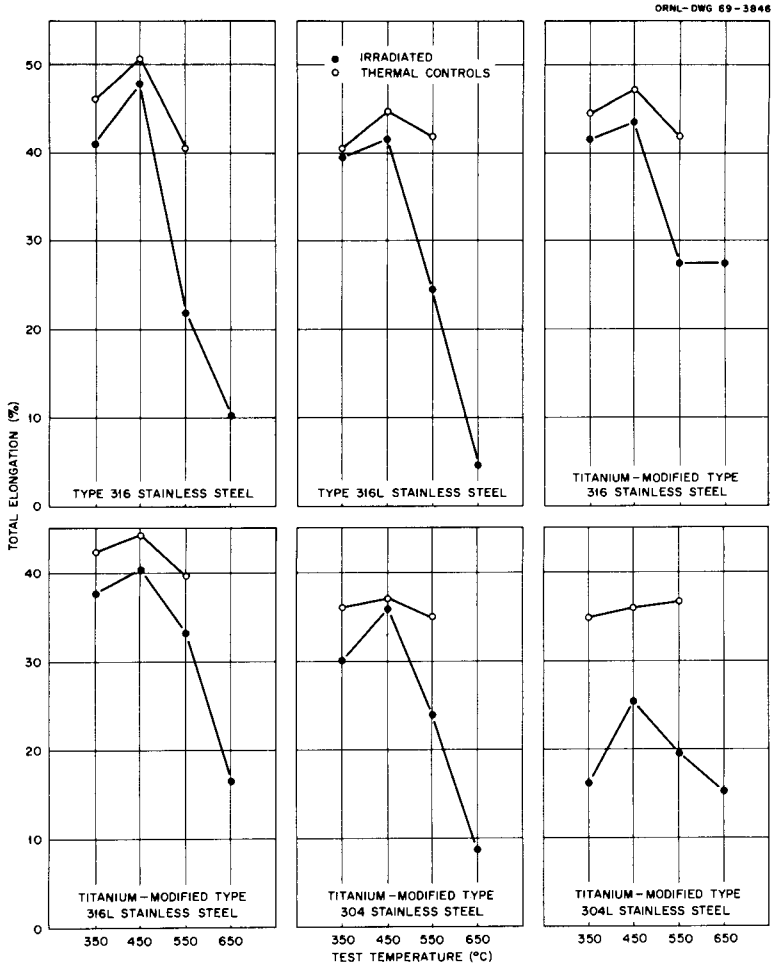

Fig. 8.2. Effect of Irradiation on the Ductility of Several Austenitic Stainless Steels. Specimens were irradiated at the test temperature to 1.8×10^{21} neutrons/cm^2 (thermal) and 1.4×10^{21} neutrons/cm^2 (> 1 Mev). Strain rate 0.002 min^{-1}.

than for those irradiated or aged at 700°C. This embrittlement was circumvented by aging 100 hr at 800°C after the 1150°C anneal or by lowering the annealing temperature to 1040°C.

When comparing the postirradiation creep tests to the corresponding control tests, we found that the irradiation at 500°C resulted in a lower minimum creep rate as well as a longer rupture life. This is shown in Fig. 8.3 for the heat with 0.12% C and 0.10% Ti that was annealed at 1150°C and then aged at 800°C. The irradiated specimen shows half the creep rate and a 27% increase in rupture life compared to the control specimen.

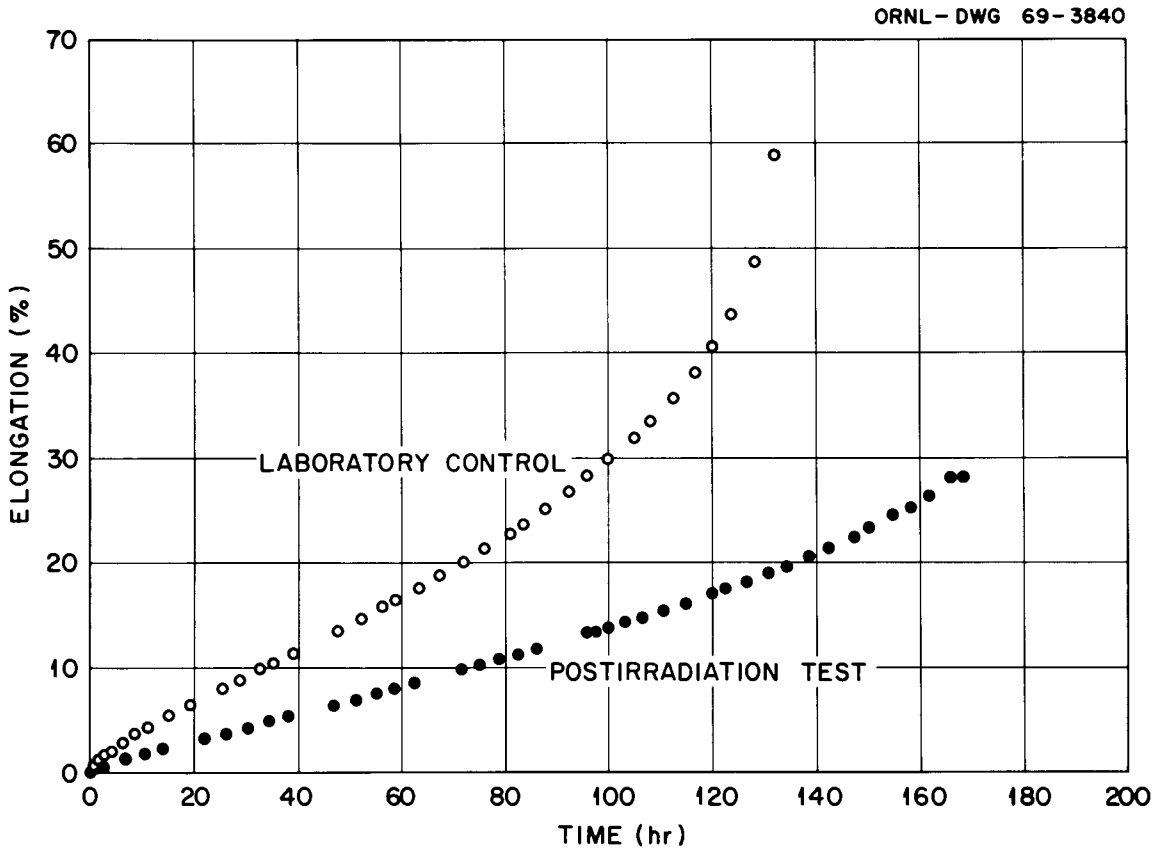

Fig. 8.3. Effect of Irradiation on Creep of Incoloy 800 Containing 0.1% Ti and 0.12% C, Annealed 30 min at 1150°C, Aged 100 hr at 800°C, and Stressed at 25,000 psi at 650°C. Test I-163 was irradiated for two cycles (about 2300 hr) in the ORR at 500°C to about 0.8×10^{21} neutrons/cm^2 (fast or thermal). Test C-152 was held in a laboratory furnace in Ar to provide an identical thermal history.

Smith and Moteff[3] noted similar effects for commercial Incoloy 800 irradiated in the Experimental Breeder Reactor-II (EBR-II) to a fast fluence of 3×10^{20} neutrons/cm^2 at 540°C and tested at 705°C.

We showed metallographic evidence that the precipitation at grain boundaries is globular and noncontinuous after aging at 700°C as contrasted with an apparently continuous film after aging at 500°C.

We have continued our investigation of these aged specimens by a standard two-stage extraction-replication technique, for which a plastic

[3]J. P. Smith and J. Moteff, Quarterly Progress Report: Irradiation Effects on Reactor Structural Materials, November, December 1967 and January 1968, BNWL-710, pp. 10.5–10.10.

replica was stripped from the heavily etched surface of each specimen. The precipitates in a selected area were analyzed by electron diffraction and with an electron microprobe attachment to an electron microscope. Electrolytic dissolution of the matrix permitted analysis of the precipitates by x-ray diffraction techniques.

A replica of the specimen aged at 500°C is shown in Fig. 8.4. There were large amounts of continuous fiber along the coherent twin boundaries, and there were cellular and dendritic precipitates along the grain boundaries. The electron microprobe showed primarily Cr with some Fe in these precipitates, and the electron diffraction patterns showed $M_{23}C_6$. Small particles throughout the matrix showed the presence of Cr and Fe. X-ray patterns showed some titanium sulfide, but $M_{23}C_6$ was the predominant phase.

Figure 8.5 shows the replica from the specimen aged at 700°C. The massive dendritic precipitate along the grain boundaries was again identified as the $M_{23}C_6$ carbide. Fairly large carbides were also noted in the matrix along with a large number of particles of titanium sulfide. X-ray diffraction showed primarily $M_{23}C_6$ with more sulfide than in the specimen aged at 500°C. It should be noted that there was 0.006% S in this heat of material (both specimens were machined from this heat).

Merica and Waltenberg[4] first showed the harmful effects of S on the malleability of Ni in the "hot short" temperature regime. As little as 0.005% S completely surrounded the grains with a eutectic of Ni and nickel sulfide that has a low melting point. Ductility was regained by adding Mn or Mg to form stable MnS or MgS particles. Olsen _et al._[5] found embrittlement at the grain boundaries in high-purity Ni containing only 0.0009% S.

We used the electron scanning microscope to examine the fracture surface of a control specimen that had been creep tested at 650°C after

---

[4]P. D. Merica and R. G. Waltenberg, "Malleability and Metallography of Nickel," U.S. National Bureau of Standards, Tech. Paper No. 281, April 2, 1925.

[5]K. M. Olsen, C. F. Larkin, and P. H. Schmitt, Jr., _Trans. Am. Soc. Metals_ **53**, 349–358 (1961).

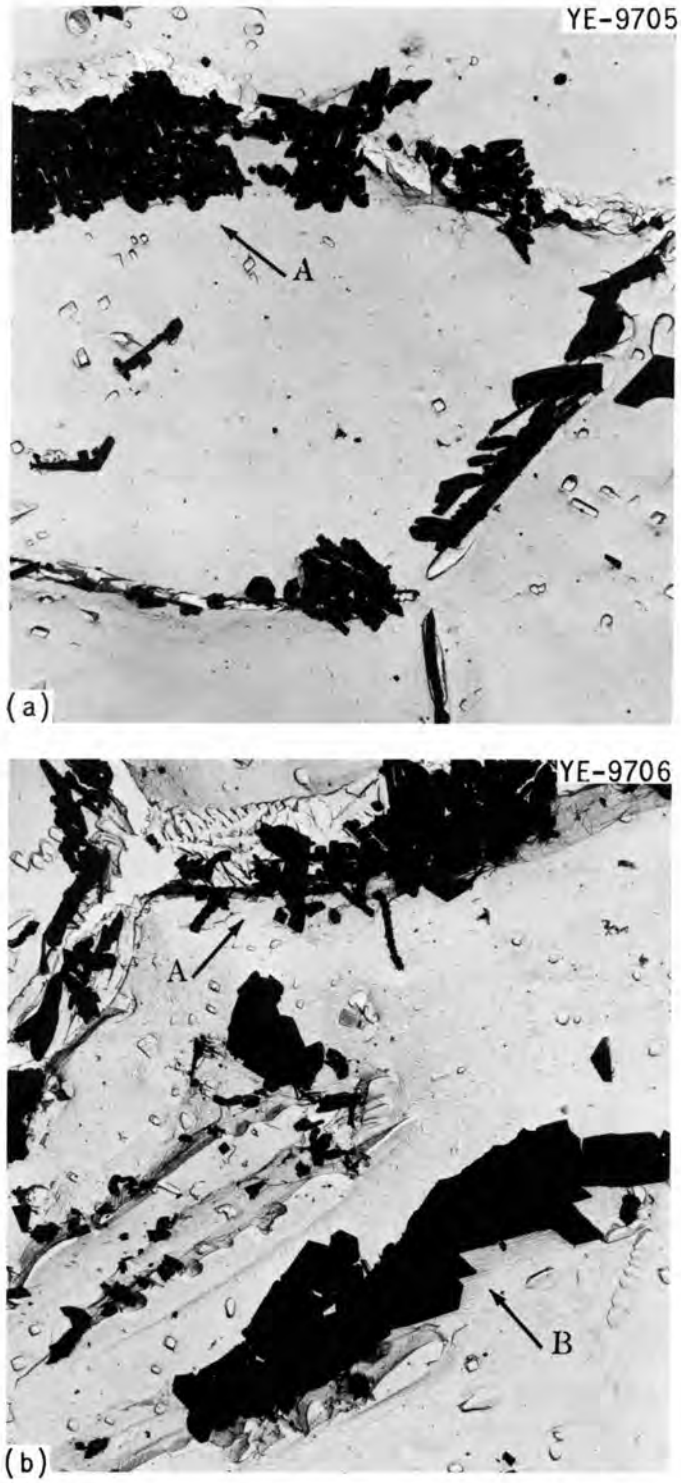

Fig. 8.4. Precipitates Extracted from Incoloy 800 Aged at 500°C for About 2300 hr. (a) There is cellular $M_{23}C_6$ at grain boundaries, A, and (b) a continuous film along the coherent twin-matrix boundary, B. The two-stage replica was obtained from a heavily etched surface. 5000×.

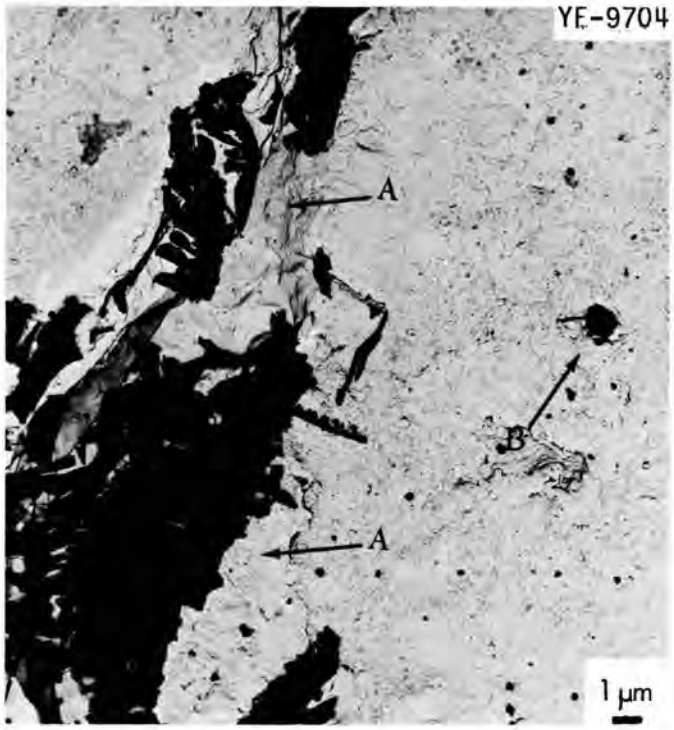

Fig. 8.5. Precipitates Extracted from Incoloy 800 Aged at 700°C for About 2300 hr. Dendritic $M_{23}C_6$ was located on all grain boundaries, A, and titanium sulfide particles were found in the matrix, B. The two-stage replica was obtained from a heavily etched surface. 5000×.

having been aged 2300 hr at 500°C. Our results are shown in Fig. 8.6. This specimen was annealed at 1150°C before aging and showed only 25% elongation as compared to the 60% we had expected because of results from aging at 700°C. Figure 8.6(a) shows a propensity toward intergranular cracks along the gage section as well as a considerable amount of shear fracture on the fracture surface itself. Figure 8.6(b) shows a view of the fracture surface centered around an area of intergranular fracture where a complete grain has been pulled out so that extensive areas of grain boundary are revealed. Figure 8.6(c) is a higher magnification of the surface of the grain boundary. The mottled appearance of this surface suggests a second phase of a cellular or continuous nature. There is the possibility that there was surface oxidation during or after the test, though the surface of the gage section did not have this same appearance.

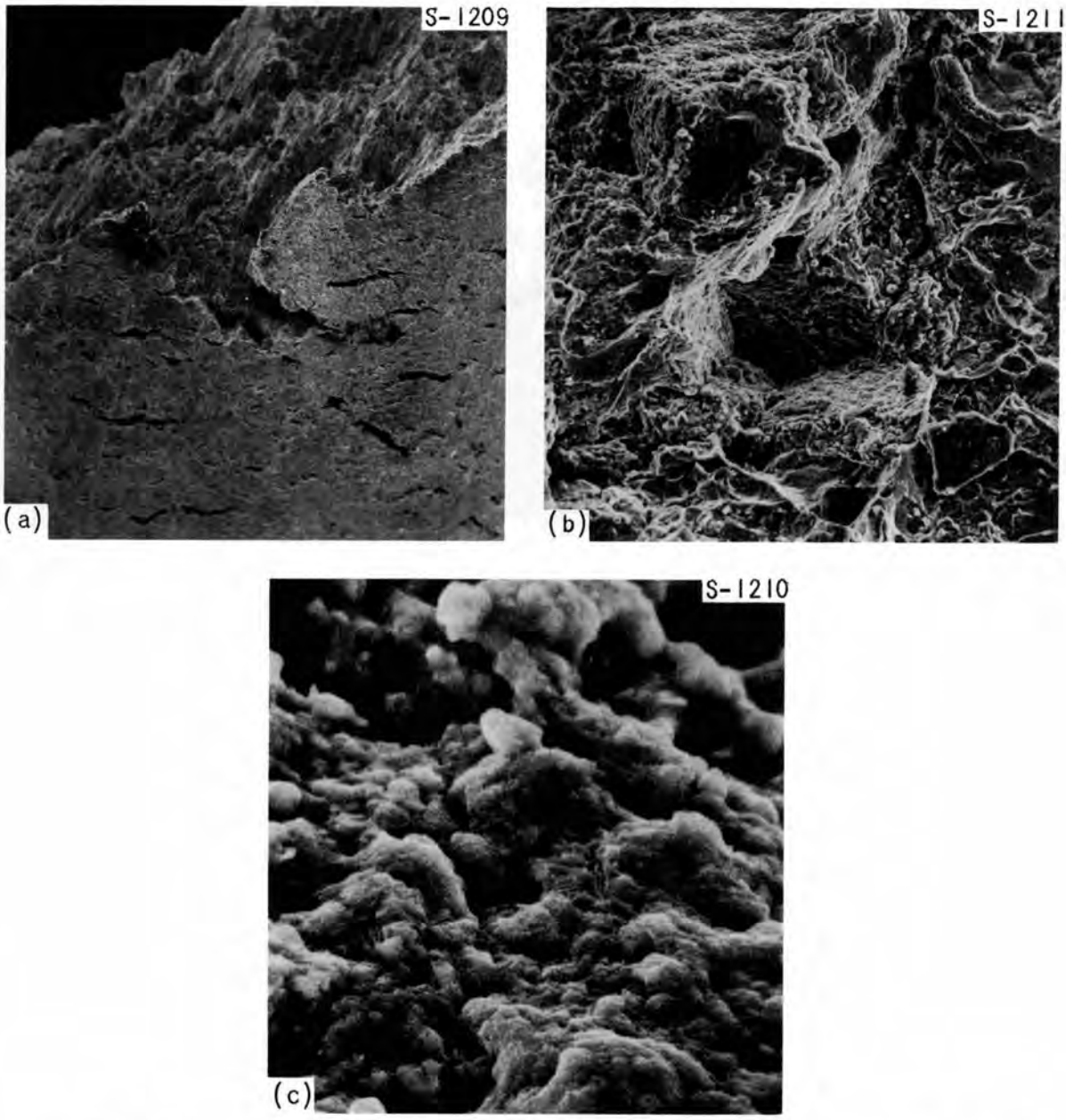

Fig. 8.6. Scanning Electron Photomicrographs of Incoloy 800 Creep Specimen. (a) Longitudinal view showing transverse cracks along gage section and overall shear fracture. 50×. (b) Area of fracture surface centered about region of intergranular fracture. 500×. (c) Grain boundary surface. 5000×. These photomicrographs were prepared by T. A. Nolan, Physics Department, ORGDP.

C. D. Lundin[6] has obtained electron scanning micrographs very similar to Fig. 8.6(c) from Ni that showed severe hot cracking during welding. He also showed a continuous phase rich in S along the grain boundaries.

Thus our observation and the previously documented cases of embrittlement by S lead us to suggest that the reduction in the fracture strain of Incoloy 800 after aging at 500°C is due to the formation of a grain-boundary phase rich in S.

Cyclotron Injection of Helium to Simulate Fast-Reactor Irradiation

The Effect of Aging on the Creep Properties of Titanium-Modified Type 304L Stainless Steel Containing Cyclotron-Injected Helium (R. T. King)

The effects of 2.0×10^{-5} atom fraction (20 ppm) of cyclotron-injected He on the creep-rupture properties of type 304L stainless steel modified with 0.2% Ti have been reported.[7] However, we were interested in determining whether structural modifications produced by thermal-mechanical treatments might improve the ductility and creep strength of this alloy, which is resistant to damage by He. Therefore, we gave groups of specimens different aging treatments and examined them by transmission electron microscopy. Specimens that were given treatments that produced promising microstructures were bombarded at the same time as those specimens for which results were reported earlier and were then creep-rupture tested in static Ar at 600°C.

All specimens were finish cold rolled 50% to 0.010 in. thick before the tensile specimens were machined from them. Sets of specimens were then prepared by annealing for 1 hr at 925°C in Ar or by annealing for 1 hr at 925°C and then aging the specimens for 100 hr at either 700, 750, or 800°C. Aging at 700°C produced a fine carbide precipitate on

---

[6]C. D. Lundin, Professor of Metallurgy at The University of Tennessee, private communication (March 1969).

[7]R. T. King and J. R. Weir, Jr., Fuels and Materials Development Program Quart. Progr. Rept. June 30, 1968, ORNL-4330, pp. 176–183.

many low-angle grain boundaries, while the high-angle boundaries were relatively free of precipitate. Aging at higher temperatures produced a coarser precipitate.

In an attempt to produce precipitate particles throughout the grain, we aged one set of specimens for 10 hr at 700°C after the cold rolling to decorate the dislocations in the worked structure. This treatment was followed by recrystallization at 925°C for 15 min and further aging at 700°C for 10 hr (multiple aging). A duplex structure with fine matrix precipitates and precipitates along some grain boundaries was produced. We believe that inhomogeneity of composition and perhaps the degree of initial cold work were responsible for the duplex structures (see Fig. 8.7).

The rupture times for specimens annealed at 925°C or annealed at 925°C and aged 100 hr at 750°C and for multiply aged specimens containing no He or 20 ppm He are plotted versus stress in Figs. 8.8 and 8.9, respectively. The specimens aged at 750°C generally have the shortest rupture lives, probably because a great amount of C is present in grain-boundary precipitates and not available to interact with matrix dislocations. The multiply aged specimens, which have a precipitate structure in the matrix, generally have the longest rupture times. The unusually long rupture life of the multiply aged specimen tested at 30,000 psi is considered unreliable and will be checked by a duplicate test. By comparing Figs. 8.8 and 8.9 it is readily seen that 20 ppm He has little measurable effect on the rupture life of this material in any of the conditions tested.

With one exception, the ductilities of all the control specimens fall within a scatter band of ±5% strain (see Fig. 8.10). The ductility of the specimens aged at 750°C or multiply aged is maximum (about 50 to 60%) in tests lasting from 5 to 50 hr; longer and shorter rupture times are associated with lower ductilities. The exception to this behavior is the material annealed at 925°C; its ductility did not decrease with increasing rupture time up to about 330 hr.

The ductilities of all specimens containing 20 ppm He also fall within a scatter band of about ±5% strain (see Fig. 8.11). The

Fig. 8.7. Type 304L Stainless Steel Modified with 0.2% Ti and Cold Worked 50%. (a) Electron photomicrograph of precipitate structure formed by annealing 10 hr at 700°C, 15 min at 900°C, and 10 hr at 700°C. 15,000×. (b) Duplex grain size formed by annealing treatment. 500×.

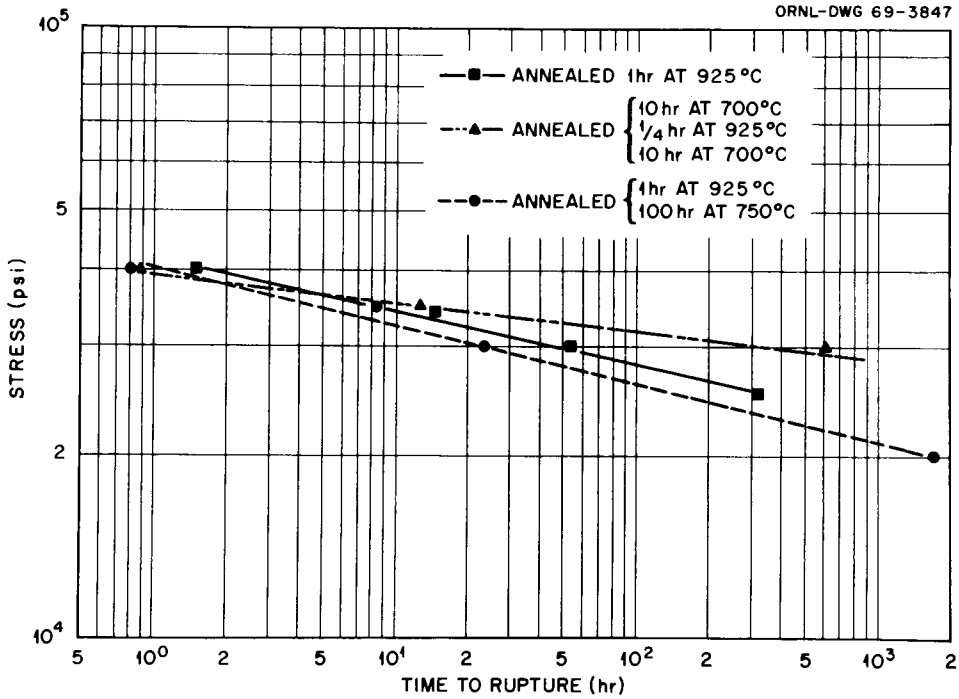

Fig. 8.8. Stress vs Rupture Life at 600°C for Type 304L Stainless Steel Modified with 0.2% Ti.

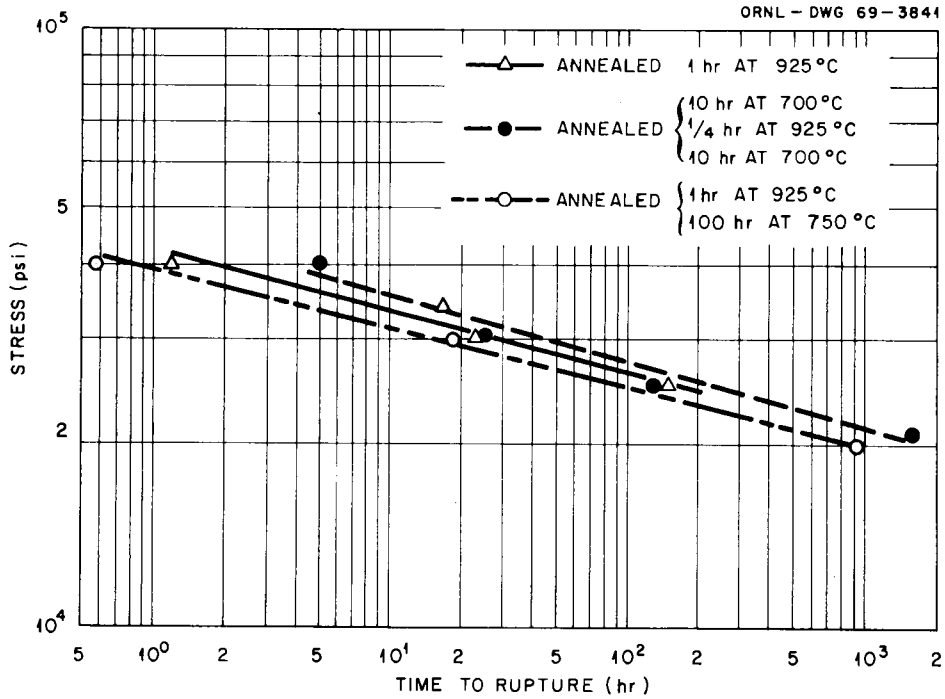

Fig. 8.9. Stress vs Rupture Life at 600°C for Type 304L Stainless Steel Modified with 0.2% Ti and Containing 20 ppm He.

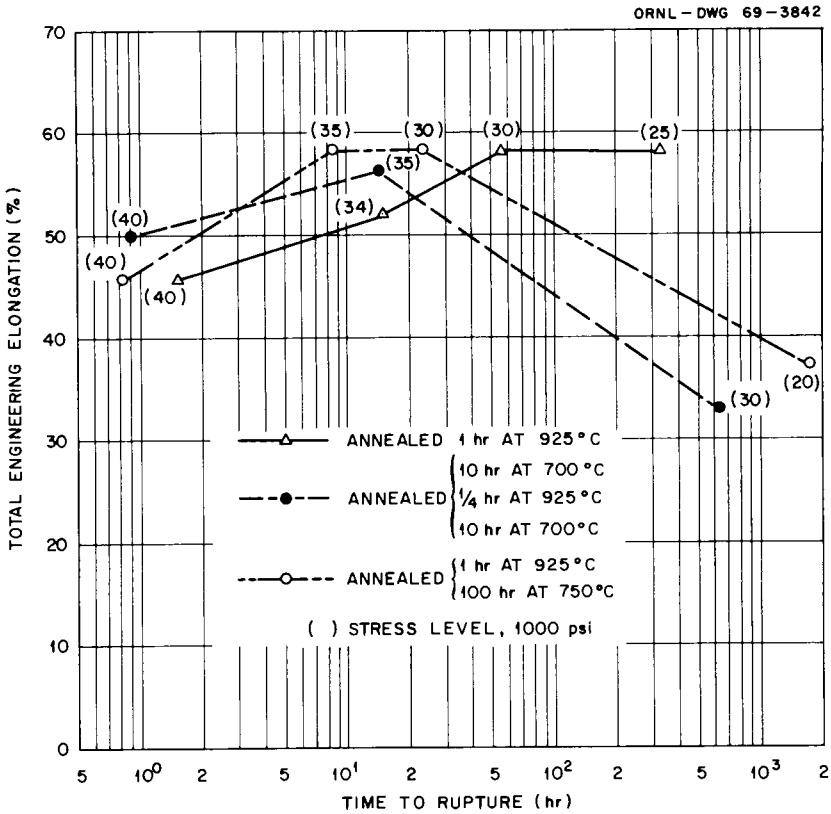

Fig. 8.10. Strain vs Rupture Life at 600°C for Type 304L Stainless Steel Modified with 0.2% Ti.

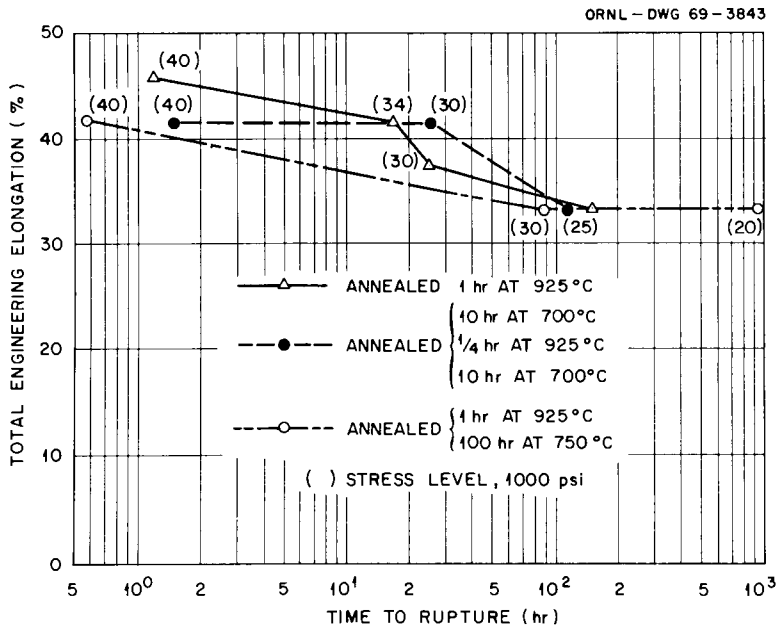

Fig. 8.11. Strain vs Rupture Life at 600°C for Type 304L Stainless Steel Modified with 0.2% Ti and Containing 20 ppm He.

ductilities decrease from about 40% strain for rupture times of 1 hr to 30% strain for 100- to 1000-hr tests. At these test times, the ductilities of specimens containing 20 ppm of cyclotron-injected He are only about 10% (strain) lower than those of the control specimens.

Utilization of EBR-II

Transmission Electron Microscopy of Stainless Steel and Nickel Irradiated in EBR-II (E. E. Bloom, J. O. Stiegler)

Several specimens of type 304 stainless steel and Ni 270 were irradiated in the EBR-II to relatively low fast-neutron fluences for study of the early stages of the formation of voids and dislocation loops. No voids were revealed by transmission electron microscopy of Ni 270 irradiated at 370°C to 1.1×10^{18} neutrons/cm^2 (> 0.1 Mev). There were perfect dislocation loops and dislocation lines or fragments. At this low fluence, the damage was very heterogeneously distributed. The dislocation loops and lines were present in clusters, with the clusters being separated by regions relatively free of damage. An example of such a cluster is shown in Fig. 8.12. No damage was visible in type 304 stainless steel irradiated at 370°C to 1.1×10^{18} neutrons/cm^2 (> 0.1 Mev).

In Ni 270 irradiated to 1.4×10^{20} neutrons/cm^2 (> 0.1 Mev) at temperatures between 384 and 524°C, there were polyhedral voids, perfect dislocation loops, and dislocation lines. Nearly all the dislocation loops appeared to be associated with the dislocation lines, as shown in Fig. 8.13. It may be that the loops nucleated preferentially in the stress field of the dislocation. At this fluence, the dislocation lines are present throughout the material instead of being clustered as they were at the lower fluence. The mean and maximum diameters of the voids increased with increasing irradiation temperature. For example, specimens irradiated at 384 and 438°C had mean void diameters of 142 and 169 A and maximum void diameters of 211 and 267 A, respectively. In type 304 stainless steel irradiated to 1.4×10^{20} neutrons/cm^2 (> 0.1 Mev) between 384 and 524°C, the visible damage was in the form of defect clusters. The concentration of defect clusters decreased with increasing

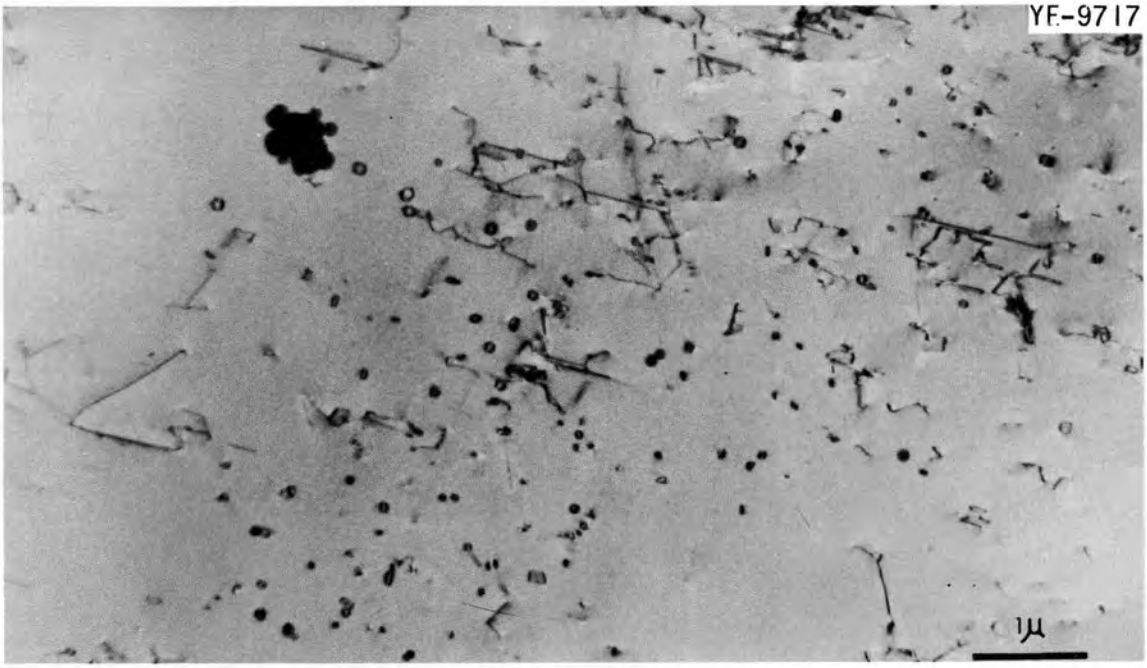

Fig. 8.12. Dislocation Loops in Nickel 270 Irradiated at 370°C to 1.1×10^{18} neutrons/cm^2 (> 1 Mev). The loops were not homogeneously distributed but rather were concentrated in clusters.

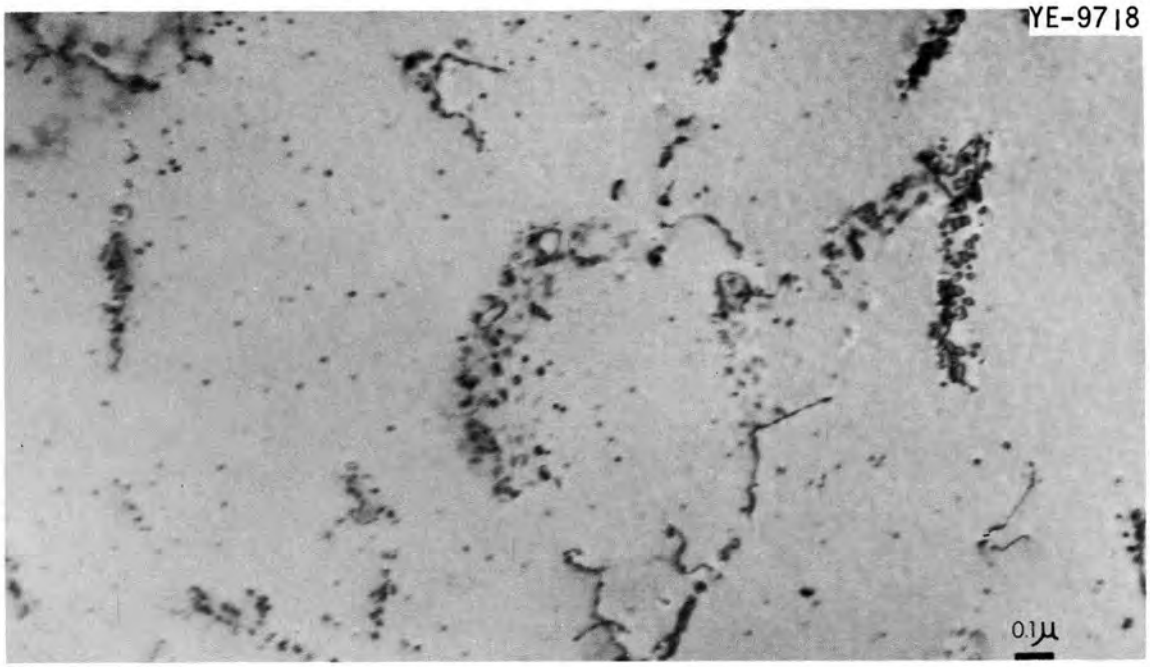

Fig. 8.13. Dislocation Lines and Loops in Nickel 270 Irradiated at 410°C to 1.4×10^{20} neutrons/cm^2 (> 0.1 Mev). Dislocation loops were always located near a dislocation line.

irradiation temperature as shown in Fig. 8.14. Three types of clusters have been identified.[8] The majority were interstitial dislocation loops that had an $\frac{a}{3}$ {111} Burgers vector. There were also perfect loops that had an $\frac{a}{2}$ {110} Burgers vector and defect clusters that were spherical or three dimensional. Significant differences in the nature of the irradiation damage were observed near grain boundaries. In stainless

[8]E. E. Bloom and J. O. Stiegler, Fuels and Materials Development Program Quart. Progr. Rept. Dec. 31, 1968, ORNL-4390, pp. 134–137.

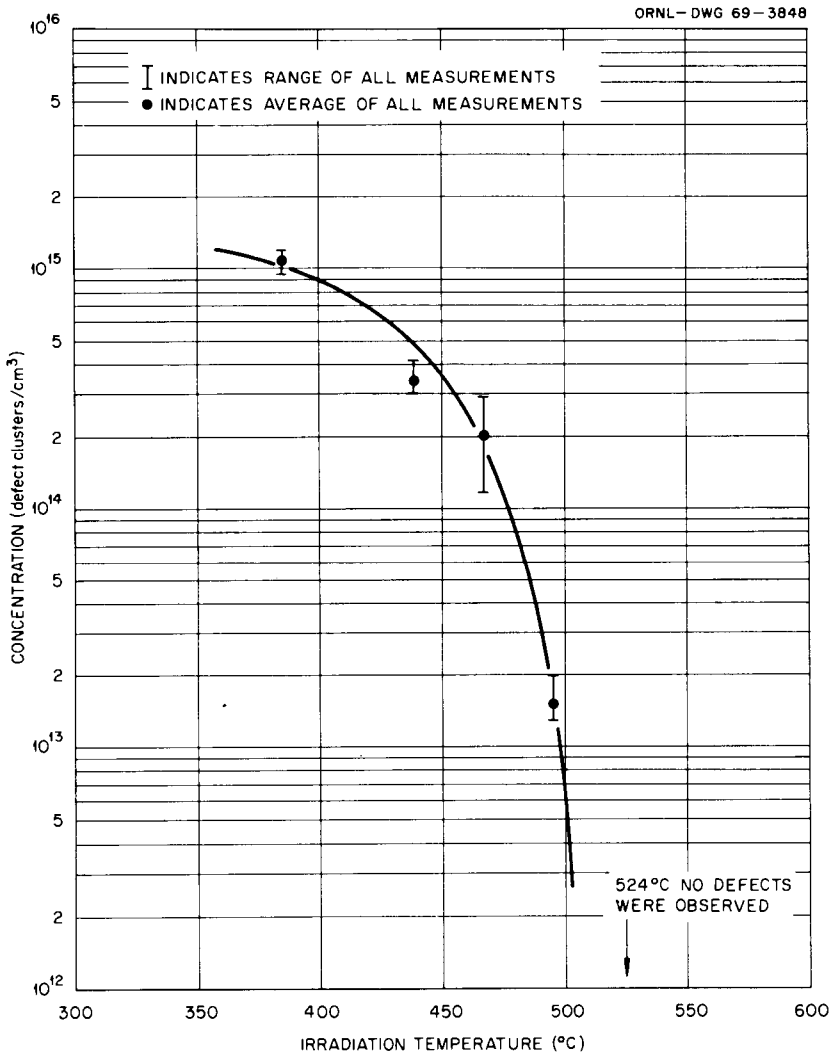

Fig. 8.14. Total Concentration of Defect Clusters as a Function of Temperature for Type 304L Stainless Steel Irradiated to 1.4×10^{20} neutrons/cm^2 (> 0.1 Mev).

steel [Fig. 8.15(a)] irradiated at 384°C to 1.4×10^{20} neutrons/cm^2 (> 0.1 Mev), there was a zone about 1000 A wide adjacent to the boundaries that was denuded of visible damage. In Ni 270 [Fig. 8.15(b)] irradiated under the same conditions, there were no dislocation structures within about 10,000 A of the boundary, while the region denuded of voids was on the order of 1000 A wide.

Several samples have been removed from a type 304L stainless steel shroud tube irradiated in subassembly XG05 and examined by transmission electron microscopy. Table 8.2 lists the measured concentrations of voids and mean and maximum void sizes and the calculated density decreases presently available.

Figure 8.16(a) shows the microstructure of a specimen removed from the top portion of the shroud tube. Using the flux data of Moteff,[9] we estimate that this specimen received a neutron fluence of 3×10^{20} neutrons/cm^2 (> 0.1 Mev) and 1.5×10^{19} neutrons/cm^2 (> 1 Mev) at about 470°C. We think the dislocations in the specimen were there before the irradiation. Some of the dislocations have split into partial dislocations separated by a stacking fault. In this specimen, the concentration of defect clusters was not uniform. Figure 8.16(b) shows a type 304 stainless steel specimen that was irradiated at 467°C to 1.4×10^{20} neutrons/cm^2 (> 0.1 Mev) and 2.6×10^{19} neutrons/cm^2 (> 1 Mev) at the midplane of a row 2 subassembly. This specimen contains a uniform distribution of defect clusters, which, as discussed previously, are primarily interstitial dislocation loops. There are three important differences in the histories of these two specimens that might have caused the different damage structures. The neutron energy spectrum was different in the two cases, the neutron flux was different by about a factor of 200, and the shroud tube apparently had a much higher density of dislocations before irradiation. We cannot now establish which of these variables might be responsible for the different damage states.

---

[9] J. Moteff, GENMPO, Cincinnati, Ohio, personal communication.

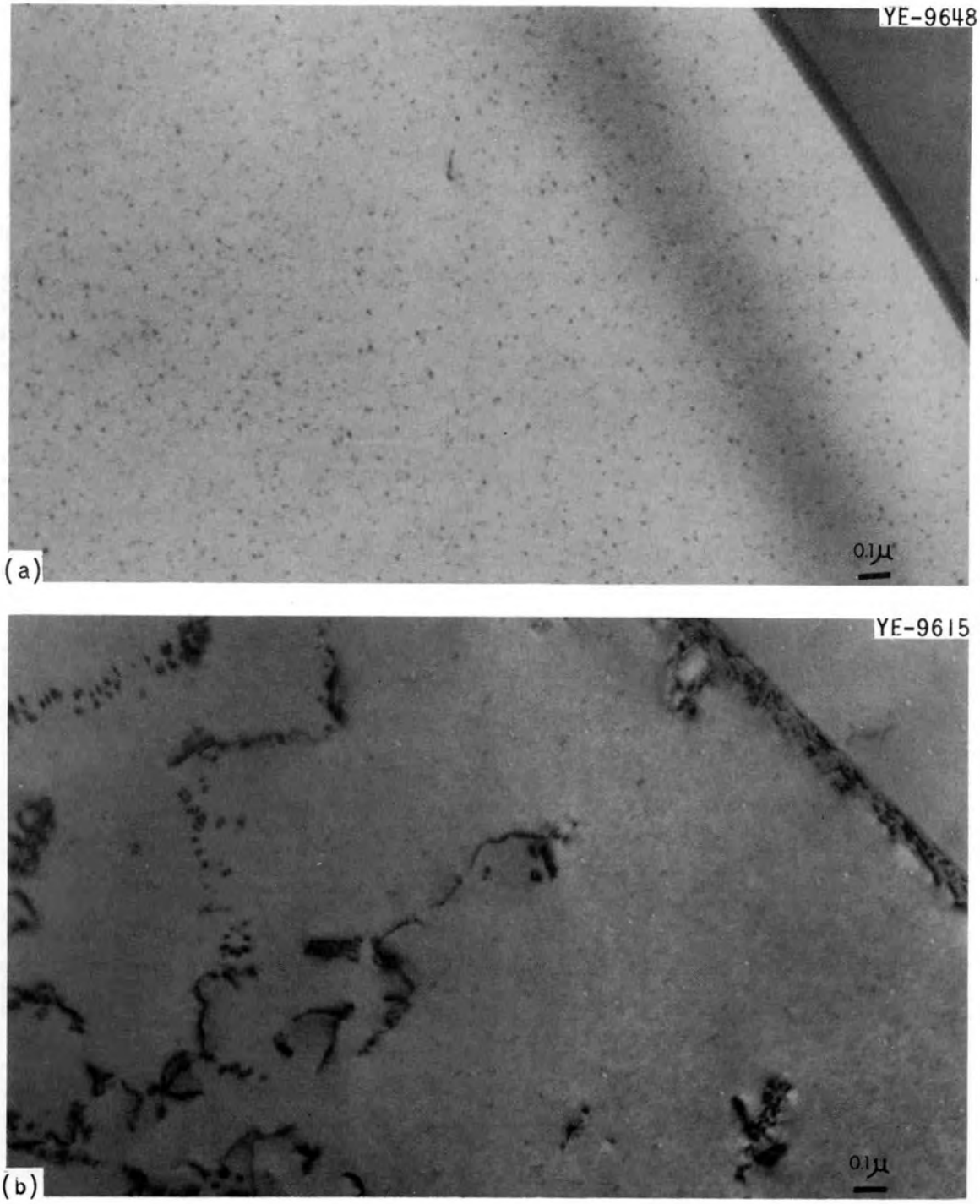

Fig. 8.15. Comparison of Damage Structures After Irradiations in EBR-II at 384°C to 1.4×10^{20} neutrons/cm^2 (> 0.1 Mev). (a) Type 304 stainless steel, and (b) nickel 270.

Table 8.2. Void Size, Void Concentration, and Irradiation Conditions for Specimens Removed from Shroud Tube

Irradiation Temperature (°C)	Neutron Fluence (neutrons/cm^2, > 0.1 Mev)	Void Concentration (voids/cm^3)	Void Diameter (A)		Calculated Density Decrease (%)
			Mean	Maximum	
370	2.9×10^{22}	3.9×10^{15}	91	156	0.16
420	5.0×10^{22}	6.5×10^{15}	154	267	1.50
470	2.5×10^{22}		142	350	
470	0.4×10^{22}		160	225	

Vanadium Alloy Studies and Effects of Impurities

Voids in Vanadium Irradiated in EBR-II (F. W. Wiffen, J. O. Stiegler)

The unalloyed V we examined was taken from part of a United Nuclear Corporation experiment irradiated in EBR-II to a total fluence of 1.7×10^{22} neutrons/cm^2 at a temperature calculated to be near 630°C. In the first report of this examination[10] we gave details of the history of the material and showed the density and size distribution of the voids produced by irradiation. Since then, a more detailed examination of the material, both as irradiated and after postirradiation annealing, has been undertaken to fully characterize the defects (especially the voids) in V.

In order to determine the void density, it is necessary to measure the foil thickness. We determined the foil thicknesses from parallax measurements on stereoscopically related pairs of photomicrographs. Measurements of foil thickness were made near the center of the area in which void counts were to be made so that the thickness obtained would be an average for any wedge shape of the foils.

The main source of error in determining foil thicknesses this way lies in correctly choosing points that are on the foil surfaces. Measurements were made either between voids which appeared to be the

[10]F. W. Wiffen and J. O. Stiegler, Fuels and Materials Development Program Quart. Progr. Rept. June 30, 1968, ORNL-4330, pp. 195–197.

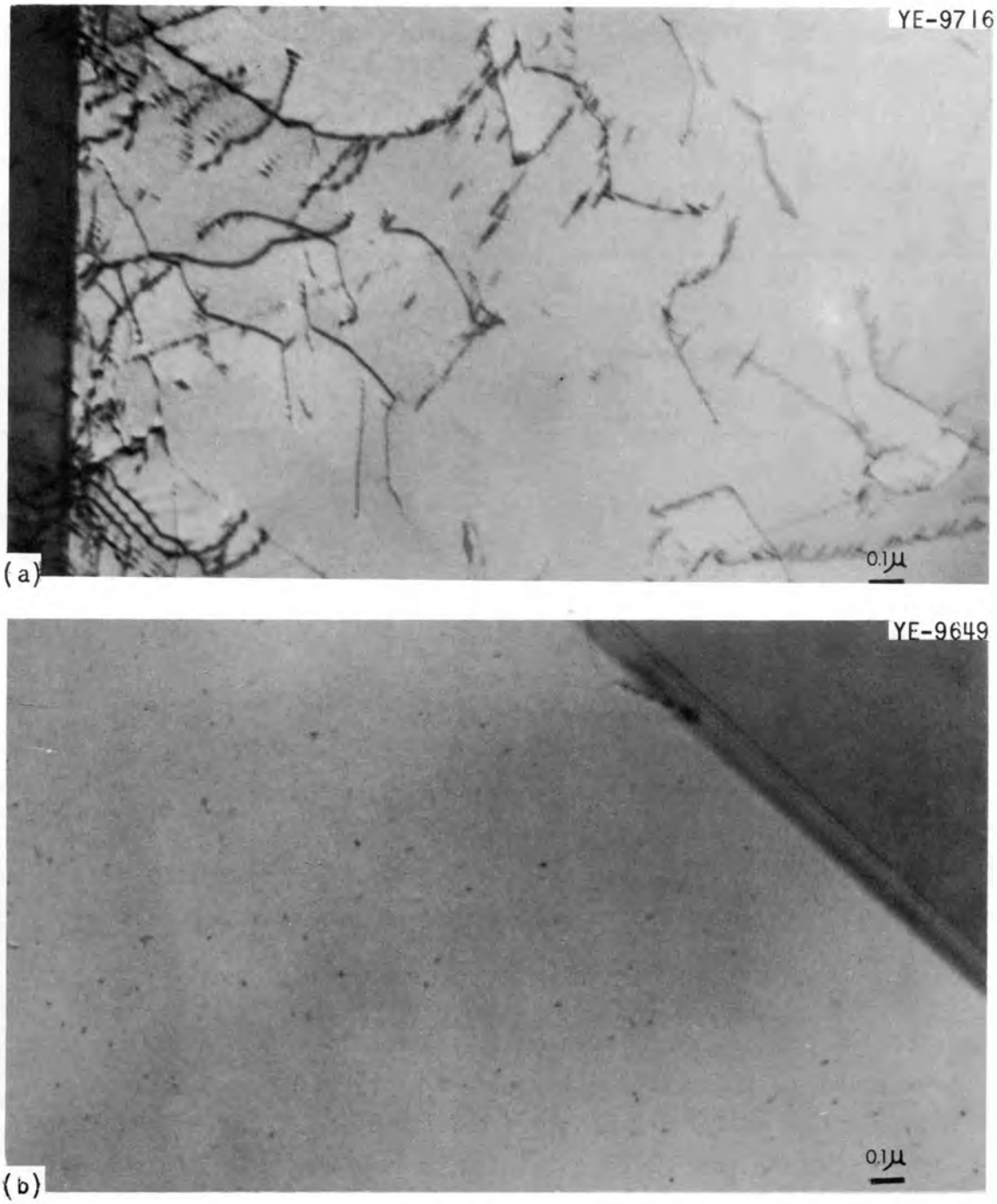

Fig. 8.16. Samples of Type 304 Stainless Steel Irradiated at the Same Approximate Temperatures but Having Different Starting Microstructures and Irradiated at Different Fluxes and Neutron Energy Spectrums. (a) Irradiated to 3×10^{20} neutrons/cm^2 (> 0.1 Mev) and 1.5×10^{19} neutrons/cm^2 (> 1 Mev) at 470°C. (b) Irradiated to 1.4×10^{20} neutrons/cm^2 (> 0.1 Mev) and 2.6×10^{19} neutrons/cm^2 (> 1 Mev) at 467°C. The neutron flux for (b) was about 200 times that for (a).

highest and lowest as seen in the stereoscopic viewer or between dirt particles on the foil surfaces. Errors in thickness introduced by a poor choice of surface reference marks could be as large as ±25%.

If foil volumes are determined this way, the density of voids in an irradiated specimen is 5.2×10^{15} voids/cm^3, a value 50% higher than that reported earlier[10] based on an assumed foil thickness. The calculated volume increase produced by the newer void density is 0.57%. The void distribution is strongly affected by the presence of grain boundaries. Voids do not occur in the boundaries themselves, and the population is reduced in a narrow strip on either side of the boundary. Outside this narrow, denuded zone is a much broader zone in which the number of voids is much increased. Still further from the boundary, the void density drops off to a value that is nearly constant throughout the remainder of the grain. The effect of the grain boundary on the distribution of voids is illustrated in Fig. 8.17. The photomicrograph shows a region containing a boundary and the two graphs show the relative number of voids in strips parallel to the boundary and in strips perpendicular to the boundary. The void density in the strips crossing the boundary shows only a statistical variation, reflecting the relatively small number of voids in each strip. The strip taken parallel to the boundary shows the denuded strip containing the boundary and the marked increase in the number of voids close to the boundary.

The thermal stability of voids in V was examined by annealing small tabs for 1 hr in vacuum between 600 and 900°C. The results are shown in Fig. 8.18. The void density is affected little by annealing to 650°C; at 750°C the void density drops by 20%; and at 900°C no voids remain. For anneals up to 800°C, the voids were distributed uniformly, but there were the grain-boundary effects discussed above. After annealing at 850°C, the distribution became patchy, often with bands of voids parallel to grain boundaries and with those voids that remained in the matrix mainly in small clusters. This is shown in Fig. 8.19. Figure 8.20 shows the effect of movement of the grain boundaries during annealing on the number of voids. The three boundaries forming the node in this figure shifted during annealing at 800°C, as interpreted in the figure caption, and swept some areas free of voids. None of the

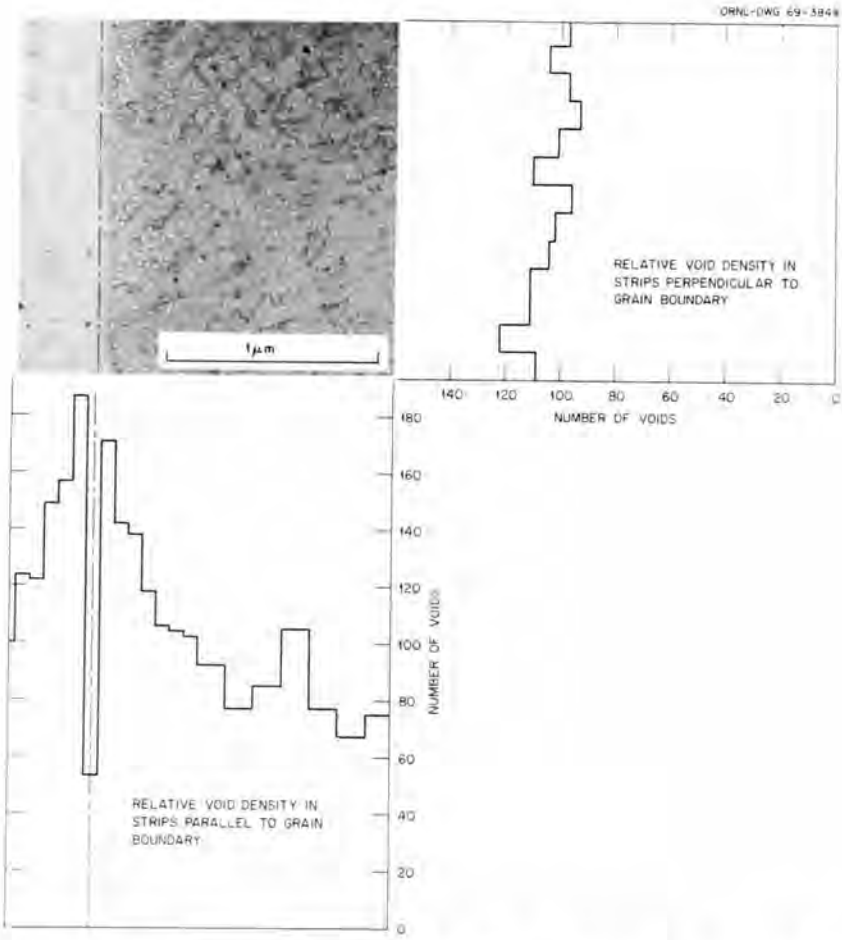

Fig. 8.17. Void Distribution in the Region of a Grain Boundary in Vanadium Irradiated in EBR-II to Approximate Total Fluence of 1.7×10^{22} neutrons/cm^2 at About 630°C.

three neighboring nodes shifted. They showed only the narrow zones denuded of voids that can be seen in Fig. 8.20 on the boundary segments that have not moved.

In a very few cases, when the resolution was better than usual, the voids were observed to project regular, crystallographic shapes. We tentatively identified this void shape as a cube formed of {100} planes with all corners truncated, possibly by {111} planes, as illustrated in Fig. 8.21(a). The only two voids seen after annealing 1 hr at 900°C are shown in Fig. 8.21(b), and the indicated crystallography is consistent with the proposed void shape.

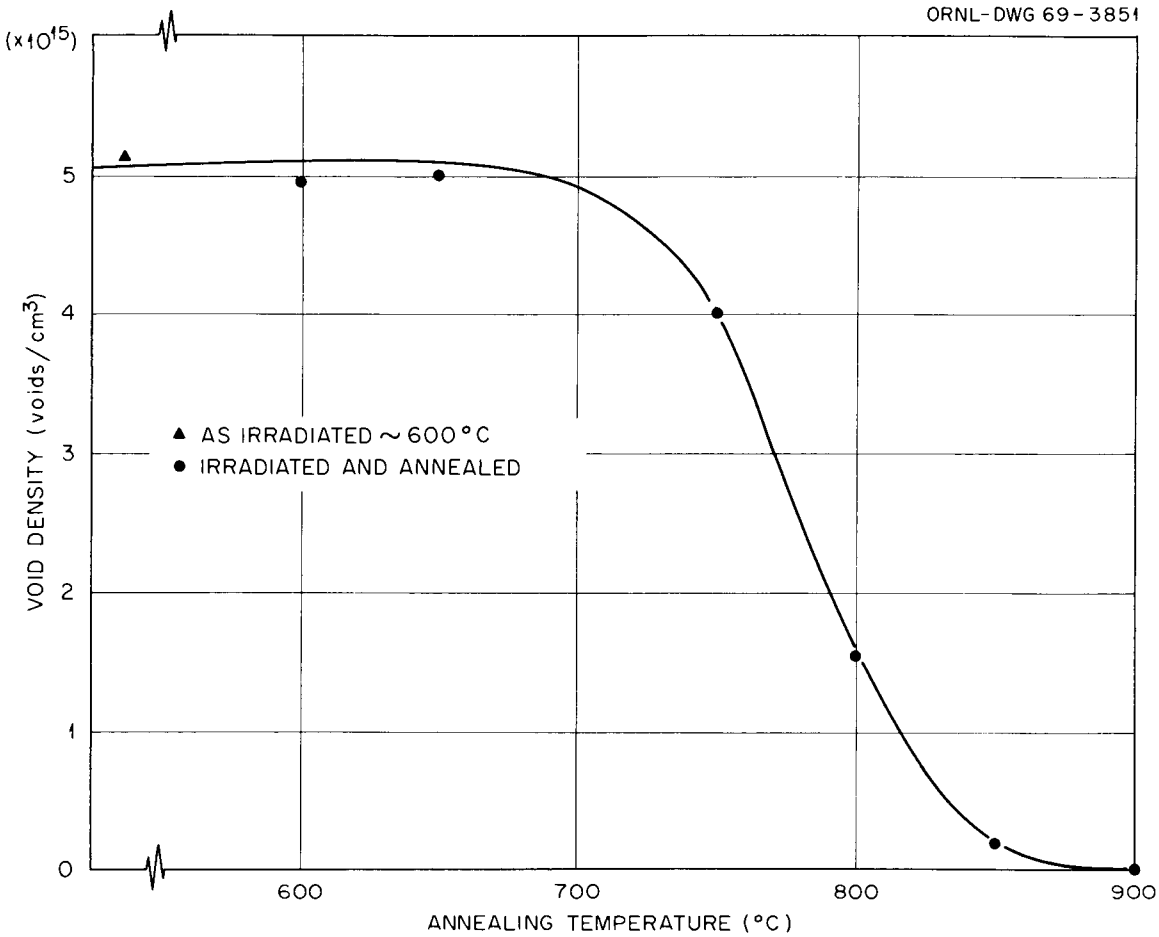

Fig. 8.18. Void Density as a Function of Postirradiation Annealing Temperature. All anneals were for 1 hr at the temperature indicated. The segments of vanadium tubing were annealed before thinning for microscopic examination.

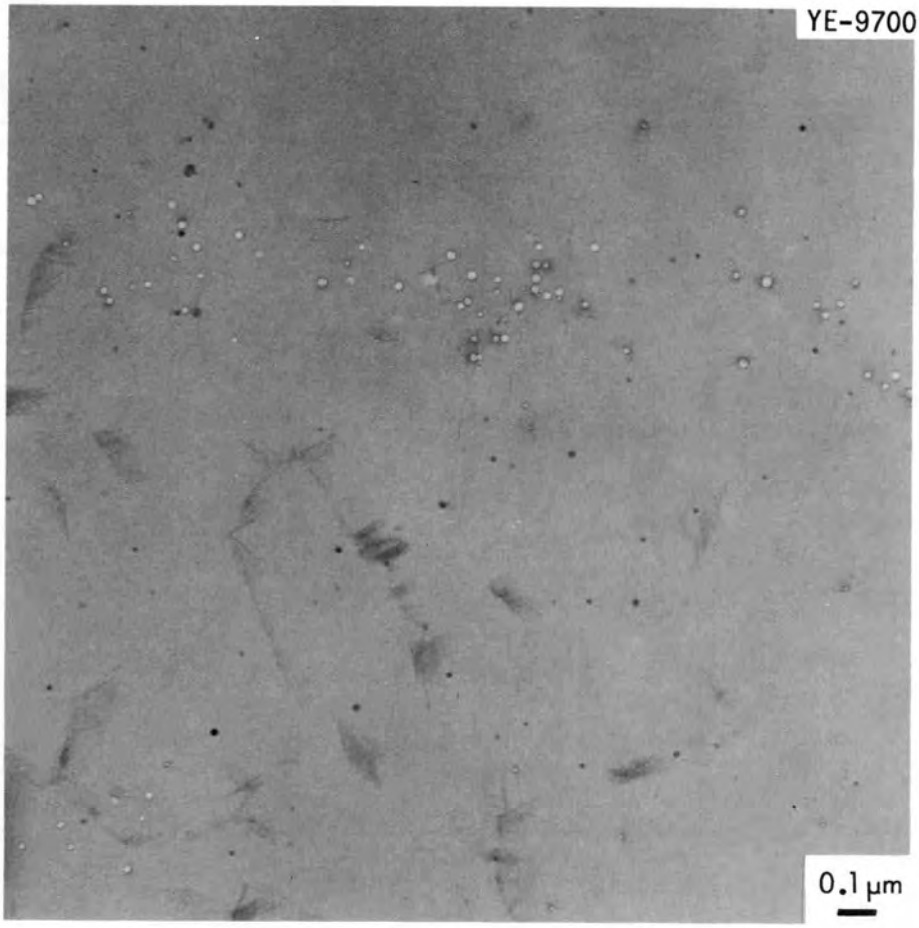

Fig. 8.19. Void Distribution in Vanadium After Postirradiation Annealing for 1 hr at 850°C.

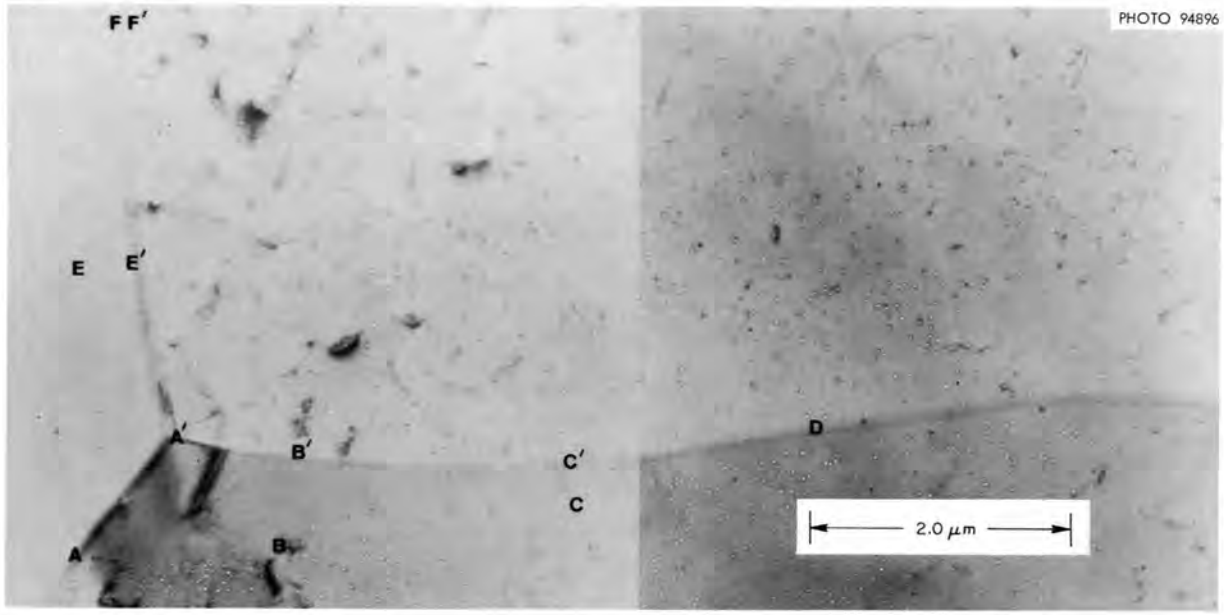

Fig. 8.20. Void Removal by Migration of the Grain Boundary During Annealing. The photomicrograph shows a triple point in vanadium that had been postirradiation annealed for 1 hr at 800°C. Before annealing, the boundaries were at ABCD and at AEF. After annealing, the boundaries moved to their present positions, indicated by the primed letters.

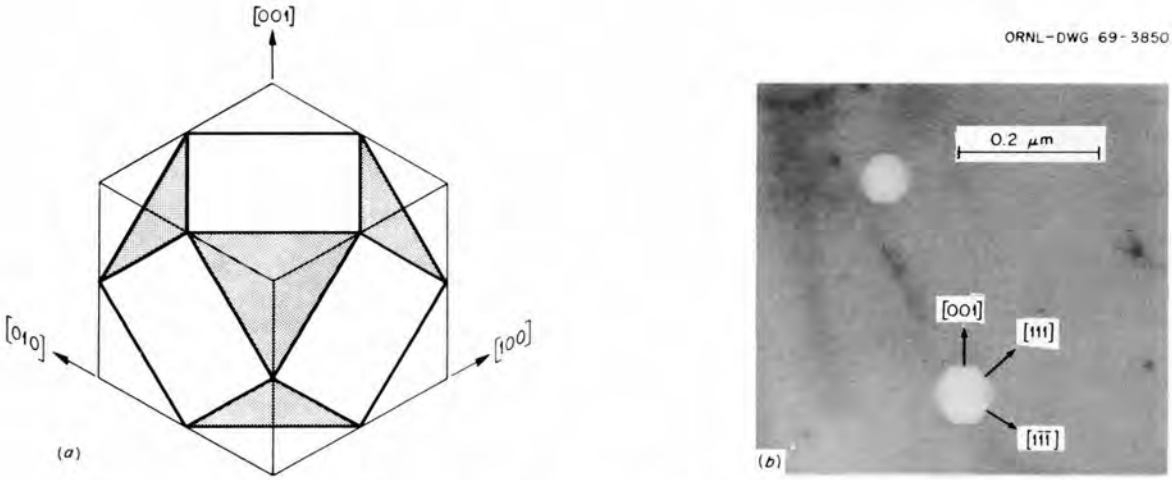

Fig. 8.21. Possible Crystallography of Voids in Irradiated Vanadium. The truncated cube shown in (a) would project as a square when viewed along ⟨100⟩ and as a hexagon when viewed along ⟨110⟩ or ⟨111⟩, consistent with the void shapes observed in a few cases. (b) The shape observed in a foil viewed along ⟨110⟩ directions. These voids were remnant from a 900°C anneal and are much larger than any voids observed for any other conditions.

Mechanical Properties of Hastelloy N and Related Compositions

Aging of Titanium-Modified Hastelloy N (C. E. Sessions, C. S. Lever)

Since we are dealing in this program with a large number of controllable variables such as alloy composition, annealing treatment, aging time, and aging temperature,[11,12] we designed the experiment so that the aging response could be assessed by standard statistical techniques. Although all the data are not yet available, we shall outline the procedure used in analyzing the significance of the results to date and shall point out problems that have been encountered in analyses of this type.

Analysis of Variance. — The aging experiments were designed as a full factorial experiment with four levels of Ti, three preaging treatments, four aging times, and two aging temperatures. With this experimental design, it is possible to assess the importance of the interaction between factors as well as the main effects.

A table for an analysis of variance was computed for each of the measures of the tensile properties. Analysis of variance is a technique for estimating how much of the total variation in a set of data can be attributable to one or more assignable causes of variation. The remainder of the variation is classed as error variation. A test of significance, the F test, is used to decide whether the assignable causes have probably resulted in real variation or are merely a result of the causes producing the error variation.

In a factorial experiment, the assignable causes are the main effects, the second-order interactions, and higher order interactions. A main effect is simply the effect of one factor considered independently of the others. A second-order interaction between two factors, A and B, is

---

[11] C. E. Sessions, H. E. McCoy, Jr., and R. E. Gehlbach, Fuels and Materials Development Program Quart. Progr. Rept. Sept. 30, 1968, ORNL-4350, pp. 163–173.

[12] C. E. Sessions, Fuels and Materials Development Program Quart. Progr. Rept. Dec. 31, 1968, ORNL-4390, pp. 144–147.

a measure of the difference between the effects of changing from a low to a high level of A with B at a low level and with B at a high level. For example, the difference in elongation between an alloy with 0.15% Ti and one with 0.5% Ti may be larger if the alloys are aged at 650°C than if they are aged at 760°C. If the second-order interaction is significant, then the effect of factor A is dependent on the level of B, and in any discussion of the effect of one factor it is necessary to specify the level of the other. The higher order interactions may be interpreted similarly but are not generally as easy to understand.

Since there was only one replication of this design, there were no degrees of freedom left for estimating the error. The fourth-order interaction was used as an estimate of the error, and the mean squares of the other effects were tested against it. In factorial experiments, the third-order interactions are frequently negligible and may be combined with the fourth-order interaction to give many more degrees of freedom for estimating the error. Unfortunately, every measure of the tensile behavior except the ultimate tensile strength has at least one significant third-order interaction. This means that in assessing the importance of one factor it is necessary to specify the level of at least two other factors.

At first, we considered all the tensile property changes for aging times up to 3000 hr and calculated a table for analysis of variance. A plot of the resulting interactions made it clear that the primary cause of third- and higher order interactions was the unusual aging response found for alloys annealed at 1260°C as compared to the other pretest treatments included in this study. An example of the different aging response for the 1260°C treatment is given in Fig. 8.22. Here we plot the second-order interaction of pretest treatment and Ti concentration on the total elongation in our 650°C tensile test. The totally different trend of the 1260°C data is clear and gives rise to the troublesome interactions. Possible reasons for this behavior are discussed below. We concluded that meaningful analysis would require omitting the 1260°C data as far as the analysis of variance was concerned.

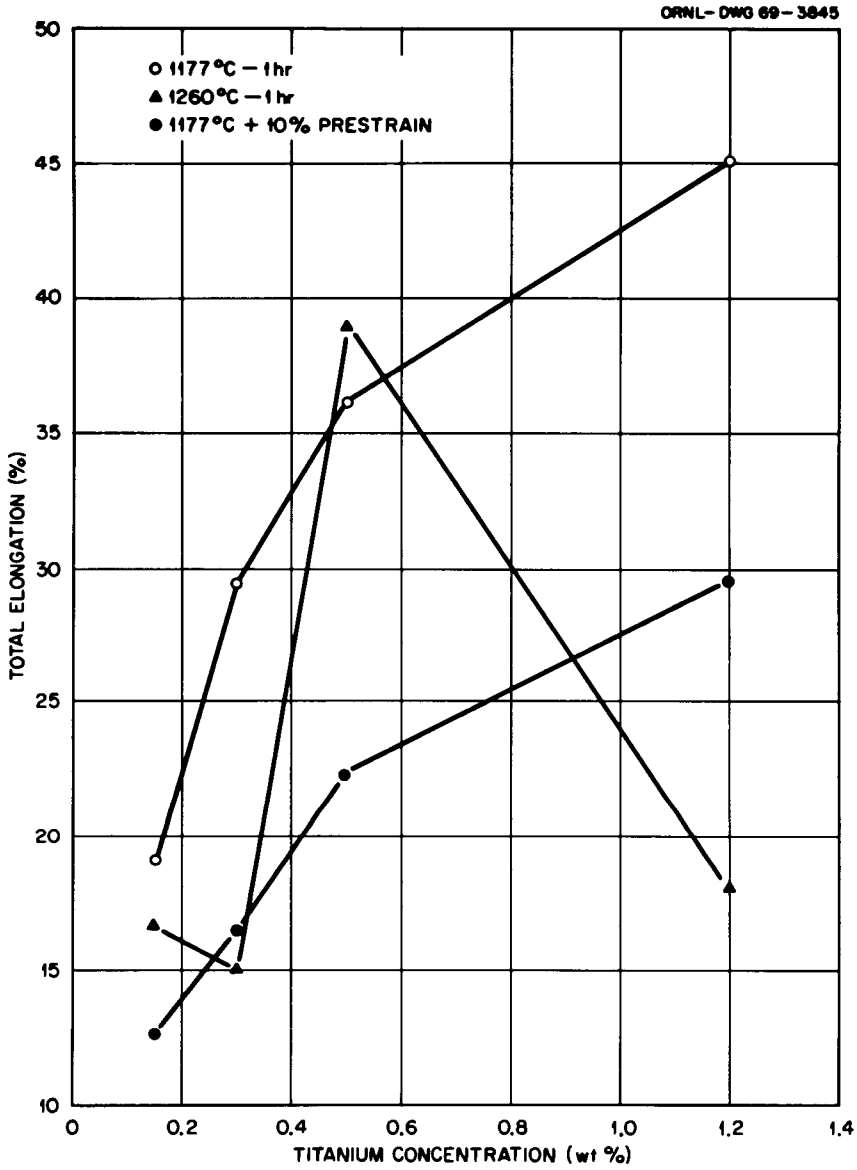

Fig. 8.22. Second-Order Interaction on Tensile Elongation.

The table for analysis of variance was computed again, including pretest treatments 1 hr at 1177°C and 1 hr at 1177°C plus 10% prestrain but omitting the data for 1 hr at 1260°C. This analysis showed that the significant main effects on the tensile behavior corresponded to those we know to be important metallurgically: composition, aging time, and aging temperature. By omitting the 1260°C data, we eliminate the third-order interactions and thus can look in detail at the significance of the second-order interactions. Table 8.3 gives the results of each possible second-order interaction on the tensile properties.

Table 8.3. Significant Second-Order Interactions at the 95% Confidence Level

Interaction[a]	Strength		Elongation		Reduction in Area
	Yield	Ultimate	Uniform	Total	
AB	yes[b]	yes	no[c]	no	no
AC	no	yes	yes	yes	no
AD	no	yes	yes	yes	yes
BC	no	no	no	no	yes
BD	yes	no	no	no	yes
CD	no	yes	yes	yes	no

[a]A = alloy composition

B = preage treatment

C = aging time

D = aging temperature

[b]Indicates that the preaging treatments affect the yield strengths differently at the various levels.

[c]Indicates that the preaging treatment and level of Ti act independently in affecting uniform elongation.

The results of this analysis indicate that the preage treatment at 1177°C plus 10% prestrain leads to higher strengths, while the pretest treatment at 1177°C leads to greater elongations. Since the elongations

are considered more important, the treatment at 1177°C is preferable to the treatment at 1177°C plus 10% prestrain. The alloy with 1.2% Ti gave the largest responses for all times and temperatures for every measurement of tensile behavior except uniform elongation. This was higher for the alloy with 0.5% Ti for some times and temperatures.

This analysis is valid only for aging behavior to 3000 hr, and the results of the 10,000 hr test could modify our concept of the importance of the variables involved. The main point, however, is that the aging response after the 1260°C treatment indicates that something different and important occurs in some alloys as a result of this preage treatment.

Influence of 1260°C Solution Annealing. – Samples of each alloy in this study showed much greater aging tendencies (i.e., lower ductility) after annealing at 1260°C than did those annealed at 1177°C before aging. Figure 8.23 compares the microstructures of the various heats after solution annealing. The samples annealed at 1260°C have grains two to three times larger than those of the samples annealed at 1177°C; thus, a detrimental distribution of carbide at the grain boundary could affect the ductility to a greater extent in this material with large grain size. In addition, however, the different aging responses could reflect different amounts and phases in solid solution before aging, and we shall evaluate this possibility in future experiments.

Electron Microscopy of Hastelloy N (R. E. Gehlbach, S. W. Cook)

We reported that carbide precipitation in Hastelloy N is sensitive to the chemical composition.[13] In the air-melted heats of the standard alloy, containing 0.4 to 0.6% Si, only M_6C-type precipitates form. They are enriched in Si and are stabilized by the presence of this element. Reduction of the Si to trace levels, as is possible by vacuum melting, results in precipitates of the M_2C type after exposure to intermediate aging temperatures. This M_2C can readily be put into solid solution at temperatures normal for solution annealing, whereas the M_6C type cannot easily be dissolved.

[13]C. E. Sessions, H. E. McCoy, Jr., and R. E. Gehlbach, Fuels and Materials Development Program Quart. Progr. Rept. Sept. 30, 1968, ORNL-4350, pp. 163–173.

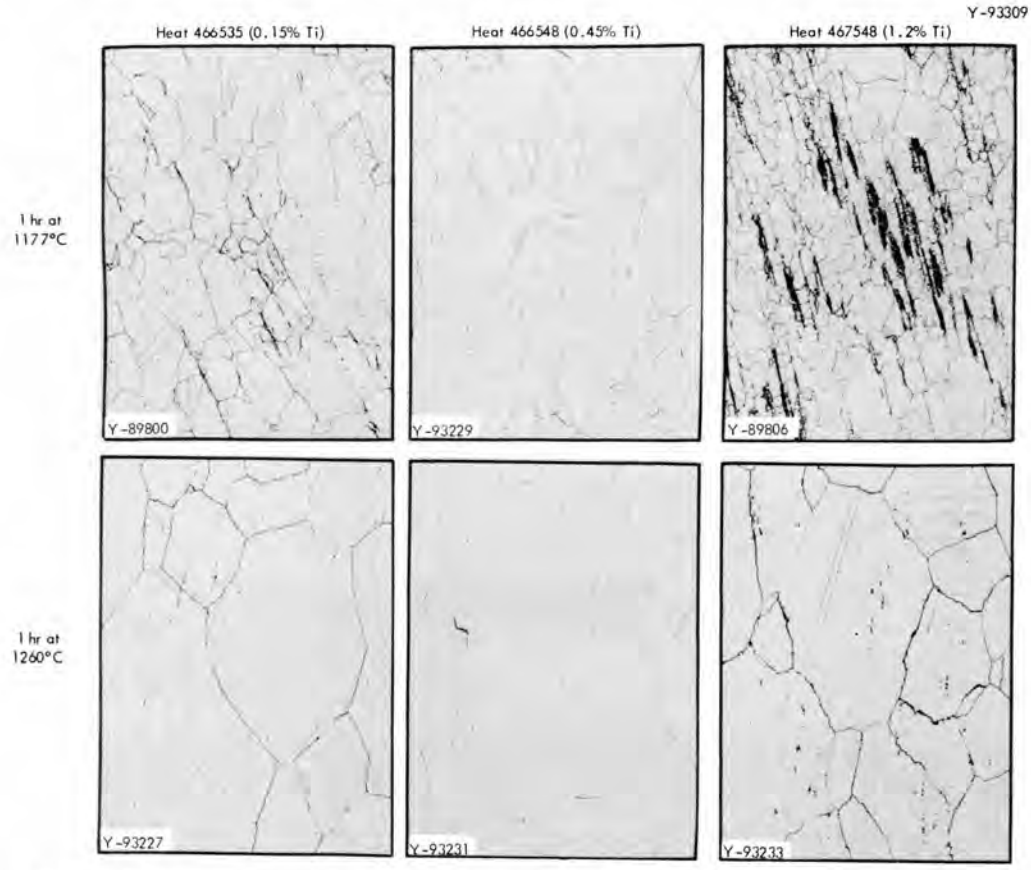

Fig. 8.23. Comparison of Structures of Alloys in Aging Study After Various Solution Anneals.

Precipitation in the modified (12% Mo) versions of the alloy is sensitive to alloying additions of Ti, Nb, Zr, and Hf (ref. 14), and when these elements are present the precipitation processes depend on temperature. Mechanical properties, particularly after irradiation, are also affected by composition and temperature.[15] We are concentrating our studies on understanding the role of these alloying additions on the types and morphologies of precipitates and evaluating the effects they have in controlling the mechanical behavior of the material after irradiation. We are studying those precipitates that result from aging at 650 and 760°C.

---

[14]Hereafter the alloying elements Ti, Zr, Nb, and Hf will be referred to as the Ti-group elements.

[15]H. E. McCoy, Jr., Fuels and Materials Development Program Quart. Progr. Rept. Dec. 31, 1968, ORNL-4390, pp. 140–144.

Since the level of Si is low, the M_6C formed in the standard material is not formed in these modified alloys. In the modified alloys without additions of the Ti-group elements, only M_2C precipitates at aging temperatures of 650 and 760°C. Additions of the Ti-group elements promote the formation and stability of carbides of the MC type that have face-centered cubic structures with lattice parameters from 4.21 to 4.68 A. Higher concentrations of the Ti-group elements are required to stabilize the MC types at 760°C than at 650°C. These trends are shown in Table 8.4.

Table 8.4. Phases Present in Various Alloys of the Hastelloy N Type After Aging (> 1000 hr) at the Indicated Temperature

Alloy	Phases Present After Aging at Temperature (°C)	
	650	760
Standard Hastelloy N (0.5% Si)	M_6C	M_6C
Standard Hastelloy N (< 0.1% Si)	M_2C	M_2C
198 (12% Mo)	M_2C	
66-535 (12% Mo–0.12% Ti)	MC + M_2C	M_2C
196 (12% Mo–0.5% Ti)	MC + $(M_2C)^a$	
66-548 (12% Mo–0.45% Ti)	MC	$(MC)^a$ + M_2C
107 (12% Mo–1.0% Ti)	MC	
67-548 (12% Mo–1.2% Ti)		MC
112 (12% Mo–1.0% Zr)	MC	
181 (12% Mo–0.5% Ti–2% Nb–0.2% Si)	MC	MC
184 (12% Mo–1% Ti–1% Hf)		MC

[a]Phase present in minor amount.

The various carbides have been identified by several techniques. The types and relative amounts of carbides present in a specimen were determined by dissolving the matrix and analyzing the remaining precipitates by x-ray diffraction. Electron diffraction and electron microscope-microprobe analysis of selected areas were used to relate the crystal

structure, morphology, and composition of individual precipitates on extraction replicas. The distribution of precipitates was observed by electron microscopy of thinned bulk specimens and extraction replicas. The M_2C carbides have the Mo_2C structure but contain about 10 to 20% Cr; thus, they would be more appropriately designated $(Mo,Cr)_2C$. The compositions of the MC types depend on the amount of the particular elements from the Ti group contained in the material. At low Ti concentration, (Mo,Cr)C is formed. Increasing the concentration of Ti in the alloy results in the substitution of some Ti for Cr in the carbides and an increase in lattice parameter. Adding Nb, Hf, or Zr promotes the stability of the carbides of that group (e.g., HfC). In general, the MC carbides are finer than the M_2C type, and their distribution in the bulk material would appear to result in superior mechanical properties after irradiation than would that of the M_2C precipitate.

The distribution of MC, or (Mo,Cr)C, in heat 66-548 (a commercial alloy with 0.45% Ti) after aging at 650°C was reported previously.[16] There is particular importance in the fact that many fine precipitates lie adjacent to the grain boundaries and extend into the matrix. In contrast, aging this material at 760°C produces larger precipitates in both the matrix and grain boundaries. Some precipitate also exists as very thin (probably < 100 A) continuous films covering extensive areas in the grain boundaries. These thin films and the He bubbles noted in this material after irradiation[17] would be expected to result in poor mechanical properties after irradiation.

The distributions of precipitates formed during irradiation and during aging (without irradiation) at similar temperatures are different. Figure 8.24 is a transmission electron photomicrograph of an unstressed specimen irradiated for 1128 hr at 635°C in the ORR. Although a considerable amount of precipitate is present in the grain boundaries,

---

[16]C. E. Sessions, H. E. McCoy, Jr., and R. E. Gehlbach, Fuels and Materials Development Program Quart. Progr. Rept. Sept. 30, 1968, ORNL-4350, pp. 163–173.

[17]R. E. Gehlbach, MSR Semiann. Progr. Rept. Aug. 31, 1968, ORNL-4344, pp. 247–250.

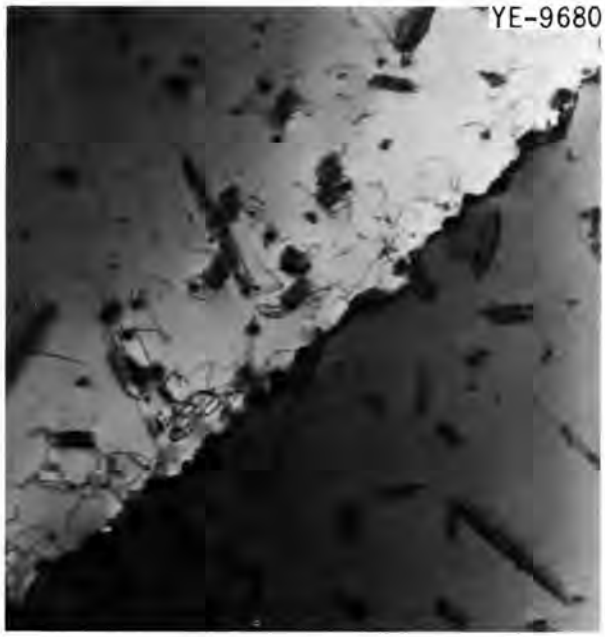

Fig. 8.24. Distribution of Precipitates in Hastelloy N (Heat 66-548, 0.45% Ti) After Irradiation for 1128 hr at 635°C. 10,000×.

the distribution is considerably different from that obtained by aging at 650°C without irradiation. There were essentially no precipitates in a specimen irradiated for 1128 hr at 703°C, but there were many bubbles on the grain boundaries and this material fractured with essentially no strain.[17] Bubbles were observed at grain boundaries in the material after irradiation at 635°C, but the irregular precipitates in the grain boundaries probably strengthen the boundaries and prevent the propagation of cracks at the grain boundaries.

It would appear that a structure similar to that shown in Fig. 8.24 would result in good properties after irradiation. The fine precipitates along grain boundaries seem characteristic of the carbides of the MC type. As shown in Table 8.4, increasing the amounts of the Ti-group elements promotes the stability of these carbides. The alloys with the higher concentrations of these elements (heats 181, 184, and 67-548) have excellent properties after irradiation at 760°C (ref. 18). Although

[18]H. E. McCoy, Jr., Fuels and Materials Development Program Quart. Progr. Rept. Dec. 31, 1968, ORNL-4390, pp. 140–144.

we have not examined the phases in these alloys after irradiation, it appears likely that the MC carbides are present and occur in a favorable distribution.

Figure 8.25 shows the morphologies of precipitates extracted from unstrained portions of samples aged 3000 hr at 760°C. The tensile ductility values at 650°C (total elongation) corresponding to these three samples were 14, 21, and 15%, respectively; these are significantly below the values for the annealed samples.[19] Thus, although we get a transition from the M_2C to the MC phases with increasing Ti concentration, each alloy loses ductility with aging. The influence of these phases and morphologies on the resistance to irradiation damage has not been specifically investigated.

---

[19]C. E. Sessions, Fuels and Materials Development Program Quart. Progr. Rept. Dec. 31, 1968, ORNL-4390, pp. 144–147.

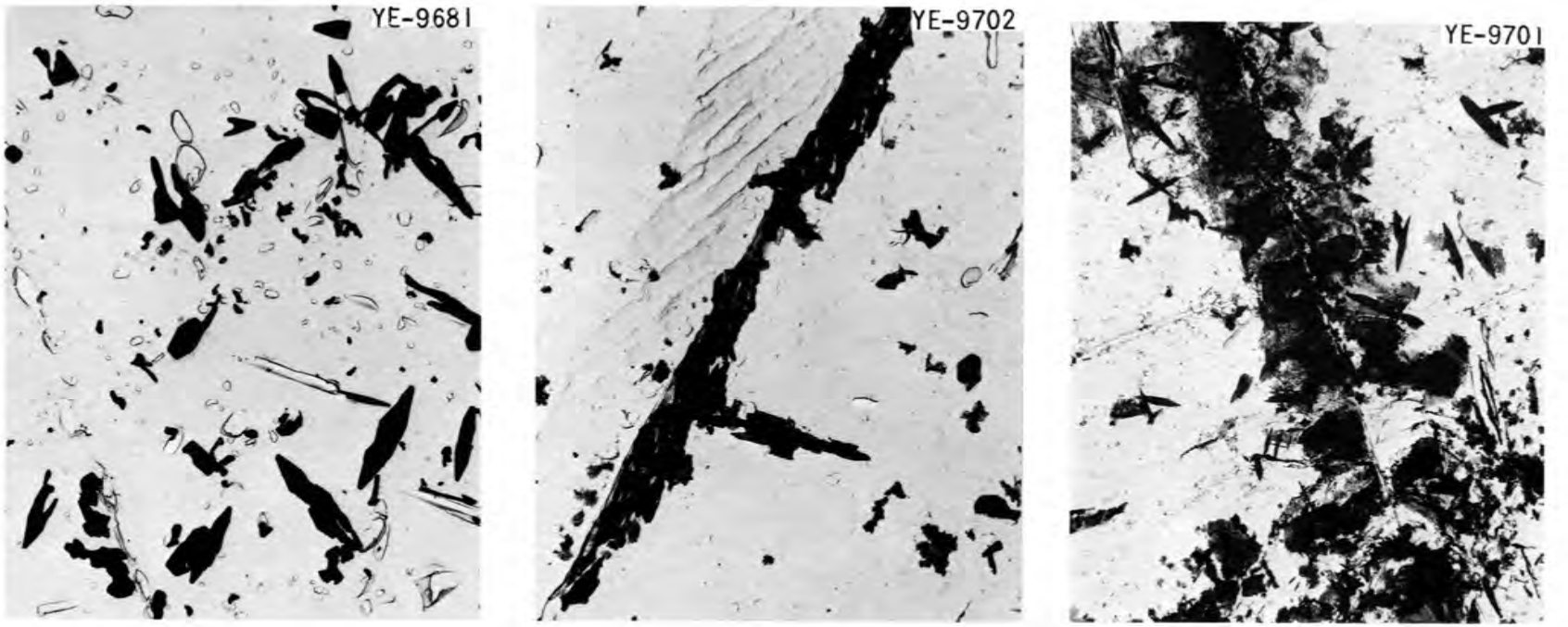

0.15% Ti
M_2C

0.45% Ti
M_2C + MC

1.2% Ti
MC

Fig. 8.25. Comparison of Precipitate Type and Morphologies for Titanium-Modified Alloys Aged 3000 hr at 760°C. 5000×.

9. RADIATION EFFECTS IN ALLOYS AND STRUCTURAL MATERIALS

M. S. Wechsler

This program is being phased out during fiscal year 1969. All progress before termination of the program in fiscal year 1970 will be documented in separate topical reports.

PART IV

TECHNIQUES OF FABRICATION AND TESTING

10. TUNGSTEN METALLURGY

P. Patriarca A. C. Schaffhauser

The object of this program is to develop economical methods for producing high-quality W and W-alloy tubing with good creep-rupture properties at high temperatures, good microstructural stability, good ductility at low temperatures, and good weldability. We fabricate tubing both by modification of conventional techniques based on extrusion, tube reduction, and warm drawing and by direct chemical vapor deposition (CVD) through the H_2 reduction of heavy-metal halides. Our program includes complete physical and metallurgical evaluation of both fabrication processes.

Primary and Secondary Working of Tungsten and Tungsten Alloys

W. R. Martin

Extrusion of Tungsten and Tungsten Alloys (R. E. McDonald)

Metallographic examination of the four duplex billets of powder-metallurgy W, described previously,[1] was completed. Figures 10.1 and 10.2 show the structure of that part of the primary extrusion that was used in the duplex extrusion, the changes that occur during the preheat period, and the final structure that results from duplex extrusion at the indicated temperatures. In this experiment the extrusion ratio, lubrication, and extrusion speed were held constant.

The microstructure of that part of the primary extrusion that was used for the 1750°C duplex extrusion was recrystallized with a grain size of ASTM 7. The preheat did not affect this structure, but the structure of the final duplex extrusion shows some coarsening of the grain size.

For the duplex extrusion at 1650°C, we used a part of the primary extrusion that had a wrought structure with elongated grains that were

[1]R. E. McDonald, Fuels and Materials Development Program Quart. Progr. Rept. Sept. 30, 1968, ORNL-4350, p. 229.

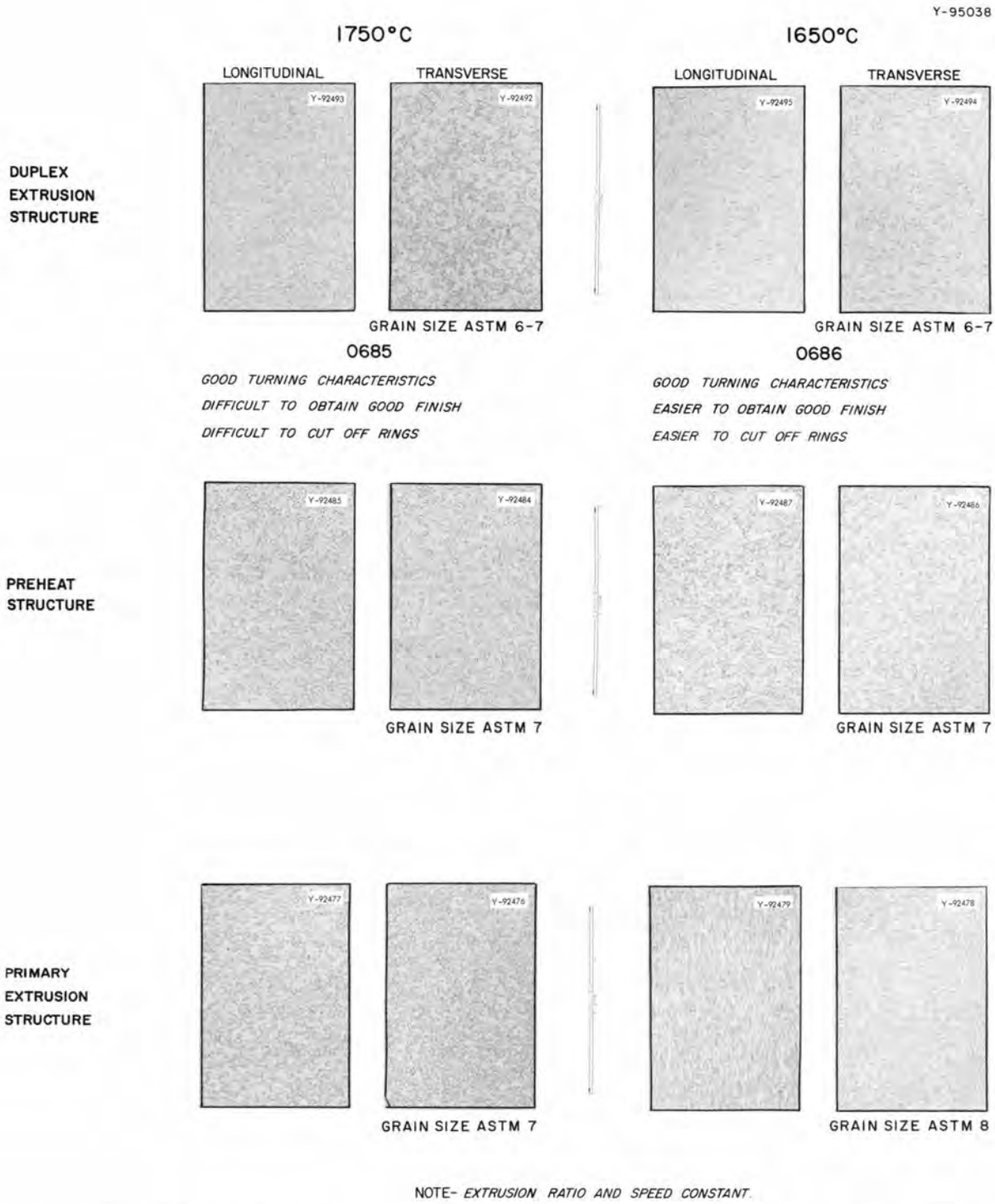

Fig. 10.1. Microstructures of the Starting Primary Extrusion of Powder-Metallurgy Tungsten After Preheating to 1650 and 1750°C and After Duplex Extrusion.

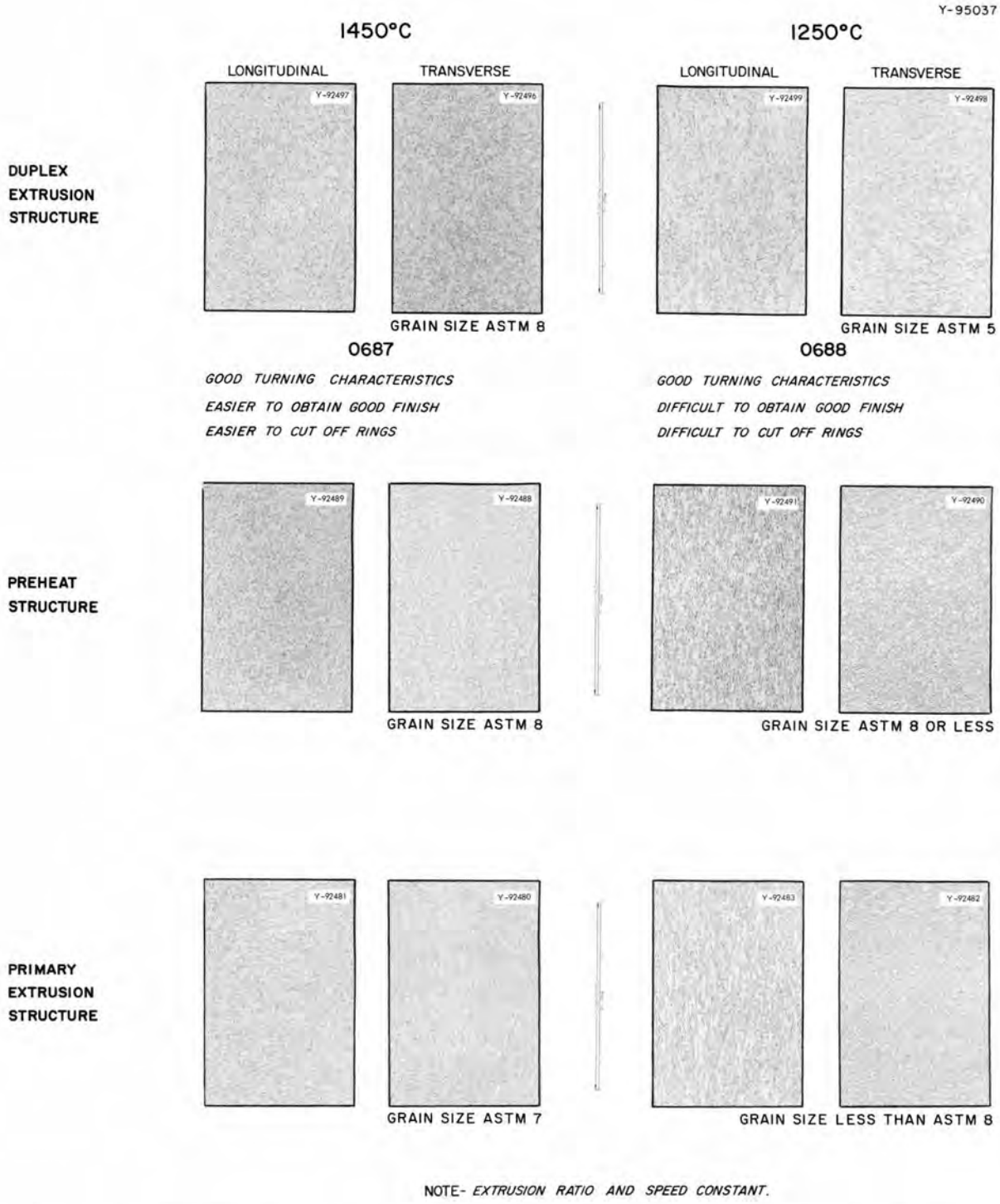

Fig. 10.2. Microstructures of the Starting Primary Extrusion of Powder-Metallurgy Tungsten After Preheating to 1450 and 1250°C and After Duplex Extrusion.

about ASTM 8 in size. The preheat resulted in a recrystallized grain size of ASTM 7, and the structure of the final duplex extrusion coarsened further to between ASTM 6 and 7.

For the duplex extrusion at 1450°C, the primary structure was similar to that of the starting billet for the extrusion at 1750°C, but virtually no change was noted during the preheat period at this lower temperature. The structure of the final duplex extrusion also showed no change.

The microstructure of the billet used for the duplex extrusion at 1250°C was wrought, like the starting billet for the 1650°C extrusion, but at this low temperature there was very little change during the preheat period. The structure of the final duplex extrusion shows considerable change, with the breaking up of most of the elongated grains and partial recrystallization.

The high rates of deformation during the extrusion process cause increases in temperature and possible changes in structure. Based on some forging tests at 1500°C, using a two-color pyrometer, we noted an increase of 150°C at a reduction ratio of three.

Four other duplex billets of powder-metallurgy W were fabricated and extruded. Three billets with wrought starting structures were extruded at 1760, 1450, and 1150°C. An additional billet with a recrystallized starting structure was extruded at 1150°C. Preliminary metallographic examination indicates that the billet extruded at 1760°C recrystallized during preheat and that grain growth occurred during extrusion. The additional heat produced by deformation could have increased the billet temperature to 1900°C. The billet extruded at 1450°C also recrystallized during preheat, but no further change was noted in the extruded structure. The wrought structure did not change during the preheat at 1150°C, but partial recrystallization occurred during extrusion. The recrystallized structure was stable during the preheat at 1150°C, and the extruded structure shows many elongated grains.

In summary, at extrusion temperatures of 1450°C and higher, wrought structures recrystallize during preheat while recrystallized structures

are stable for the short preheat times. The wrought structure and the recrystallized structure are both stable during preheat at 1150°C, but the increase of 150 to 200°C during the extrusion process is enough to recrystallize the starting wrought structure.

Installation of Experimental Tube Reducer (R. E. McDonald)

The Aetna-Standard tube reducer was installed, and its operation was checked by an engineer from Aetna-Standard. We used it to tube reduce Cu tube shells by two methods, one designated "wedges in," in which the tube shell is worked on both the forward and reverse stroke, and the other designated "wedges automatic," in which the tube shell is worked only on the forward stroke.

Several Cu, brass, and stainless steel tube shells were tube reduced from 2 in. in outside diameter by 0.250 in. in wall thickness to 1 in. in outside diameter by 0.100 in. in wall thickness — a 79.5% reduction in area. In reducing the stainless steel, the machine operated at 25 strokes/min with a feed of 0.250 in./stroke and an 89° turn/stroke. Figure 10.3 shows sections cut from the tail end of tube-reduced Cu and stainless steel tube shells.

Chemical Vapor Deposition of Tungsten Alloys

W. R. Martin

Deposition of Tungsten-Rhenium Alloys (J. I. Federer)

Deposition of W–5% Re alloy sheet material continued. A number of techniques were used in attempts to overcome gas depletion and related nonuniformity of thickness: increased flow rates, smaller substrates, Ar diluent, lower ratio of H_2:WF_6 + ReF_6, and baffles in the reaction chamber.[2] None of these techniques altered the usual thickness profile; that is, the deposit was always thicker near the gas inlet than near the

[2]J. I. Federer, Fuels and Materials Development Program Quart. Progr. Rept. Dec. 31, 1968, ORNL-4390, pp. 162–165.

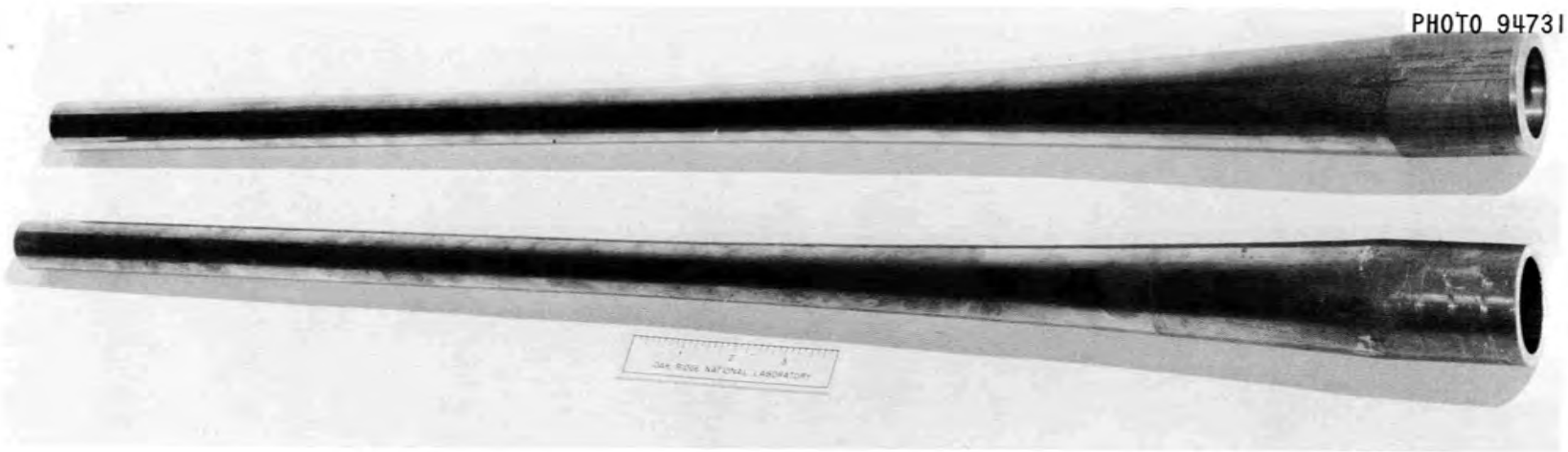

Fig. 10.3. Tube-Reduced Tube Shells Showing Starting and Finished Sizes. Lower tube is copper and upper tube is stainless steel.

outlet. However, pressures between 10 and 200 torr greatly affect the thickness profile of W–5% Re deposits. Figure 10.4 shows the thickness as a function of length for deposits prepared under conditions that were similar except for pressure and ratio of H_2:WF_6 + ReF_6. An increase in pressure from 10 to 100 torr caused the thickness profile to shift from greater thickness near the gas inlet to greater thickness near the gas outlet for H_2:WF_6 + ReF_6 ratios of 7.5 and 15.0. The most uniform deposits were obtained at 50 and 75 torr; the optimum pressure for uniformity of thickness is probably between these limits.

The efficiency of the reduction reaction, obtained by comparing the weight of the deposit with the metal content of the metered fluorides, is also a function of pressure, as shown in Fig. 10.5. The lowest efficiencies for H_2:WF_6 + ReF_6 ratios of 7.5 and 15.0 occur near 75 and 50 torr, respectively. Since the greatest uniformity of thickness occurs near these pressures, uniformity of thickness must require operating under conditions of low efficiency, a situation we also found to be true for sheet deposits of unalloyed W. Low efficiencies are undesirable for W-Re deposits because of the high cost of Re compared to that of W; therefore, the highest efficiency consistent with deposit quality is preferred. If low efficiencies are necessary for thickness uniformity, provisions for recycle of unreacted ReF_6 may be required.

The following additional observations were made:

1. A black powder, identified by x-ray diffraction as W, deposited on cold surfaces inside the reaction chamber at a H_2:WF_6 + ReF_6 ratio of 7.5. Such powder occasionally blocks gas transfer lines and causes termination of the experiment. Increasing the H_2:WF_6 + ReF_6 ratio to 15.0 eliminated the powder deposit and increased the deposition efficiency.

2. The surface texture of the deposits became more nodular with increasing pressure.

3. The microstructure of deposits prepared at 50 torr consisted of broken columnar grains and growth cones (Fig. 10.6), while the microstructure of deposits prepared at 100 and 200 torr consisted of broken

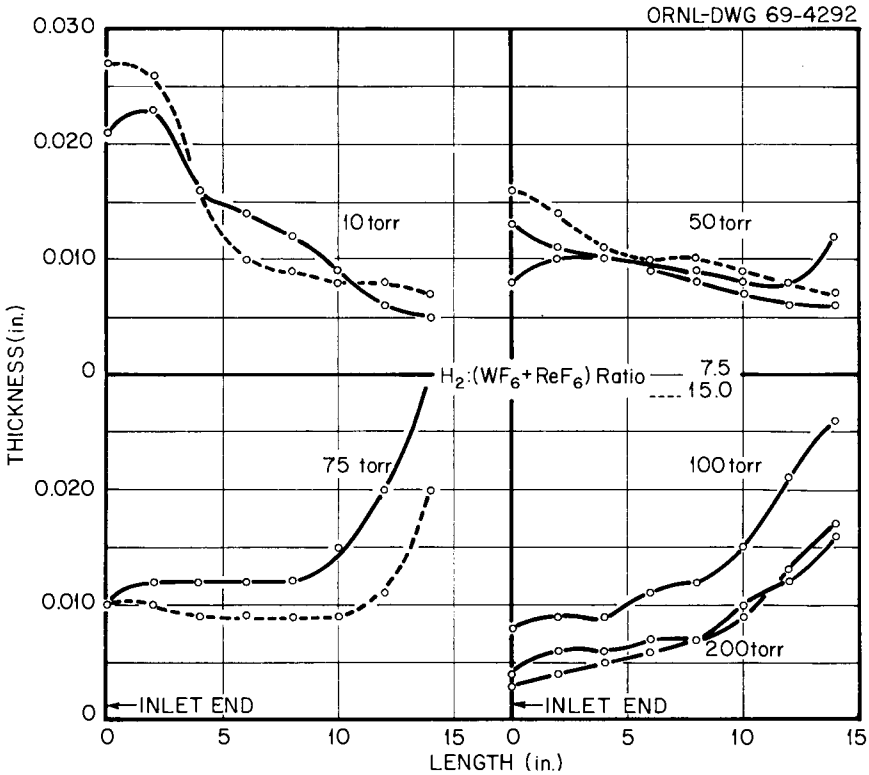

Fig. 10.4. Thickness of Nominal W–5% Re Deposits as a Function of Length.

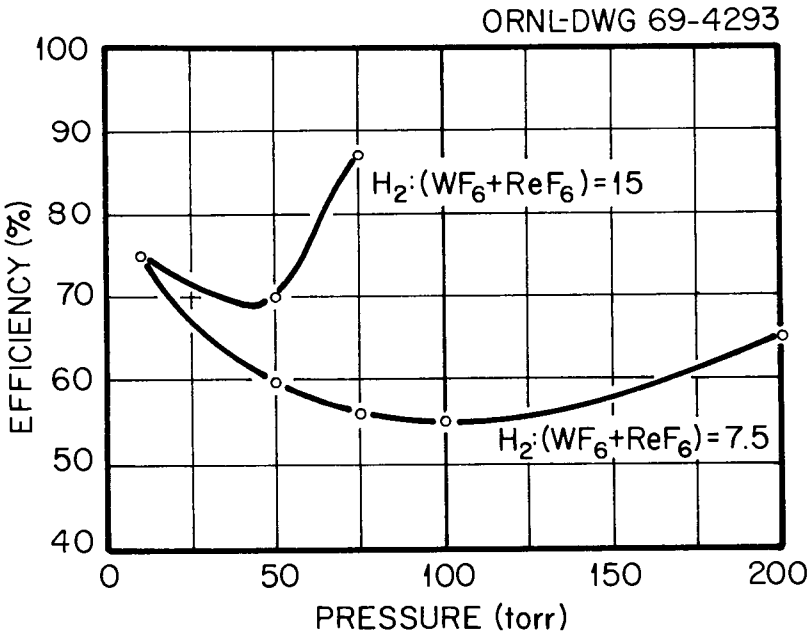

Fig. 10.5. Deposition Efficiency as a Function of Pressure.

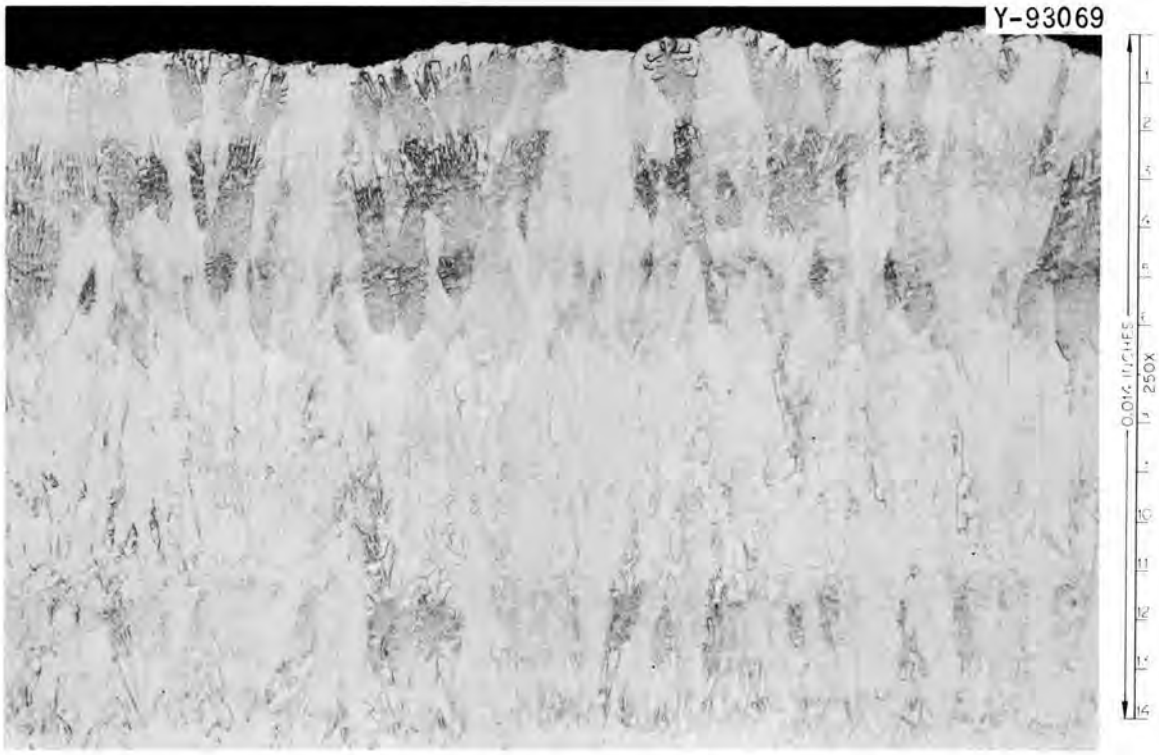

Fig. 10.6. Microstructure of W–5% Re Alloy Deposited at 50 torr. Etchant: 1 part NH_4OH (reagent grade) and 1 part H_2O_2 (30%).

columnar grains only (Fig. 10.7). The relative roughness of the surfaces deposited last, shown in Figs. 10.6 and 10.7, was typical of deposits prepared at these pressures.

Effect of Hydrogen Fluoride on Deposit Morphology

Additional experiments were conducted at constant temperature and pressure to determine whether HF causes nodular growths in W. Up to 25 vol % HF was added to the reacting gases while the amounts of H_2 and WF_6 were held constant. In order to obtain higher HF contents the amounts of H_2 and WF_6 had to be decreased in two experiments due to a limited capacity for metering HF. The conditions and efficiencies obtained in these experiments are shown in Table 10.1.

Previous results indicated,[3] contrary to expectation, that the efficiency of deposition increased with increasing HF content of the

[3]J. I. Federer, Fuels and Materials Development Program Quart. Progr. Rept. Dec. 31, 1968, ORNL-4390, pp. 165–167.

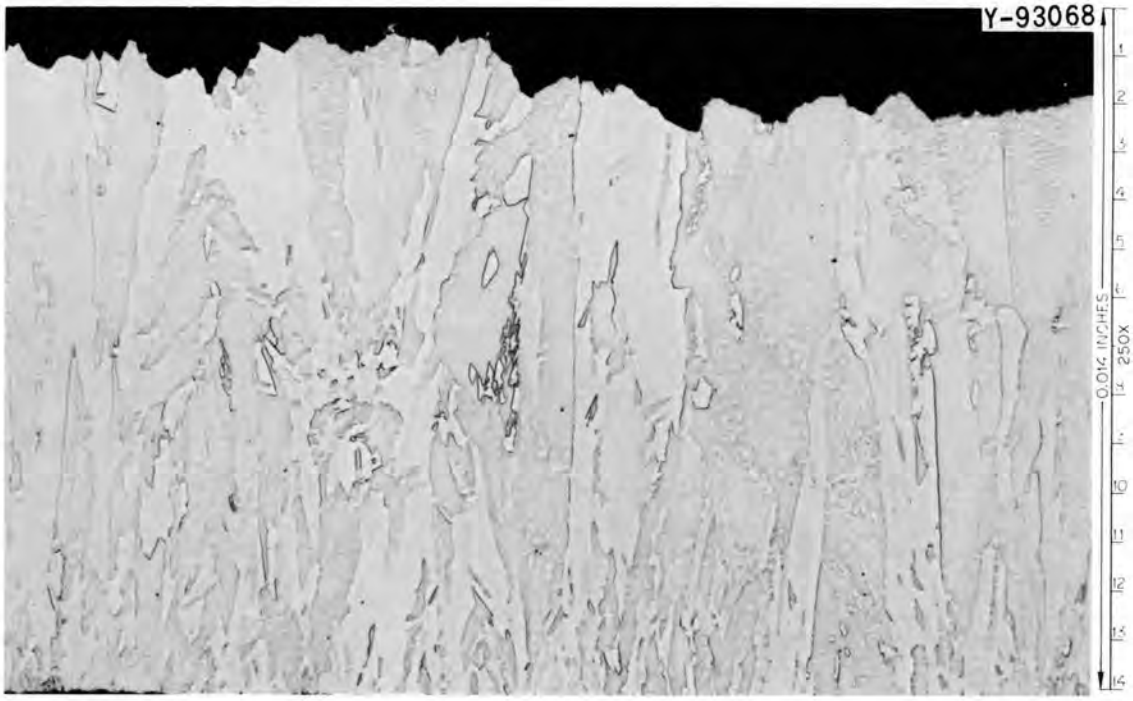

Fig. 10.7. Microstructure of W–5% Re Alloy Deposited at 100 torr. Etchant: 1 part NH_4OH (reagent grade) and 1 part H_2O_2 (30%).

Table 10.1. Conditions[a] and Efficiencies of Tungsten Deposits Prepared with H_2-WF_6-HF Mixtures

H_2 (cm^3/min)	WF_6 (cm^3/min)	HF (cm^3/min)	H_2:WF_6 Ratio	HF (vol %)	Efficiency (%)
2000	204	0	9.8	0	98
2000	218	0	9.2	0	97
2000	205	75	9.8	3.3	91
2000	202	253	9.9	10.3	94
2000	218	250	10.1	10.1	95
2000	201	380	10.0	14.7	93
2000	212	702	9.4	24.1	72
600	85	572	7.1	45.5	95
300	20	535	15.0	62.6	99

[a]Temperature: 700°C; pressure: 5 torr.

reacting gases. Those results are now known to be in error due to a faulty WF_6 flowmeter. The WF_6 and HF flow rates shown in Table 10.1 were determined from weight changes of the gas cylinders, and the efficiencies were obtained by weighing the deposits.

The data in Table 10.1 show that the efficiency of deposition is not clearly dependent upon the HF content of the reacting gases within the range of HF contents used. The low efficiency obtained with an HF content of 24.1 vol % may be an anomaly within the group. The efficiencies for the last two experiments cannot be compared with the others because the H_2 and WF_6 flow rates were substantially lower.

A visual inspection of the surfaces of the deposits revealed no definite trend in surface roughness with increasing HF content in the gas mixture. All deposits were generally smooth with a few, randomly spaced nodules. The deposits made with HF in the gas mixture were smoother than those made without HF, although the texture appeared to be of the same type.

Although limited in scope, these experiments indicate that HF does not adversely affect deposition efficiency or surface texture of W deposits.

Metallurgical Properties of Tungsten Alloys

Formation of Gas Bubbles in CVD Materials (K. Farrell, J. I. Federer, W. C. Robinson, Jr., A. C. Schaffhauser)

We are continuing our studies on the formation of gas bubbles in CVD materials. Previously,[4,5] the formation and growth of gas bubbles

---

[4]A. C. Schaffhauser and R. L. Heestand, "Effect of Fluorine Impurities on the Grain Stability of Thermochemically Deposited Tungsten," pp. 204–211 in 1966 IEEE Conference Record of the Thermionic Conversion Specialist Conference, Nov. 3 and 4, 1966, Houston, Texas, The Institute of Electrical and Electronics Engineers, New York, 1966.

[5]J. V. Festa and J. C. Danko, "Some Effects of Fluorine Content on the Properties of Chemically Vapor Deposited Tungsten," p. 349 in Proceedings of the Conference on Chemical Vapor Deposition of Refractory Metals, Alloys, and Compounds, Gatlinburg, Tennessee, September 12–14, 1967, ed. by A. C. Schaffhauser, American Nuclear Society, Hinsdale, Illinois.

during annealing at high temperatures in CVD tungsten deposited from WF_6 at 600 to 800°C were correlated with the fluorine impurity content in the metal. But since then we have found that no gas bubbles develop during annealing of W deposited at 1000 to 1200°C from WCl_6 containing fluorine impurities.[6]

Examination of other CVD materials after annealing has revealed a correlation between formation of gas bubbles and the fraction of the absolute melting point at which the material was deposited (Table 10.2).

Table 10.2. Formation of Bubbles in Chemically Vapor Deposited Materials

Metal	Volatile Compound	Deposition Temperature (°C)	$\frac{T_d}{T_m}$ [a]	Presence of Gas Bubbles After Annealing
W	WF_6	600–800	0.24–0.30	Yes
W	WCl_6	1000–1200	0.35–0.40	No
Mo	MoF_6	770–950	0.36–0.42	No
Ta	$TaCl_5$	1000–1200	0.39–0.45	No
Ni	$Ni(CO)_4$	150–250	0.24–0.30	Yes
V	VCl_3	1000–1200	0.50–0.60	No
W	WF_6	1000–1200	0.35–0.40	No
Mo	MoF_6	600–700	0.30–0.34	?

[a] Ratio of the deposition temperature to the absolute melting point of the material.

It seems that materials deposited at temperatures below about 0.3 of the absolute melting temperature (0.3 T_m) develop gas bubbles during annealing, whereas materials deposited at higher fractions of their melting temperatures remain free of bubbles. Since nucleation and growth of bubbles result from the coalescence of gaseous impurities with lattice vacancies, the probability of nucleation will be dependent on

[6] A. C. Schaffhauser, Fuels and Materials Development Program Quart. Progr. Rept. Sept. 30, 1968, ORNL-4350, pp. 237–241.

the amounts and the ratio of impurities and vacancies. Our interpretation of the evidence in Table 10.2 is that the deposition temperature influences the supersaturation of vacancies produced during deposition and thus determines the probability of bubble formation during subsequent annealing.

During deposition, lattice vacancies are created because the newly-deposited atoms do not immediately attain their equilibrium lattice positions. Rearrangement of the atoms and the consequent elimination of vacant sites takes place by diffusion of atoms over the surface. Low temperatures and high rates of deposition will therefore favor a high supersaturation of vacancies, which in turn will ensure bubble formation during subsequent annealing, provided sufficient gases are present. At higher deposition temperatures, surface diffusion is enhanced, and the supersaturation of vacancies is low — and so is the probability of bubble formation.

To test this hypothesis we are attempting to produce deposits over a wide range of temperature and purity. In the most recent experiments, 10-in.-long W tubes were deposited from WF_6 at 1100 and 1200°C. The portions of these deposits that have the highest deposition rates contained grown-in porosity similar to that observed in previous deposits on small substrates at high temperature.[7] But samples taken about 7 to 8 in. from the end of the deposit near the gas inlet, where the rate of deposition was lower due to depletion of WF_6, were fully dense as deposited. Preliminary examination of these deposits after annealing 1 hr at 2400°C showed no evidence of gas bubbles.

Long-Time Creep-Rupture Properties of Tungsten Alloys

R. L. Stephenson

We are continuing our comparisons of the creep-rupture properties of arc-melted W, W–5% Re, W–26% Re, and W–25% Re–30% Mo. The stress

---

[7]J. I. Federer, W. C. Robinson, and R. M. Steele, "Effect of Deposition Conditions on the Orientation of Chemical Vapor-Deposited Tungsten and Molybdenum," pp. 287–295 in 1967 IEEE Conference Record of the Thermionic Conversion Specialist Conference, October 30–November 1, 1967, Palo Alto, California, The Institute of Electrical and Electronics Engineers, New York, 1967.

rupture data for W–25% Re–30% Mo are shown in Fig. 10.8. A computer program was used to determine the Larson-Miller constant by least-squares fitting. The master curve thus obtained was used to generate the isotherms shown. The computed curves seem to be in good agreement with the experimental data. This alloy is weaker than unalloyed W at long times and high temperatures.

In view of the intense interest in these alloys at low strains, we have used preliminary data and a computer program to determine Larson-Miller master curves for time to 1% creep. Figure 10.9 shows master curves for each of the alloys. The inset shows the stress to produce 1% creep in 1000 hr versus temperature as predicted by these curves. Since the longest time represented by these data is 210 hr, these values are subject to refinement after further testing.

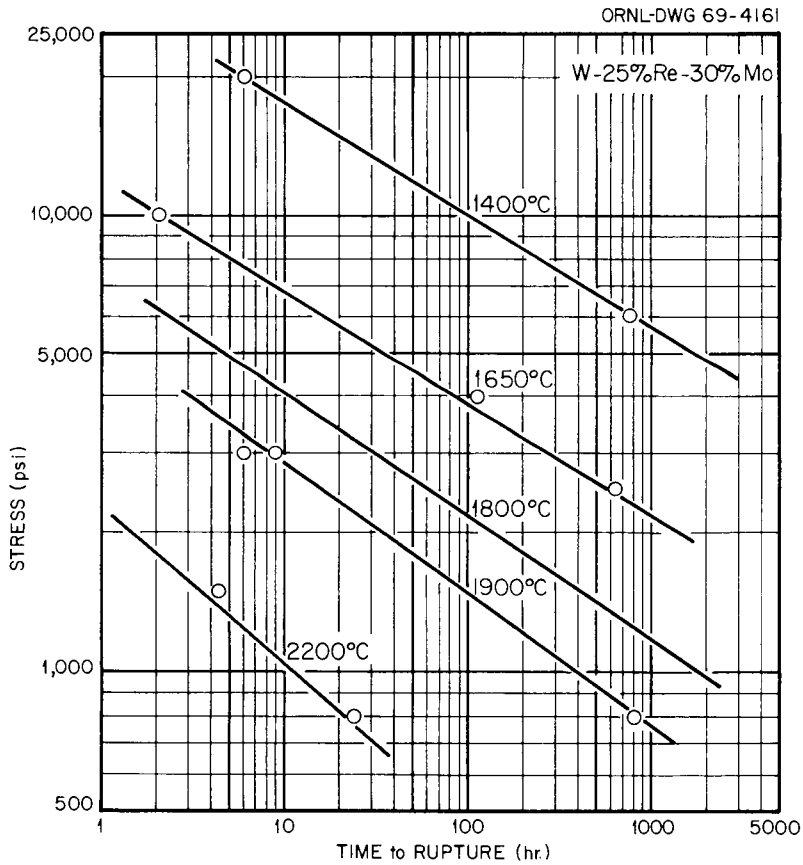

Fig. 10.8. Stress-Rupture Data for Arc-Cast W–25% Re–30% Mo Compared with Isotherms Derived from Larson-Miller Constants.

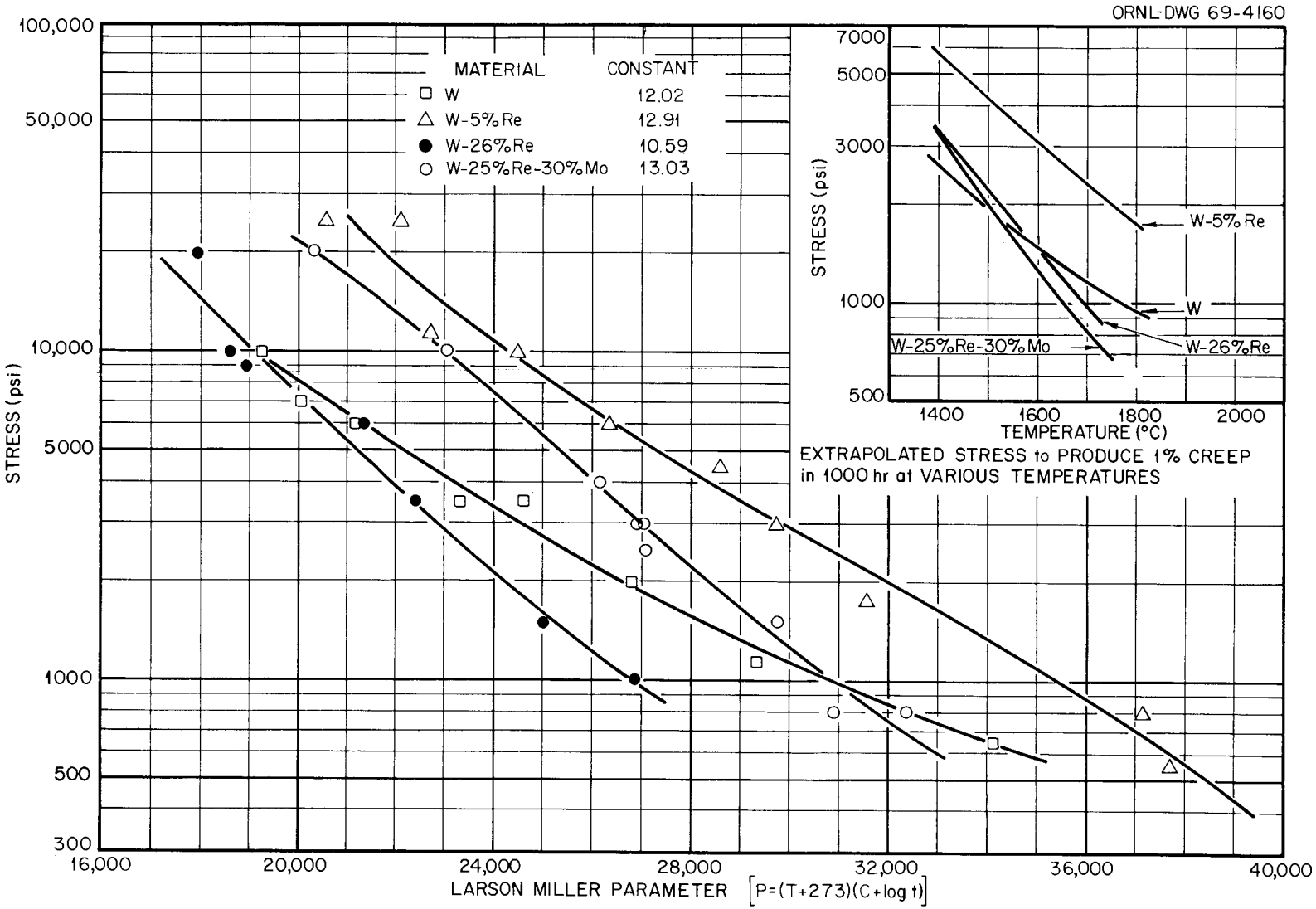

Fig. 10.9. Larson-Miller Master Curves for Time to 1% Creep in Arc-Cast Tungsten Alloys.

11. NONDESTRUCTIVE TEST DEVELOPMENT

W. O. Harms R. W. McClung

Our task is to develop new and improved methods of nondestructively testing reactor materials and components. We are studying various physical phenomena, developing instruments and other equipment, devising techniques, and designing and fabricating reference standards. Among the methods being studied for both normal and remote inspection are electromagnetics (with major emphasis on eddy currents), ultrasonics, penetrating radiation, and holography.

Electromagnetic Inspection Methods

C. V. Dodd J. W. Luquire[1]
W. E. Deeds[1] W. G. Spoeri

We continued research and development on both analytical and empirical bases.

Eddy Currents

In our analytical research we are continuing to derive integral equations for problems of interest and are using our computer programs to provide numerical solutions directly applicable to actual eddy-current tests.

One practical goal is to optimize the design of eddy-current coils for inspecting tubing.[2] We began with the case of a coil encircling a tube and calculated the signal due to a defect on the inner surface of the tube directly under the coil. This is the defect farthest from the coil and thus, in principle, the most difficult to detect. We varied both the product of frequency, conductivity, and permeability and the wall thickness of the tubing to produce a family of curves that showed[2]

---

[1]Consultant from the University of Tennessee.

[2]C. V. Dodd, J. W. Luquire, W. E. Deeds, and W. G. Spoeri, Fuels and Materials Development Program Quart. Progr. Rept. Dec. 31, 1968, ORNL-4390, pp. 177–179.

that for a given wall thickness and type of tubing there is an optimum operating frequency for maximum sensitivity to defects on the inner surface of the tubing. We then selected the minimum thickness and one of the thicker sections and varied the dimensions of the coil. This demonstrated that the optimum operating conditions were independent of the size and shape of the coil. We are now studying the ability of a differential coil system to "focus" on a defect as the coil system is scanned past the defect. Figure 11.1 shows the relative change in impedance produced as a differential coil system is scanned past a defect on the inner surface of the tube. The various curves represent different spacings between the coils. We have defined the "focus" of the coil system as the width of the envelope of the curve representing the factor for sensitivity to a defect at half its maximum value. Figure 11.2 shows how the focus varies as a function of spacing between the coils. We also plotted the relative maximum amplitude as a function of the spacing between the coils. The focus improves, but the relative amplitude decreases as the spacing between the coils decreases. For these particular variables of coil and conductor, there is no clear choice for maximum sensitivity to defects. These studies should lead to more sensitive eddy-current tests.

We have prepared a report[3] that gives a detailed derivation of many of our theoretical calculations for eddy currents. The abstract is given below:

> We have obtained integral representations for the vector potential produced by a circular coil for a number of different geometrical configurations. From the vector potential we can calculate any observable electromagnetic induction phenomenon. Our present solutions are limited to cases with axial symmetry and linear media. The solutions are in the form of multiple integrals of ordinary and modified Bessel functions.
>
> The configurations that we have already solved include coils with rectangular cross sections in the following locations: above or on each side of a two-conductor sheet

---

[3]C. V. Dodd, W. E. Deeds, J. W. Luquire, and W. G. Spoeri, Some Eddy-Current Problems and Their Integral Solutions, ORNL-4384 (April 1969).

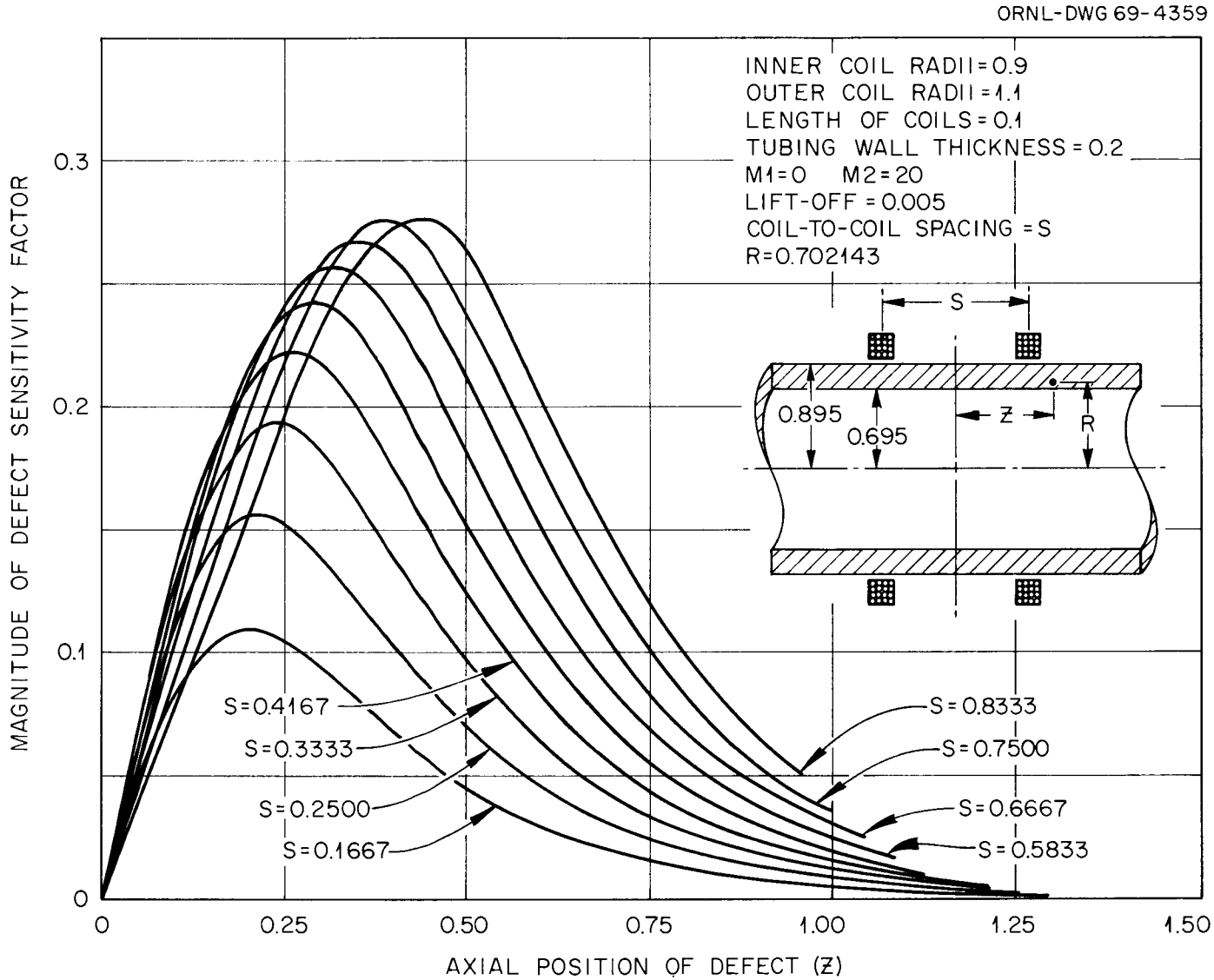

Fig. 11.1. Relative Change in Impedance as a Differential Eddy-Current Coil System is Scanned Past a Defect in a Tube.

ORNL-DWG 69-4358R

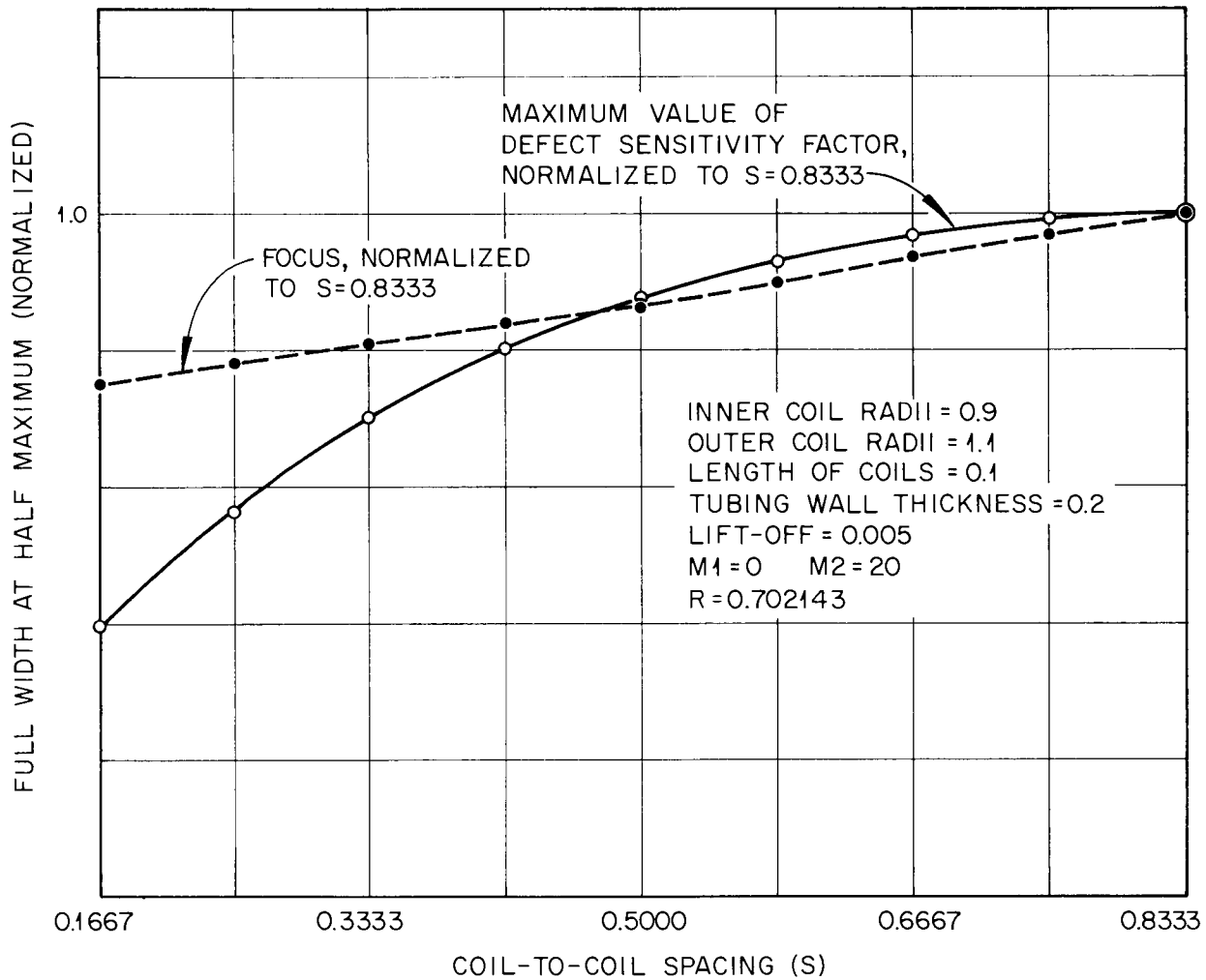

Fig. 11.2. Change in Focus and Sensitivity of Probe as a Function of Spacing Between Coils for Inspection of Tubing.

bounded by parallel planes, between two parallel-plane conductors, encircling a tube or a rod consisting of one metal clad on another, and inside a tube. The electromagnetic phenomena that we have calculated include the coil impedance, the phase and amplitude of the voltage induced in pickup coils, the effects of small spheroidal defects on the impedance and phase, and the forces generated in a metal by the eddy currents. The agreement between calculated and measured phenomena is excellent in most cases and within experimental error in all cases.

Infrared

A paper[4] with the following abstract reported work done on infrared studies under a small, continuing subcontract with the University of Tennessee:

> A microscope was designed and constructed to detect surface and internal discontinuities in materials which are opaque to visible radiation but transparent at infrared frequencies. Flaws were made by ruling a number of lines on the surfaces of sample materials which were then examined under the microscope. Internal flaws were simulated by clamping two samples together and observing the defects in the boundary layer. We found that the microscope could easily detect surface and internal flaws about 10 microns in size. The microscope is used with a mechanical scanning table and a storage oscilloscope to provide a visual display of the detected signal.

Ultrasonic Inspection Methods

H. L. Whaley K. V. Cook

Optical Visualization of Ultrasound

One of the application we plan for the schlieren system is a study of some of the techniques for ultrasonic inspection of welds. Models of butt welds in plate were designed and fabricated from 1-in.-thick

---

[4]W. A. Simpson, C. C. Cheng, W. E. Deeds, and C. V. Dodd, "An Infrared Microscope System for the Detection of Internal Flaws in Solids," paper presented at the Spring meeting of the American Society for Nondestructive Testing, Los Angeles, March 10–13, 1969, and submitted for publication to Materials Evaluation.

Plexiglas sheet. The weld area in the first models was simulated by sawing a wedge out of the plate and then gluing it back with a special cement. In later models the weld metal was simulated with epoxy. Selected defects were simulated in the following ways:

1. Porosity — a cluster of small holes was drilled into the base material and filled with cork.

2. Slag — a small piece of rubber was fused into the interface.

3. Lack of fusion — glue was omitted from a portion of the interface.

4. Lack of penetration — a notch was cut into the bottom of the wedge (i.e., the "weld metal") and filled with cork.

Each model contained one or more of these artificial defects. We wanted to determine the effect of each type of discontinuity on the propagation of ultrasound through the weld area.

Preliminary results have not been encouraging because the intensity of ultrasound leaving the weld area is very low. This seems to be due both to the high attenuation of ultrasound by the Plexiglas and to the relatively poor interfaces obtained in the simulated weld zone. Although the models differ from actual welds in basic ways, they will provide useful information if these problems can be overcome.

Frequency Analysis

The system for analysis of frequency spectra was used to examine those characteristics of good and poor bonding in a brazed joint between stainless steel and Cu that affect frequency. The specimen was a large piece of Cu clad with 0.067-in. thick type 310 stainless steel. At areas of poor bonding (as identified from previous, unrelated tests), the spectrum of the signal reflected at the nonbonded interface contained a series of evenly spaced maxima in the frequency-amplitude display, as shown in Fig. 11.3. These maxima consisted of frequencies that were resonant in the stainless steel cladding. At areas of good bonding, the maxima do not appear, as shown in Fig. 11.4 (the frequency span in Fig. 11.4 is the same as that for Fig. 11.3).

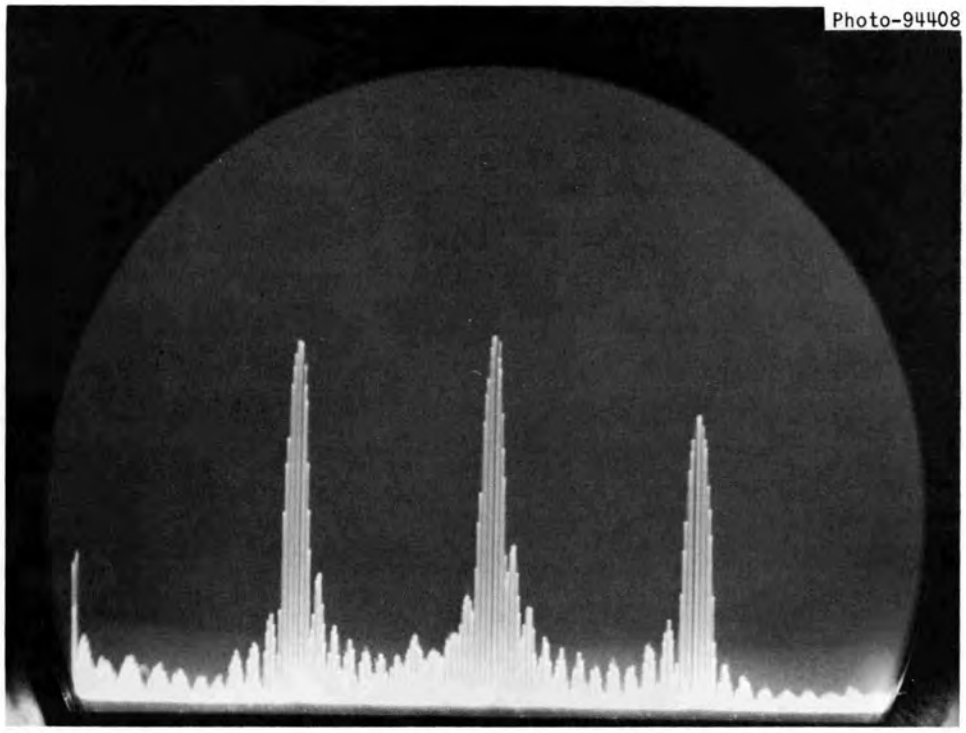

Fig. 11.3. Spectral Analysis of Ultrasonic Signal Reflected from an Area of Poor Bonding. Maxima are at 1.75, 3.70, and 5.60 MHz.

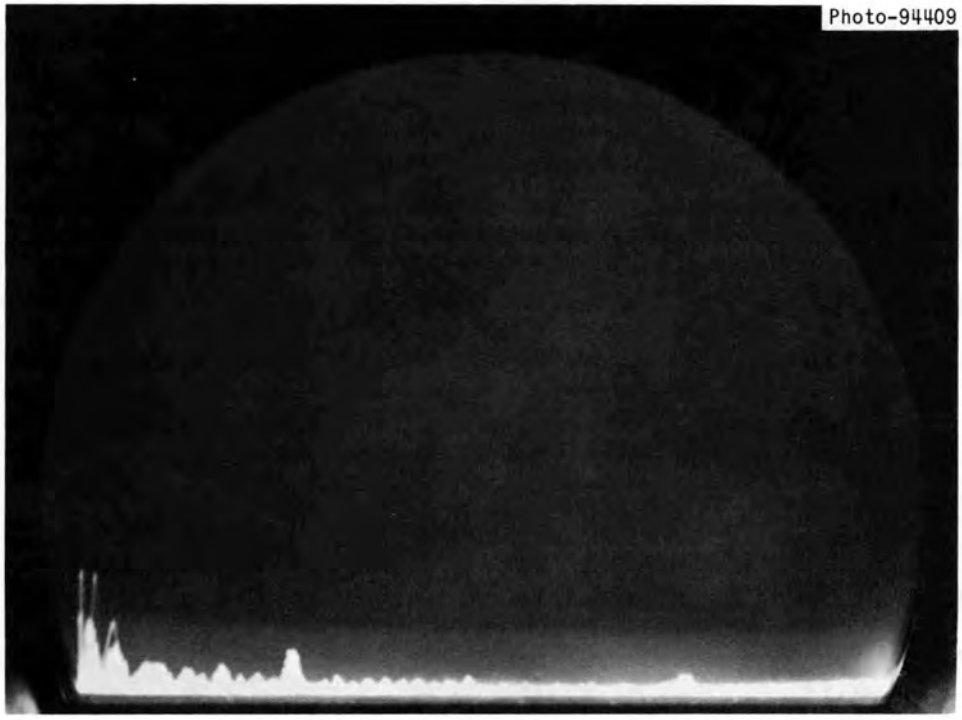

Fig. 11.4. Spectral Analysis of Ultrasonic Signal Reflected from an Area of Good Bonding.

Grooves machined into the surface of a flat steel plate had an effect on the frequency spectrum of the reflected pulse. Evenly spaced minima appeared in the spectrum of the signal from the front surface whenever the transducer was positioned directly over a groove. The separation of these minima increased with decreasing notch depth. We examined a series of notches with depths from 0.006 to 0.094 in.; Fig. 11.5 shows the relationship between the frequency separation of the interference minima, ΔF, and the depth of the notch. The calculated values were determined by interference considerations from the known velocity of ultrasound in water and the depth of the notch.

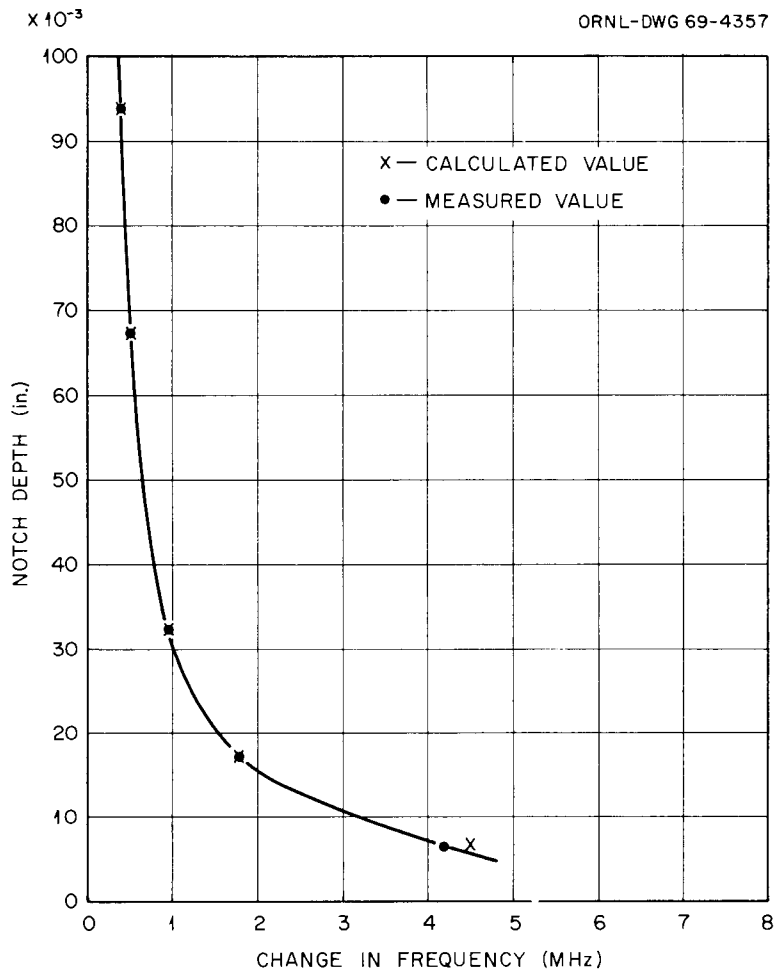

Fig. 11.5. Separation of Ultrasonic Interference Minima as a Function of the Depth of a Notch in the Surface.

Penetrating Radiation and Holographic Inspection Methods

B. E. Foster S. D. Snyder

Radiation Attenuation[5]

We developed a computer program that will calculate the mass absorption coefficients for the Al and U_3O_8 in a 0.050-in.-thick fuel plate. The fifth-degree polynomial equation of the attenuation curve is used to determine the U content of a 5/64-in.-diam right circular cylinder through the fuel plate, the thickness of U_3O_8, and the thickness of Al for chart readings (attenuation values) from 20 to 100. The mass absorption coefficients, along with the density of a sample cut from a fuel plate, are used to calculate the weight percent of U in the sample. This provides a method, based on theoretical considerations, for comparing our determinations of fuel content with determinations by chemical analysis.

The following is the abstract of a paper[6] to be presented next quarter:

> We developed an x-ray attenuation technique to measure the thickness of vapor-deposited tungsten on the inside wall of copper tubing. The radiation source was a Norelco MG-150 x-ray unit operated at 150 kVcp and 3 ma with copper filtration to reduce the overall beam intensity and absorb the low-energy x rays. We used narrow beam collimation and directed the beam radially into the duplex tube. The detector, placed in the bore of the tube, consisted of a NaI(Tl) crystal optically coupled to a commercial fibre optics bundle. The bundle was, in turn, optically coupled to a photomultiplier tube. The output signal from the photomultiplier was monitored by a digital voltmeter. The detector was held stationary in the beam and positioned for maximum signal. The tube to be measured was translated with the detector remaining on the axial center of the tube. Measurements were made at specified circumferential

---

[5]These studies are also of interest to the Aluminum Technology Program and are partially funded by them.

[6]B. E. Foster and S. D. Snyder, "An X-Ray Technique for Measuring Thickness of Tungsten on Copper," paper to be presented at Seventh Symposium on Nondestructive Evaluation of Components and Materials in Aerospace, Weapons Systems, and Nuclear Applications, San Antonio, Texas, April 23–25, 1969. To be published in the proceedings and as ORNL-TM-2524.

and longitudinal positions. Our calibration curve was obtained by plotting the voltmeter reading versus the thickness of rolled tungsten sheet specimens. As the x rays passed through the duplex wall, the tungsten attenuation had the greatest effect per unit of thickness, thus minimizing the effect of any variations in copper wall thickness. A copper thickness change of 0.005 in. was equivalent to a 0.0005-in. tungsten thickness and produced that tolerance on the final thickness determinations.

Radiation Scattering

We have continued preliminary investigations of the use of Compton backscattered radiation for measuring the thickness of the coatings or claddings on reactor components. A check of the linearity of the 1600-channel analyzer is in progress.

12. JOINING RESEARCH ON NUCLEAR MATERIALS

G. M. Adamson, Jr. G. M. Slaughter

The purpose of this program is to gather fundamental and applied data needed for a better understanding of the weldability of materials that are either being considered or now used for nuclear applications. Fundamental studies are concerned with the effects of minor constituents on the behavior of weldments. We are especially interested in the austenitic stainless steels and the Ni-rich alloys such as Incoloy 800 and Inconel 600.

Our applied studies emphasize the application of stainless steels in the Fast Flux Test Facility (FFTF). Our investigations will help define the influence of welding process, welding variables, and heat treatments after welding on the microstructure and mechanical properties of irradiated and unirradiated weldments. In addition, a modest program concerned with the influence of weld defects will provide base-line results in this much-talked-about but little-investigated field.

This broad-based research should enable us to develop the modifications in both alloy composition and procedures needed to improve the quality of weldments used in the various activities of the Commission. The work is immediately and directly applicable to such components as the Fast Test Reactor vessel, since it will provide the data necessary for predicting the effects of chemical composition and welding procedure on overall behavior.

Effect of Minor Variations in Chemical Composition on Weldability

Our continuing investigation of the effect of minor variations in the quantity of those elements usually present in small quantities in structural materials has included Incoloy 800, Inconel 600, and stainless steel.

Effect of Minor Elements on Hot Ductility of Inconel 600 (D. A. Canonico, W. J. Werner)

We are obtaining data on the hot ductility on cooling for the various experimental Inconel 600 alloys previously discussed.[1] These data are obtained by fracturing the specimens at progressively lower temperatures after they have undergone a thermal excursion to their zero-ductility temperature (ZDT). The ductilities observed are related to an alloy's weldability. In addition, data for hot ductility on cooling are being obtained for specimens exposed to 1343°C. This is the highest ZDT observed for the Inconel 600 series. It corresponds to a peak temperature 25 to 35°C above ZDT for a number of the experimental alloys.

We have found the choice of temperature to influence very definitely the ability to recover hot ductility. Although the tests are still under way, preliminary data indicate that ZDT differences of as little as 25°C can cause ductility reductions of about 90% (95 vs 8%). This lack of recovery can prevail to temperatures as low as 1200°C.

Effect of Minor Elements on Hot Cracking in Inconel 600 (W. Dickinson, W. F. Savage)[2]

This work, as previously discussed, is a continuation of the investigation of Inconel 600 being conducted under subcontract at Rensselaer Polytechnic Institute.[3] A statistically based analytical study was used to determine the effect of six minor elements, S, P, Si, Mn, Ti, and Al, on the propensity of Inconel 600 for hot cracking. Current work has been concentrated on the effect of these elements on the cross-sectional area, depth of penetration, and diameter of gas tungsten-arc (GTA) spot welds.

---

[1]D. A. Canonico and W. J. Werner, Fuels and Materials Development Program Quart. Progr. Rept. Dec. 31, 1968, ORNL-4390, pp. 190–192.

[2]Department of Materials Engineering, Rensselaer Polytechnic Institute, Troy, N.Y.

[3]G. M. Goodwin and W. F. Savage, Fuels and Materials Development Program Quart. Progr. Rept. Sept. 30, 1968, ORNL-4350, pp. 250–252.

The results to date are startling: penetrations varied from 17/64 to 45/64 in. (over 2.5 to 1); widths from 74/64 to 119/64 in. (about 1.5 to 1); and areas from 0.015 to 0.041 in.^{2} (almost 3 to 1). These large variations existed in Inconel 600-type alloys, all of which were within the allowable specification limits.

It should be emphasized that that part of the weld that is easiest to see (the width of the weld) is least affected by the slight variations in minor constituents.

These data were subsequently analyzed by the standard method of factorial analysis developed by Yates.[4] Figure 12.1 (Rensselaer Polytechnic Institute drawing) contains the results from the factorial analysis. The various elements exhibited different effects depending upon the criterion involved; for instance, Al drastically decreased penetration while having a much smaller effect on increasing the spot width. The overall effect of Al is a moderate decrease in the area of the welds. Sulfur somewhat increases weld area, mainly because of its effect on penetration. Some interaction effects, such as those from Al-S, S-Mn, and Si-Al, are also evident.

The factorial analysis identified the gross effect of minor elements but could not evaluate the effect of varying their amounts. This determination is more amenable to analysis by linear regression, and we are now working toward this.

Weldability of the 18% Cr–8% Ni Class of Stainless Steels (W. J. Werner, D. A. Canonico)

Eight experimental compositions[5] of type 308L stainless steel were fabricated into 1/8-in.-thick sheet, chemically analyzed, and metallographically examined (in the wrought condition) for delta-ferrite. These compositions were selected to provide a wide range of delta-ferrite contents in weld metal (to prevent hot cracking) through various combinations

---

[4]F. Yates, Design and Analysis of Factorial Experiments, Imperial Bureau of Soil Science, London, 1937.

[5]W. J. Werner and D. A. Canonico, Fuels and Materials Development Program Quart. Progr. Rept. Sept. 30, 1968, ORNL-4350, pp. 252–254.

ORNL DWG. NO. 69-5160

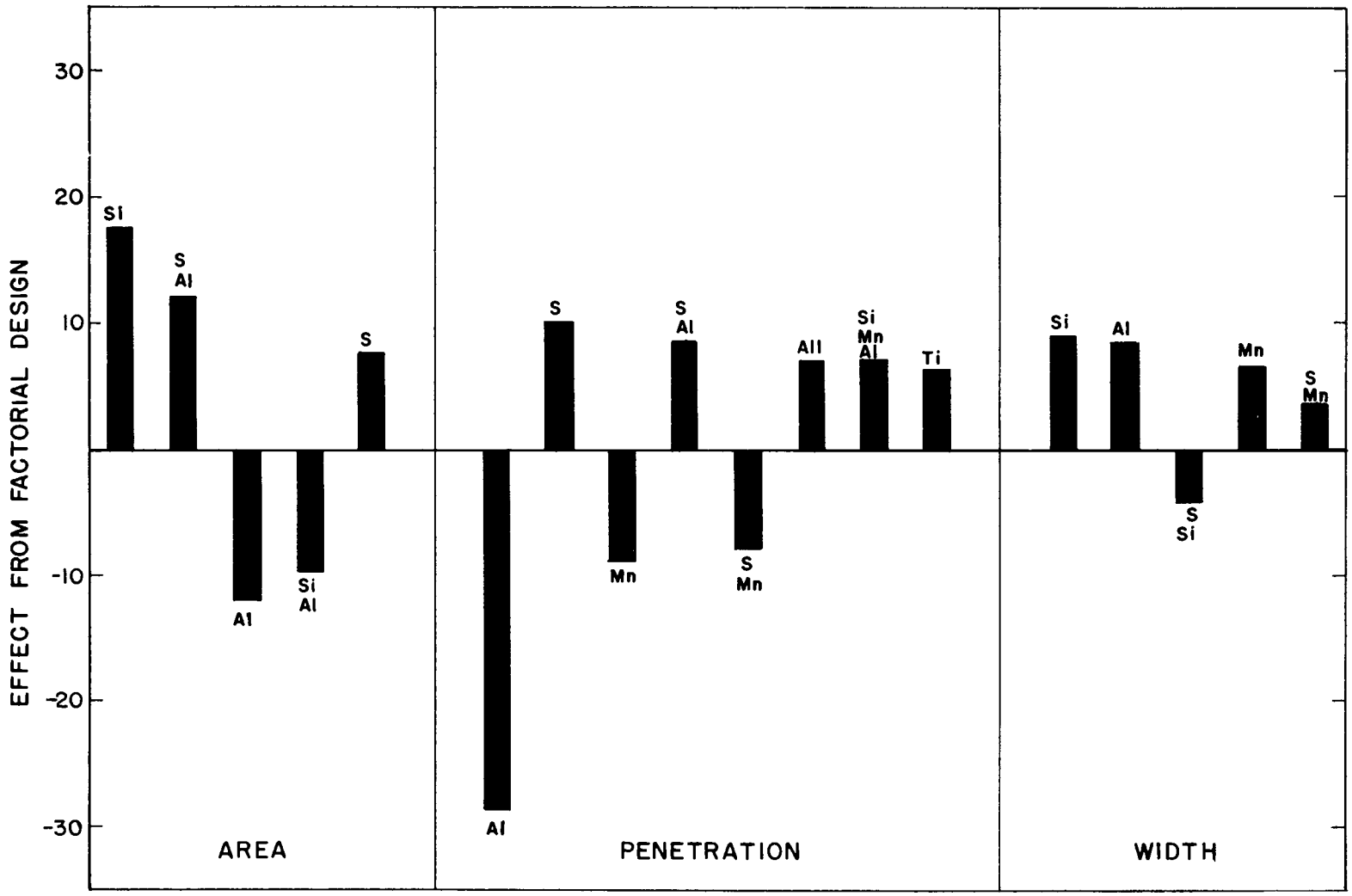

Fig. 12.1. Statistical Analysis of Effect of Minor Elements on Area, Penetration, and Width of Welds in Inconel 600.

of Ni and Cr equivalents as noted on the Schaeffler Diagram.[6] Excellent control was obviously maintained in fabricating these alloys, for the desired and actual metal equivalents are very close (Fig. 12.2).

The quantitative television microscope was used to determine the percentage of ferrite in wrought samples of each composition, and it will be used later to examine weld deposits made under these same compositions. We have found significant differences in delta-ferrite content between that predicted by the Schaeffler Diagram (weld metal) and that in the actual wrought product. For example, alloy E has a predicted ferrite content of 12% in the weld metal and an actual content of 8% in the wrought product (Fig. 12.3). The actual content in the weld metal will be determined later.

Gas tungsten-arc bead-on-plate welds were made on the 1/8-in.-thick sheets under two different sets of welding conditions:

Welding Current (amp)	Travel Speed (in./min)
100	6
150	9

The electrode size (1/8 in. in diameter) and distance between electrode and workpiece (1/8 in.) were constant for both welds. These weldments are being evaluated.

This study of the very important relationship between major elements and microstructure will enable us to determine the role of minor constituents on weldability more effectively.

Effect of Certain Minor Elements on the Ductility of Incoloy 800 at Intermediate Temperatures (W. J. Werner)

We reported[7] that tensile tests of experimental heats of Incoloy 800 at slow strain rates permitted us to divide these heats into two classes: (1) those that exhibited ductility minimum at

---

[6]A. L. Schaeffler, Welding J. (N.Y.) 26(10), 601-s–620-s (1947).

[7]W. J. Werner, Fuels and Materials Development Program Quart. Progr. Rept. Dec. 31, 1968, ORNL-4390, pp. 192–199.

ORNL DWG. NO. 69-5161

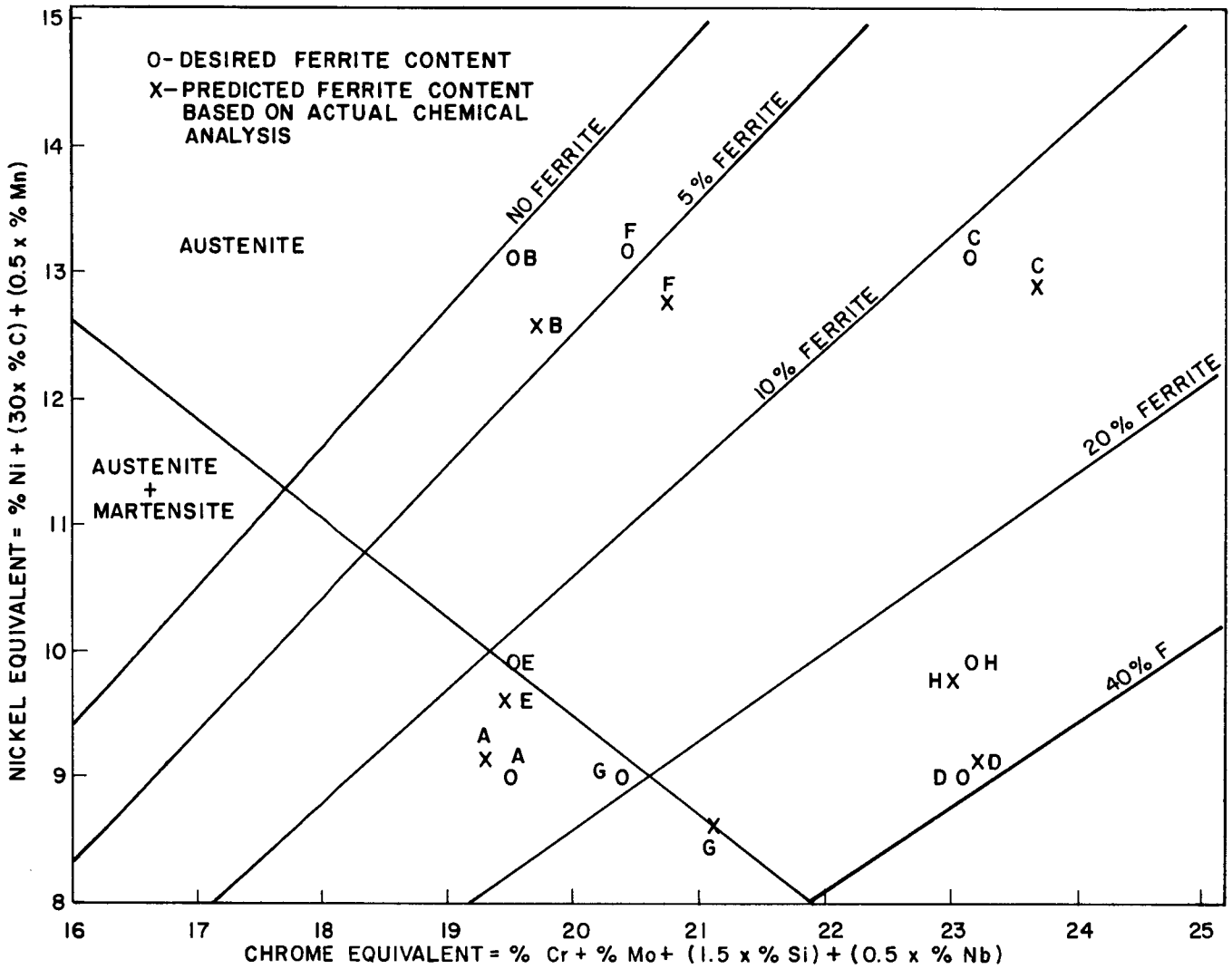

Fig. 12.2. Schaeffler Diagram for Location of Experimental Stainless Steel Compositions.

Fig. 12.3. Transverse Section of Wrought Alloy E Showing 8% Ferrite. The amount of the light etching ferrite was measured by quantitative television microscopy. Etchant: glyceria regia. 150×.

intermediate temperatures (near 600°C) and subsequent recovery at elevated temperatures, and (2) those that exhibited a continuous decrease in ductility with increasing test temperature. Furthermore, we found that only those alloys that recovered ductility at elevated temperatures contained Ti. We metallographically examined the tensile specimens near their fracture surfaces; representative microstructures of specimens tensile tested at 600 and 700°C are shown in Figs. 12.4 and 12.5, respectively. The Ti-bearing alloys are compared to Ti-free alloys in each case. At 600°C, sharp, intergranular voids are present in all the samples. The length and number of voids are related to grain size: the alloys with larger grains had both longer and fewer voids. The voids were not limited to the fracture area, and, in some cases, they extended the entire gage length of the sample. Note that the grain boundaries in the photomicrographs have a wavy or jagged

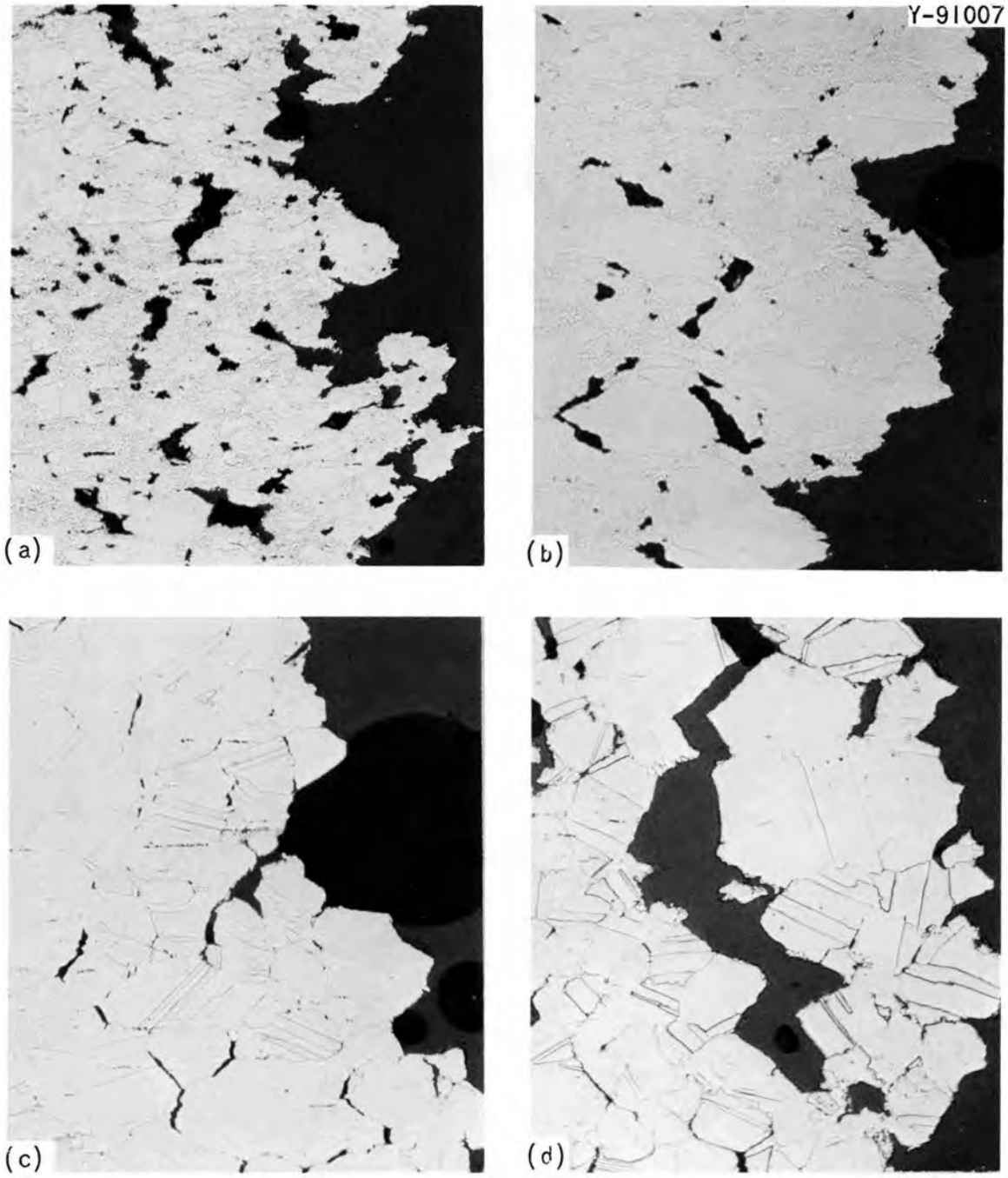

Fig. 12.4. Microstructures of Special Incoloy 800 Alloys Tensile Tested at About 600°C. The alloys contain (a) Ti + Al + S, (b) Ti + Al + S + P, (c) S, (d) P. Etchant: glyceria regia. 100×.

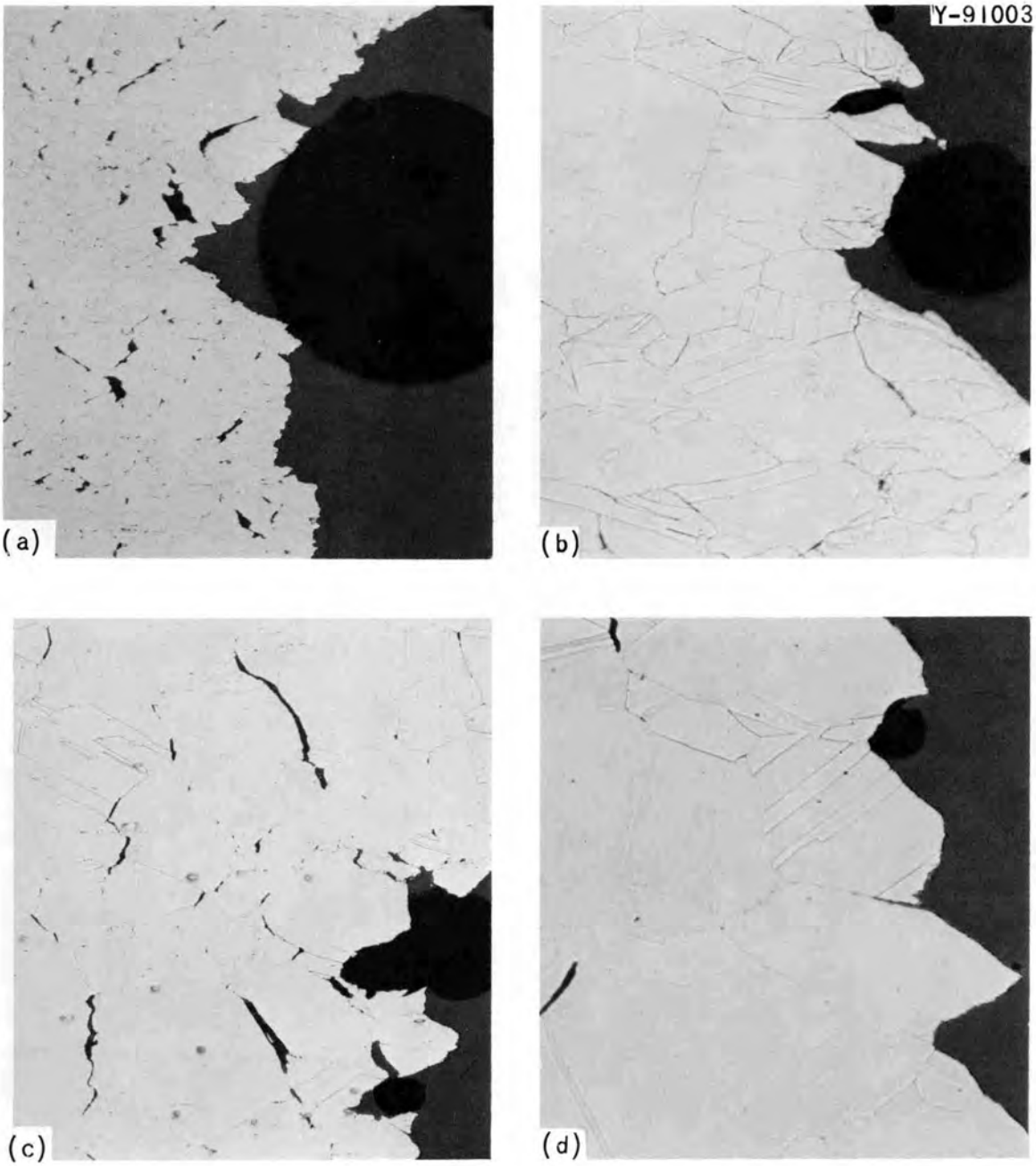

Fig. 12.5. Microstructures of Special Incoloy 800 Alloys Tensile Tested at About 700°C. The alloys contain (a) Ti + Al + S, (b) Ti, (c) S, (d) no additions (Fe-Ni-Cr ternary composition). Etchant: glyceria regia. 100×.

appearance; this was most pronounced in the specimens with larger grains. Finally, fracture was predominantly intergranular in all of the alloys tested at 600°C, and it appeared to propagate by the growth and linking of cracks. The Ti-bearing alloys show more plastic deformation within the grains than do the Ti-free alloys.

At 700°C, there are marked microstructural differences between the two classes of alloys (Fig. 12.4). First, the Ti-bearing alloys have begun to recrystallize, while the others have not. Second, the voids in the Ti-bearing alloys are rounded and not connected and in some cases are not on the existing grain boundaries. Voids in the Ti-free alloys are sharp, interconnected, and oriented on the grain boundaries. The mode of failure in the Ti-bearing alloys was predominantly transgranular, whereas that of the other alloys was predominantly intergranular and apparently caused by the linking of intergranular voids. The Ti-free class of alloys showed no evidence of recrystallization and continued to fail intergranularly even at temperatures approaching 900°C.

The results of a study with an electron microscope will be reported next quarter to provide more information regarding the very potent influence of Ti on the behavior of Incoloy 800.

Development of Welding Procedures for Commercial and Modified Alloys

This task has as its objective the development of welding data that can be applied directly to the fabrication of a particular component. Our current efforts are directed toward the FFTF primary containment vessel. The information being obtained contains welding data per se as well as information on the mechanical properties of both the unirradiated and irradiated material.

Joining Development in Support of the Fast Flux Test Facility
(G. M. Goodwin)

The program for supplying weld specimens to Battelle Northwest Laboratory (BNWL) for irradiation is nearing completion. All of the welds have been produced, and machining of the final lot of specimens

is under way. The weldment specimens listed in Table 12.1 have been shipped to BNWL.

The final shipment, which will contain about 35 gas metal-arc weld specimens from each of the two locations, will be shipped about April 10, 1969.

Table 12.1. Summary of Weldment Specimens Furnished to Battelle Northwest Laboratory

Welding Process	Date Shipped	Specimen Location	Number of Specimens
Submerged-arc	12/12/68	All weld metal	66
Submerged-arc	12/12/68	Fusion line	64
Shielded metal-arc	3/11/69	All weld metal	68
Shielded metal-arc	3/11/69	Fusion line	68
Gas metal-arc	3/27/69	All weld metal	31
Gas metal-arc	3/27/69	Fusion line	31

Using procedures similar to those previously described[8] for the submerged-arc welds, we prepared shielded metal-arc and gas metal-arc welds. The following welding conditions were used:

(1) Shielded metal-arc process:

Current, amp	140 (root pass) 170 (all subsequent passes)
Voltage, v	23 (root pass) 25 (all subsequent passes)
Travel speed, in./min	7.5–8.5
Electrode	5/32-in.-diam type 16% Cr–8% Ni–2% Mo stainless steel (Champion heat 53011)
Power supply	Hobart motor generator

[8]G. M. Goodwin, Fuels and Materials Development Program Quart. Progr. Rept. Dec. 31, 1968, ORNL-4390, pp. 199–203.

(2) Gas metal-arc process:

Current, amp	290–320
Voltage, v	35–37
Travel speed, in./min	11.3
Filler wire consumption rate, in./min	195
Filler wire material	1/16-in.-diam type 308L stainless steel (Airco heat 705001)
Shielding gas	90% He–7.5% Ar–2.5% CO_2 (Linde 1025), 45 ft^3/hr
Power supply	Linde SVI 300

Specimens were cut from the weldments as described.[8]

Effect of Defects on Mechanical Properties of Weldments

C. D. Lundin[9]

This task was initiated to determine when a discontinuity becomes unacceptable. It is a known and accepted fact that discontinuities generally exist in the structural components. Our objective is to characterize various discontinuities and establish their effects on the mechanical properties of the materials being joined.

The program involves five areas: (1) location and evaluation of discontinuities by nondestructive testing; (2) study of the effect of welding variables on the occurrence of discontinuities in weld metal; (3) production of discontinuities in types 310 and 304 stainless steel (in addition to the discontinuities previously produced in Inconel 600 alloy[10]); (4) characterization of the discontinuities by surface topography with the scanning electron microscope; and (5) characterization of other discontinuities that occur naturally in welds on TZM, Ta–10% W,

---

[9]Consultant from The University of Tennessee, Department of Chemical and Metallurgical Engineering.

[10]C. D. Lundin, Fuels and Materials Development Program Quart. Progr. Rept. Sept. 30, 1968, ORNL-4350, pp. 256–259.

and Inconel X750 by fracture-surface topography (at the discontinuity interface).

The discontinuities in electron-beam welds in Inconel 600 were examined by radiographic techniques. These tight cracks with little or no width cannot be located and characterized by x-ray techniques unless the rough roots and faces of the full-penetration welds are ground smooth, since the normal irregularities of the surface mask the indications from the discontinuities. Even when the surfaces are ground to a 15 rms finish, it is necessary to have the x rays intersect the discontinuity at an oblique angle so that the thickness of the discontinuity, as presented to the x-ray beam, is maximized with respect to the thickness of the total section. These two factors (roughness of the surface and orientation of the discontinuities) must be considered when discontinuities are small and tight; otherwise, the discontinuities will not be detected. Ultrasonic detection of discontinuities is still under investigation.

Electron-beam welds identical to those made in Inconel 600 were made on types 310 and 304L stainless steel to evaluate the tendency of these alloys to form discontinuities. As anticipated, the type 310 stainless steel formed fewer discontinuities per cross section examined than did the Inconel 600. The defects that did form, however, were similar in size and orientation. The type 304L stainless steel did not exhibit any discontinuities when welded under the conditions used for Inconel 600. This behavior was not surprising, for type 304L stainless steel is generally considered more resistant to formation of discontinuities. These results do suggest, however, that the electron-beam welding method of predicting discontinuities may lend itself to evaluating the sensitivity of different alloys and heats of similar alloys to the formation of discontinuities.

The use of the scanning electron microscope to characterize discontinuities by surface topography is continuing. This study has been extended to Inconel X750, TZM, and Ta–10% W. In TZM, the studies have shown that cracking in the liquid-solid region while the weld is being made (hot cracking) may lead to more extensive cracking upon cooling through the ductile-to-brittle range (cold cracking).

13. DEVELOPMENT OF LMFBR TUBING FABRICATION

G. M. Adamson, Jr.

The tubing fabrication program involves development of fabrication techniques for the manufacture of high-quality type 316 and modified type 304 stainless steel tubing in sizes of interest to the liquid-metal fast breeder reactor (LMFBR) program.

The general scope includes using fabrication techniques that may be transferred to commercial vendors and sufficient nondestructive and destructive testing of the intermediate and final products to assure and demonstrate the quality. The initial studies used Ti-modified type 304 stainless steel, and recently work has begun on type 316 stainless steel.

Fabrication Studies on Type 316 Stainless Steel

W. R. Martin

Drawing of Type 316 Stainless Steel Tubing (G. A. Reimann)

The preliminary studies involving drawing of type 316 stainless steel have been completed. This work involved limited experimentation on a small quantity of tubing with 0.375-in. outside diameter and 0.035-in. wall thickness. This material was produced by Greenville Tubes, Inc., to commercial tolerances; it is identified as heat 303407 and was procured by ORNL as redraw stock solely for this preliminary study.

Only eight draws were required to achieve the desired tubing size of 0.250-in. outside diameter and 0.016-in. wall thickness, and it soon became apparent that this heat of type 316 stainless steel could be more easily fabricated into tubing than could the Ti-modified type 304 stainless steels investigated earlier. The drawing and annealing schedule was arranged so that tubing samples with 0.250-in. outside diameter and 0.016-in. wall thickness were produced with 5, 10, 20, 30, 40, and 50% cold work. This tubing was cursorily examined for hardness at

room temperature, response to heat treatment, burst strength, and defect level.

The plot of hardness at room temperature is shown in Fig. 13.1. Note that the Vickers diamond pyramid hardness at 20% cold work exceeds the value of 290 that is specified for Fast Flux Test Facility (FFTF) tubing.

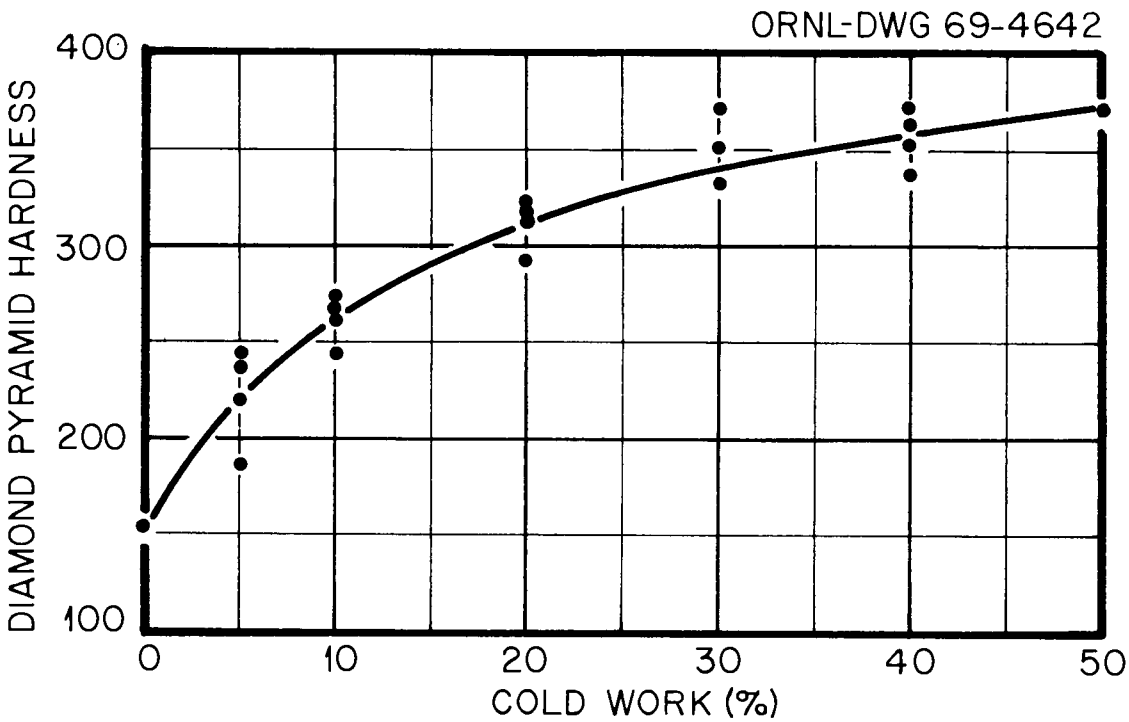

Fig. 13.1. Diamond Pyramid Hardness vs Percentage of Cold Work for Heat 303407 Type 316 Stainless Steel.

Samples were annealed 1 hr at 700, 800, 925, and 1050°C. Metallographic preparation of these samples was difficult because of the great number of inclusions. We noted, however, that the recrystallized grain size remained a relatively constant ASTM 5 or 6 at 1050°C when more than 10% cold work was present. When the material was annealed at 950°C, increasing cold work decreased the grain size from ASTM 5 or 6 at 5% to 7 or 8 at 50%. A very fine grain size of about ASTM 12 was obtained by annealing the 50% cold-worked material at 800°C, and no recrystallization was detected in any sample annealed at 700°C.

Tubes containing the six levels of cold work were examined by limited nondestructive testing — by the Vidigage test for eccentricity and by ultrasonic techniques for defects. Eccentricity ranged between 3 and 6%, or about the same as existed in the tubing as it was received. A reference notch 1 mil deep by 30 mils long was used for the ultrasound standard. No discernible trends were noted, either with eccentricity or defect level, that could be related to the amount of cold work in the tubing.

Where a defect indication was noted, the location was marked and a 3-in.-long tube-burst specimen was cut with the defect indication approximately in the center. Three other burst specimens were cut from portions of the tubing where no indications were found and were considered to be free of defects.

This experiment could not be completed because the maximum pressure we could obtain from the tube-burst apparatus was 30,000 psi. Also, fittings began to leak or were blown off the specimens when the pressure reached the 23,000 to 26,000 psi. As a consequence, burst specimens containing 30% or more cold work could not be tested. If test results are needed from the tubing with 30 to 50% cold work, tubing with 0.250-in. outside diameter and 0.010- to 0.012-in. wall thickness will have to be manufactured.

The results of tests of the samples containing 5, 10, and 20% cold work are summarized in Table 13.1.

None of the burst specimens with indications of defects showed loss of burst strength at room temperature. Either the defects were on the thick side of the tubing wall or the defect specifications are unrealistically stringent or the testing technique requires additional study.

The tubing from Allegheny-Ludlum heat 65808 is under investigation as part of an FFTF pilot production study in which we plan to simulate commercial processes of tubing manufacture as closely as practical with our equipment while at the same time trying to produce tubing with 0.250-in. outside diameter and 0.016-in. wall thickness that meets the present FFTF specifications. Additional equipment is being sought or

Table 13.1. Results of Burst Tests of Tubing Samples

Cold Work (%)	Average Burst Pressure (psi)	Average Hoop Stress at Fracture (psi)	Average Elongation (%)	Average Hardness (Vickers DPH)
5	13,720	106,600	27.4	220
10	17,510	133,600	8.7	260
20	22,080	172,300	2.2	310
20[a]		105,000–120,000	15	290

[a]Preliminary specifications for tubing for Fast Flux Test Facility.

will be constructed in order to obtain the desired monthly output. We obtained a furnace for continuous hydrogen annealing to relieve the annealing bottleneck. Degreasing, pickling, and rinsing facilities of sufficient capacity are being designed.

We received 103 ft of type 316 stainless steel seamless-tube hollows from Atomics International for use in the study. This material is identified as Allegheny-Ludlum heat 65808 and was received in five lengths of tubing with 1 1/2-in. outside diameter and 0.134-in. wall thickness. This tubing is part of a 10-ton heat melted from virgin materials by Allegheny-Ludlum's "standard melting procedures." The analysis of this heat follows:

Element	Content (wt %)	Element	Content (wt %)
C	0.060	Al	0.012
Mn	1.72	Ti	0.003
P	0.012	Pb	0.0014
S	0.007	Sn	0.013
Si	0.40	Co	0.030
Cr	17.30	B	0.0005
Ni	13.30	N_2	0.048
Mo	2.33	Ce	0.0006
Cu	0.065	Total rare earths	0.0010

A 12- by 12-in. ingot was rolled in 16 passes at 1260°C to a 5 5/8-in. round and machined into extrusion billets approximately 25 in. long with 5.625-in. outer diameter and 1.625-in. inner diameter. The billets were heated to 1220°C and extruded to a 1.9-in. outside diameter and 1.5-in. inside diameter. They were then straightened, conditioned, inspected, drawn in one pass to a 1.625-in. outside diameter and 1.357-in. inside diameter (46%), and sized to the specified 1.500-in. outside diameter and 1.230-in. inside diameter by free sinking. The tubes were annealed at 1070°C and are estimated to contain 2 to 3% cold work from final straightening and finishing operations.

Mechanical properties of the finished tubes are reported by Allegheny-Ludlum as follows: ultimate tensile strength, 90,500 psi; 0.2% yield strength, 42,600 psi; total elongation, 49.5%; Rockwell B hardness, 77/78; ASTM grain size, 5 to 6. Allegheny-Ludlum noted that dimensions were within "standard tolerance," but inspection of the five tubes received by ORNL indicated that only two met the 5% eccentricity requirement specified for FFTF starting stock.

One length of tubing from heat 65808 was selected for study. Eccentricity was determined by the Vidigage test to be 4.4% or less, and three sections, each 34 in. long, were cut in order to follow three drawing schedules to reach final size. One schedule was intended to duplicate commercial drawing practice by obtaining 40% reductions at maximum bench speed and by annealing 15 min at 950°C between each pass. Eight passes and seven anneals were required to achieve final size. The other two drawing schedules very closely resembled the practice as developed at ORNL for Ti-modified type 304 stainless steels: three passes totaling 50% reduction between each anneal. Sixteen passes and five anneals were required to achieve final size. The two schedules differed only in that the 15-min anneal for one was at 1050°C while that for the other was at 950°C. This difference produced an ASTM grain size of 3 to 5 in the first set and 6 to 8 in the second set of tubing. All three schedules included a 15-min anneal at 925°C just before the final plug-drawing pass.

Since this work was just completed, nondestructive testing has not begun, nor have the benefits or consequences of the drawing variables

been evaluated in any detail. Observations of the process lead to the following preliminary conclusions, which we believe will prove valid.

1. The "commercial" drawing schedule is preferred over the "ORNL" schedule developed for the Ti-modified stainless steel because it lends itself to higher production rates, minimizes handling and intermediate operations, and shows potential for higher recovery of material.

2. The maximum bench speed (about 35 fpm) can be used on the commercial drawing schedule but not on the other, since smaller reductions tend to cause chatter.

3. The maximum reduction attainable by mandrel drawing a single pass is about 45%; at higher reductions, the tubes fail in tension. If more cold work is desired between anneals, one or more additional draws must be made. The maximum total amount of cold work is estimated to be 60 to 70%, with the limiting factor being the ability to swage a suitable point for gripping.

4. Achieving the specified straightness in the final tube could be a problem. Straightening by conventional rotary operations should be avoided since it tends to introduce ovality. We are considering the use of a straightening operation just before the final draw.

5. With close attention to the cleanliness of the H_2 annealing atmosphere, all tubing emerged clean and bright. If this condition can be maintained reliably, then perhaps the importance of intermediate pickling steps is overemphasized. Pickling was also considered as a step in minimizing Cl contamination. Even though the more common pickling solutions use HNO_3-HF, the F should be less objectionable as a contaminant.

Work is under way to compare the effect of drawing heat 65808 with C either in or out of solution. Samples were drawn 40% and annealed 15 min at 1050°C. One sample is undergoing a 100-hr precipitation heat treatment. The "commercial" schedule with eight passes and seven anneals will be used if we can obtain recrystallization of 40% cold-worked material without redissolving the C. Otherwise an additional drawing pass will be used to increase the level of cold work.

Tube-burst samples will be tested to determine the effect of the schedule described above as well as to determine the effect of the drawing variables described previously.

A planetary swaging machine was designed at ORNL after the pattern used by the British. This machine is intended for work with alloys such as stainless steel that are difficult to deform. Work has been concentrated mainly on testing this machine, and little significant information has been developed with regard to the suitability of using this machine to produce tubing for the FFTF.

Effect of Boron on the Hot Ductility of Type 316 Stainless Steels
(A. K. Chakraborty)

The effect of B on the hot ductility of type 316 stainless steels is being investigated from 900 to 1300°C. Boron is commonly added to Inconel and less commonly to type 316 stainless steel to obtain improved fabricability at high temperatures. Inconel 600 was selected to be studied also since it was expected that the Ni-base alloy would behave differently than the Fe-base alloy. Commercial alloys were remelted, and from 5 to 200 ppm B was added to both alloys.

These alloys containing B were drop cast in a 1-in.-diam mold and later hot swaged at 1000°C to slightly more than 1/4 in. in diameter. We experienced no difficulty during hot swaging. We annealed the deformed alloys 1 hr at 1050°C under H_2.

The high-temperature mechanical properties were examined with a Gleeble testing apparatus. Gleeble tests have been used on other programs as an indicator for the degree of hot fabricability. The machined specimen was 0.25 in. in diameter and 3 in. long.

Figure 13.2 shows the reduction in area of type 316 stainless steel as a function of deformation temperature and B content. The reduction in area in the lower temperature range, up to 1100°C, does not change with B content. At higher temperature, the ductility is lost rapidly with higher B content, and at 1300°C ductility is lost even with decreased B content. The Inconel alloy shows better ductility than does type 316 stainless steel at 1300°C and otherwise remains fairly constant with more B and increases with increasing temperature.

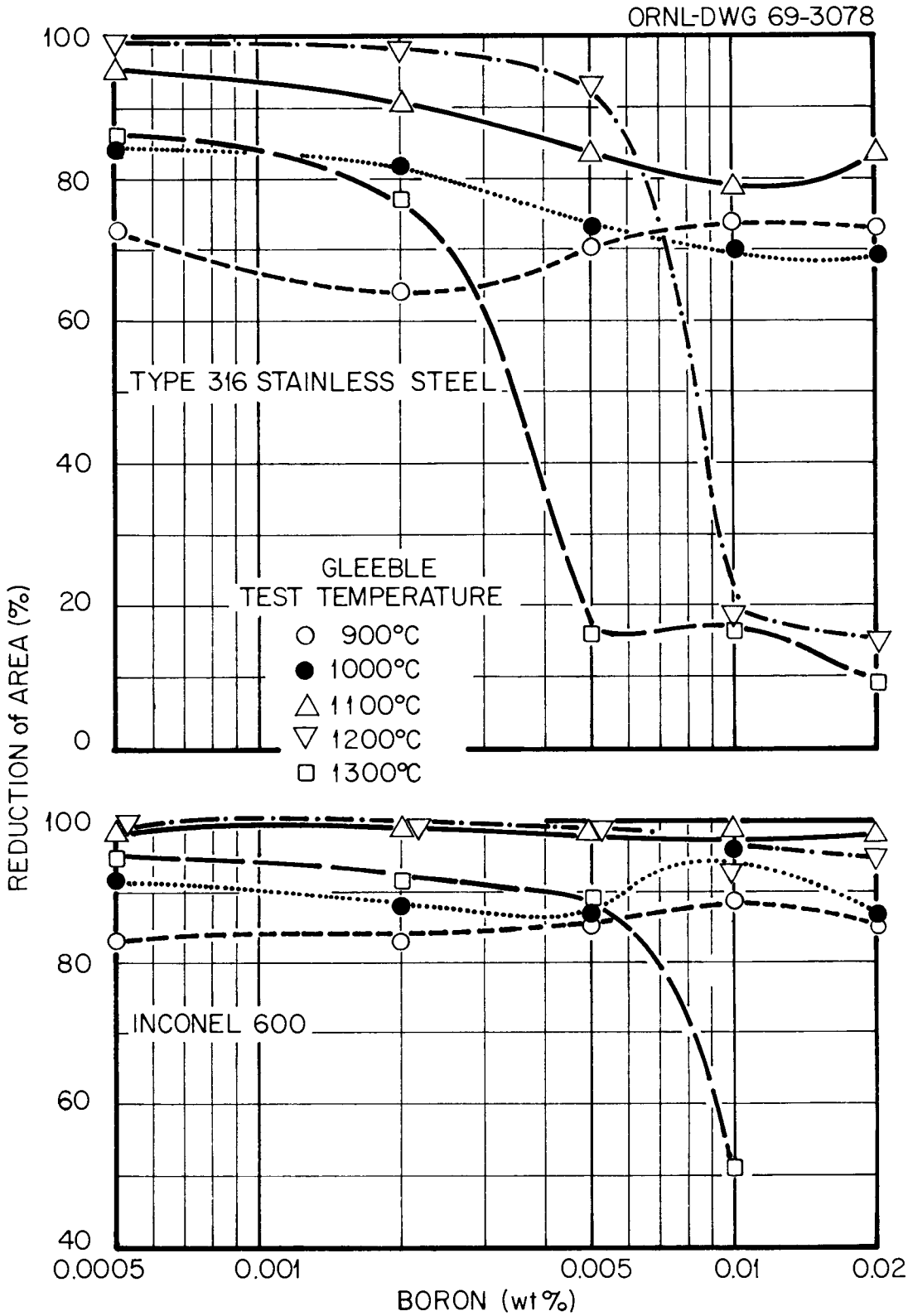

Fig. 13.2. Hot Ductility of Type 316 Stainless Steel and Inconel 600 as a Function of Boron Content.

The microstructures of these alloys are being examined. Our tentative conclusion is that B itself has no beneficial effect on the hot fabricability of either type 316 stainless steel or Inconel 600. If the addition of B to the initial melt of these alloys can be beneficial, then the role of B must be related to some other chemical element that is not present in our alloys.

Fabrication Studies on Titanium-Modified Type 304 Stainless Steel

W. R. Martin

Evaluation of Drawn Titanium-Modified Type 304L Stainless Steel Tubing (T. M. Nilsson)

The metastable austenite starts to decompose during the cold working of Ti-modified type 304L stainless steel. We presented[1] electron photomicrographs that show the development of a hexagonal close-packed ϵ phase and a martensitic ferrite α' phase in addition to the development of dislocations in the austenite matrix. The ϵ phase is formed as thin disks on the $(111)_\gamma$ planes, presumably[2,3] by the movement of 1/6 [112] partial dislocations on every second slip plane. The ϵ phase contains stacking faults, which show that the transformation is not completely regular. The presence of the martensite is confirmed by electron diffraction studies of selected areas. The martensite usually forms as fine needles inside the ϵ phase, but because of the complexity of ordinary transmission electron photomicrographs (see Fig. 13.6 in ref. 1) it is very difficult to identify the individual phases. It is possible to identify them by dark-field electron microscopy, and we are now attempting to do so.

In a few cases, the martensite formation occurs independently of the ϵ phase; this greatly facilitates identification of the martensite.

---

[1]T. M. Nilsson, Fuels and Materials Development Program Quart. Progr. Rept. Dec. 31, 1968, ORNL-4390, pp. 205–213.

[2]A. Seeger, Z. Metallk. 47, 653 (1956).

[3]W. Bollmann, Acta Met. 9, 972 (1961).

Figure 13.3 shows the structure of a tube of modified type 304L stainless steel after 12% cold work by drawing. The martensite needles are primarily oriented in one direction. The corresponding selected-area diffraction pattern shows the $(111)_\gamma$ planes parallel to the $(110)_{\alpha'}$ planes and the $[T01]_\gamma$ direction close to the $(\bar{1}11)_\gamma$ direction. Several crystallographic relationships between the austenite matrix and the martensite have been proposed[4] that are quite close to this, but due to the distortion of the lattice and the resulting diffraction spots we have not been able to distinguish between the various possibilities. Figure 13.3 also shows another set of martensite needles at an angle of about 50° to the predominant set. Both of these sets have $(111)_\gamma$ as a habit plane.

---

[4]R. Lagneborg, Acta Met. 12(7), 823 (1964).

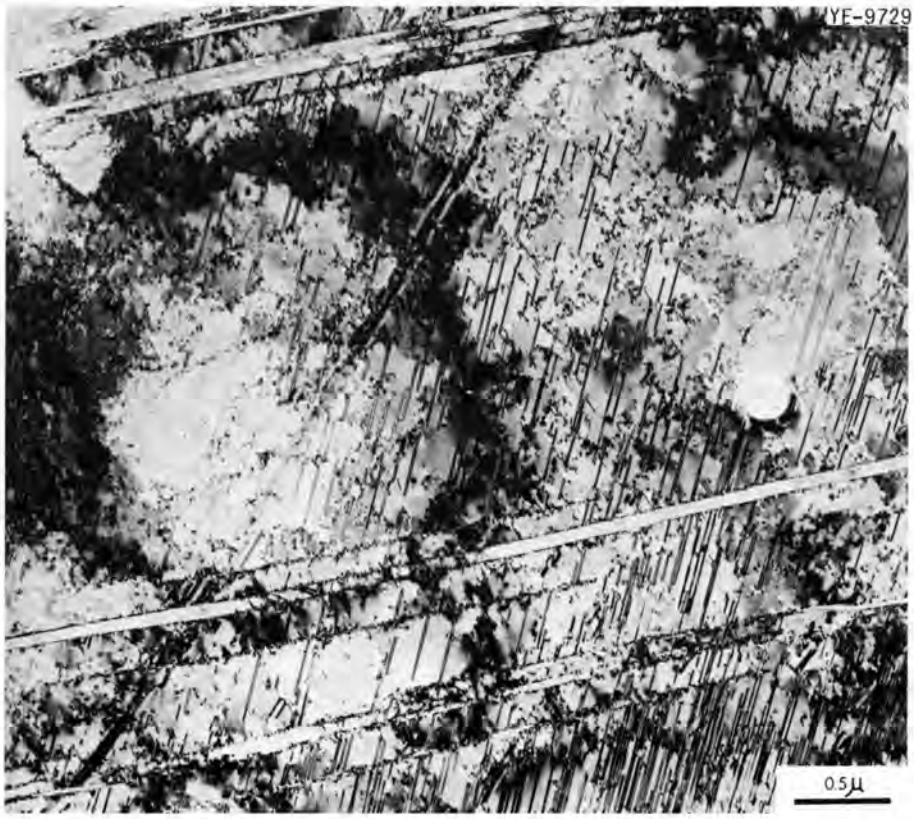

Fig. 13.3. Microstructure of Titanium-Modified Type 304L Stainless Steel Tube, Cold Deformed 12% by Drawing. The electron photomicrograph shows ε disks and martensite needles in a deformed austenite matrix. 35,000×. 25% reduction.

The ϵ disks are also present in Fig. 13.3 as long streaks, lying on a third set of $(111)_\gamma$ planes. Inside this phase, small martensite needles can be seen parallel to the larger needles.

The morphology of the martensite phase is very important to the workability of these steels, and we will, therefore, investigate the conditions under which the martensite forms as relatively large needles as compared to the conditions under which the martensite forms exclusively as fine needles inside the ϵ phase. We will also examine the cold-worked microstructures after tempering heat treatments at relatively low temperatures (less than 700°C), since future nuclear power reactors will operate at about 500 to 600°C, at which temperatures the martensite will start to transform.

14. DEVELOPMENT OF FUEL ELEMENT FABRICATION

G. M. Adamson, Jr.

The purpose of these programs is to devise new combinations of materials or new fabrication techniques to advance the technology for fabricating fuel elements and components for research reactors. We are attempting to improve the performance of advanced research reactors, such as the High Flux Isotope Reactor (HFIR) and Advanced Test Reactor (ATR), by developing fuel elements with lower production cost, longer lives, increased safety or reliability, or all three. The studies include factors affecting both fabrication and irradiation performance. We must also develop sufficient knowledge of the processes used for fabricating Al-based dispersion fuel elements so that we can adequately assist commercial fabricators, purchasers, specification writers, and technical inspectors. Other studies are aimed at improving the reliability and reducing the cost of the required nondestructive inspection techniques.

Fabrication Studies of Dispersion Fuel Plates

W. R. Martin

Effect of Hydrogen in Aluminum — Blisters in Fuel Plates (M. M. Martin, R. T. King)

The formation of blisters continues to plague the fabricators of Al-base fuel plates for research reactors.[1] We believe that many of the blisters contain primarily diatomic hydrogen that, according to Kostron,[2,3] results from desorption of dissolved monatomic hydrogen on free internal surfaces. Past studies on blistering were complicated by the lack of an analytical method that would permit determination of the H content in

---

[1]M. H. Binstock, Advanced Test Reactor (ATR) Fuel Plate Development, AI-68-88 (November 1968).

[2]H. Kostron, Z. Metallk. 43(8), 269–284 (1952).

[3]H. Kostron, Z. Metallk. 43(11), 373–387 (1952).

solid Al easily and reliably enough. The introduction of known quantities of protons into Al with a cyclotron offers an experimental technique for studying H in Al.

We are investigating the effect of injecting H into consolidated Alcoa 101 Al. Our experimental specimens simulate the clad filler section of the HFIR fuel plate. The 0.050-in.-thick plates had a 0.0155-in. cladding and 0.0190-in. core thickness. Their preparation included (1) pressing of −100 mesh Alcoa 101 Al powder at 30 tsi to 97% dense compacts 0.73 in. long by 0.96 in. wide by 0.15 in. thick; (2) degassing the compacts for 15 min at 500°C to remove adsorbed gases and pressing lubricants; (3) cladding the degassed compacts with type 6061 Al by hot rolling at 500°C to a total reduction in thickness of 8; (4) heating the hot-rolled plate for 1 hr at 500°C to test for blisters; and (5) pickling in Oakite 160 to clean and brighten the surfaces of the plates.

We fabricated ten miniature composite plates according to the above procedures. Visual and ultrasonic inspection revealed the plates to be sound with no indication of blistering. As calculated from measurements of the densities of the material and plates, the Alcoa 101 Al cores within the fabricated plates were essentially 100% dense.

Hydrogen was injected into the Al with the 86-in. cyclotron at the Y-12 Plant. Two specimens were scanned before a polyenergetic proton beam (produced by a rotating energy degrader) for a sufficient time to inject 0.33 wt ppm H uniformly throughout the front 0.020 in. of the specimens, and two other specimens were injected to contain 0.11 wt ppm H. The injection temperature was below 120°C, as measured by thermocouples embedded in a dummy specimen. A schematic illustration of the specimen is shown in Fig. 14.1.

Since working may facilitate the formation of blistering,[4] the specimens injected with protons to 0.33 wt ppm are being examined in both the irradiated and 20% cold-worked conditions. To stimulate blistering, we repeatedly annealed the specimens in air for 1 hr and then

---

[4]L. H. Melacek and R. D. Daniels, J. Appl. Phys. 39(6), 2803–2815 (1968).

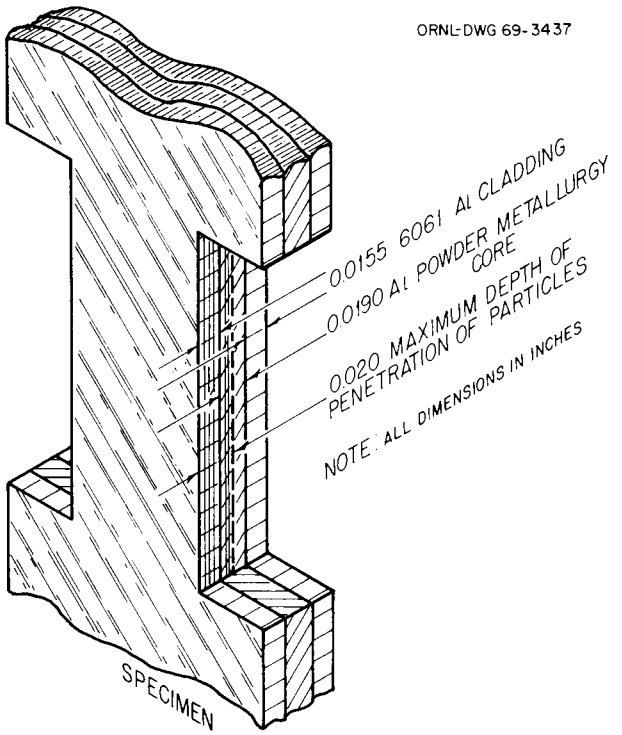

Fig. 14.1. Deposition of Hydrogen in Clad Specimens. Cross-hatched regions contain a uniform distribution of cyclotron-injected hydrogen to a depth of 0.020 in.

cooled and visually examined them at room temperature. In all runs, controls with identical fabrication history accompanied the test specimens.

No blisters were formed even though the initial heating temperature of 100°C has been progressively increased, in 100°C increments, to 500°C. The absence of blisters is surprising, since the initial concentration of 0.33 ppm H in the specimen exceeds the solid solubility by at least one order of magnitude. Figure 14.2 shows the surfaces of the specimens from the side nearest the region of highest H concentration, which should exhibit the first blisters. The two specimens injected with protons are identified as "3" and "3 of 3"; the latter has the cold work. These specimens have been sectioned for detailed optical and electron microscopy of their internal structure.

Part of the specimens were also subjected to 550°C for 1 hr and then for an additional 24 hr. After both heatings, we could not detect blisters on their surfaces. These specimens will also be submitted for microscopic examination.

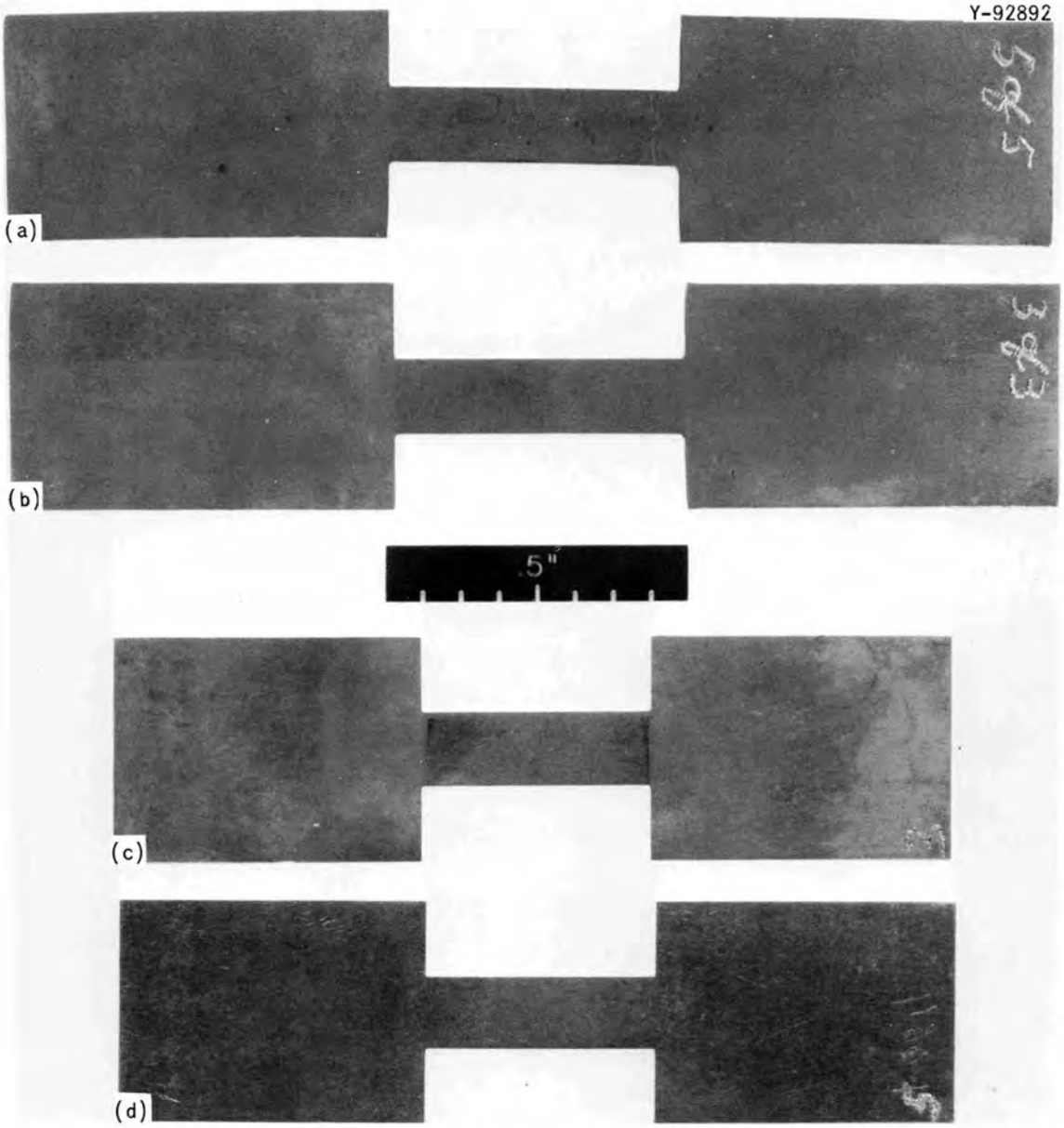

Fig. 14.2. Appearance of Aluminum Specimens After Being Heated for 1 hr at 100, 200, 300, 400, and 500°C. (a) and (d) Control specimens. (b) and (c) Test specimens injected with 0.33 ppm of protons in the gage length. (a) and (b) Specimens cold worked 20%.

Fabrication of Plates Containing Burned U_3O_8 (M. M. Martin, J. H. Erwin)

We are investigating the chemical compatibility of burned U_3O_8 with Alcoa 101 Al at fabrication temperatures up to 600°C. Since the last report, sections of the fabricated miniature plates[5] were polished and examined visually for evidence of reaction between the fuel and matrix and/or cladding. As shown by the absence of reaction products in Fig. 14.3, the burned U_3O_8 fuel particles appear to be completely compatible with the Alcoa 101 Al matrix. No evidence of reaction with the type 6061 Al cladding was found, though this cannot be judged from the figure. This specimen had been fabricated at 600°C and then heated for 93 hr at 600°C.

[5]M. M. Martin and J. H. Erwin, Fuels and Materials Development Program Quart. Progr. Rept. Dec. 31, 1968, ORNL-4390, pp. 239–241.

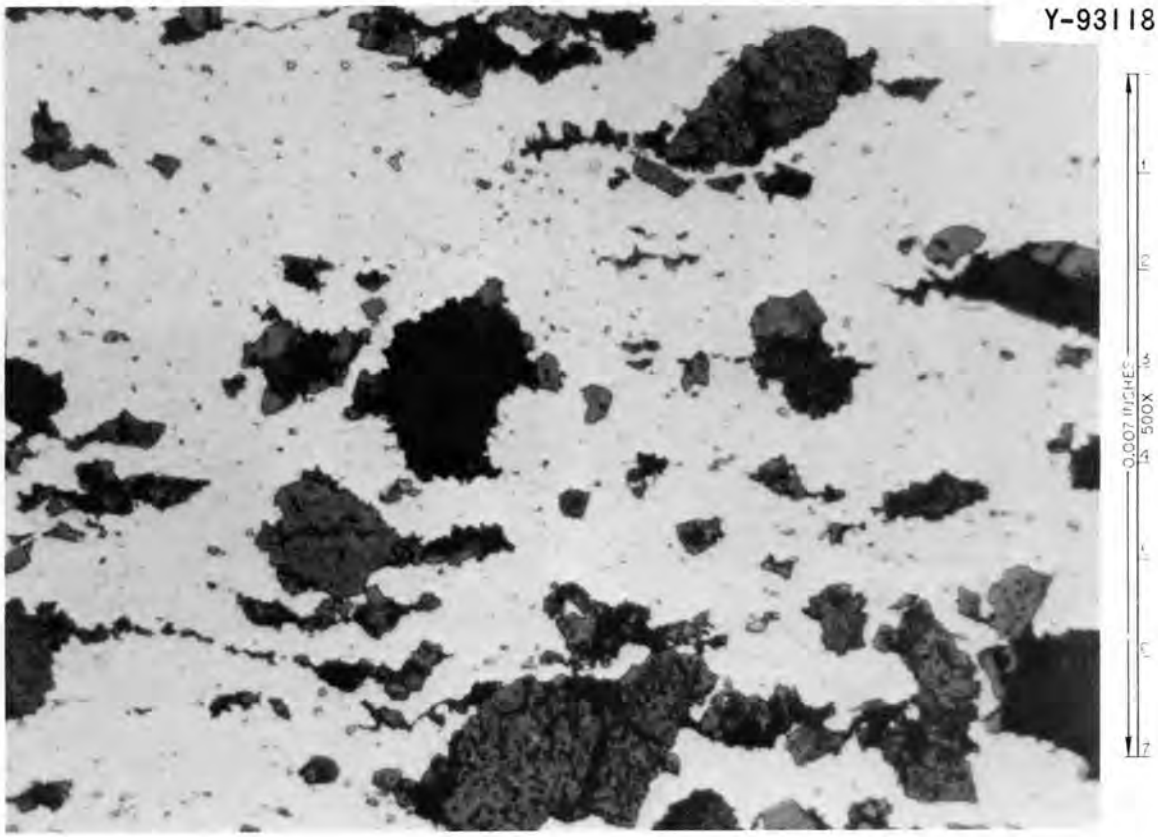

Fig. 14.3. Appearance of Al–53% Burned U_3O_8 Dispersion in Miniature Irradiation Test Plate After Being Heat Treated for 93 hr at 600°C. As polished.

Characterization of Electrolessly Deposited Nickel Coatings (M. M. Martin, J. H. Erwin)

Miniature plates electrolessly coated with Ni-P alloy were fabricated and shipped to the Experimental Test Reactor (ETR) site for irradiation testing in the G-12 loop. For better characterization, we measured the hardness of electrolessly deposited Ni coatings at room temperature and the apparent thickness of the interface of electrolessly deposited Ni and Al on Al plates of both types 6061 and 2219 Al. Coated plates were examined both as plated and after heat treatment in Ar. The treatment consisted of heating the plates to either 300 or 500°C, holding them at temperature for 48 hr, and then cooling them to room temperature while still shielding them with Ar. Table 14.1 shows the range of hardness values found for the Ni deposits on plates without heat treatment and with the 300°C heat treatment and for the Al-base alloys. Since the coating spalled completely from the plates heat treated at 500°C, no hardness measurements were made on these plates.

Table 14.1. Hardness of Electrolessly Deposited Nickel Coating on Types 6061 and 2219 Aluminum Plates

Type of Al-Base Alloy	Heat Treatment Temperature[a] (°C)	Hardness (DPH)		
		Al[b]		Ni Coating[c]
		(Vickers)	(Knoop)	(Knoop)
6061	None	68–69	74–77	385–457
6061	300	38–40	38–42	295–550
2219	None	69–77	76–86	317–385
2219	300	59–64	69–74	457–550

[a]Heated at temperature for 48 hr in Ar.

[b]Conditions: Kentron No. 1 testing device; 20× objective; 100-g load.

[c]Conditions: Kentron No. 1 testing device; 50× objective; 65-g load.

As expected, the heat treatment decreased by half the hardness of type 6061 Al in the 20% cold-rolled condition but caused little softening of type 2219 Al. The measurements of the Al alloys were quite uniform. There was considerable variation in the hardness of the electrolessly deposited Ni coatings, however. The great range of hardness values perhaps arises from the extreme thinness of the coating (about 0.001 in.). In fact, the coating appeared to flow somewhat into the mounting material when the test load was applied. The true hardness of the coating is probably greater than that shown in Table 14.2. Because of this deviation, little can be said about the apparent increase in hardness for the heat-treated coating. More importantly, it appears that the coating is surprisingly ductile. This suggests that coated plates can be used with small surface indentations and that abnormal limitation on handling will not be required during fabrication.

Table 14.2. Thickness of Electrolessly Deposited Nickel Coating on Types 6061 and 2219 Aluminum Plates

Type of Al-Base Alloy	Heat Treatment Temperature[a] (°C)	Thickness of Electrolessly Deposited Nickel Coating,[b] mils		
		Layer A	Layer B	Width of Interface Between Ni and Al (B-A)
6061	None	0.81	1.02	0.21
6061	300	0.53	0.95	0.42
6061	500	0.53	1.30	0.77
2219	None	0.53	0.81	0.28
2219	300	0.53	0.88	0.35
2219	500	0.53	1.02	0.49

[a]Heated at temperature for 48 hr in Ar.

[b]Layer A: thickness where the relative x-ray intensity of Ni is > 98.0%. Layer B: thickness where the relative x-ray intensity of Ni is > 0.54%.

With the aid of the electron probe in the Analytical Chemistry Division of ORNL, we distinguished two layers in the coating: layer A, which contains only electrolessly deposited Ni, and layer B-A, which corresponds to the width of the interface between Ni and Al. Table 14.2 shows the thicknesses found for these two layers on the samples used for the hardness tests. The effect of the heat treatment is quite evident for both types of Al alloys. In general, the width of the interface between Ni and Al increased with the higher heat-treatment temperatures; a larger increase was noted for type 6061 Al than for type 2219 Al.

Flakes of coating from the spalled plates that were heat treated at 500°C were analyzed by x-ray diffraction. Only Al_3Ni_2 was identified on the sides of flakes that had contacted the two Al-base alloys; on the opposite side, only NiO was identified. Many diffraction lines from both sides of the flakes, however, have defied identification.

When viewed at 500× under bright-field illuminations, the spalled flakes of Ni are composed of two layers of single-phase materials. Such layers were not observed in the coatings that were not heat treated or in those heat treated at 300°C, but these coatings also appeared to be single phase.

The Ni coatings electrolessly deposited on both types 6061 and 2219 Al alloys resisted spalling from thermal shock treatments. The treatment consisted of repeatedly heating coated specimens for 15 min and then quenching them into water. The initial heating temperature of 200°C was progressively increased, in 25°C increments, to 350°C for type 6061 Al and to 475°C for type 2219 Al. The specimens were heated and quenched six times at each temperature. No spalling was evident after any test, and metallographic examination verified that the coating was still intact.

D. L. McElroy of ORNL's Metals and Ceramics Division has reviewed the technology of electroless Ni plating and measured electrical resistivity on some plated wires and tubes of Al. His work revealed electrolessly plated Ni to be nonmagnetic but to become magnetic after 72 hr at 300°C and have an electrical resistivity of about 105 ± 5 microhm-cm at 25°C, which corresponds to a calculated electronic thermal conductivity of 0.065 w cm^{-1} $°K^{-1}$. This is a high thermal conductivity in

comparison to Griess's[6] value of 1.3 Btu hr^{-1} ft^{-1} $°F^{-1}$ (0.022 w cm^{-1} $°K^{-1}$) for alumina formed on unirradiated Al in corrosion tests in hot water. Calculations using these values of thermal conductivity indicate that the temperature drop across a 0.001-in.-thick alumina film would be six times greater than that expected across a 0.0005-in.-thick coating of electrolessly deposited Ni on a dispersion-type fuel plate that generates 10^6 Btu hr^{-1} ft^{-2}.

Irradiation Testing of Dispersion Fuel Plates

Status of Current and Planned Tests in the ETR (M. M. Martin)

Our experiment at the ETR continues the investigation of the effect of powder fines on the irradiation performance of burned and high-fired U_3O_8 dispersed in Al (refs. 7,8). A malfunction in the monitoring system of the G-12 loop during ETR cycle 100, however, resulted in the premature removal of the test plates after a total exposure of 9200 Mwd. Since we desire at least 10,000 Mwd, the experiment will be reinserted into the reactor at the earliest opportunity, probably during an unscheduled shutdown in cycle 102. Irradiation of our Ni-coated test plates[8] will begin at the start of cycle 102.

ORNL's remaining experiments for ETR irradiation in FY 1969 are limited to 12 plates containing B_4C, sol-gel U_3O_8, and burned U_3O_8 dispersed in Al. Table 14.3 lists their core compositions and other pertinent information. Barring a significant failure in instrumentation and/or the loop, these irradiations will start in ETR cycle 103.

---

[6]J. C. Griess, H. C. Savage, and J. L. English, Effect of Heat Flux on the Corrosion of Aluminum by Water. Part IV. Tests Relative to the Advanced Test Reactor and Correlation with Previous Results, ORNL-3541 (February 1964).

[7]M. M. Martin, J. H. Erwin, A. E. Richt, W. R. Martin, and K. V. Cook, Fuels and Materials Development Program Quart. Progr. Rept. Sept. 30, 1968, ORNL-4350, pp. 260–265.

[8]M. M. Martin, J. H. Erwin, A. E. Richt, B. E. Foster, S. D. Snyder, K. V. Cook, and C. V. Dodd, Fuels and Materials Development Program Quart. Progr. Rept. Dec. 31, 1968, ORNL-4390, pp. 246–251.

Table 14.3. Compositions for ETR G-12 Loop Irradiations in Cycle 103

Composition Number	Core Material[a]	Dispersoid Particle Size: Major Range (Mesh)	Dispersoid Particle Size: Fines, < 325 mesh (wt %)	^{235}U or ^{10}B Content (g)
83	Al	−325	88	0.0000
84	Al + 0.52% B_4C	−325	100	0.0015
85	Al + 0.78% B_4C	−325	100	0.0022
86	Al + 1.05% B_4C	−325	100	0.0030
87	Al + 1.75% B_4C	−325	100	0.0050
88	Al + 2.00% B_4C	−325	100	0.0057
89	Al + 51% sol-gel U_3O_8	−140 +170	0	1.200
89	Al + 51% sol-gel U_3O_8	−170 +325	10	1.200
89	Al + 51% sol-gel U_3O_8	−170 +325	50	1.200
90	Al + 53% burned U_3O_8	−170 +325	11	1.190
90	Al + 53% burned U_3O_8	−170 +325	26	1.190
90	Al + 53% burned U_3O_8	−170 +325	54	1.190

[a]Cores clad with type 6061 Al alloy.

We have modified the geometry of the irradiation test specimen. Figure 14.4 shows the desired dimensional requirements of our new mini-type test plate. This design, which effectively permits two tests to occupy a single slot in the standard G-12 tier, will double our experimental space in the ETR without increasing the neutron charges. The only additional restriction is one arising from a consideration of flux peaking: the two fueled regions in a particular slot must be less than 0.25 in. apart.

Preparation and Characterization of Mini-Type Test Plates Containing U_3O_8 (M. M. Martin, J. H. Erwin)

As indicated in Table 14.3, we are fabricating mini-type test plates for testing in another experiment in the G-12 loop of the ETR. Our experiment includes six plates with two types of oxide: burned and sol-gel U_3O_8. The characteristics of these fuels and of the matrix Al are tabulated in Table 14.4. The principal variables in the experiment are overall particle size and the content of fines in the two oxides.

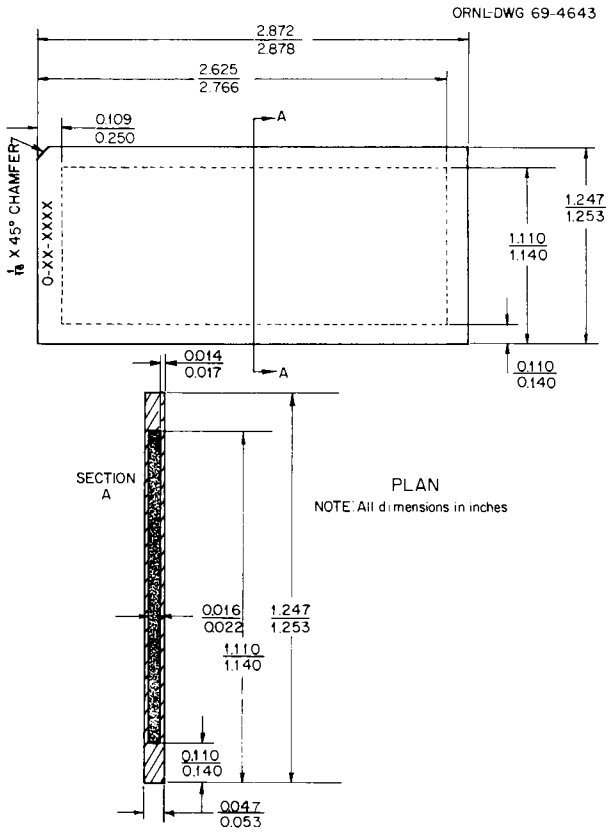

Fig. 14.4. Design of Mini-Type Test Plate for Irradiation Testing.

For these irradiations, the Chemical Technology Division supplied us with 224 g of −60 mesh sol-gel U_3O_8 prepared as follows:

1. Starting with 93% enriched uranyl nitrate solution, UO_2 sol was prepared by standard procedures.[9] This involved reduction to U(IV), ammonia precipitation at pH 7.5, and peptization. About 2 liters of approximately 0.5 N was obtained.

2. The sol was dried to shards at 110°C in air.

3. The dried gel was crushed to pass 60-mesh sieve.

4. The crushed gel was air-fired to 980°C over a 6-hr period, cooled overnight, and bottled.

Chemical attributes of the sol-gel blends (PBSG1, PBSG2, and PBSG3) were determined from one sample of −100 +325 mesh material that contained 12 wt % fines (< 325 mesh). Consequently, the values in Table 14.4 for

[9] J. T. McBride, Laboratory Studies of Sol-Gel Processes at Oak Ridge National Laboratory, ORNL-TM-1980 (1967) p. 27.

Table 14.4. Characterization of Components of Fuel Core

	Core Materials						
	Sol-Gel U_3O_8 (Batch 1)			Burned U_3O_8 (Batch 30-2615)			Matrix Al
Powder blend designation	PBSG1	PBSG2	PBSG3	PB4	PB5	PB6	G-12
U, wt %	84.50	94.50	84.50	84.28	84.39	84.14	
^{235}U in U, wt %	92.24	92.24	92.24	93.16	93.16	93.16	
Toluene density, g/cm^3	8.082	8.082	8.082	7.641	7.647	7.653	2.719
Surface area, m^2/g	0.041	0.041	0.041	0.341	0.382	0.352	0.195
Sieve analysis, wt %							
+140	0.0	0.0	0.0	0.0	0.0	0.0	0.0
−140 +170	100.0	0.0	0.0	0.0	0.0	0.0	0.0
−170 +200	0.0	22.5	12.5	23.0	19.7	3.8	0.1
−200 +230	0.0	22.5	12.5	22.3	17.5	19.6	0.2
−230 +270	0.0	22.5	12.5	21.5	17.6	10.8	2.2
−270 +325	0.0	22.5	12.5	22.3	19.0	12.0	9.2
−325 + dust	0.0	10.0	50.0	10.9	26.2	53.8	88.3

U content, density, and surface area are constant for the three sol-gel blends. Direct weighing of separated size fractions followed by blending established the distribution of particle sizes shown for the sol-gel materials. The small quantity of material available made it impossible to analyze the actual blends used in fabricating the plates for irradiation testing.

Note in Table 14.4 that the toluene density of the sol-gel material is quite high. In terms of closed porosity based on 8.30 g/cm^3 for theoretically dense enriched U_3O_8, this oxide contains 2.6 vol % internal voids. We had planned to irradiate a sol-gel U_3O_8 with 12.0 vol % of closed porosity. However, the experiment will be run with the lower porosity oxide since we need reference data for future irradiation on more porous U_3O_8 made by the sol-gel process.

We have pressed and degassed five compacts from each of the six fuel blends. Table 14.5 records their average attributes and changes from the degassing operation. The fuel compositions are 51 wt % sol-gel and 53 wt % burned oxides, both dispersed in Alcoa 101 Al. In terms

Table 14.5. Average Attributes of Mini-Type Fuel Plate Compacts[a]

	Al–51.16 wt % Sol-Gel U_3O_8 Compacts[b]			Al–53.04 wt % Burned U_3O_8 Compacts[b]		
Core order number	1026	1027	1028	1029	1030	1031
Dispersoid powder blend	PBSG1	PBSG2	PBSG3	PB4	PB5	PB6
Degassed composition						
Dispersoid, vol %	24.6	24.5	24.3	25.3	25.3	25.3
Voids, vol %	5.8	6.0	6.8	11.7	11.7	11.7
Standard deviation	0.14	0.36	0.22	0.16	0.47	0.42
Matrix Al	bal	bal	bal	bal	bal	bal
Degassed physical properties						
Weight, g	3.013	3.018	3.017	2.857	2.856	2.855
Density, g/cm^3	3.879	3.868	3.838	3.647	3.646	3.647
Dimensions, in.						
Length	0.3232	0.3233	0.3235	0.3244	0.3245	0.3245
Width	0.9646	0.9651	0.9656	0.9681	0.9683	0.9686
Thickness	0.1521	0.1526	0.1536	0.1522	0.1522	0.1520
Changes from degassing						
Dimensions, mils						
Length	+0.4	+0.3	+0.4	+1.3	+1.3	+1.3
Width	+0.9	+1.1	+1.3	+3.3	+3.4	+3.6
Thickness	+0.8	+0.8	+0.9	+2.0	+2.1	+2.0
Weight, mg	−2.2	−2.7	−2.5	−5.1	−5.7	−5.7
Density, %	−0.8	−0.8	−0.9	−2.2	−2.3	−2.2
Standard deviation	0.07	0.09	0.08	0.06	0.03	0.18

[a]Five compacts were made from core order number.

[b]Pressed at 30 tsi, then degassed for 1 hr at 500°C.

of fissile material, these compacts contain about 1.57 g $^{235}U/cm^3$ of fabricated core volume and represent a 37.5% increase over the current concentration for the HFIR outer annulus.

The plates were rolled but have not been fully evaluated. Difficulties in keeping the billets flat during rolling, however, produced extensive flaking observed in radiographs of the plates. This was especially

evident for plates containing compacts from core order Nos. 1027, 1029, and 1030. Fortunately, a sufficient quantity of PBSG2 remained from the initially prepared 14.2 g to make three additional compacts from core order No. 1027. We are also remaking two compacts from both core order Nos. 1029 and 1030.

Preparation and Characterization of Mini-Type Test Plates Containing B_4C
(M. M. Martin, J. H. Erwin)

The present fuel plates for the inner annulus of the HFIR contain 0.55 wt % B_4C in the filler section of the duplex fuel core. In one of the designs for increasing the total ^{235}U loading of the reactor to 12.0 kg, the B_4C content of the filler section in the plates for the inner annulus will be increased to about 1.10 wt %. We do not know the irradiation performance of plates containing this concentration of B_4C. In fact, no irradiation tests of dispersion of B_4C in Al have been conducted in the G-12 loop of the ETR, whose conditions closely simulate those of HFIR.

The proposed increase in B will double, to a first approximation, the He content in the irradiated filler portion of the fuel plate for the inner annulus. The limiting criterion for irradiation performance could then conceivably be swelling of the region that contains B_4C. For example, the standard plate accommodates, at standard temperature and pressure, about 4 cm^3 of He per unit volume of filler section. An additional 4 cm^3 of He will undoubtedly lower the breakaway swelling temperature at which blisters can form and block a coolant channel.

We plan to determine the breakaway swelling temperature of irradiated dispersions of B_4C in Al clad with type 6061 Al alloy. The concentrations of B_4C to be investigated are 0.00, 0.52, 0.78, 1.05, 1.75, and 2.00 wt %. To achieve the highest temperature possible, the irradiation will be carried out in the sixth tier position of the G-12 loop, probably during ETR cycle 103. Tier 5 will contain the sol-gel and burned U_3O_8 mini-type test plates described above.

We have pressed and degassed five compacts for each of the six B_4C concentrations. Table 14.6 records their average attributes. These

Table 14.6. Record of Irradiation Test Compacts[a] Containing B_4C

	Average Attributes of Compacts[b]					
Core order number	1019	1020	1021	1022	1023	1024
Degassed composition						
Dispersoid[c]						
By weight, %	0.00	0.52	0.78	1.05	1.75	2.00
By volume, %	0.00	0.54	0.81	1.10	1.82	2.09
Voids, vol %	3.40	2.98	3.12	2.95	3.27	3.12
Standard deviation	0.31	0.21	0.09	0.23	0.08	0.30
Matrix Al	bal	bal	bal	bal	bal	bal
Degassed physical properties						
Dimensions, in.						
Length	0.3227	0.3228	0.3228	0.3228	0.3228	0.3229
Width	0.9630	0.9630	0.9630	0.9630	0.9630	0.9629
Thickness	0.1529	0.1527	0.1529	0.1529	0.1534	0.1532
Weight, g	2.0449	2.0515	2.0503	2.0530	2.0518	2.0529
Density, g/cm^3	2.6264	2.6368	2.6325	2.6367	2.6264	2.6299
Degassing changes						
Dimensions, mils						
Length	+0.1	+0.1	+0.1	+0.1	+0.1	+0.1
Width	0.0	0.0	−0.3	0.0	−0.1	0.0
Thickness	+0.2	0.0	+0.1	+0.1	+0.2	+0.1
Weight, mg	−0.9	−1.0	−0.7	−0.2	−0.3	−0.2
Density, %	−0.20	−0.06	−0.10	−0.06	−0.19	−0.10

[a]Five compacts were made from each core order number.

[b]Pressed at 30 tsi, then degassed for 15 min at 500°C.

[c]Concentration represents 0.752 g B/g B_4C or 0.1836 g ^{10}B/g B.

compacts have been clad with type 6061 Al but have not been fully evaluated in plate form.

When we proposed our B_4C experiment, INC personnel expressed concern about excessive neutron poisoning of regions adjacent to the G-12 loop. Six plates containing the desired B_4C contents were immediately fabricated and shipped to ETR site on January 19, 1969. Since then, they

have informed us by telephone that our plates contain an acceptable level of B_4C for insertion into the G-12 loop.

Determination of Homogeneity in Fuel Plates

B. E. Foster S. D. Snyder R. W. McClung

Radiographic Densitometry

We are continuing our extensive study on the use of radiography and densitometry to determine their qualitative and quantitative capabilities and limitations for detecting and measuring fuel inhomogeneity in dispersion-core fuel plates.[10]

The uniformity of the x-ray beam was determined by exposing x-ray film 42 in. long in the conventional manner with both 100 and 50 kv at a distance of 84 in. from film to focal plane. The film density was 0.98 in the center portion of the radiograph but decreased to 0.92 at each end. This nonuniformity could be interpreted as a change of about 12% in fuel concentration if a fuel plate were radiographed with these energies. When similar exposures were made with the longitudinal axis of the x-ray tube parallel to that of the x-ray film, however, the film density at one end for each exposure decreased to 0.81, which could result in an even larger bias if related to changes in fuel concentration.

Additional data were obtained regarding the use of safelights versus total darkness during the loading of cassettes and processing of film and regarding the localized variations in density that result. Individual sheets of x-ray film were exposed to red safelights and amber safelights before exposure to the x-ray beam and vice versa. The film exposed to a red safelight before being exposed to x rays showed no change in density from the film not exposed to the safelight, but the film that was exposed to the red safelight after being exposed to x rays showed an increase of 0.04 in film density. Similar experiments with the amber safelight showed an increase in film density of 0.30 when the

---

[10]B. E. Foster, S. D. Snyder, and R. W. McClung, Fuels and Materials Development Program Quart. Progr. Rept. Dec. 31, 1968, ORNL-4390, pp. 261–266.

film was first exposed to the safelight but an increase of 0.60 in film density when the film was exposed to safelight after it was exposed to the x rays.

X-Ray Attenuation

Two fuel plates for the Advanced Test Reactor (ATR), ZAY-18-4 and ZBB-18-14, were scanned on the x-ray attenuation scanner. We do not have a calibration relating U content per 5/64-in.-diam spot to x-ray attenuation for the UAl_x fuel, but we calculated the average U concentration per spot from the charged U loading and fuel area (measured from radiographs of the core outline). The average attenuation (chart reading) was obtained from a cursory examination of the scans of the fuel plates. The average values for loading and attenuation were compared to the U_3O_8 (HFIR) calibration to determine the attenuation bias between U_3O_8 and UAl_x. This bias correction was applied to establish the attenuation values that represented deviations from nominal loadings of −12, −8, +8, and +12% for fuel more than 1/2 in. long but 5/64 in. wide and a deviation of +27% for 5/64-in.-diam spots of fuel. These tolerances were selected by R. W. Knight.

We also inspected these plates according to the specifications for "Mark VI Fuel Element Advanced Test Reactor," dated May 26, 1967, using radiography both with and without the aid of a stepped calibration wedge. The comparative data for the three methods are shown in Table 14.7. Almost an order of magnitude more manhours were required to do the radiography than for the x-ray scanning.

Figure 14.5 is an X-Y map (plan view) that shows the location on the fuel plates of the areas that exceeded tolerances according to the inspection by x-ray scanning.

A report on evaluation of homogeneity in dispersion fuel plates has been written for presentation at the conference of the American Society for Quality Control in Los Angeles, California, May 7, 1969.

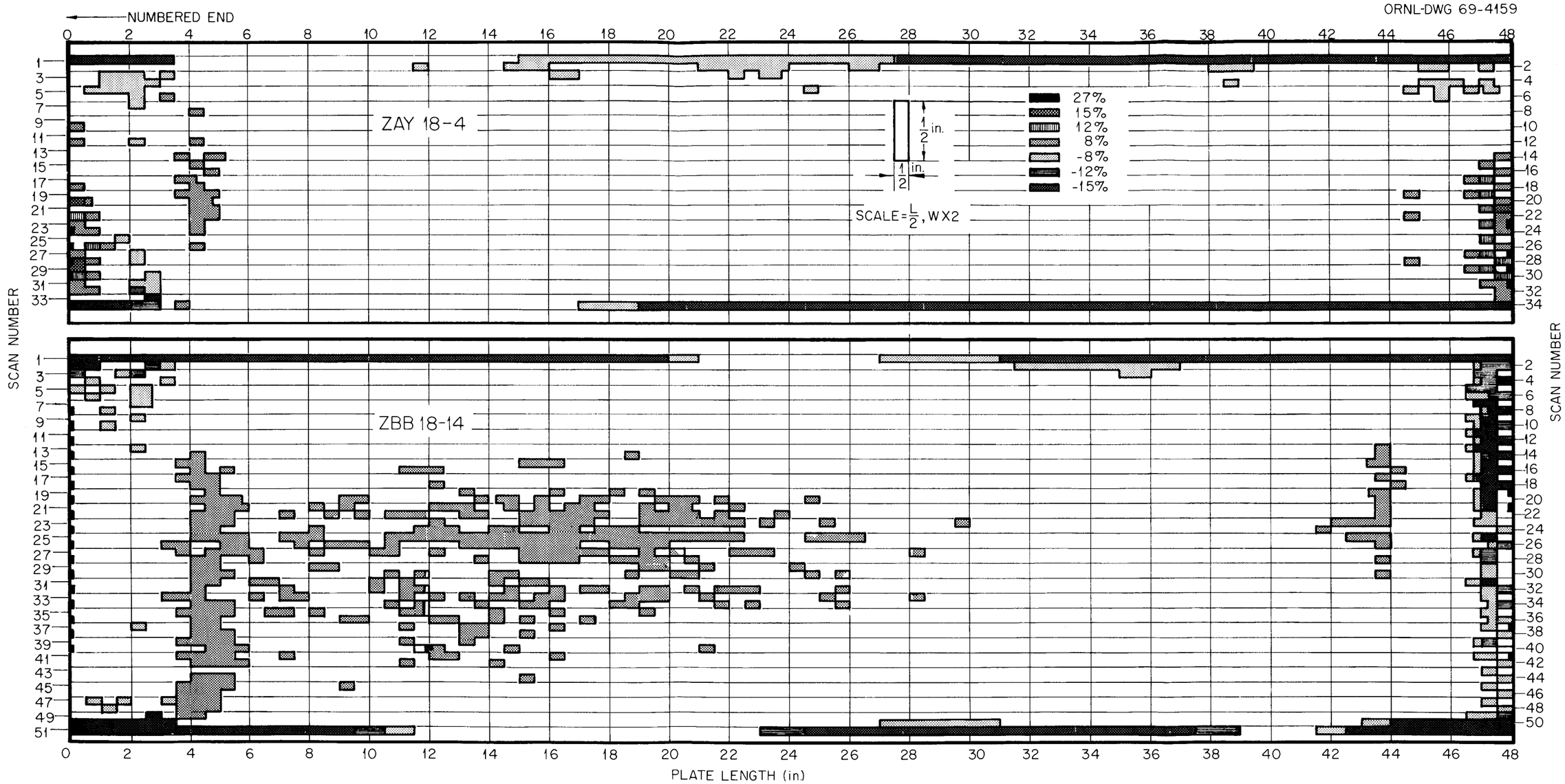

Fig. 14.5. Map of Fuel Homogeneity Showing Areas Deviating from Nominal Loading by ±8, ±12, and ±15% as Averaged Over a 1/2- by 5/64-in. Area and by +27% in a 5/64-in.-diam Spot for ATR Plates, Types 4 and 14, Loaded with UAl_x and Supplied by Idaho Nuclear Corporation.

Table 14.7. Comparative Data for X-Ray Scanning and Radiography

	Number of Areas More than 1/2-in. Long and Exceeding the Listed Percentages of Nominal Loading				Number of Spots Above +27% of Nominal Loading
	−12%	−8%	+8%	+12%	
	Plate ZAY-18-4				
X-ray scanning	6	37	54	14	10
Radiography					
With stepped calibration wedge	(a)	(a)	(a)	(a)	1
Without stepped calibration wedge	(a)	(a)	(a)	(a)	0
	Plate ZBB-18-14				
X-ray scanning	41	80	199	0	21
Radiography					
With stepped calibration wedge	(a)	(a)	(a)	(a)	0
Without stepped calibration wedge	(a)	(a)	(a)	(a)	0

(a) The specifications did not call for this evaluation of 1/2-in.-long fuel areas; therefore, it was not performed.

PART V

ENGINEERING PROPERTIES OF REACTOR MATERIALS

15. PHYSICAL AND MECHANICAL METALLURGY OF REFRACTORY ALLOYS

P. Patriarca

The purpose of this program is to provide a broad, base-technology evaluation of high-temperature alloys for use in high-performance nuclear reactors and isotopic heat sources for advanced space, terrestrial, and civilian power applications. Principal emphasis is placed on materials problems involving Ta-, Nb-, Mo-, and V-base alloys for systems that use alkali metals as thermodynamic working fluids and heat-transfer media.

Basic Physical Metallurgy Studies

H. Inouye

Solubility, Diffusivity, and Permeability of Interstitials in Refractory Metals (R. L. Wagner)

The diffusion, solubility, and permeation constants of N in W between 1000 and 1800°C were determined. A least-squares fit to the data gives the following equations for a 90% confidence limit:

$$D = 2.37 \pm 0.43 \times 10^{-3} \exp(-35{,}800 \pm 3{,}900 \text{ cal/RT}) \text{ cm}^2/\text{sec},$$

$$S = 0.21 \pm 0.06 \exp(-17{,}600 \pm 5{,}900 \text{ cal/RT}) \text{ torr liter (ref. 1) cm}^{-3} \text{ torr}^{-\frac{1}{2}},$$

$$K = 4.98 \times 10^{-4} \exp(-53{,}400 \text{ cal/RT}) \text{ torr liter cm}^{-1} \text{ sec}^{-1} \text{ torr}^{-\frac{1}{2}}.$$

Development of Age-Hardening Refractory Alloys (C. T. Liu, R. W. Carpenter)

We are attempting to strengthen refractory alloys at high temperature through precipitation mechanisms that produce fine particles distributed uniformly throughout the matrix. We are studying the four binary systems that possess this potential, Nb-Hf, Ta-Hf, Nb-Zr, and Ta-Zr.

---

[1] 1 torr liter = 1.205 cm^3 or 5.87×10^{-5} mole at standard temperature and pressure.

The formation of coarse, rosette precipitates was reported[2] for the aged Nb-Hf alloys quenched slowly from the homogenization temperature (about 1820°C). Figure 15.1 shows that the branches of rosette lie on two sets of mutually perpendicular planes separated 45° from each other. This crystallography suggests that the precipitates lie on the {100} and {110} planes of Nb-rich matrix. The kinetics of isothermal aging in the Nb–53% Hf alloy is shown in Fig. 15.2, which indicates (1) that the aging hardness for the oil-quenched specimens is higher than that for the furnace-cooled ones, and (2) that the curves for hardness versus time for the oil-quenched specimens are characterized by a portion of "fast precipitation reaction" at times of about 10 min for 1000°C aging, and 100 min for 600°C aging. There is a lack of such a portion on the curves for specimens cooled in the furnace. We believe that the vacancies produced by quenching are responsible for the initial, very rapid rate of precipitation. As aging proceeds, the excess vacancies gradually fall to their equilibrium value, and the precipitation reaction returns to its normal rate (i.e., slow precipitation reaction).

The morphology and rate of precipitation in Ta-Hf alloys are also sensitive to the quenching rate. The aged microstructure changes progressively from a uniform precipitate [Fig. 15.3(b)] to a Widmanstätten-type structure (Fig. 15.4) with a decreasing rate of quenching. Composition also plays an important role in the precipitation. Quenched specimens aged 4 hr at 1000°C show grain-boundary precipitation in the Ta–50% Hf alloy but not in the Ta–65% Hf alloy (Fig. 15.3). The former structure would be expected to show brittle fracture under a tensile test.

The tensile properties of Nb–70% Hf and Ta–29.5% Hf alloys at room temperature are summarized in Table 15.1. The quenched Ta-Hf alloy has reasonably good ductility but poor ductility when aged because of the formation of lamellar patches at grain boundaries (Fig. 14.2 of ref. 3).

---

[2]C. T. Liu and R. W. Carpenter, Fuels and Materials Development Program Quart. Progr. Rept. Dec. 31, 1968, ORNL-4390, pp. 274–280.

[3]C. T. Liu, Fuels and Materials Development Program Quart. Progr. Rept. Sept. 30, 1968, ORNL-4350, pp. 296–300.

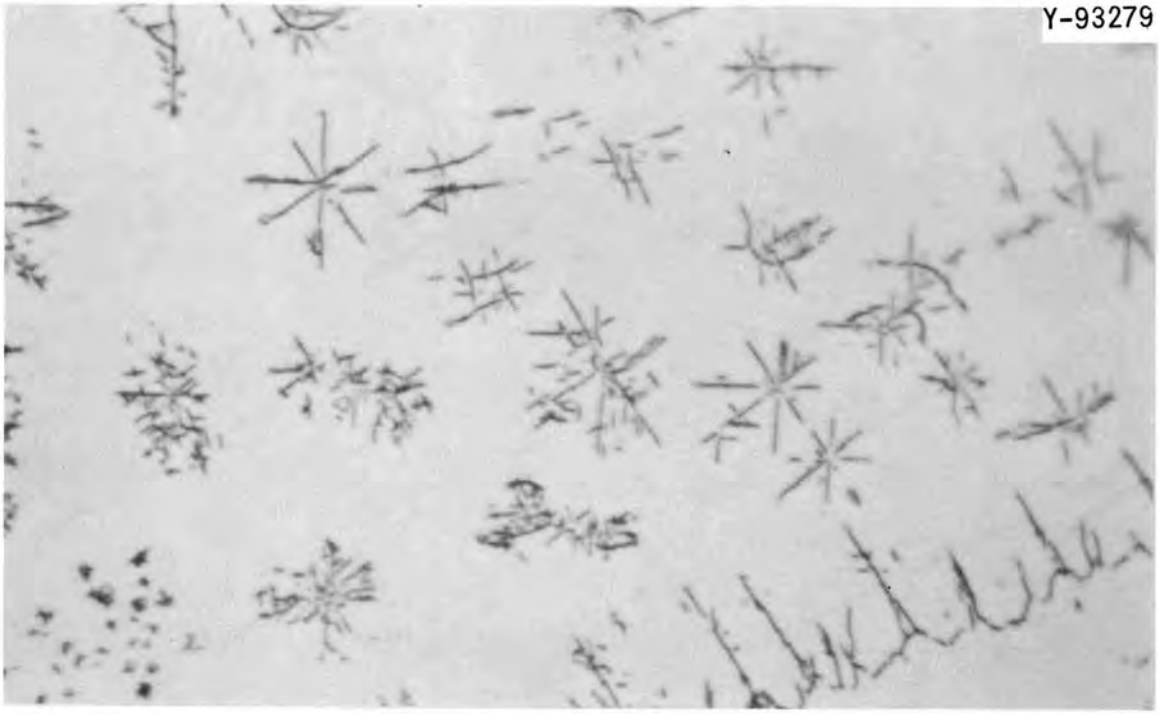

Fig. 15.1. Optical Photomicrograph of Nb–53% Hf Alloy Radiation-Quenched and Aged 3 hr at 1100°C. 1000×.

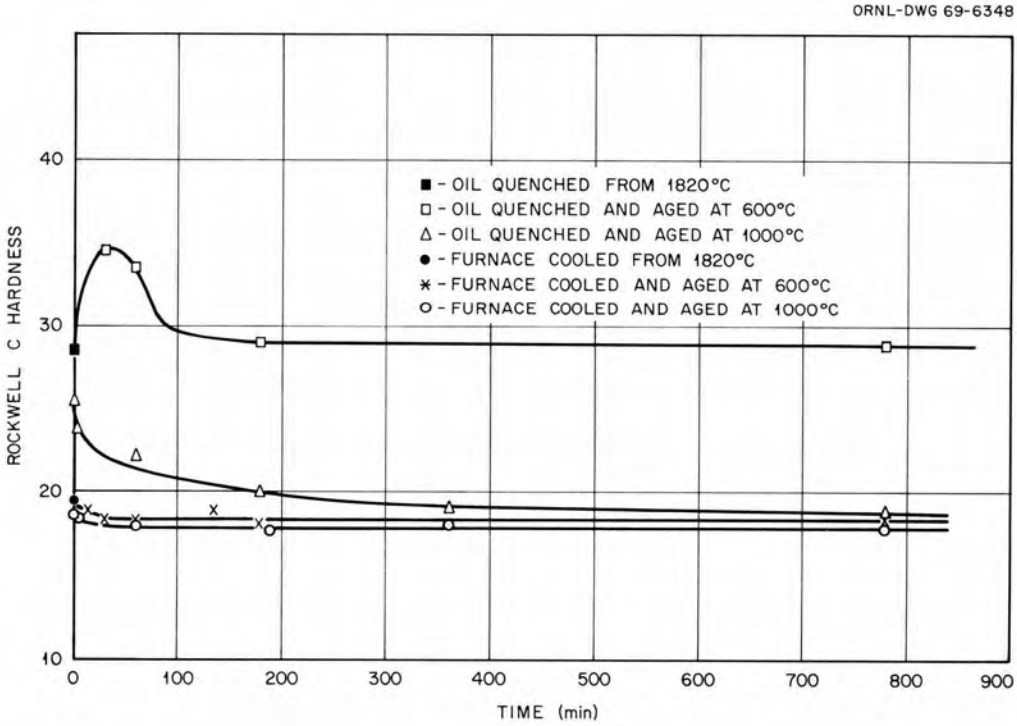

Fig. 15.2. The Effect of Quenching Rate on the Isothermal Aging of Nb–53% Hf Alloy.

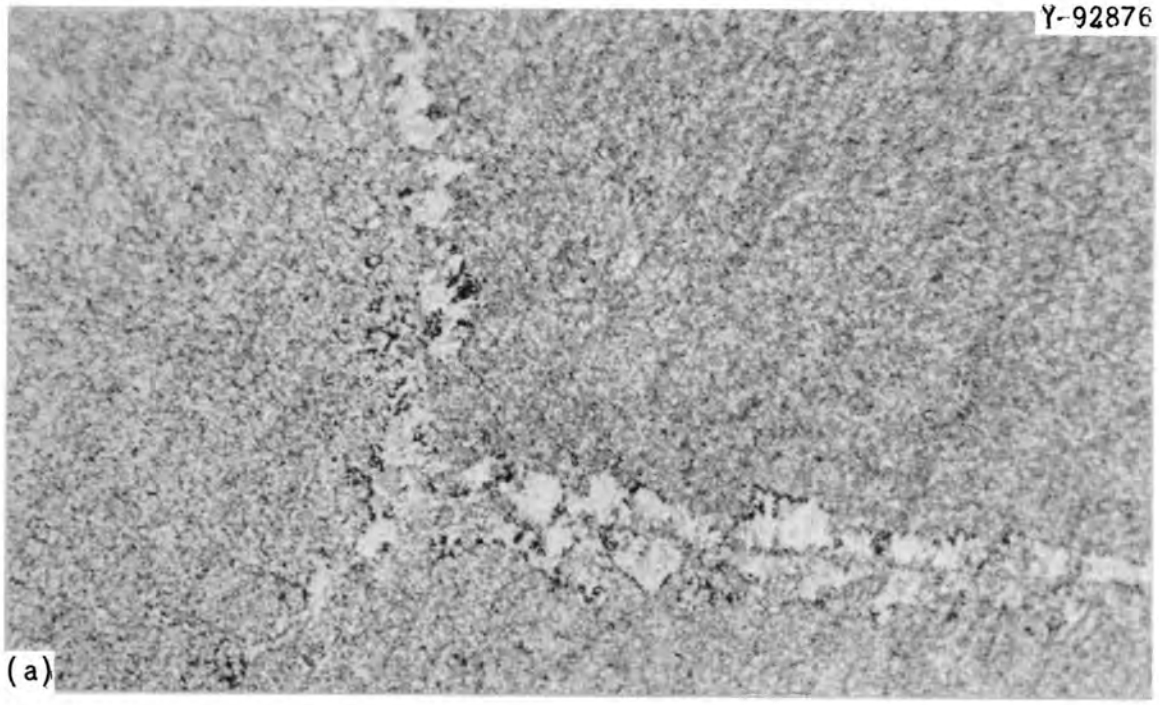

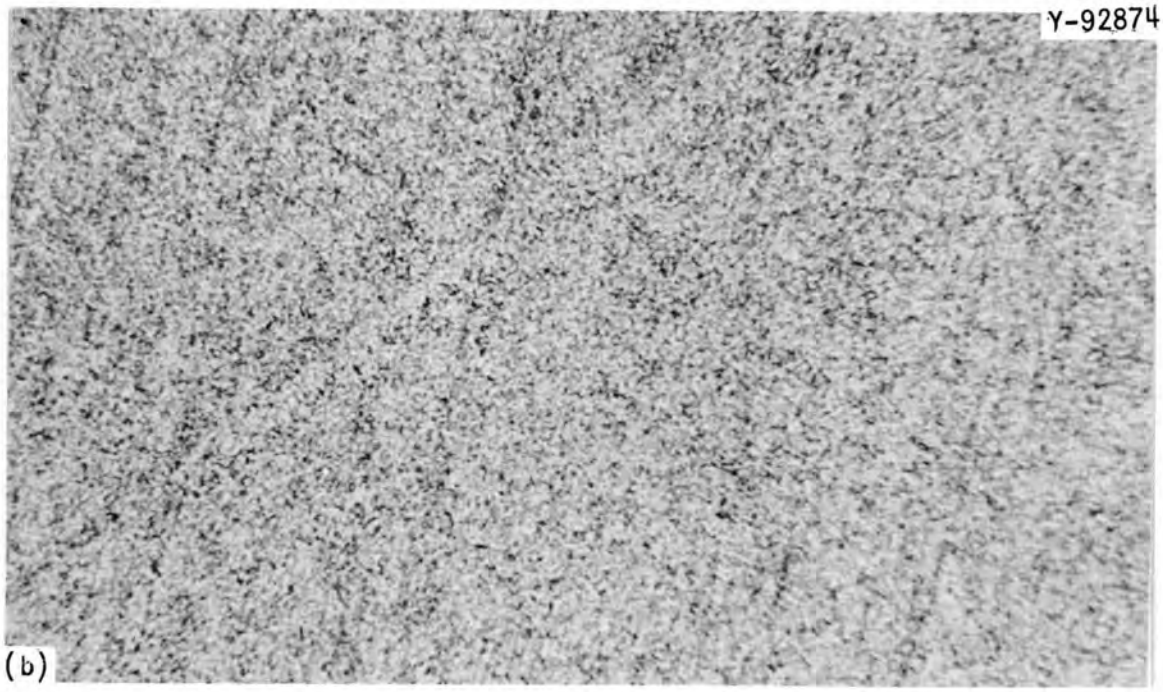

Fig. 15.3. Photomicrographs of Tantalum-Hafnium Alloys Cooled from 1820 to 1000°C in 40 sec and then Aged 4 hr at 1000°C. (a) Ta–50% Hf, 500×. (b) Ta–65% Hf, 500×. There is no precipitation at grain boundaries in the Ta–65% Hf alloy.

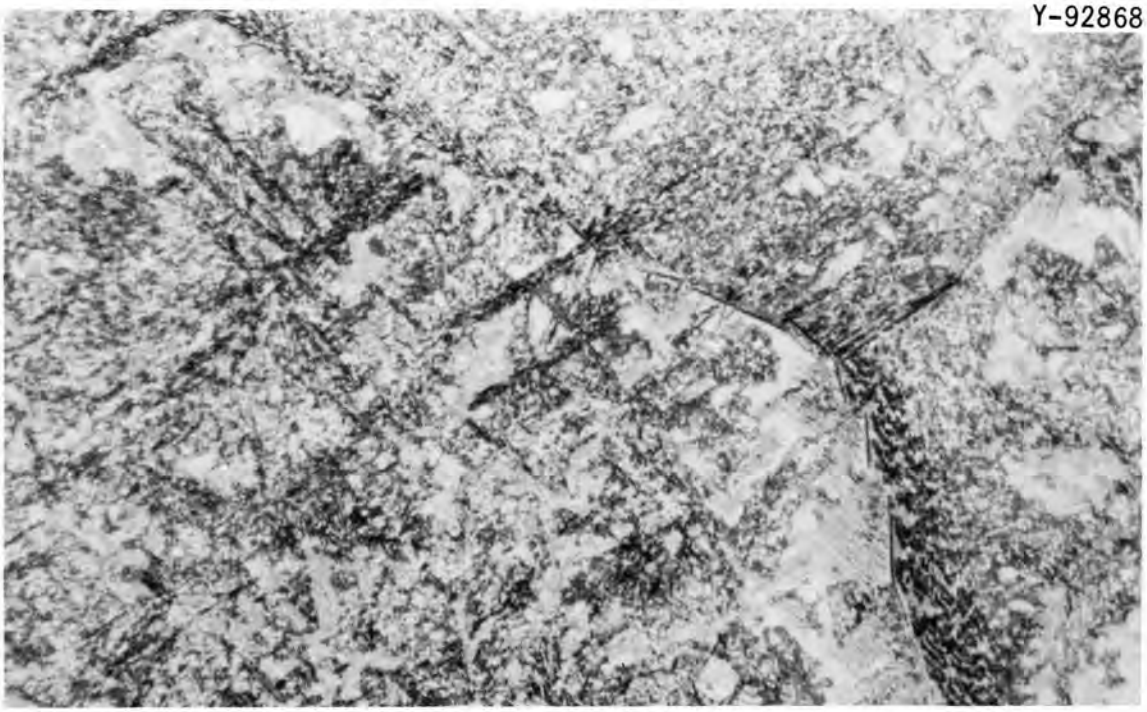

Fig. 15.4. Optical Photomicrograph of Ta–65% Hf Alloy Cooled at a Rate of 100°C in 3 min from 1820 to 1000°C and then Aged 4 hr at 1000°C. 300×.

Table 15.1. Effect of Aging on the Tensile Properties of Nb–70% Hf [N(30)-1-series] and Ta–29.5% Hf [T(70.5)-1-series] Alloys at Room Temperature

Specimen Number	Aging Treatment		Yield Strength (10^3 psi)	Strain to Fracture (%)
	Temperature (°C)	Time (hr)		
N(30)-1-60	As quenched		108	6.5
N(30)-1-58-a	1000	4	95.4	10
N(30)-1-62-a	1200	4	107	2.1
N(30)-1-54-a	1400	4	118	3.5
T(70.5)-1-54	As quenched		127	6.4
T(70.5)-1-54-c	850	4.2	157	0.85
T(70.5)-1-54-b	1100	0.1	131	0.72
T(70.5)-1-55-a	1100	4	122	0.6
T(70.5)-1-54-a	1300	5	120	1

Specimen N(30)-1-58-a (Table 15.1) had the best ductility because of the uniform distribution of precipitates observed on aging (Fig. 15.3 of ref. 4). The rate of work hardening in the Nb-Hf alloy is low in all cases. The fractures were primarily at grain boundaries.

Alloy homogenization is a difficult problem in Ta-Zr alloys due to low diffusivities, a low solidus temperature, and serious evaporation of Zr during extended heat treatments. A lamellar phase was present at grain boundaries in the specimens solution treated for short times at 1820°C. Most of this phase disappeared after 5 hr at this temperature. The critical temperature of the miscibility gap in the Nb-Zr system is 970°C; however, we found that a single-phase quenched structure can only be obtained by homogenizing 1 hr at 1400°C.

Long-Time High-Temperature Mechanical Properties of Commercial Refractory Alloys

R. L. Stephenson

The object of this program is to evaluate the creep-rupture properties of promising refractory metal alloys at high temperatures. In order to provide an adequate evaluation, stress-rupture curves are determined from 10 to 1000 hr at several temperatures from 1000 to 1650°C. In addition, the effects of annealing treatment and fabrication variables are studied in an effort to improve and better understand the most promising alloys.

Niobium Alloys

We are studying the effect of heat treatment on the creep-rupture properties of SU-16. Specimens were annealed at successively higher temperatures and then tested at 40,000 psi and 980°C. Figure 15.5 shows the times to 1 and 2% creep and to rupture as a function of

---

[4]C. T. Liu and R. W. Carpenter, Fuels and Materials Development Program Quart. Progr. Rept. Dec. 31, 1968, ORNL-4390, pp. 274–280.

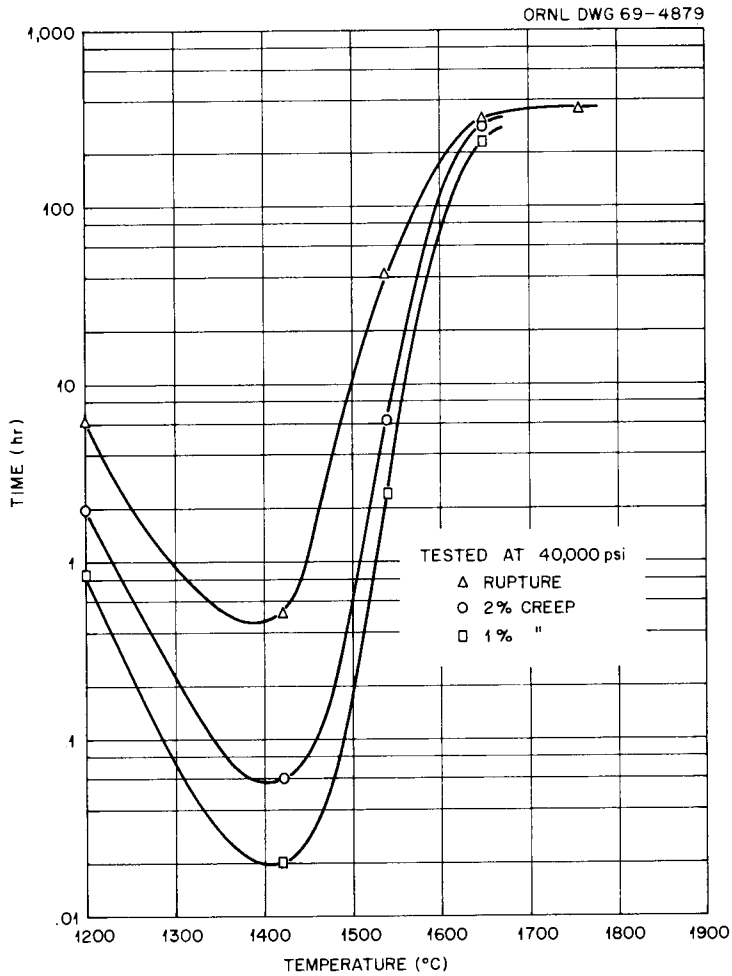

Fig. 15.5. Effect of Pretest Annealing Temperature on Creep-Rupture Properties of SU-16 at 980°C.

pretest annealing temperature. The microstructures of these specimens are being studied in the hope of explaining the features of these curves.

We are also studying the creep-rupture properties of C-129Y. The stress-rupture properties at 980, 1095, and 1205°C are shown in Fig. 15.6.

Molybdenum and Tantalum Alloys

We are continuing our study of the microstructure of specimens of Mo alloy. Transmission electron photomicrographs reveal very fine subcells about 0.5 μ in diameter. We are also studying the effect of heat treatment on the creep properties of T-111.

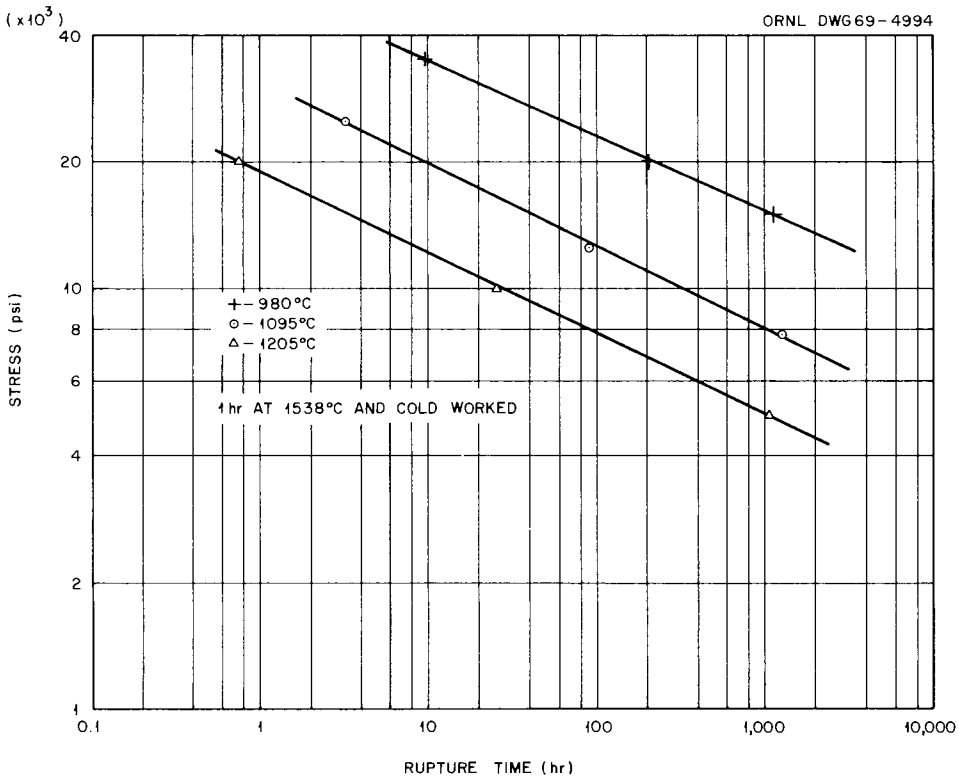

Fig. 15.6. Stress-Rupture Properties of C-129Y.

Studies of Physical Properties

High-Temperature Electrical Resistivity (R. K. Williams)

Our ultrahigh-vacuum high-temperature furnace has been used to measure electrical resistivity at temperatures up to 2600°K. A fairly pure, electron-beam-melted Ta specimen (resistivity ratio, 128) was used for the first run. Data were obtained from 300 to 1700°K using Pt–10% Rh vs Pt thermocouples and (above 1100°K) our automatically balancing optical pyrometer. Between 1100 and 1600°K, the two methods of measuring temperature gave results that agreed to ±2°K or better, well within the combined uncertainties of the two measurements (±5°K). All data obtained during the test lay within about ±0.1% of a smoothed curve, and no evidence of hysteresis was found after measurements at 2600°K. Pressures of about 5×10^{-8} torr were obtained at the highest temperature. The electrical resistivity data for Ta lie within the ±5% band of values found by other investigators, but are about 2 to 4 microhm-cm below some investigations. This proof testing represents

a major expansion of our measurement capacity, and data from this equipment will also extend our temperature range for estimates of thermal conductivity by 900°K (from 1700 to 2600°K). A detailed examination of the ρ:T data obtained on Ta is in progress.

Development of an Electrical Heating Method to Measure Thermal Conductivity (K.-H. Bode)

Final assembly of the component parts for this apparatus is in progress. Initial testing will be conducted during the next quarter on a Nb–10% W alloy for which we have previously measured thermal conductivity to 1250°K.

Welding and Brazing

G. M. Slaughter

Development of Brazing Alloys (D. A. Canonico, Nancy C. Cole)

Studies this quarter centered on joining graphite with an experimental brazing filler metal, No. 8H (Ti–20% Zr–15% Ge). Other work on this alloy composition has been described previously.[5,6] The excellent flowability of this alloy is typified by Fig. 15.7. Its ability to flow the entire length of the inverted T-specimen and also into the capillary formed between the base and leg of the specimen is impressive. The presence of the filler metal in the interstices of the low-density grade of graphite is also evident.

Studies were begun to determine the strength of these graphite brazes. Figure 15.8 shows a specimen both as brazed and after testing. Failure in all tests occurred through the base graphite, but always near the braze. The 7× photomacrograph in the lower portion of Fig. 15.8 further illustrates the location of failure and indicates the

[5]D. A. Canonico and Nancy C. Cole, Fuels and Materials Development Program Quart. Progr. Rept. June 30, 1968, ORNL-4330, pp. 352–354.

[6]Nancy C. Cole and D. A. Canonico, Fuels and Materials Development Program Quart. Progr. Rept. Dec. 30, 1968, ORNL-4390, pp. 285–290.

Y-93511

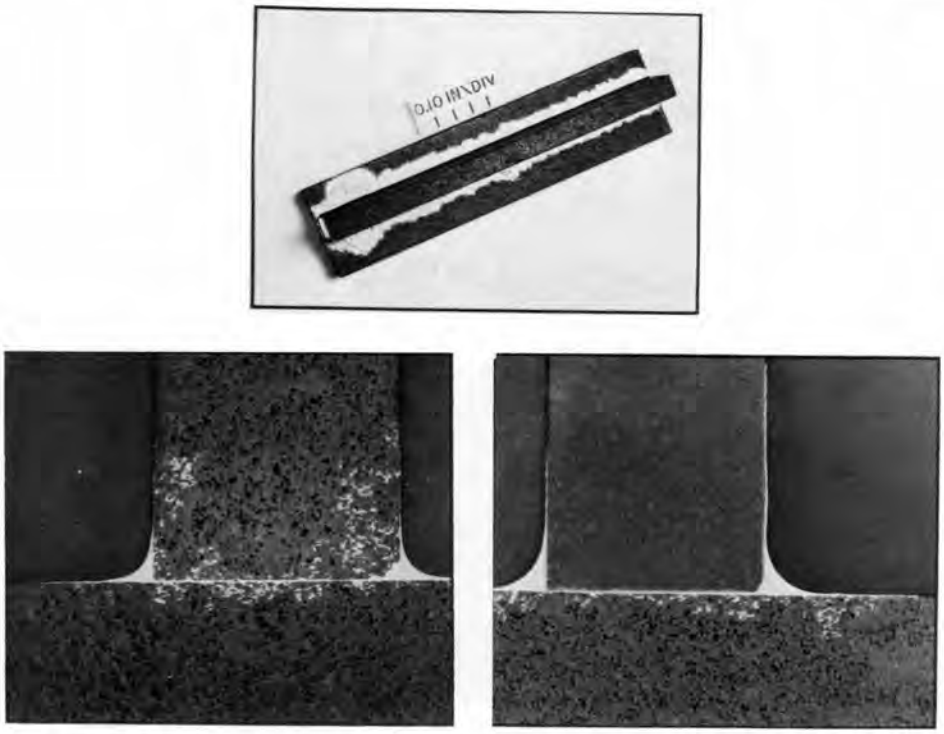

Low Density Brazed to Low Density

High Density Brazed to Low Density

Fig. 15.7. Graphite Brazes Made with Titanium-Zirconium-Germanium Filler Metal.

excellent flowability of the filler metal. No doubt much of the strength of these graphite brazes is due to the "mechanical locking" of the filler metal in the graphite interstices.

We are still trying to obtain accurate values for the actual strength of the braze joint itself. A new type of test specimen has been designed in which the joint will be loaded in compressive shear.

Y-93529

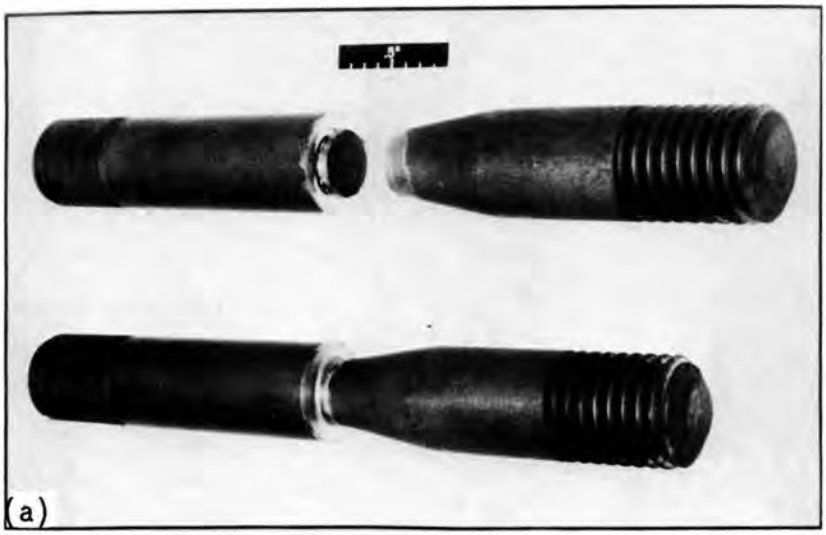

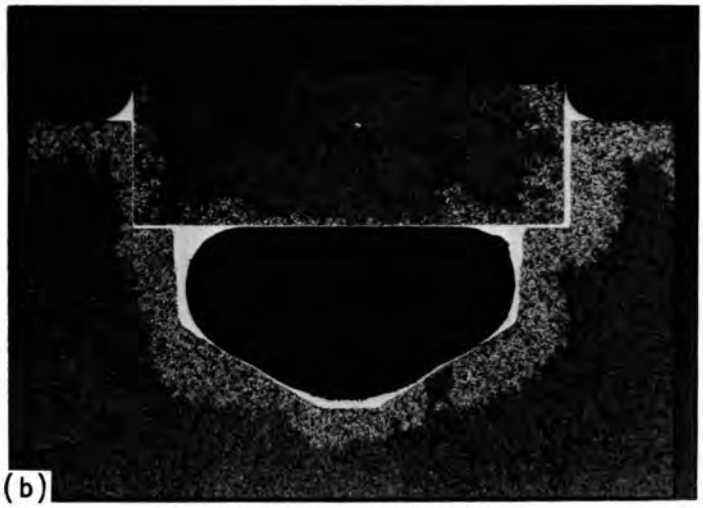

GRAPHITE BRAZE TEST RESULTS

Filler Metal: 65% Ti - 20% Zr - 15% Ge

Fig. 15.8. Test Specimens Used to Obtain Mechanical Properties of Graphite Brazes. (a) Specimens before and after testing. (b) Fracture area showing that failure occurred in base graphite.

16. CLADDING MATERIALS FOR SPACE ISOTOPIC HEAT SOURCES

P. Patriarca R. G. Donnelly

The immediate tasks of this program are (1) to evaluate the more promising superalloys that are available commercially and (2) to develop improved alloys and eventually qualify those that show greatest promise for containment of radioisotopes in space power systems. The superalloy studies include creep testing, evaluation of embrittling aging reactions, determination of evaporation characteristics, and studies of the interaction of stress and vacuum on properties at elevated temperatures. In the alloy development portion of the program, the strength, air-oxidation, aging, and evaporation properties will be determined.

Studies of Commercial Superalloys

Creep Testing of Haynes Alloy No. 25 (R. W. Swindeman)

Since the service conditions for isotopic heat sources differ from the normal conditions under which superalloys are used, some mechanical testing is necessary to determine the behavior of weldments under stress for very short times and temperatures between 1000 and 1300°C, conditions that are typical of exposures that might be expected during abort on the launch pad or during reentry. Another condition being investigated, typical of normal service, is the behavior of weldments after long exposure to modest temperatures, 600 to 900°C. Our data on weldments show that they have essentially the same strength as base metal under both testing conditions. Between 600 and 900°C, however, failures are quite common in the heat-affected zone near the fusion line. Figure 16.1(a) is a parametric curve showing data from the literature for the base metal. Figure 16.1(b) shows our data for weldments superimposed on the scatterband generated by Fig. 16.1(a).

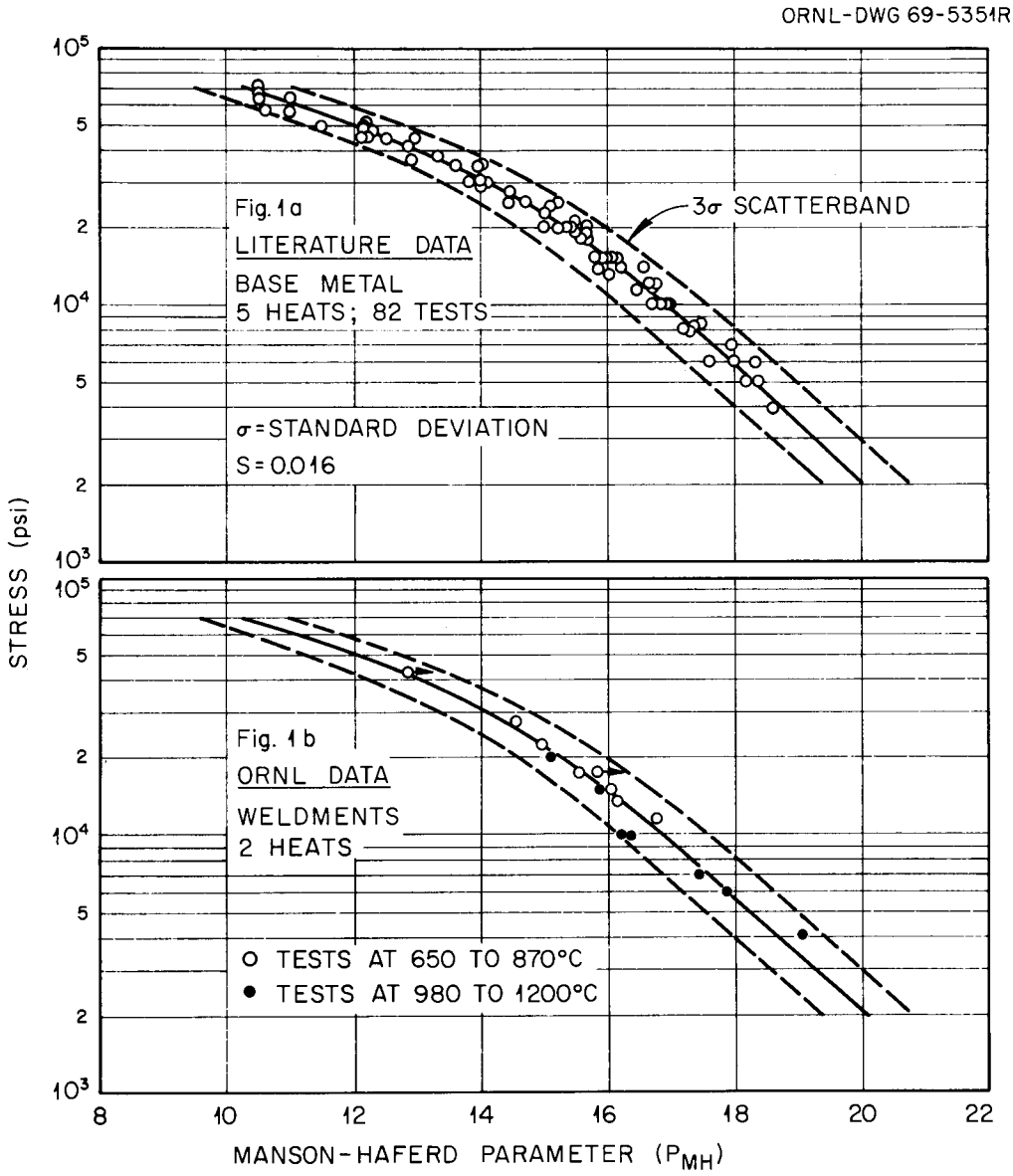

Fig. 16.1. Comparison of the Rupture Strength of Haynes Alloy No. 25 Weldments with the Scatterband Generated by Rupture Tests on Base Metal. Time-temperature correlation is based on the Manson-Haferd Parameter, P_{MH} = log time + $ST_{°C}$.

Interaction of Stress and Vacuum on Properties of Superalloys at Elevated Temperatures (D. T. Bourgette)

Haynes alloy No. 25 (Co–20% Cr–15% W–10% Ni) in high vacuum continues to show serious degradation of creep strength due to evaporation. Current results show that as the thickness of the specimen is increased, the vacuum effects are greatly diminished. For example, the time necessary to reach 1% creep strain at 15,000 psi and 800°C in vacuum is 60 hr for a 0.060-in.-thick specimen and 25 hr for a 0.030-in.-thick specimen. This trend was also observed at lower stress levels. At 900°C, the creep rate of specimens tested in vacuum is about 40 times greater than that of specimens tested in air; the rupture life of specimens tested in vacuum is only about one twenty-fifth that of those tested in air.

The evaporation kinetics of Haynes alloy No. 25 between 800 and 1150°C and the resulting changes in microstructure and composition have been reported.[1] The objective of current studies is to determine the evaporation behavior of other superalloys that have lower concentrations of elements, such as Cr and Mn, with high vapor pressures. We have found that the initial evaporation rate of Hastelloy N (Ni–17% Mo–7% Cr–5% Fe) is only one-sixth to one-tenth that of Haynes alloy No. 25. After 1000 hr, however, the rates are comparable due to the early loss of elements with high vapor pressures from the Haynes alloy.

Development of Improved Alloys

C. T. Liu H. Inouye

Studies of aging and hardness have shown that the rate and temperature of ordering of the experimental alloys differ. When the stable, ordered state is reached, however, there is little tendency for overaging.

Quenched-and-aged alloys S-1 to S-4 (compositions given in Table 16.1) are single phased and characterized by regular grains, large twin bands, and microtwins. The formation of microtwins, observed

[1]D. T. Bourgette, Vaporization Phenomena of Haynes Alloy No. 25 to 1150°C, ORNL-TM-1786 (May 1967).

Table 16.1. Tensile Properties of Experimental Cladding Alloys S-1 Through S-6 at Room Temperature

Alloy Number	Composition (wt %)	Heat Treatment	Alloy State	Strength: Yield (psi)	Strength: Ultimate Tensile (psi)	Total Elongation (%)
				$\times 10^3$	$\times 10^3$	
S-1	26 Co–74 Ni	Quenched from 1000°C	Disordered	16.1	66.2	42.4
		5 hr aging[a] at 700°C	Ordered $CoNi_3$	14.1	46.1	15.3
S-2	4.7 V–22 Co–73.3 Ni	Quenched from 1000°C	Disordered	22.5	81.2	43.1
		5 hr aging[a] at 700°C	Ordered $(Co,V)Ni_3$	24.7	75.6	38.4
S-3	9 V–46 Co–45 Ni	Quenched from 1150°C	Disordered	22.4	83	54.5
		5 hr aging[b] at 800°C	Short-range order	31.9	84	39.5
S-4	24 V–32.5 Co–43.5 Ni	Quenched from 1150°C	Disordered	67	134	63
		5 hr aging[b] at 600°C	Partially ordered $(Co,Ni)_3V$	83.2	143	59.7
		5 hr aging[b] at 700°C	Partially ordered $(Co,Ni)_3V$	117	183	13.7
		5 hr aging[b] at 800°C	Ordered $(Co,Ni)_3V$	125	131[c]	0.7[d]
S-5	45 Fe–55 Pt	Quenched from 1000°C	Disordered	72.8	102	33
		24 hr aging[a] at 700°C	Ordered Fe_3Pt	97.8	127.5	22

Table 16.1. (continued)

Alloy Number	Composition (wt %)	Heat Treatment	Alloy State	Strength Yield (psi)	Strength Ultimate Tensile (psi)	Total Elongation (%)
				$\times 10^3$	$\times 10^3$	
S-6	23.2 Co–76.8 Pt	Quenched from 1000°C	Disordered	44.5	121	41.5
		40 hr aging[a] at 500°C	Ordered CoPt	69	101[c]	4.7

[a]Quenched from 1000°C before aging.

[b]Quenched from 1150°C before aging.

[c]Fracture stress.

[d]Fractured on the shoulder of specimen.

at an early stage of aging, causes rapid increase of hardness[2] in alloys S-2 to S-4. These features disappear in fully ordered S-4; instead, the grains become very irregular and contain a substructure that cannot be resolved by the optical microscope. Transmission electron photomicrographs of alloy S-4 show numerous microtwins and stacking faults in addition to a small amount of acicular precipitates that are probably complexes of V and interstitials.

The tensile properties of alloys S-1 through S-6 are summarized in Table 16.1. From these, the following observations can be made. (1) As a general rule, the strength increases at the expense of ductility. However, both the strength and ductility of alloys S-2 to S-4 in the quenched condition increase steadily with the V content. Comparison of the tensile data for alloys S-3 and S-4 indicates that the formation of long-range order between V, Ni, and Co atoms is a very effective strengthening mechanism in this ternary alloy system. (2) The tensile properties of alloy S-4 in the disordered condition are comparable to those of Haynes alloy No. 25 in the annealed condition (Table 16.2), but, in the aged condition (ordered), alloy S-4 is stronger than aged Haynes alloy No. 25. (3) Alloy S-5 has good ductility and strength in both quenched and aged conditions (i.e., in both disordered and ordered states).

The creep behavior of ordered alloys S-5 (Fe_3Pt) and S-6 (CoPt) is being determined in high vacuum as a function of temperature. A log plot of the steady-state creep rate of alloy S-5 versus $\frac{1}{T}$ (T = absolute temperature) shows a discontinuous change of creep rate near 770°C, indicating the critical ordering temperature, T_c. The creep rate of ordered alloy S-5 at 750°C is about one-third the rate obtained by extrapolating the data for the disordered phase at high temperatures. This result clearly indicates the increase of creep strength upon ordering. The creep curves of ordered alloys show an interesting "inverse" transition during which the creep rate steadily accelerates to a steady-state value. This would be an advantage for capsules designed to low creep strain.

---

[2]E. Lamb, ORNL Isotopic Power Fuels Quart. Rept. Dec. 31, 1968, ORNL-4388, pp. 16–19. CLASSIFIED

Table 16.2. Comparison of Tensile Properties of Alloy S-4 and Haynes Alloy No. 25

Property	Unaged		Aged	
	S-4 (disordered)	Haynes alloy No. 25 (ref. a) (solution treated)	S-4 (5 hr at 700°C)	Haynes alloy No. 25 (ref. b) (500 hr at 760°C)
Yield strength, psi	67,000	62,000	117,000	77,000
Ultimate tensile strength, psi	134,000	139,000	183,000	
Total elongation, %	63	62.2	13.7	16

[a] Haynes Alloy No. 25, Data Sheet F-30,041D, Materials Systems Division, Union Carbide Corporation (February 1969).

[b] D. R. Ireland, The Effects of Aging on Dissimilar Metal Welded Joints with Multipass Welding of Hastelloy X and Hastelloy W Filler Metal, BNWL-290 (July 1966).

Table 16.3 summarizes the evaporation rates of several experimental alloys at 1000°C in vacuums of about 10^{-7} torr. The data are compared with the rates measured for Haynes alloy No. 25 and the calculated rates for Co, Ni, and Fe from their vapor pressure. The evaporation rates of the binary alloys decrease with the Pt content and in all cases are lower than the rate for Haynes alloy No. 25.

The activity of the vaporizing species in the binary alloys (Co, Ni, or Fe) was calculated from the ratio G_a/G_*, where G_a is the evaporation rate of the alloy, and G_* is evaporation rate of the pure metal. The Pt concentration, calculated from the thermodynamic properties of the binary alloys, was assumed to be the surface concentration of the evaporated alloys since the weight losses accounted for a maximum increase in composition of less than 0.4% Pt.

Alloy S-3 is in the disordered state, and S-4 forms the ordered phase $(Co,Ni)_3V$ at these test conditions. Comparison of the evaporation rates of these two alloys indicates that ordered alloys evaporate more slowly than disordered alloys.

Table 16.3. Evaporation Rates of Experimental Alloys at 1000°C and 10^{-7} torr

Alloy Number	Composition (wt %)	Evaporation Rate (mg cm^{-2} hr^{-1})	Activity of Co, Ni, or Fe	Concentration of Platinum at Surface (wt %)
		$\times 10^{-3}$		
S-3	Ni–46.4 Co–9 V	4.6		
S-4	Ni–32.5 Co–24.0 V	2.0		
S-5	Pt–45 Fe	6.9	0.31	71.4
S-6	Pt–23.2 Co	0.16	0.02	99.4
S-11	Co–27 Pt	2.8	0.59	69.8
S-12	Ni–27 Pt	2.8	0.72	56.3
S-13	Fe–28 Pt	12.0	0.69	63.1
	Co	7.7		
	Ni	4.6		
	Fe	22.0		
Haynes alloy No. 25	Co–20 Cr–15 W–10 Ni	23.0		

The experimental alloys that exhibit transformation from disorder to order exhibit their expected mechanical and evaporation behavior. The data reinforce our initial conclusion that ordered alloys are most suitable as the cladding for isotopic fuels because of their aging stability, creep behavior, and lower evaporation rates. Selective evaporation to form a surface layer high in Pt has been demonstrated.

Previous reports in this series:

ORNL-4330	Period Ending June 30, 1968
ORNL-4350	Period Ending September 30, 1968
ORNL-4390	Period Ending December 31, 1968

ORNL-4420
UC-25 – Metals, Ceramics, and Materials

INTERNAL DISTRIBUTION

1–3. Central Research Library
4–5. ORNL – Y-12 Technical Library
Document Reference Section
6–20. Laboratory Records Department
21. Laboratory Records, ORNL RC
22. ORNL Patent Office
23. R. E. Adams
24. G. M. Adamson, Jr.
25. S. E. Beall
26. R. L. Beatty
27. R. J. Beaver
28. M. Bender
29. R. G. Berggren
30. D. S. Billington
31. E. E. Bloom
32. A. L. Boch
33. K.-H. Bode
34. E. S. Bomar
35. C. D. Bopp
36. B. S. Borie
37. D. T. Bourgette
38. G. E. Boyd
39. R. A. Bradley
40. R. J. Breeding
41. R. B. Briggs
42. R. E. Brooksbank
43. W. E. Brundage
44. D. A. Canonico
45. R. W. Carpenter
46. R. M. Carroll
47. J. V. Cathcart
48. A. K. Chakraborty
49. Ji Young Chang
50. D. L. Clark
51. G. W. Clark
52. N. C. Cole
53. K. V. Cook
54. W. H. Cook
55. G. L. Copeland
56. W. B. Cottrell
57. C. M. Cox
58. F. L. Culler
59. C. W. Cunningham
60. J. E. Cunningham
61. H. L. Davis
62. V. A. DeCarlo
63. W. E. Deeds
64. J. H. DeVan
65. J. R. DiStefano
66. C. V. Dodd
67. R. G. Donnelly
68. D. A. Dyslin
69. T. Eck
70. W. S. Ernst
71. J. H. Erwin
72. R. B. Evans III
73. K. Farrell
74. J. I. Federer
75. D. E. Ferguson
76. R. B. Fitts
77. B. Fleischer
78. B. E. Foster
79. A. P. Fraas
80. J. H Frye, Jr.
81. W. Fulkerson
82. L. C. Fuller
83. R. E. Gehlbach
84. T. G. Godfrey, Jr.
85. G. M. Goodwin
86. J. M. Googan (Y-12)
87. R. J. Gray
88. W. R. Grimes
89. A. G. Grindell
90. H. D. Guberman
91. L. L. Hall
92. D. G. Harman
93. W. O. Harms
94–97. M. R. Hill
98. N. E. Hinkle
99. D. O. Hobson
100. H. W. Hoffman
101. F. J. Homan
102. R. W. Horton
103. W. R. Huntley
104. H. Inouye
105. D. H. Jansen
106. J. D. Jenkins
107. W. H. Jordan
108. G. W. Keilholtz
109. R. T. King

110. R. L. Klueh
111. R. W. Knight
112. J. Komatsu
113. J. A. Lane
114. J. M. Leitnaker
115. B. C. Leslie
116. C. S. Lever
117. T. B. Lindemer
118. A. P. Litman
119. C. T. Liu
120. H. R. Livesey
121. B. T. Loh
122. E. L. Long, Jr.
123. A. L. Lotts
124. C. D. Lundin
125. J. W. Luquire
126. R. N. Lyon
127. H. G. MacPherson
128. R. E. MacPherson
129. M. M. Martin
130. W. R. Martin
131. R. W. McClung
132. H. E. McCoy, Jr.
133. H. C. McCurdy
134. R. E. McDonald
135. W. T. McDuffee, Jr.
136. D. L. McElroy
137. C. J. McHargue
138. A. J. Miller
139. E. C. Miller
140. J. P. Moore
141. R. E. Moore
142. W. L. Moore
143. C. S. Morgan
144. J. G. Morgan
145. F. H. Neill
146. T. M. Nilsson
147. T. A. Nolan (K-25)
148. K. Notz
149. S. M. Ohr
150. A. R. Olsen
151. M. F. Osborne
152. P. Patriarca
153. W. H. Pechin
154. R. B. Perez
155. A. M. Perry
156. S. Peterson
157. R. A. Potter
158. R. B. Pratt
159. M. K. Preston
160. R. E. Reed
161. G. A. Reimann
162. A. E. Richt
163. P. L. Rittenhouse
164. H. E. Robertson
165. M. W. Rosenthal
166. D. J. Rucker
167. C. F. Sanders
168. G. Samuels
169. A. W. Savolainen
170. J. E. Savolainen
171. A. C. Schaffhauser
172. J. L. Scott
173. J. D. Sease
174. C. E. Sessions
175. O. Sisman
176. G. M. Slaughter
177. S. D. Snyder
178. K. E. Spear
179. I. Spiewak
180. P. Spindler
181. W. G. Spoeri
182. J. E. Spruiell
183. W. J. Stelzman
184. R. L. Stephenson
185. J. O. Stiegler
186. D. A. Sundberg
187. R. W. Swindeman
188. E. J. Tenckhoff
189. V. J. Tennery
190. K. R. Thoms
191. D. B. Trauger
192. R. L. Wagner
193. G. M. Watson
194. S. C. Weaver
195. M. S. Wechsler
196. A. M. Weinberg
197. J. R. Weir, Jr.
198. W. J. Werner
199. H. L. Whaley
200. G. D. Whitman
201. F. W. Wiffen
202. J. M. Williams
203. L. C. Williams
204. R. K. Williams
205. R. O. Williams
206. J. C. Wilson
207. R. G. Wymer
208. F. W. Young, Jr.
209. C. S. Yust
210. C. M. Adams, Jr. (Consultant)
211. Leo Brewer (Consultant)

212. L. S. Darken (Consultant)
213. J. A. Krumhansl (Consultant)

EXTERNAL DISTRIBUTION

AIR FORCE MATERIALS LABORATORY, Wright-Patterson Air Force Base

214. C. H. Armbruster
215. H. M. Burte
216. G. Glenn
217. Technical Director

AIR FORCE WEAPONS LABORATORY, Kirtland Air Force Base

218. D. Brooks

AMES LABORATORY

219. O. N. Carlson
220. W. L. Larsen
221. M. Smutz
222. F. H. Spedding

ARGONNE NATIONAL LABORATORY

223. L. Baker
224. J. H. Kittel
225. M. V. Nevitt
226. P. G. Shewmon
227. R. C. Vogel

LMFBR PROGRAM OFFICE, Argonne National Laboratory

228. A. Amorosi
229. L. Burris
230. L. Kelman
231. J. M. McKee

AEC-RDT SITE REPRESENTATIVES

232. M. E. Jackson, Argonne National Laboratory
233. D. J. Wille, Atomic Power Development Associates
234. R. L. Morgan, Atomics International
235. J. V. Levy, General Electric, Cincinnati
236. J. F. Weissenberg, General Electric, Cincinnati
237. R. H. Ball, Gulf General Atomic
238. J. E. Hebert, Idaho
239. D. A. Moss, Idaho
240. K. A. Trickett, Idaho
241. D. F. Cope, Oak Ridge National Laboratory
242. C. L. Matthews, Oak Ridge National Laboratory
243. P. G. Holsted, Pacific Northwest Laboratory
244. J. Sako, Pacific Northwest Laboratory
245. Atomic Energy Commission Library, Washington

DIVISION OF NAVAL REACTORS, AEC, Washington

246. R. H. Steele

DIVISION OF REACTOR DEVELOPMENT AND TECHNOLOGY, AEC, Washington

247. J. C. Crawford, Jr.
248. G. W. Cunningham
249. A. Giambusso
250. H. G. Hembree
251. J. R. Hunter
252. E. E. Kintner
253. W. H. Layman
254. W. H. McVey
255. J. J. Morabito
256. R. E. Pahler
257. A. J. Pressesky
258. M. A. Rosen
259. J. M. Simmons
260. E. E. Sinclair
261. A. Taboada
262. A. N. Tardiff
263. A. Van Echo
264. C. E. Weber
265. M. J. Whitman

DIVISION OF RESEARCH, AEC, Washington

266. P. W. McDaniel
267. D. K. Stevens

DIVISION OF SPACE NUCLEAR SYSTEMS, AEC, Washington

268. R. E. Anderson
269. D. Beard
270. J. F. Griffo
271. F. D. Haines
272. C. E. Johnson
273. J. A. Powers
274. F. C. Schwenk

OAK RIDGE OPERATIONS OFFICE

275. W. J. Larkin
276. Laboratory and University Division

ATOMIC POWER DEVELOPMENT ASSOCIATES

277. E. C. Kovacic
278. A. A. Shoudy

ATOMICS INTERNATIONAL

279. H. Pearlman
280. J. G. Asquith

BABCOCK AND WILCOX COMPANY, Lynchburg, Virginia 24505

281. C. Baroch
282. S. P. Grant
283. C. Johnson
284. L. Weissert

BATTELLE MEMORIAL INSTITUTE, Columbus, Ohio

285. W. Berry
286. D. Keller
287. S. J. Paprocki
288. Defense Materials Information Center

BATTELLE MEMORIAL INSTITUTE, PNL, Richland, Washington

289. A. L. Bement
290. J. J. Cadwell
291. T. T. Claudson
292. D. L. Condotta
293. E. Evans
294. B. R. Hayward
295. B. M. Johnson
296. W. E. Roake
297. D. W. Shannon
298. J. C. Tobin
299. R. G. Wheeler
300. Technical Information File

FAST FLUX TEST FACILITY, Battelle-Northwest

301. E. R. Astley

BROOKHAVEN NATIONAL LABORATORY

302. D. H. Gurinsky
303. C. Klamut

BUREAU OF MINES

304. Haruo Kato, Albany Metallurgy Research Center, P. O. Box 70, Albany, Oregon 97321
305. T. Sullivan, Bureau of Mines, Boulder City, Nevada 89005

COMBUSTION ENGINEERING

306. W. P. Chernock
307. S. S. Christopher

GENERAL ELECTRIC, Cincinnati

308. D. H. Ahmann
309. H. C. Brassfield
310. V. P. Calkins
311. E. Hoffman
312. J. McGurty
313. J. Moteff

GENERAL ELECTRIC, Nuclear Systems Programs, Cincinnati

314. E. E. Hoffman

GENERAL ELECTRIC, San Jose

315. R. Duncan
316. H. Klepfer

GENERAL ELECTRIC, Pleasanton

317. H. W. Alter

GENERAL ELECTRIC, Sunnyvale

318. K. P. Cohen
319. F. Comprelli
320. R. Skavdahl
321. C. Spalaris
322. E. L. Zebroski

GULF GENERAL ATOMIC

323. D. B. Coburn
324. A. J. Goodjohn
325. J. P. Howe
326. S. Jaye
327. J. F. Watson

IDAHO NUCLEAR CORPORATION

328. W. C. Francis

ILLINOIS INSTITUTE OF TECHNOLOGY RESEARCH INSTITUTE

329. D. J. McPherson

JET PROPULSION LABORATORY (NASA)

330. J. Davis

KNOLLS ATOMIC POWER LABORATORY

331. R. F. Wojciescak
332. Document Library

LOS ALAMOS SCIENTIFIC LABORATORY

333. R. D. Baker
334. D. B. Hall
335. J. A. Leary
336. R. Perkins
337. R. E. Peterson
338. Reports Library

MOUND LABORATORY

339. R. G. Grove

NASA HEADQUARTERS

340. J. J. Lynch

NASA, LEWIS RESEARCH CENTER

341. M. Ault
342. J.W.R. Creagh
343. J. J. Lombardo
344. T. P. Moffitt
345. T. A. Moss
346. F. E. Rom
347. L. Rosenblum
348. N. D. Sanders
349. N. Saunders
350. C. M. Scheuermann
351. H. Schwartz

NAVAL RESEARCH LABORATORY

352. J. R. Hawthorne
353. C. Serpan
354. L. E. Steele

NORTH CAROLINA UNIVERSITY, Raleigh, North Carolina 27607

355. J. Beeler
356. R. E. Dahl

NUCLEAR MATERIALS AND EQUIPMENT CORPORATION

357. C. Caldwell
358. K. Puechl

OHIO STATE UNIVERSITY, Columbus, Ohio 43212

359. M. G. Fontana
360. R. W. Staehle

RENSSELAER POLYTECHNIC INSTITUTE

361. W. Dickinson
362. W. F. Savage
363. C. B. Willingham, Jr.

SANDIA CORPORATION

364. J. Read Holland
365. J. Jacobs
366. D. R. Johnson

SAVANNAH RIVER LABORATORY

367. P. H. Permar
368. S. P. Rideout

TRW SYSTEMS (NASA), Redondo Beach, California 90278

369. H. Lurie

UNION CARBIDE CORPORATION, New York

370. J. A. Swartout

UNION CARBIDE CORPORATION, Materials Systems Division, Indianapolis

371. C. F. Leitten, Jr.

UNITED NUCLEAR CORPORATION

372. A. Strasser

UNIVERSITY OF CALIFORNIA, Lawrence Radiation Laboratory, Livermore

373. W. R. Holman
374. J. S. Kane
375. L. W. Roberts
376. A. J. Rothman
377. B. Rubin

U.S. NAVAL AIR SYSTEM COMMAND (AIR-52031B)

378. T. Kearns
379. I. Machlin

USAEC Scientific Representative, American Embassy, Box 40 FPO, N.Y. 09510

380. W.L.R. Rice

WESTINGHOUSE, Advanced Reactor Division, Waltz Mill Site

381. E. C. Bishop
382. J.C.R. Kelly
383. P. J. Levine
384. P. Murray
385. W. E. Ray
386. G. A. Whitlow

WESTINGHOUSE, Astronuclear Laboratory

387. R. T. Begley
388. D. C. Goldberg

WESTINGHOUSE, Atomic Power Division

389. T. Stern

WESTINGHOUSE, Bettis

390. R. H. Fillnow
391. P. N. Gustafson
392. Westinghouse Bettis Laboratory Library

393–614. Given distribution as shown in TID-4500 under Metals, Ceramics, and Materials category (25 copies – CFSTI)